CALIFORNIA STATE POLYTECHNIC UNIVERSITY, POMONA
THESIS ELECTRONIC SIGNATURE PAGE

Submitted: Term Spring Year 2022
Bronco ID: 014288443
Email Address: gstewart1@cpp.edu

THESIS INFORMATION

THESIS TITLE	A Structural and Geochemical Characterization of Early Artisinal Gold Mines in t
AUTHOR	Garrett Llewellyn Stewart
PROGRAM	Geology, M.S.

SIGNATURES

Jonathan A. Nourse
Committee Chair Name
Thesis Committee Chair
Position
Geological Sciences
Department

Organization

DocuSigned by: Jonathan A. Nourse
562E96F6E80E44B...
5/16/2022
Signature
janourse@cpp.edu
Email

Stephen G. Osborn
Committee Member 2 Name
Committee Member and Professor
Position
Geological Sciences
Department

Organization

DocuSigned by: Stephen G. Osborn
B1E6BFB18441457...
5/16/2022
Signature
sgosborn@cpp.edu
Email

Bryan P. Murray
Committee Member 3 Name
Committee Member and Associate Professor
Position
Geological Sciences
Department

Organization

DocuSigned by:
20873EBAB5874F6...
5/16/2022
Signature
bpmurray@cpp.edu
Email

Upload Thesis Attachment:

Revised August 2020,
Graduate Studies Office

A STRUCTURAL AND GEOCHEMICAL CHARACTERIZATION OF EARLY ARTISANAL GOLD MINES IN THE CENTRAL AND SOUTHWESTERN RAND MOUNTAINS, MOJAVE DESERT, CALIFORNIA

A Thesis

Submitted to the

Faculty of

California State Polytechnic University, Pomona

In Partial Fulfillment

Of the Requirements for the Degree

Master of Science

In

Geology

By

Garrett L. Stewart

2022

SIGNATURE PAGE

THESIS:	A STRUCTURAL AND GEOCHEMICAL CHARACTERIZATION OF EARLY ARTISANAL GOLD MINES IN THE CENTRAL AND SOUTHWESTERN RAND MOUNTAINS, MOJAVE DESERT, CALIFORNIA
AUTHOR:	Garrett L. Stewart
DATE SUBMITTED:	Spring, 2022
	Department of Geological Sciences

Dr. Jonathan A. Nourse
Thesis Committee Chair
Geological Sciences
____

Dr. Stephen G. Osborn
Geological Sciences
____

Dr. Bryan P. Murray
Geological Sciences
____

AKNOWLEDGEMENTS

These past three years of school have been the toughest and most rewarding academic challenge of my life thus far. I am very proud of the work I have accomplished and am extremely grateful for the tremendous amount of support I have received from a multitude of people while I completed my thesis. First, I would like to thank my thesis advisor, Dr. Nourse, for accepting me into the program and putting together a project that perfectly fit my interests in exploration and economic geology. His constant support and encouragement throughout the entire graduate school process provided me with all of the opportunities I needed to succeed. Next, I would like to express my gratitude to Dr. Murray, Dr. Osborn, and Dr. Van Buer for their assistance and advice with various stages of my thesis. I also greatly appreciate the enthusiastic and fantastic geochronologic work done by Dr. Hames of Auburn University. Additionally, I would like to acknowledge American Assay Laboratories for their excellent assay results and the Washington State University Geology Department for their superb XRF work.

The field work for this project would have been nearly impossible without the assistance of Ben Rucker. He was always willing and eager to lend his time and 4runners to transport me in and out of the most rugged areas of my field site. His friendship and company during my field visits is appreciated more than I can express with words.

Outside of school, I would like to thank my parents for encouraging my pursuit of a Master’s Degree. Their excitement and interest in everything I have done kept me motivated over the last few years. Lastly, I extend my deepest gratitude to Greg, Kristin, and Kari Middleton. They have treated me as family this past year and provided me with

a home away from home. I can only hope to one day return to them a fraction of the warm hospitality and immeasurable generosity they showed me.

ABSTRACT

The gold-silver-tungsten ore deposits of the Randsburg Mining District at the northeastern end of the Rand Mountains have been heavily exploited and studied. However, ore mineralization in the poorly explored central and southwestern portions of the mountain range has not been studied until now. The purpose of this study is to determine the arial extent of gold mineralization, its structural control, the geochemical changes from related hydrothermal alterations, its relative timing, and its relationship to the various ore deposits of the Randsburg Mining District. Systematic field mapping, sampling of targeted ore structures, and generation of assay and XRF data has revealed several clear trends and relationships of the gold mineralization in the central and southwestern Rand Mountains.

Results clearly indicate that gold mineralization is ubiquitous in the Rand Mountains and not confined to the primary mining district. The highest concentration of gold found was 10 ppm in a small prospect 9 km southwest of the Yellow Aster Pit. Concentrations as high as 2.15 ppm Au were found in the Desert Tortoise Wilderness 12 km to the southwest. The targeted lithologies were almost exclusively Plate I Rand Schist and Plate III Atolia Granodiorite. The few prospects targeting Plate IV were barren of gold. Gold mineralization is structurally controlled by NE striking faults with moderate to steep dips. This differs from the Randsburg Mining District in which gold is generally concentrated in NW striking faults (Yellow Aster faulting episode of Morehouse (1986)). The observed northeasterly structural control may be due to clockwise rotation of Yellow Aster faults or entirely be generated by Morehouse's younger 15 Ma Kelly faulting episode. The age of the gold mineralization is narrowed down to two options: 1) 19 Ma

during the Yellow Aster Intrusion, 2) 15 Ma during left lateral transtensional faulting accommodating movement along the Garlock Fault to the north. Low grade gold appears to be related to high angle faults cutting the lower Rand Thrust where it is folded. This could be due to brecciation creating space and the thrust acting as an impermeable barrier.

XRF data indicates that gold generally correlates positively with hydrothermally altered rocks that record significant loss on ignition LOI, gain in CaO, and leaching of alkalis. It is also evident that within Plate III, gold is hosted in argillic alteration zones and is often accompanied by small silver anomalies and moderate arsenic anomalies. Large arsenic anomalies are only observed in mineralized NW trending faults, with the exception of one NE striking fault. Lastly, gold anomalies in schist hosted faults are often associated with high chromium, nickel, and antimony anomalies. The association of gold with these elements provides a good framework for future exploration in the central and southwestern portions of the Rand Mountains.

TABLE OF CONTENTS

LIST OF TABLES

LIST OF FIGURES

INTRODUCTION

Motivation and Purpose:

The following thesis project addresses the structural and geochemical characteristics of old mines, prospects, and trenches in the Rand Mountains of California's Mojave Desert (Figures 1 and 2). This region was extensively prospected and mined for gold, silver, and tungsten from the late 1800s to the mid-1930s as well as the 1990s to early 2000s. While significant amounts of ore were produced, there is a notable lack of geologic research focusing on those ore deposits. In the early 1920s, Hulin (1925) described the petrology, mineralogy, and general structure of the mines of the Randsburg Mining District. However, there is no detailed geochemical analysis of host rock alterations and gold bearing structures. An unfinished MS thesis by Morehouse (1986) also details the structural controls and geochronology of the ore deposits in the Randsburg Mining District. Neither Morehouse's nor Hulin's reports address the more central and southwestern regions of the Rand Mountains where there are numerous smaller mine workings. This project looks to extend our understanding of the ore mineralization in the Rand Mountains beyond the borders of the Randsburg Mining District by analyzing geochemical measurements and the structural relationships of many of these smaller mines. Afterall, geologic processes do not abide by arbitrarily drawn borders.

The purpose of this study is multifaceted and broad in nature. One goal is to develop an understanding of how hydrothermal alteration from mineralizing fluids changed the chemistry of the host rock units. Because of the significant gold mining history of the Rand Mountains, it is also a goal to catalogue assay results in order to map out gold concentrations and other metal and trace element anomalies. Additionally, the study aims to map the numerous faults, fractures, and veins within the various prospects in order to deduce the common structural orientations that were targeted by the miners with relation to the larger fault systems of the Rand Mountains. This could have significant implications regarding the source of the gold and pathways through which hydrothermal fluids travelled and provide insight into why there are so many mine workings in the underexplored southwestern region of the Rand Mountains. My specific objectives are outlined below.

Because the gold production from the Rand Mountains was economically significant, further investigation of more remote regions of the mountain range is important. The hydrothermal alteration of the host rocks accompanying the gold mineralization extended beyond the Yellow Aster intrusion (the focus of the Randsburg mining district) southwest into the central and southwestern Rand Mountains where there are a significant number of mine workings. Although Andrew McLarty's thesis work in 2014 describing the kinematics and geometries of structural features cross cutting the Rand thrust overlaps with my study area, there is no published research regarding the hydrothermal system that ore was produced from in these workings. There is also no known structural control on the ore deposits of the southwestern Rand Mountains. My thesis will address this system by using assays and XRF analysis to compare changes in chemistry between host rocks and altered rocks targeted by the miners in the early 1900's. The study will also map out the prevalent structural features within the workings to develop an understanding of the structural control and timing of ore mineralization and to refine areas that have not been mapped in great detail with regard to ore deposits.

Objectives:

This thesis has several objectives:

1. Determine the most southwestern distribution of mine workings.
2. Assess whether the prospects follow specific lithological or structural geologic trends and controls.
3. Assay mine workings within different geologic settings for gold and other geochemical tracers to determine the extent of gold mineralization.
4. Systematically map out structures and host lithologic units within and around mines, prospects, and new targets.
5. Examine and analyze the significance of the geochemical changes between fresh and altered host rocks.
6. Speculate on possible connections with the once prolific Yellow Aster gold deposit 9-12 km to the northeast of the study location. Also discuss possible scenarios for gold deposition and its timing relative to the various ore mineralizing events of the Randsburg Mining District, as well as, the regional tectonic history.

Location:

The Rand Mountains are situated along the northern edge of the Mojave Desert block which is bounded to the north by the left lateral Garlock Fault and to the southwest by the right lateral San Andreas fault (Figure 1). The range extends approximately 28 kilometers to the southwest of the towns of Randsburg, Johannesburg, and Red Mountain, and U.S. Route 395 and is within Bureau of Land Management property. The

Red Mountain volcanic system protrudes on the eastern side of 395. The study site is located in the central and southwestern portion of the Rand Mountains (Figure 2) primarily between R43 that bounds the Desert Tortoise Natural Area to the southwest and R83 to the northeast. Both the northern and southern fronts of the mountain range along R50 and R20 were covered extensively in this study. Several quick visits to mines within the main Randsburg Mining District were carried out but were not the focus area of the study. Access required offroad driving along designated dirt roads and hiking on and off trail when necessary.

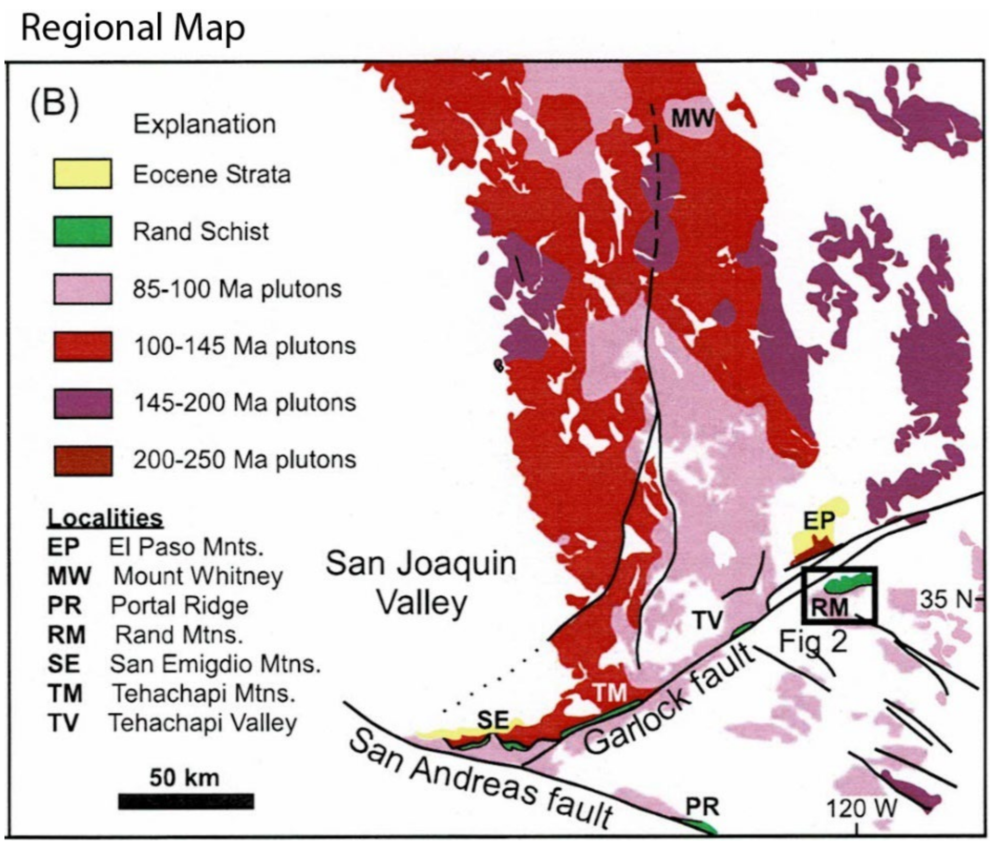

Figure 1: Regional geologic map depicting general study area of the Rand Mountains in relation to major fault systems and lithologic units of the Mojave Desert. Adapted from Grove et al., in preparation.

Geologic Framework:

The Rand Mountains are a northeast – southwest trending Tertiary antiform stretching approximately 18 km (Figure 2). The range is composed of four stacked plates separated by two low angle thrust faults and a late reactivated detachment fault that are labeled all together as the Rand Thrust Complex, abbreviated as "RTC". These thrust faults are subsequently cut by approximately five high angle northeast striking oblique-left-lateral normal faults (McLarty, 2014).

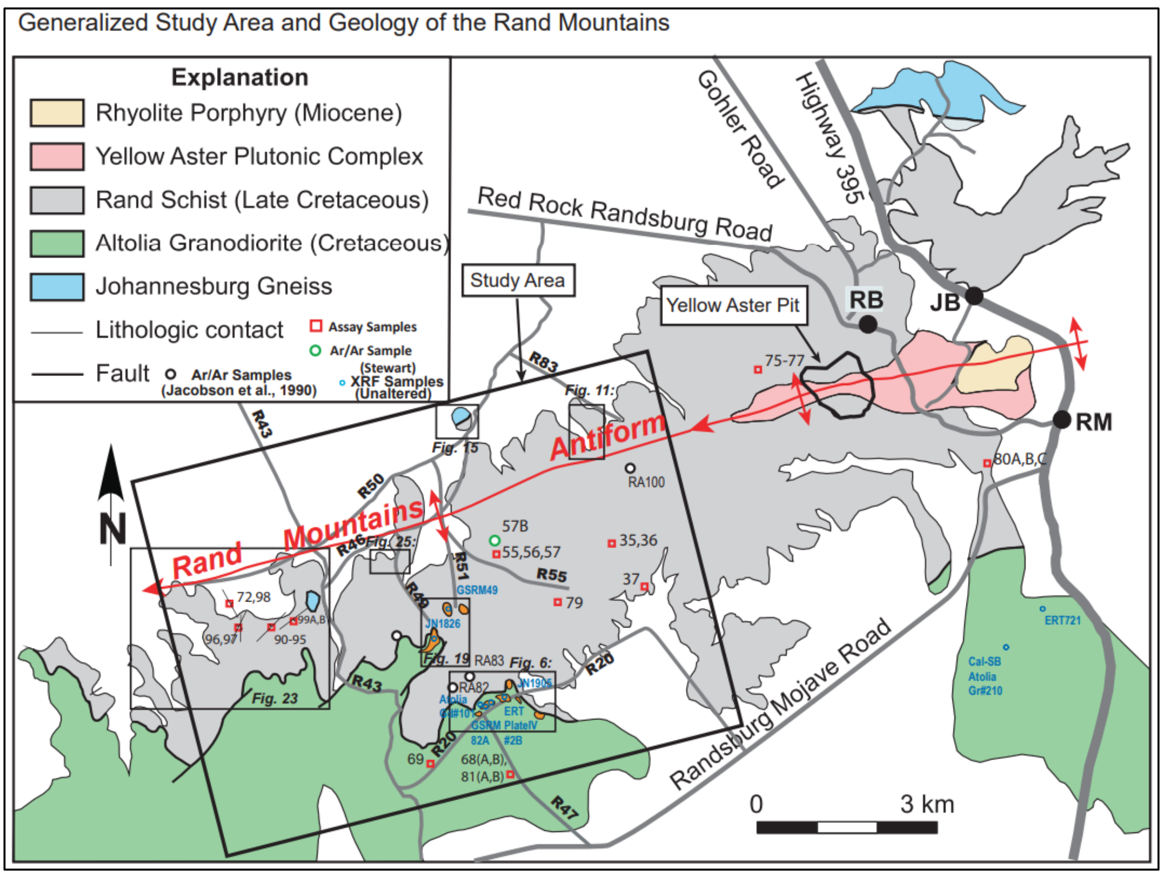

Figure 2: Geologic map showing major lithologic units, structure, study area, and focus areas within the Rand Mountains. Note the location of the Yellow Aster Mine within the Yellow Aster Plutonic Complex. Also located are various roads (R43, etc.) mentioned in text. Modified from Grove et al., in preparation.

The plates from structurally lowest to highest are: Plate I Rand Schist, Plate 2 Johannesburg Gneiss, Plate 3 Atolia Granodiorite, and Plate 4 Sierra batholith granites. Stacking of these plates and development of the RTC was probably related to shallow, flat slab subduction during the Late Cretaceous Laramide orogeny. (Grove et al.). Specifically, the individual plates were associated with subduction of the Farallon Plate beneath the North American Plate (Chapman et al., 2010). Initially, the lowest unit, Plate I protolith, was emplaced during late Cretaceous flat slab Laramide subduction. Plates II – IV of continental origin were then accreted and stacked over Plate I by the low angle thrust faults of the RTC (McLarty, 2014; Nourse, 1989).

The Rand Schist (Plate I), composed of metamorphosed basalt, chert, and greywacke, originally part of from an oceanic protolith that was accreted to the continental plate at approximately 79 Ma. Blueschist and greenschist facies metamorphism occurred 78-40 Ma as recorded by 40Ar/39Ar ages on muscovite and hornblende (Grove et al., in preparation). The Rand Schist is overlain along a low-angle fault contact by the Johannesburg Gneiss (Plate II). Plate II is a garnet amphibolite facies orthogneiss, marble, and calc-silicate assemblage. Above this is Plate III, an 87 Ma hornblende – biotite granodiorite named Atolia Granodiorite by Hulin who first described it in 1925. Throughout much of the study area, Plate III is highly fractured and filled by veins of quartz and quartz-carbonate material. Much of the altered granodiorite shows extensive replacement of biotite and hornblende with epidote or chlorite and addition of iron oxides and clays. A thrust fault reactivated as a detachment fault during Miocene extension separates Plate III from remnants of the highest unit, Plate IV biotite alkali granite (McLartyy, 2014). The base of Plate IV is locally characterized by a zone of quartz mylonite. Both Plate II and Plate IV represent remnants of the Sierra Nevada batholith.

Previous works regarding the Rand Mountains have primarily focused on developing an orogenic or tectonic model based on the timing and mechanisms of ductile faulting, intrusions, and metamorphism of the various geologic features and units. There are two proposed hypotheses for the orogeny of the Rand Mountains and the emplacement of the Plate I schist. The first, called the subduction hypothesis, dictates that the Rand Schist was subducted and accreted during the Laramide orogeny when shallow subduction halted continental margin magmatism and moved it eastward (Grove et al., Best and Christiansen, 1991; Jacobson et al., 1988). The second hypothesis, referred to as the forearc thrust hypothesis, says that forearc basin sediment was thrust under the magmatic arc by a fault within the North American plate where it was metamorphosed into the Rand Schist (Barth and Scheiderman, 1996). While the two theories are controversial, the subduction hypothesis is generally preferred.

Approximately 30 Ma, the Farallon/Pacific plate spreading center met the continental margin of North America. It was during the subsequent time period that the plate motion transitioned from a transtensional regime to a predominantly right lateral San Andreas fault system. This resulted in the well documented late Oligocene-Miocene extension, volcanism, and later (12 ma) prevalent strike-slip faulting of the Mojave block (McQuarrie and Wernicke, 2005). Based on the manuscript by Grove et al. and the extensive work done by Hulin in 1925, it was during early Miocene magmatism that the gold and silver ore of the Rand Mountains was likely deposited by mineralizing fluids. Many of these Miocene age gold deposits of southern California, southwestern Arizona, and northwestern Sonora are epithermal in nature and were likely deposited by hydrothermal fluids generated from magmatism during slab roll back 32 – 17 Ma (Izaguirre et al., 2017).

Chronology of Mineralization in the Randsburg Mining District

Within the Rand Mountains, the majority of research on the ore bodies has focused around the Yellow Aster Mine and the nearby tungsten mines around the town of Atolia. The most prominent of the deposits are tungsten, silver, and gold. Hulin determined that the region experienced multiple stages of mineralization of which tungsten is the oldest, then gold, followed by silver. While the majority of the gold was produced within a mile of the town of Randsburg and within the Stringer District south of Randsburg, gold was also produced from mines throughout much of the Rand Mountains. The gold was likely deposited in one mineralizing event and postdates prevalent rhyolite and diabase dikes. Within the Rand mining district, the gold is primarily contained in quartz veins along faults as well as in disseminated form within rock surrounding mineralized fractures (Hulin, 1925). Hulin (1925) and Hart (1986) both noted that gold was also present in small amounts in quartz free fractures. In the Yellow Aster Mine specifically, the gold typically is richest within stockwork veinlets or where fractures and faults intersect. The strike and dips of gold bearing structures is variable. However, Hulin noted that there were two general systems of veins: one striking approximately N80E and the other striking northwest – southeast. Morehouse (1988) describes mineralized northwest veins and faults as the predominant gold bearing structures and as having two phases. The first were NNW trending. These are then cut by the second phase of WNW trending veins with dips ranging from a shallow 20 degrees to often vertical. The ore is primarily hosted within the Rand Schist and Atolia or Randsburg? Granodiorite where they are stained red by the mineralizing fluids and oxidized pyrite but is also found in the margins of Tertiary rhyolitic and dioritic dikes (Troxel and Morton, 1962). The vast majority of the gold was produced from zones of red coloration due to the oxidation of arsenopyrite and pyrite (Hart, 1986). Hulin found that many of the mines in the Rand Mountains stopped where un-oxidized sulfides began to fill the fractures. This was likely due to lower grades of gold and the fact that the mills were unable to process un-oxidized sulfide hosted gold.

The late Jeff Morehouse of The University of Arizona partially completed a thesis in 1988 prior to his tragic passing, that detailed the timing and structural controls of the gold, silver, and tungsten deposits within the Rand Mining District at the northeastern point of the Rand Mountain range. He identified three separate episodes of faulting accompanied by different ore mineralization. The first of these episodes, termed the Atolia Episode, initiated at 32 Ma (based on K/Ar dating of sericite) and introduced significant amounts of tungsten in the form of scheelite into the Atolia Granodiorite. The ore bodies were concentrated in NE to E (averaging about N80E) trending faults and fractures dipping variably northward. Following the Atolia Episode, the gold mineralization occurred as the Yellow Aster Episode. Morehouse determined this event happened 18 Ma by K/Ar dating of sericite from an auriferous quartz vein. However, recent work by Grove et al, (in progress), has refined the timing of the gold producing granodiorite intrusion to 19 Ma. The Yellow Aster Episode emplaced gold into extensional NNW and WNW trending faults that dip to the NE at shallow to moderate angles. Faults of this episode are present and mineralized at least as far north as the hills on the east side of Highway 395, north of Randsburg and Johannesburg and as far south as half of a mile southwest of Government Peak. The last of the ore producing events identified by Morehouse, the Kelly Episode, deposited localized silver into left lateral normal en echelon faults striking NE-SW and dipping steeply to the SE. These faults, concentrated directly southwest of the town of Red Mountain, are linked by tensional faults striking N-S and dipping E-W. The Kelly episode occurred continuously from 10 to 15 Ma according to K/Ar dating of several sericite samples from silver bearing quartz veins. Interestingly, this silver mineralizing event coincides with the timing of the onset of the Garlock Fault and its left lateral motion.

Research Questions

Few studies of the Rand Mountains fully examine the geochemical and structural nature of its ore deposits and the related hydrothermal alterations, especially southwest of the once prosperous Yellow Aster Mine. Additionally, much of the study site where the highest density of mine adits are located has not been mapped in detail. In order to address these gaps in knowledge, the following research questions are posed:

1) What are the distribution and extent of artisanal mines and prospects in the southwestern Rand Mountains?
2) What are the gold concentrations for the prospects within the study area and what types of geologic structures contain anomalous gold? Published data regarding gold concentration is extremely limited and only refers to ore from the Yellow Aster Mine and several other large gold mines in the immediate vicinity. The fact that there are so many significant prospects within the study area suggests that

there must have been an economically viable amount of gold in the southwestern region of the Rand Mountains.

3) What host rock lithologies were targeted by prospectors and what type of alterations were they using as visual clues?
4) Is there a significant shift in chemistry between unaltered host rocks and hydrothermally altered and mineralized rocks along targeted zones? Are there trace elements or specific alteration zones that can be used to vector in on gold bearing structures?
5) What were the structural trends and features targeted by past prospectors? According to McLarty (2014), there are northwest-striking shallow angle thrust faults as well as cross cutting northeast striking high angle faults within the study area. Can the mines be grouped based on the structural styles of these fault systems? What are the cross-cutting age constraints of these faults?
6) Is there a preferred structural control on gold mineralization is in the southwestern Rand Mountains?
7) How does the structural control and mineralization style relate to what is found in the main Randsburg Mining District?
8) Can the absolute timing of gold mineralization be determined? How does it fit in with the timing of the various tectonic regimes of the Mojave Desert?
9) There are several interesting features within the study area that lack mine workings but may merit exploration. One such feature is a prominent quartz carbonate limonite breccia whose outcrops are localized along one of the high angled cross faults cutting through the northern part of the study area. Several

smaller outcroppings of the same material are exposed along several other northeast striking faults throughout the study area. Additionally, rhyolite dikes have been previously noted to exist within the study area by Andrew McLarty and Jonathan Nourse, but were unfortunately not mapped in great detail. Hulin recognized that rhyolite dikes in the Yellow Aster Mine, as well as many others, were closely associated with gold. Many of the gold bearing quartz veins intersect the dikes and often times follow along their margins. Prospectors may have failed to recognize this relationship within the study area. These features warrant further investigation into whether they hold future exploration and exploitation potential.

Methods

This study required extensive field and lab work as follows.

Field Work, Mapping, and Sampling

Many overnight trips to the field site were taken in order to find and map as many prospects, trenches, and other targets as possible. A Garmin GPSmap 76Cx unit set up for the NAD27 CONUS UTM datum was used to locate each adit or prospect pit to within a 3-meter error. A Brunton compass was used to measure the strike and dip of structural features (foliations, faults, contacts, veins) at the mouths of the adits as well as further within the prospects. This structural data was projected onto stereonets for visualization and further analysis using Allmendinger Stereonet software. Using OziExplorer and ArcMap, waypoints were transferred from the GPS onto the USGS 1967 Randsburg 15’ quadrangle topographic map to mark the locations of samples and mapped features.

Surface mineralogy was mapped using LANDSAT 8 imagery and ArcMap remote sensing multi-band ratio methods. The three surface mineralogy categories used for multi-band mapping were carbonate minerals, ferrous minerals, and iron oxide minerals. The band ratio for carbonates was 6/7 and represented by blue coloration; for ferrous minerals the ratio was 6/5 and represented by red coloration; iron oxides used the ratio 4/2 and were portrayed by green coloration. Maps were then edited and finalized in Adobe Illustrator.

At each prospect and trench, chip transect samples are taken using a rock hammer and sample bags. Some sampling of waste and tailings piles were done when in-place sampling was impossible. Sample collection was done with the primary purpose of assaying for gold and determining the change in chemistry between fresh, unaltered protolith and its hydrothermally altered form.

Gold Assays and Multi-Element Analyses

All samples were taken to the Cal Poly Pomona rock lab where they were prepared to be sent off for analysis at American Assay Laboratories in Sparks, Nevada. The first step in sample preparation was to break up the rocks into fingernail sized pieces using a steel hammer and plate. Next, the crushed sample was poured into a rock pulverizer that breaks the rock bits into 1mm pieces. Using a sample splitter that ensures full sample representation, at least 100 grams of each pulverized sample were collected into separate bags. Lastly, the separated samples were powdered in a SPEX Shatterbox 8500 to at least a 200µm sieve size. This was approximated by touch (a fine powder with no grittiness in the texture). Each powdered sample was packaged and mailed to American Assay Laboratories.

The lab performs an initial "ICP – 5AO35" 35-element 5 acid digestion ICP - OES assay on each sample. Because the primary concern for these assays is to determine the concentration or "grade of gold" within each sample, an additional Fire ICP assay was performed if the initial ICP assay detected greater than .003 ppm of gold or .2 ppm of silver. If gold concentrations are between 10 and 1,000,000 ppm, a final Fire Gravimetric assay was performed to most accurately measure the grade of the gold. The 35 elements chosen as part of the assay package are Au, Ag, Al, As, Ba, Be, Bi, Ca, Cd, Ce, Co, Cr, Cu, Fe, Ga, K, La, Mg, Mn, Mo, Na, Ni, P, Pb, S, Sb, Sc, Sr, Th, Ti, Tl, U, V, W, Y, and Zn.

XRF Analyses

Further chemical analysis of each sample was carried out on the Washington State University XRF to provide a measurement of the major oxides and trace elements present in the samples that can be added to standard geochemistry plots. This aided in determining the style of alteration that occurred while allowing for a more in-depth comparison of the chemistry between hydrothermally altered rock and its unaltered protolith. The same sample preparation was carried out for XRF as for the assays. The major oxides measured in weight % are SiO2, TiO2, Al2O3, FeO, MnO, MgO, CaO, Na2O, K2O, P2O5. LOI% was also measured. Reported trace elements in ppm are Ni, Cr, Sc, V, Ba, Rb, Sr, Zr, Y, Nb, Ga, Cu, Zn, Pb, La, Ce, Th, Nd, U, and As.

$^{40}Ar/^{39}Ar$ Analyses

Lastly, two samples, GSRM-57B and GSRM-85, underwent the Ar-Ar geochronology method to delineate the timing of a widespread Cr-Ni-Co-carbonate alteration event that is in some cases associated with gold and antimony enrichments. Minerals targeted for separation were fuchsite/mariposite (a chromian phengite mica), white mica, and feldspar. The micas, particularly fuchsite, are commonly temporally associated with gold mineralization in greenstone metamorphic belts and used to date mineralization. The geochronologic work was carried out by Dr. Willis Hames at Auburn University's Ar-Ar "ANIMAL" lab. Additional microprobe work of the two samples is being undertaken to confirm the identity of several cryptic Cr and Ni bearing minerals within the samples.

RESULTS

Geologic and Structural Mapping

Large Scale Spectral Map of the Rand Mountains

The general geologic map of the Rand Mountains from Figure 2 (Grove et al. in preparation) represents a simplified distribution of the four lithologic units and large-scale structures. For this thesis, a surface mineralogy spectral map of the Rands was made to further aid in differentiating between the rock units. It was overlain by the Grove et al. map in order to confirm the viability of remote sensing for mapping the Rand Mountains (Figure 3). The spectral map was designed so that bright greens represent iron oxides (hematite and goethite), blues represents carbonate minerals, and reds represent ferrous mineralogy (generally actinolite and chlorites). While the spectral map delineates almost perfectly the contact between Plates 1 and III, it also visually separates various sub-units of Plate I, as described below:

The large bright red mass represents the blue schist core of the antiform, derived mainly from mafic igneous protoliths. Random dispersed red patches are prevalent throughout much of the Rands. Several of these were field checked and confirmed to also be isolated pieces of blue schist. Chlorite - muscovite grayschist is represented by the blue green coloration seen in the southwestern region of the mountains. The purplish-blue area between the grayschists and the red mass appears to indicate a greenschist-blueschist transitional zone. It is difficult to differentiate Plate II from Plates III and IV because Plate II is very thin at this scale. Plate III ranges from mottled pink to mottled pink-green-magenta. Based on field observations, the pink-green-magenta coloration marks hydrothermally altered granodiorite while mottled pink typically indicates un-altered granodiorite. Plate IV is portrayed by bright white-pink coloration. Figure 4 very clearly highlights these units which align perfectly with the outlines of the corresponding lithologies from the overlaying Grove et al. map. It is possible that due to the similar mineralogy, the Plate II Johannesburg Gneiss unit blends in with the Plate III granodiorites. Unfortunately, it appears that carbonate mineralization in the form of Plate II marble is not distinguishable on this map. That would have been helpful in the identification of Plate II locations.

Approximately 75 mines, prospects, trenches, and undisturbed targets were mapped and sampled from within the central and southwestern extent of the Rand Mountains. All visited prospects, mines, and unexplored geologic targets are located in Figure 4. While these represent the vast majority of the mines in the central and southwestern Rand Mountains, there certainly are numerous others that were not visited.

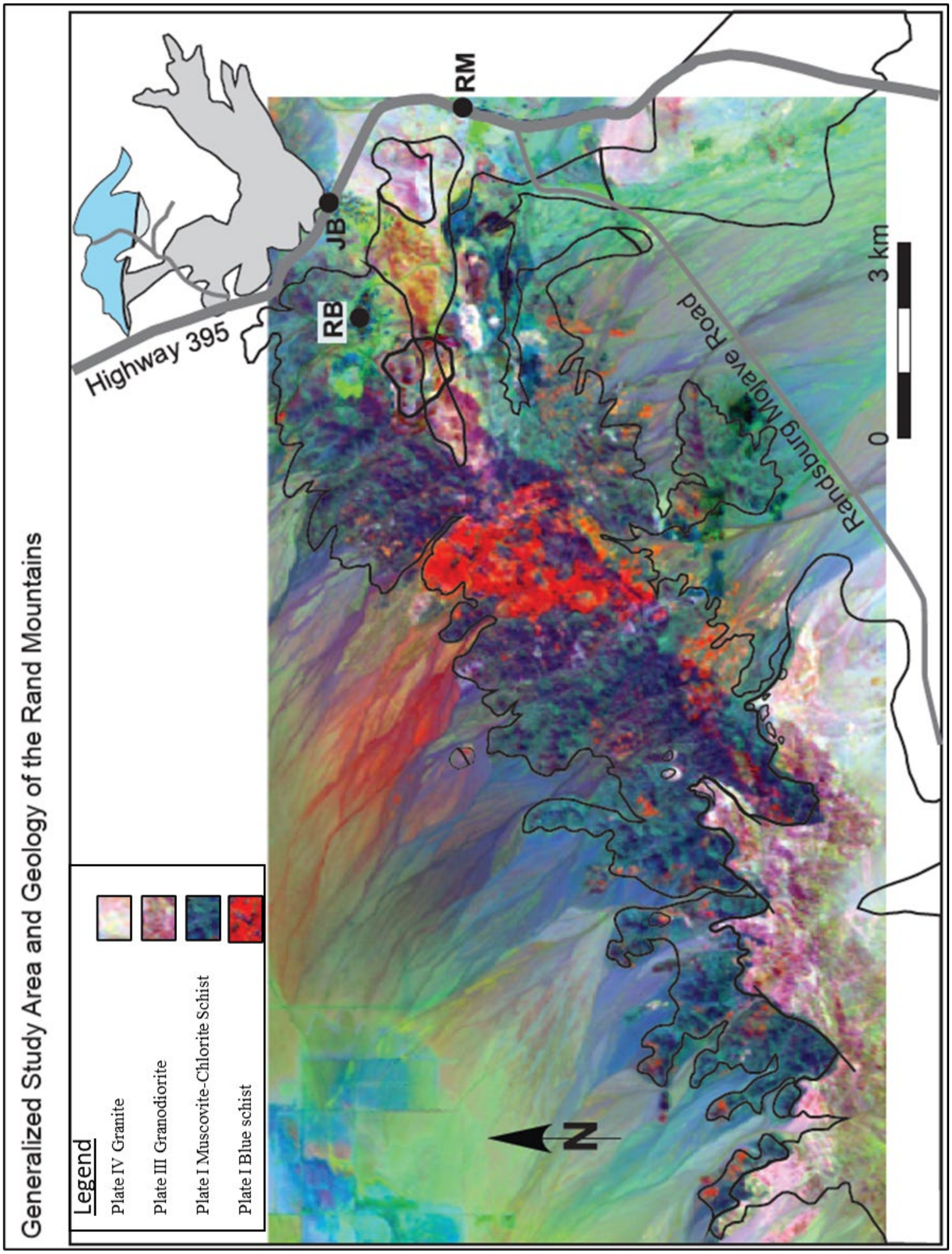

Figure 3: The surface mineralogy map is overlain with the outlines of the Grove et al. generalized geology map (Figure 2) to illustrate how well the remote sensing method of mapping correlates with field mapping in the Rand Mountains. The spectral map allows for quick differentiation of sub-units within Plate I and distinguishes easily between Plates III and IV (see text for details).

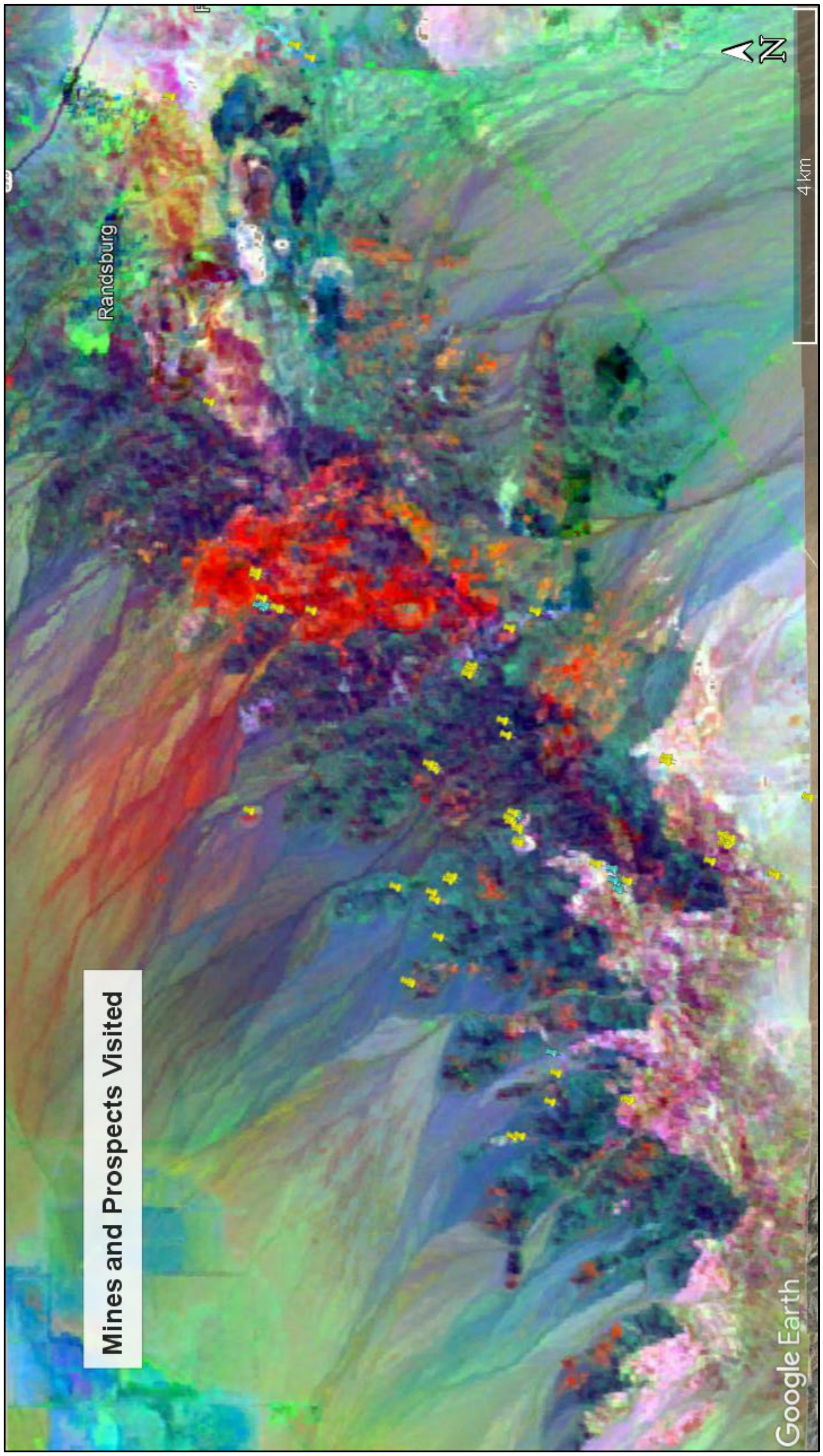

Figure 4: Spectral map of the Rand Mountains with all visited mines and prospects located with yellow pins. Blue pins represent locations of unmined geologic features that were sampled for this study. This illustrates the sporadic and widespread locations of the workings and the lithologies targeted by miners. Imagery uploaded to Google Earth for locating mines.

Geological Maps of Focus Areas

Results of the fieldwork have been broken up into seven focus areas:

1. Trenches along Plate III/ Plate IV contact
2. Darn Peak prospects
3. Route 83 fault zone
4. Lone standing knob along Route 50
5. Route 43 Cross-Fault and northern extension
6. Desert Tortoise Wilderness
7. Ridgeline south of the R49-R46 intersection

The seven focus areas are located on the Figure 2 map and in the composite geologic map of Plate I in Appendix A. Focus areas 1 and 2 (Figures 7 and 10 respectively) explore the upper two plates of the Rand Mountains where they are exposed on the southern front. The contact area between Plate III and IV contains shallow angle faults that differ significantly from the moderate to high angle faults that are ubiquitous in the Rand Mountains. Focus area 3 (Figure 11), defined by major intersecting faults, is the northern most part of the study area and is entirely within Plate I. Focus areas 4 and 7 are primarily within Plates I and II and exhibit tight synform folding (Figures 15 and 25 respectively). The Route 43 cross fault location (Figure 19) is characterized by a large quartz-carbonate-limonite outcropping along a large crossfault that cuts through Plate I schist and is surrounded by several klippens of Plates III and IV. The Desert Tortoise Wilderness area marks the southernmost focus area of the study (Figure 23).

Trenches along Plate III / Plate IV Contact

This location, just northwest of R20 and northeast of the Darn Peak locality, illustrates the contact between Plate III Atolia Granodiorite and Plate IV biotite alkali granite (Figure 6). Much of this contact is composed of a quartz rich mylonite illustrating the ductile shearing that occurred between the two plates, likely during Late Oligocene – Early Miocene detachment faulting. Faulting at this location is characterized generally by northwest strikes and shallow dips to the northeast. Several trenches and small prospects targeted these shallow angle faults and mylonitized zones (Figures 5 and 7). Assayed samples from these targets were all barren of gold.

Figure 5: This photo shows a small prospect targeting the shallowly dipping quartz rich mylonite zone at the base of Plate IV. Samples from this prospect were barren of gold.

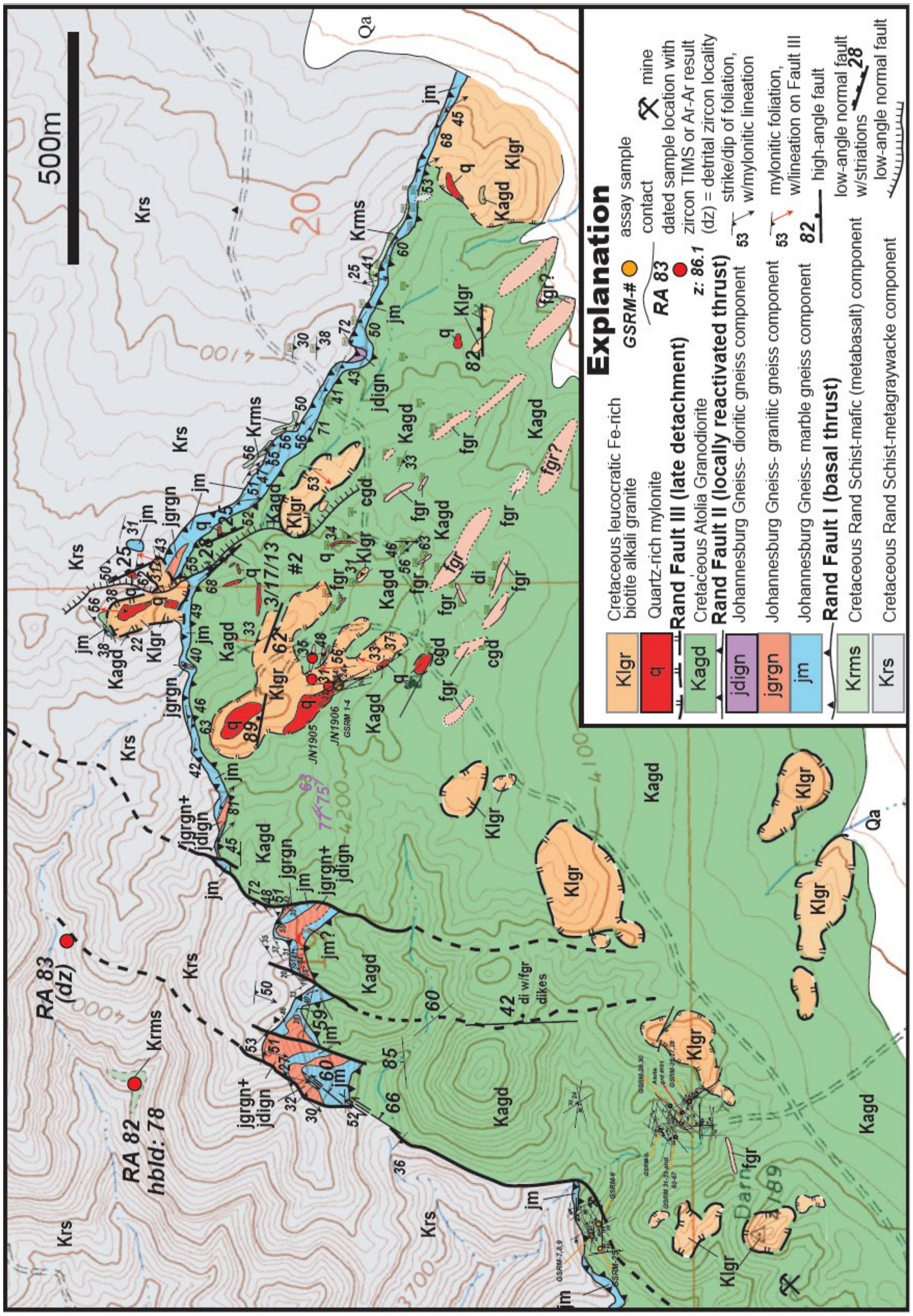

Figure 6: The geologic map of the Darn Peak and Plate 4 trenches locations modified after J. Nourse and A. McLarty (2014). Several zoomed in clips of this map are provided in Figures 7, 10A, and 10B. Note that north is to the left.

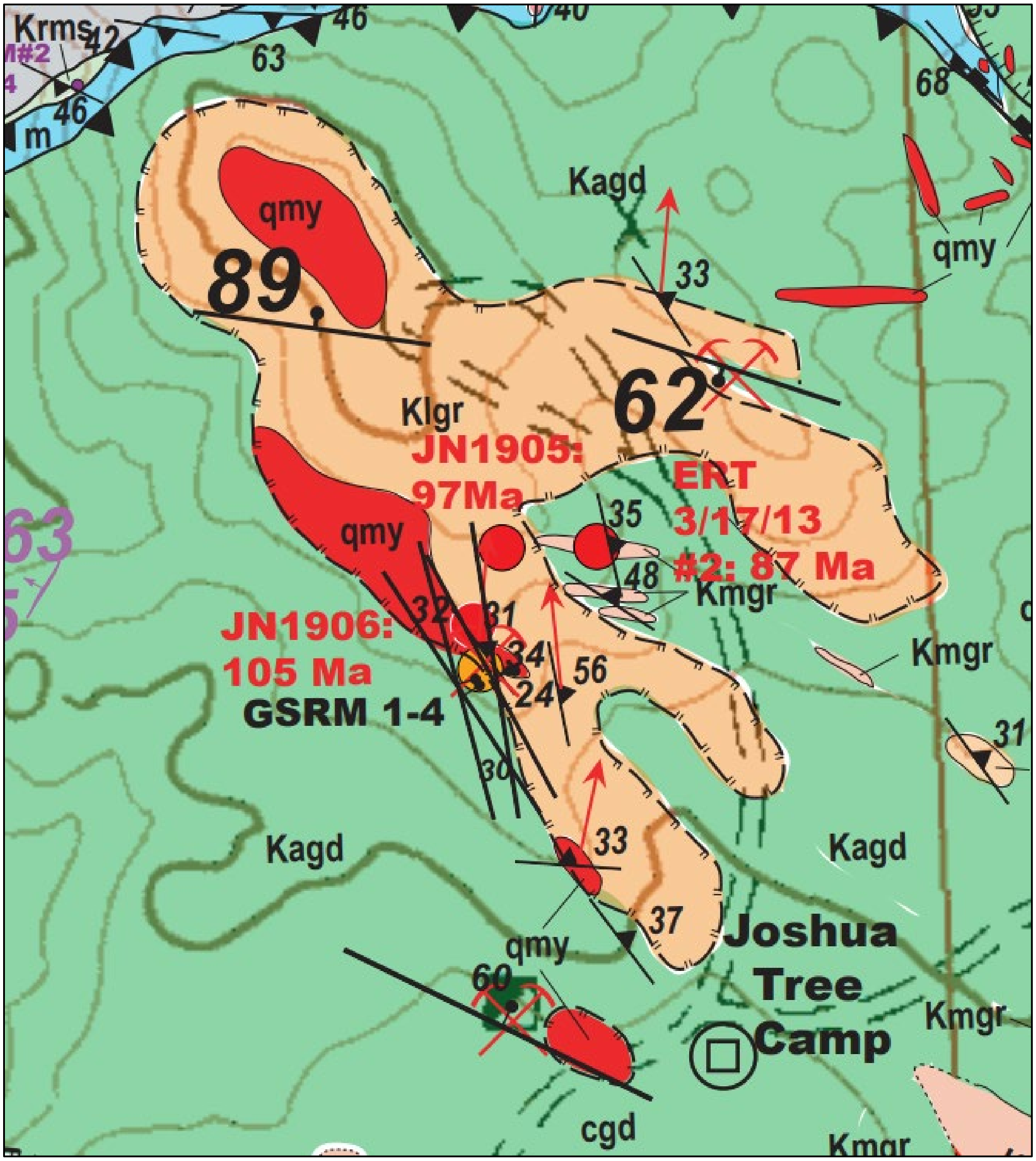

Figure 7: This clip map of Figure 6 zooms in on the mylonitic contact between Plates III and IV. Most of the faults at this location are oriented NNW and dip shallowly to the NE. The orange circle represents the location of samples GSRM-1 through 4. The red circles are the location of samples JN1905 and JN1906 that were used for assay and XRF analysis. North is up. Refer to the legend on Plate I in the Appendix.

Darn Peak Prospects

The Darn Peak location on the southern flank of the range north of R20 hosts a tightly clustered group of small mines and prospects entirely within the Atolia Granodiorite. Figures 10A and 10B show a detailed geologic map of this area with all the mines precisely located along with sampling sites. Several small to moderate sized intrusions of Cretaceous leucocratic Fe-rich biotite alkali granites are present and cap the main ridge line, including Darn Peak. These granites become more prevalent to the northeast where they contain quartz rich mylonite at the contacts with Plate III. Schist underlies the granodiorite and is exposed downslope immediately to the north (refer to map of Focus area 1.

The Plate III unit in the Darn Peak area is highly faulted and thus, has been highly altered from hydrothermal fluids (Figures 8 and 9). This leaves large portions of the granodiorite highly bleached, hematitic, and clay rich. Faults with various preferred orientations are present and discussed further in later sections (Figure 10). Most mine workings are excavated along fault trends. This location was heavily sampled and produced the highest-grade material at 10 ppm Au.

Figure 8: A northerly looking overview of the Darn Peak cluster of mines. Aside from sporadic leucocratic granite intrusions, this location is entirely composed of Plate III Atolia Granodiorite.

Figure 9: One of the Darn Peak prospects displays the complex network of faults and extreme nature of hydrothermal alteration that renders the granodiorite nearly unrecognizable. Photo taken by Dr. Nourse.

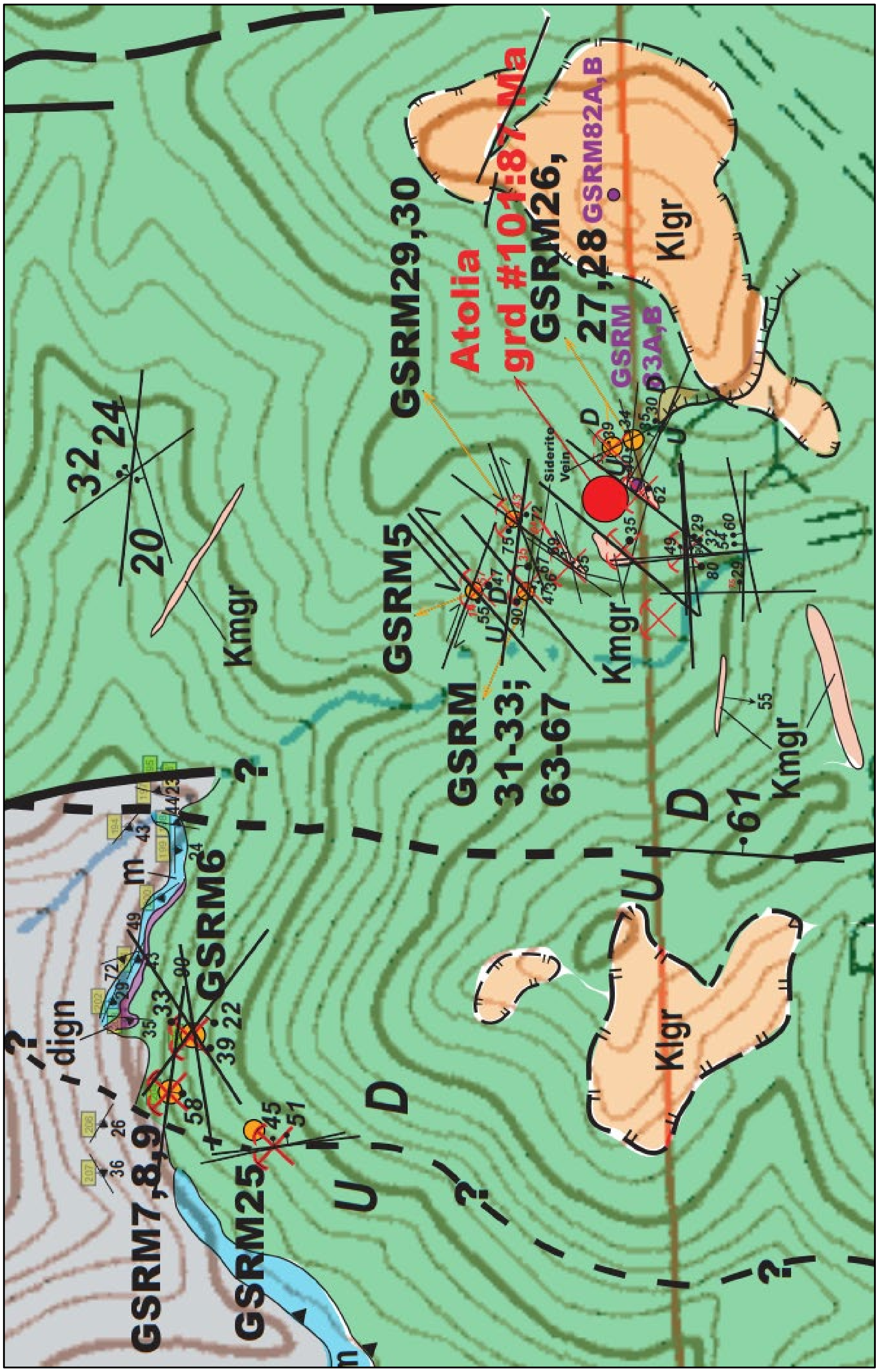

Figure 10A: This clip map of Figure 6 illustrates the highly faulted nature of the Plate III Atolia Granodiorite at the Darn Peak focus area. The orange circles show the locations of assayed samples. The richest gold sample, GSRM-33, contained 10 ppm Au and was collected from a sub-vertical NE striking fault here. North is to the left. Refer to the legend on Plate 1 in the Appendix.

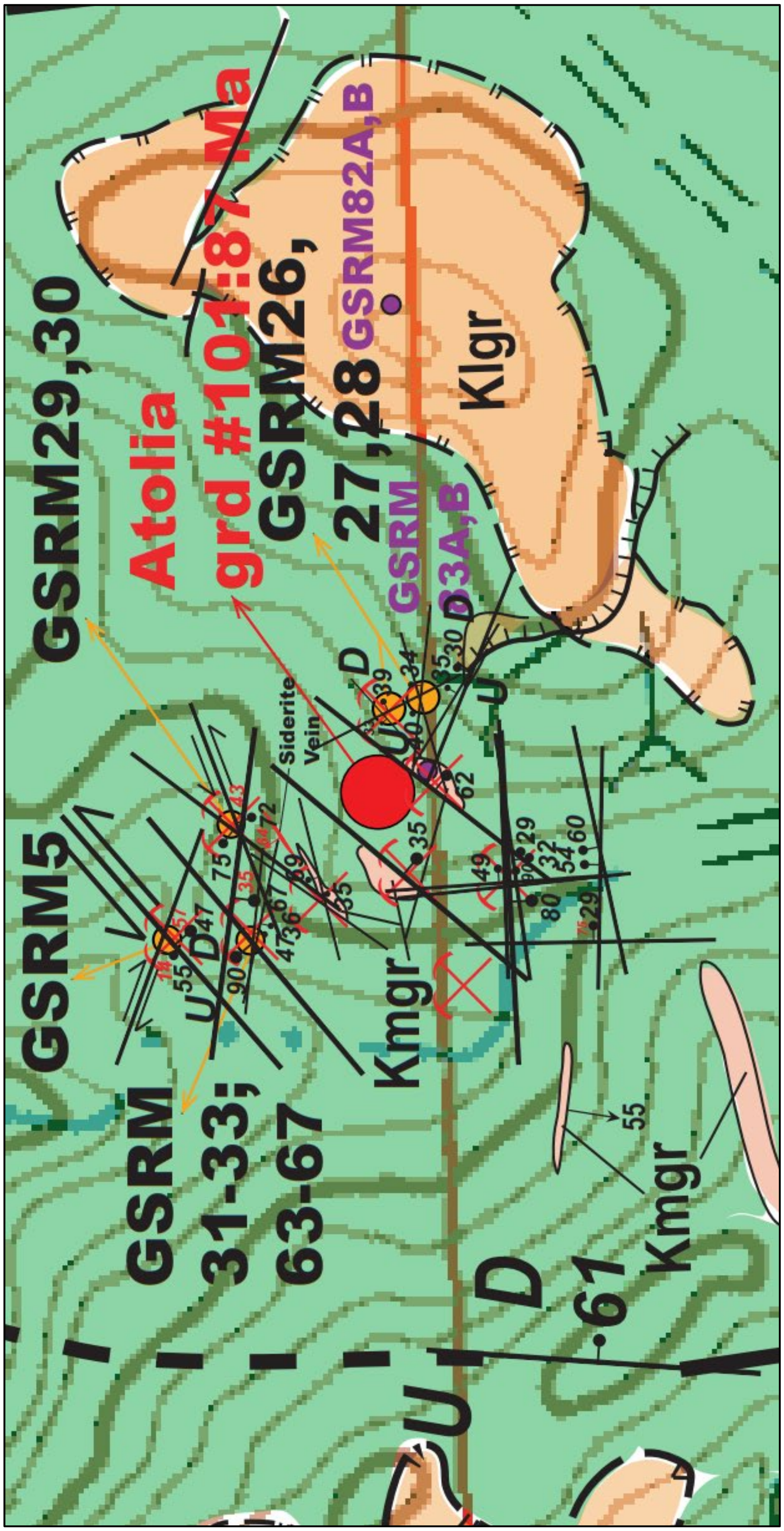

Figure 10B: This cropped map from Figure 10A shows the prominent NE to EW strikes of the most highly mineralized faults in the Darn Peak locality. NW trending faults were far less numerous. North is to the left. Refer to the legend on Plate 1 in the Appendix.

Route 83 Fault Zone

On the north flank of the central Rand Mountains immediately south of R83 where it enters into a canyon, is a zone of prominent striated fault outcrops (Figures 12, 13, and 14). These outcrops are composed of very resistant quartz-carbonate-limonite breccia entirely within the metabasaltic blueschist and occasional manganiferous metachert. The schist often contains large aggregates and pods of epidote. There are generally two sets of intersecting extensional faults in this location (Figure 11). While both are steeply dipping, one trends to the NW and the other trends to the NE. Detailed fault-slip analysis reveals that the north-northeast trending structures represent a major normal fault that has cause an apparent right-lateral offset of the northwest-trending fault, which records earlier right-lateral-oblique normal displacement. The younger northeast structure appears to be on strike with a prominent normal fault mapped to the south. However, it may be a separate sub-parallel fault.

Higher up on the slope face, shallow to flat dipping faults are present. This location forms a large mountain front scarp with steep vertical relief (Figure 11). Most of the limonite breccia zones have not been mined, with the exception of a steep shaft excavated along the NNE structure in the west-central part of Figure 11. Four mines were located and explored in this focus area.

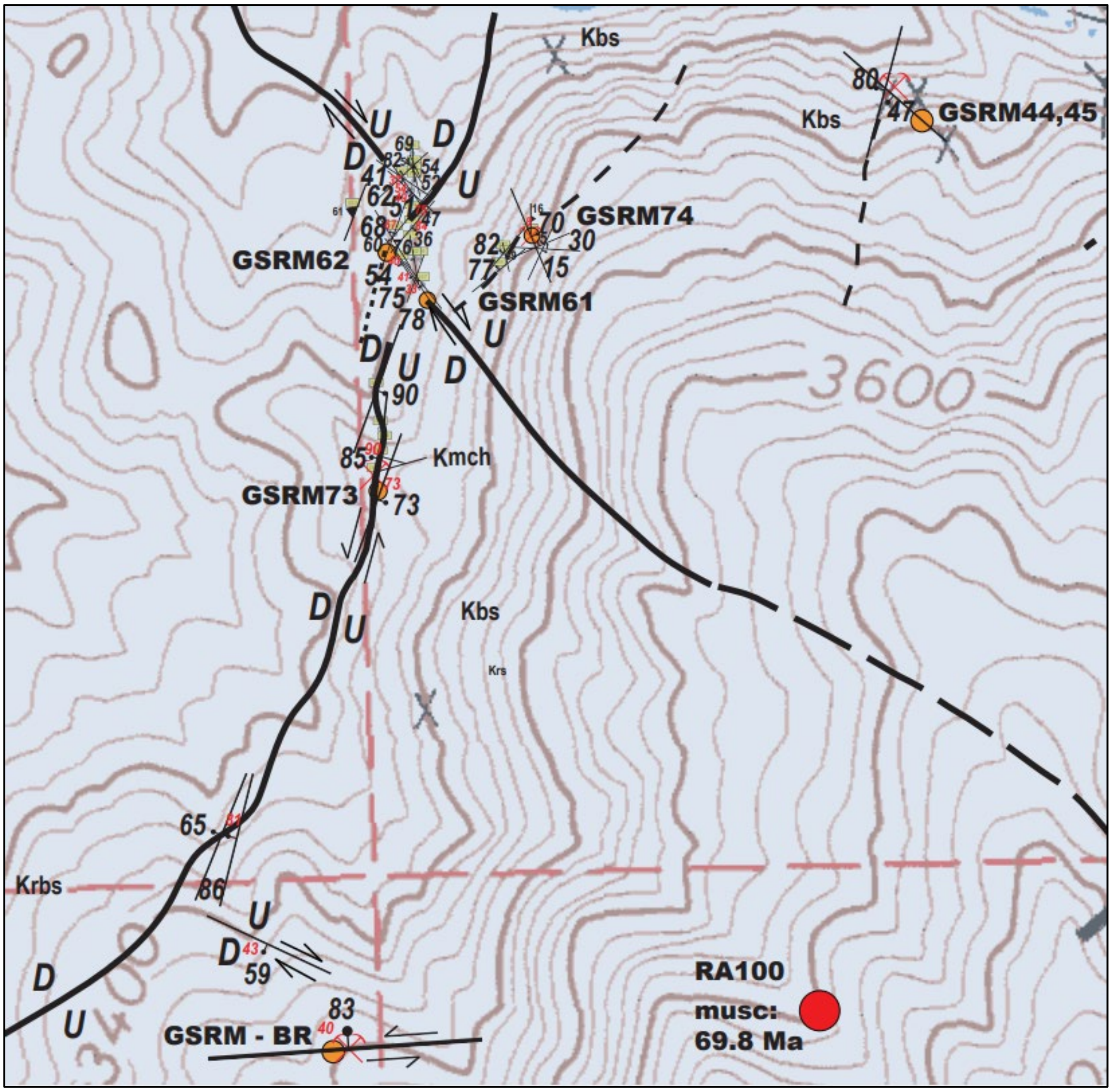

Figure 11: Geologic map of the R83 Fault Zone depicts the prevalence of NE striking faults cutting and displacing NW striking right-lateral faults through normal motion. Refer to the legend on Plate 1 in the Appendix. Details of the main fault intersection are better viewed on Plate 1.

Figure 12: The NE and SE trending quartz-carbonate-limonite fault breccias outcropping in blueschist south of R83. Arrows indicate trend and picture was taken by Dr. Nourse looking roughly east.

Figure 13: View of the SE trending fault outcrop with remnant polished and striated surfaces that record oblique right-lateral-normal displacement in dark gray. Me for scale. Picture taken by Dr. Nourse.

Figure 14: Close up of the large SE trending fault outcrop with rock hammer indicating the attitude of oblique-slip striations. These striations indicate a moderate rake to the NW. Right-lateral brittle slip indicators, including Riedel shears, were observed here Photo taken by Dr. Nourse.

R50 Knob Location

This location is a small isolated hill surrounded by alluvium on the north side of the Rands. Route 50 contours around the eastern edge of the knob. One large mine with multiple daylighted stopes and several small surface workings is easily visible from the road. The geology of this location is illustrated in Figure 15. Composing the bottom third of the northern, eastern, and southern sides of the hill is typical silvery Rand grayschist with patches of mafic Rand Schist. Above this unit, the lower Rand Thrust brings the schist into contact with Plate II Johannesburg Gneiss and several slivers of marble. Small units of gneissic diorite and mylonitic granodiorite are scattered throughout Plate II. Foliations in both Plate I and Plate II show a dip reversal such that foliation on the south side dip to the north and foliations on the north side dip to the south. This creates a synform structure with an axis tracing roughly through the middle of the knob and plunges gently to the northwest.

Several large, striated NE trending high angle faults are present. One of which intersects with the mine adit over a 4-meter-wide exposure and was an important target of the mining operation (Figures 15, 17, and 18). This fault was sampled and contained 1ppm Au. A detailed mine map presented in Figure 18 illustrates the intersections of these faults with the mine adit. The majority of the mine is within Rand Schist. However, Plate II mylonitic granodiorite makes up most of the left branch of the T at the end of the main adit. As a result, it is assumed that the Rand Thrust must be exposed at some point in the mine. Unfortunately, due to the rather cryptic appearance of the thrust, this exposure was never identified. Most of the faults within the mine had strikes between N26E and N54E with dips from 50 to 64 degrees to the NW. One NE striking fault had a dip to the SE. Six of the NE trending faults contained striations. Four of these contained rakes to the SW between 7 and 76 degrees. The steeper rakes are associated with the large fault exposure that was sampled. Shallower rakes may be associated with the assumed location of the Rand Thrust. Two rakes were to the NE at 76 and 84 degrees. Three NW striking faults intersected with the adit. These varied between 5 and 40 degrees. Two had dips to the SW and one dipped to the NE between 32 and 81 degrees. Two of these faults were striated; one with a rake at 40SE and the other at 45NW. Five schist foliations were measured. Four of these struck to the NE and dipped moderately to the NW. One schist foliation struck to the NW and dipped shallowly to the NE. A single foliation of the Plate II mylonitic granodiorite had a NE strike and shallow NW dip.

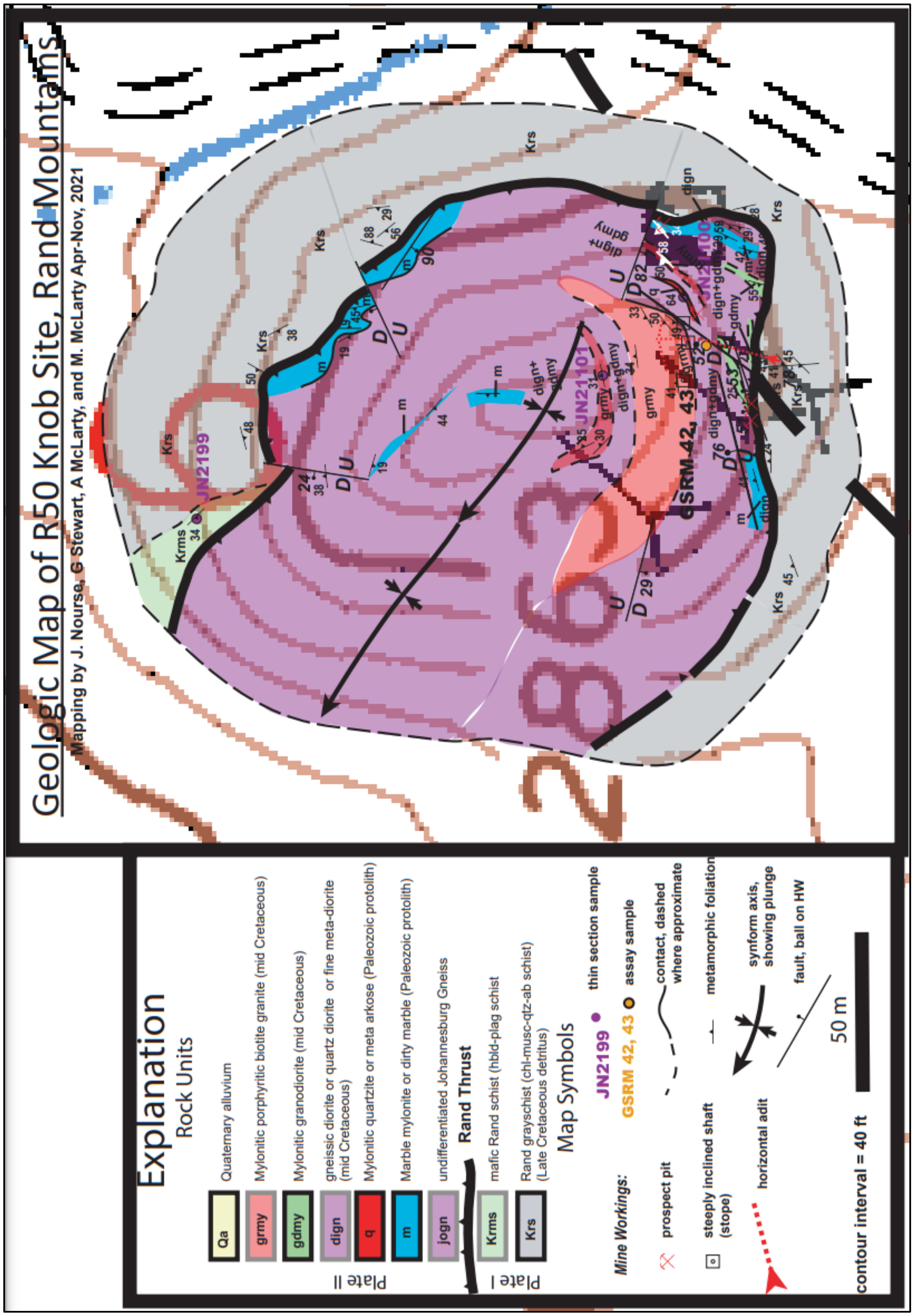

Figure 15: Geologic map of the R50 Knob location. It is a tight synform structure composed of Plates I and II separated by the Rand Thrust. Several large NE trending high angle normal faults are present along the southern edge of the hill and were the targets of the mining operations. Mapping of this site was carried out by Dr. Nourse, Garrett Stewart, Andrew McLarty, and Mark McLarty during a GSC 4910L outing. The map figure was generated by Dr. Nourse. North is to the left. A map of the horizontal mine working is presented in Figure 18.

Figure 16: The mouth of the mine adit in the R50 Knob; view is N10E. This mine begins within the Rand Schist with foliations dipping to the northwest. The horizontal tunnel intersected the Rand Thrust along its left branch. Some of the stopes also did. Other stopes follow major NE-striking normal faults.

Figure 17: Striated fault within the mine with a wide gouge zone that was targeted by the miners. Sample GSRM-42 from the gouge contained 1 ppm Au. Brittle slip indicators detail a dominantly dip slip motion with a minor left-lateral component.

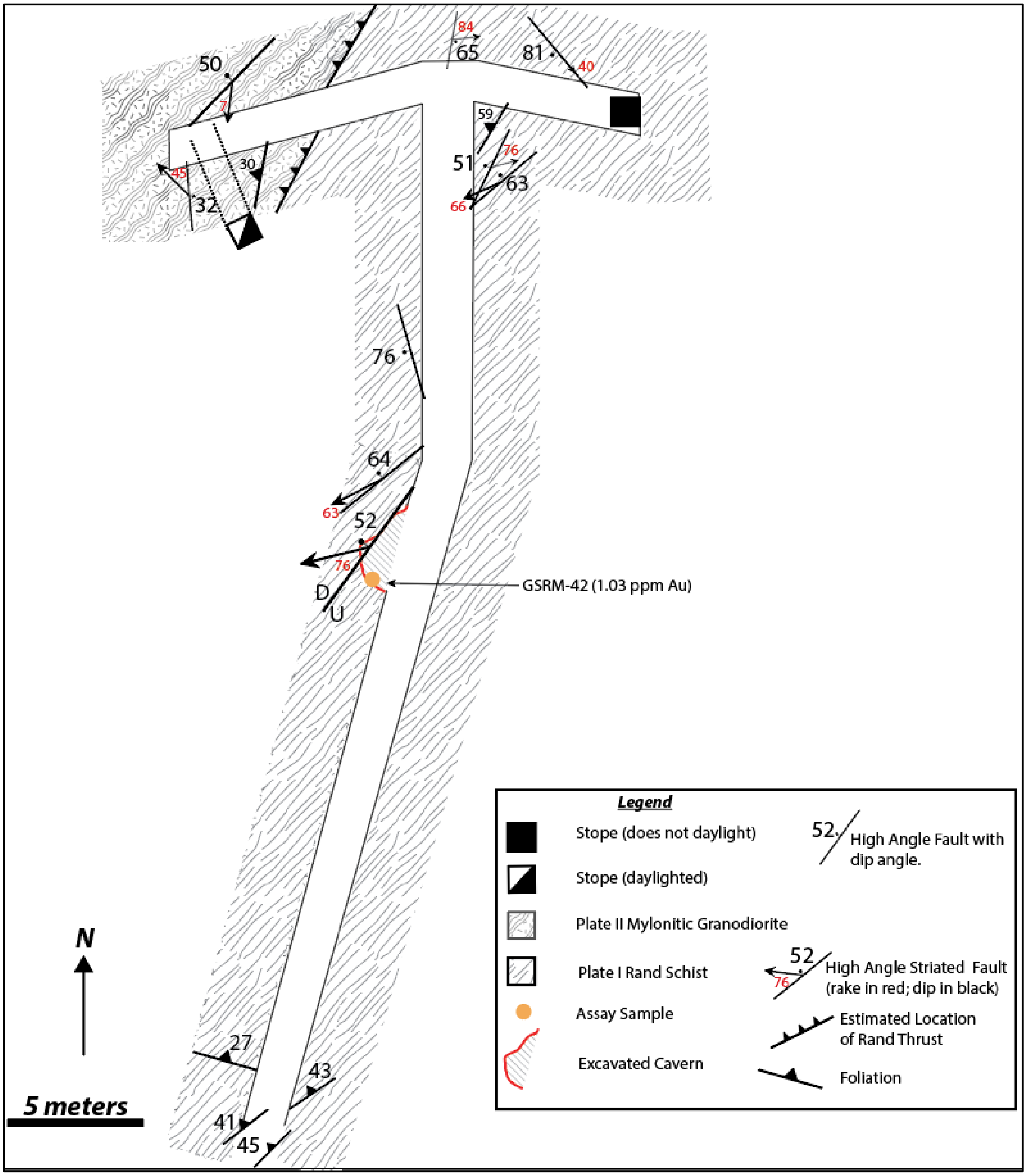

Figure 18: Mine map shows the main adit with a T at the end. Several stopes or caverns are located and sample GSRM-42's location is plotted. Faults where they intersect with the adit and foliations of the Rand Schist and Plate II mylonitic granodiorite are plotted. The actual location of the Rand Thrust was never identified within the mine, so its position and orientation are estimated. I mapped this mine with Ben Rucker and Dr. Nourse in April and November of 2021.

Route 43-Route 51 Cross-fault

Branching east off of R43 and curving northward until it adjoins with the southern end of R51, is a resistant large orange quartz-carbonate-limonite fault breccia outcrop (Figures 20 and 21). This fault is a steeply dipping, normal fault, with minor left-lateral component, striking to SW and dipping NW. The upthrown block on the east side of the fault is composed primarily of Rand Schist and metachert. Certain portions of the schist proximal to the fault display high amounts of hydrothermal alterations and addition of blue-green nickel and chromium bearing minerals. Rarely, listwanitic fuchsite-quartz-carbonate veins are present. The down dropped block on the west side of the fault is Atolia Granodiorite and scattered klippens of leucocratic granites.

Towards the southern end of R51, outcropping of what is assumed to be the same fault separates two hills topped by granite units. On the east side, schist underlies highly altered Plate III which is highly chloritized and but retains its plutonic texture (Figure 22). The schist exhibits various grades of talc-carbonate alteration as an envelope around the contact with Plate III. Farther up the hill, the granodiorite is then capped by several small klippen of iron rich leucocratic granite. The granite has several small felsite dikes outcropping along minor faults. Larger amounts of granite and granodiorite are exposed on the west side of the fault (Figure 19).

Several samples were collected from various sections of the cross-fault and prospects targeting the granodiorite and granite klippen. The highest grade of gold encountered was .024 ppm Au from silicic and limonitic schistose rock with cryptic blue-green chromium and nickel bearing minerals.

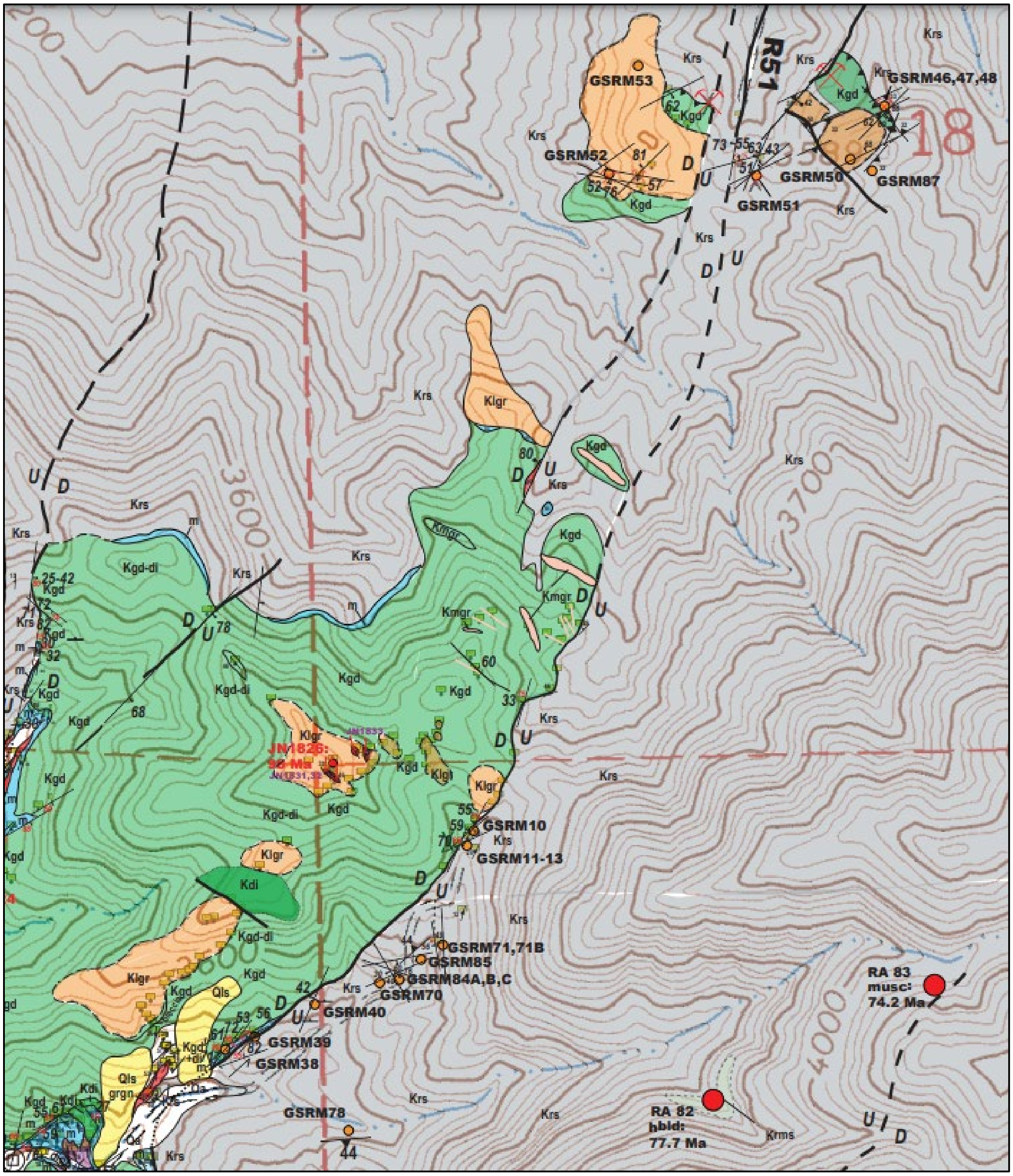

Figure 19: This map illustrates the lengthy contact between Plates I and III adjacent to the long NE trending cross-fault that traces up to the southern end of R51. Many samples were collected from various components of this trend. However, only a few contained slightly anomalous gold. Refer to the legend on Plate 1 in the Appendix.

Figure 20: Outcropping quartz-carbonate-limonite fault breccia of the left lateral normal fault off of R43. Photo was taken looking NW.

Figure 21: Outcropping quartz-carbonate-limonite fault breccia of the left lateral normal fault off of R43. Outcrops are highly resistant to weathering and often form hilltops. Photo was taken looking NNE.

Figure 22: Highly altered granodiorite intrusion overlying schist along a low angle fault in hill on the east side of R49. Lightly altered granite forms hill top several meters above this opencut. The red lines mark the fault contact between chlorite and hematite altered Plate 3 and talc-carbonate altered Plate 1 schist. Photo taken looking SW. Refer to north end of Figure 19

Desert Tortoise Wilderness

Much of the northern stretch of the desert tortoise wilderness is composed of Plate I muscovite grayschist and small isolated knobs of Plate II marble (Figures 23 and 24). Several large-scale NE trending faults transect this area and sometimes are accompanied by adjacent felsic intrusives and iron carbonate altered zones. One large moderately dipping NW trending fault was targeted by miners and was found to contain 2.15 ppm Au and highly anomalous arsenic. However, all other mines visited at this location targeted NE striking faults. 12 samples from this location were assayed. All but one contained anomalous gold. The highest gold anomaly was sample GSRM-72 with 2.15 ppm (refer to Fig 23). A high-grade antimony, low grade gold mine targeting a NE striking brecciated fault zone produced a sample with 1.24 ppm Au and 16% Sb. Another mine west of this antimony mine targeted two small NE striking faults within schist. One of these faults produced weakly anomalous gold.

The southern stretch of the Desert Tortoise Wilderness gives way to Plate III granodiorite (Figure 23). While largely unaltered, one area focused around a high angle mylonitic shear zone showed greenschist facies mineralogy with abundant chlorite and epidote alterations. In contact with this was a zone of limonite and silica alteration. Several small prospects and trenches explored this alteration zone but likely found it to be barren of gold. No significant mine workings are present.

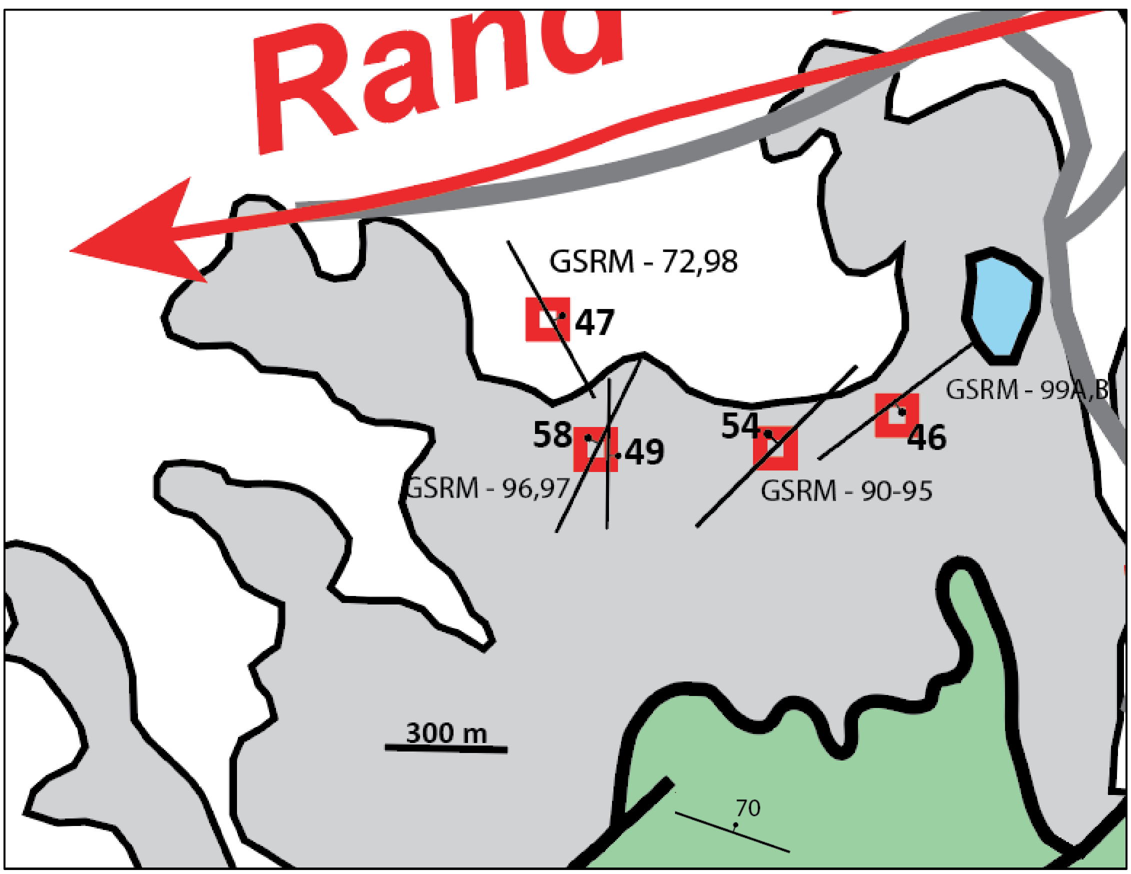

Figure 23: The general geology of the Desert Tortoise Wilderness features primarily schist with occasional patches of Plate II marble. To the south, Plate III becomes the predominant lithology. Assay results show that this focus area is highly anomalous in gold.

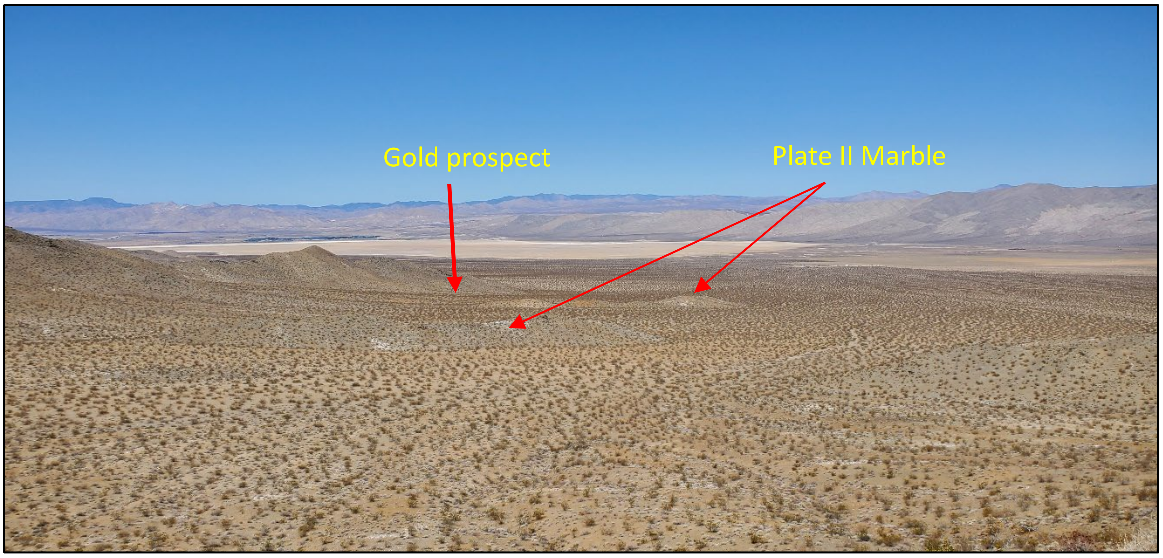

Figure 24: The Desert Tortoise Wilderness is primarily within schist but contains several small hills of Plate II marbles. The prospect located in this image is targeting a NW trending fault. However, all other visited prospects in this area are targeting NE striking faults. View is to the NW.

Hills South of R46-R49 Intersection

Directly south of the intersection of R46 and R49 is a ridgeline defined by an outcropping, steeply dipping NW striking fault (Figure 26). This fault continues downslope to the SE and crops out again at the hills on the east side of R49 (Figure 27). The rock units here are primarily muscovite grayschist. However, the top several meters of the hills on the west side of R49 are composed of Plate II marble cut by veinlets of siderite. The large fault here appears to outcrop as the contact between Plates I and II, and thus, may be interpreted as an exceptional outcropping of the lower Rand Thrust. However, due to its high angle of dip, it is more likely a normal fault that happens to crop out between Plates I and II. Schist and marble foliations from this hill indicate a tight northwesterly trending synform (Figure 25). Three small vertical prospects target the fault directly, while one large horizontal mine is dug into the east facing slope of the hill. Four of the five samples from this area were barren of gold, while just GSRM-86A contained an anomalous .117 ppm Au.

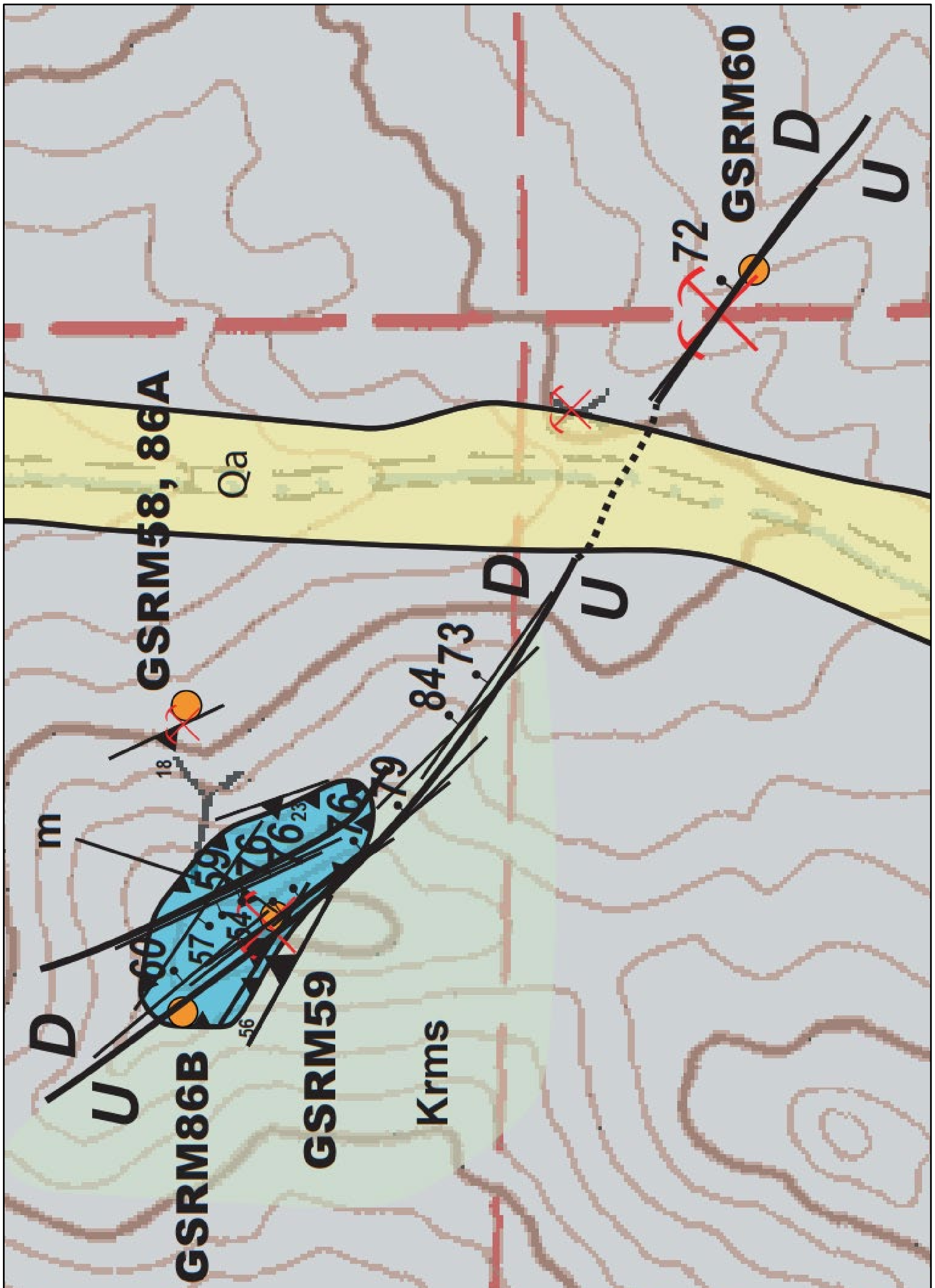

Figure 25: This clip map shows the continuity of the main NW striking fault and how it was the main target of prospectors at this location. The geometry of the long fault and that of the shorter fault to its immediate east suggest a possible conjugate relationship. While most samples from this focus area were barren of gold, one sample, GSRM-86A, contained an anomalous .117 ppm Au. North is to the left. Refer to the legend on Plate 1 in the Appendix.

Figure 26: The vertical prospect at the top of the hill is targeting a high angle NW striking fault separating schist on the southwest side (left) from marble on the northeast (right). Foliation reversals here indicate a synform structure.

Figure 27: The fault pictured in Figure 26 continues through this prospect to the southeast across R49. This location is entirely within schist and silicified hydrothermal breccia lies adjacent to the fault where the elbow shadow is.

Structural Analysis

Structural data has also been organized according to the seven focus areas described previously. Several fault trends were recognized and are discussed in detail below. Fault data is presented with (1) stereonets showing contours of poles to fault planes, and (2) Rose diagrams that statistically and visually quantify fault strike. All contoured stereonets use the Kamb method.

Plate 4 Trenches

5 fault measurements were taken at several open cut trenches 1.3 km to the NE of the Darn Peak group of prospects. All strikes and dips were within the same quadrant as seen in the contoured stereonet of Figure 28. Strikes ranged from 298 to 353 degrees while dips were primarily 24 to 34 degrees to the NE. One dip was steeper at 60 degrees. These faults were primarily associated with the shallow angle quartz rich mylonitized contact between Plate 3 granodiorite and Plate 4 granite. Previous work by A. McLarty, 2012 found that the foliations of the quartz rich mylonitic contact also displayed shallowly dipping NW striking attitudes. This was interpreted to be a detachment fault predating the higher angle NE striking faults seen elsewhere in the Rand Mountains. Assays of all samples from these trenches were completely absent of any anomalous gold values.

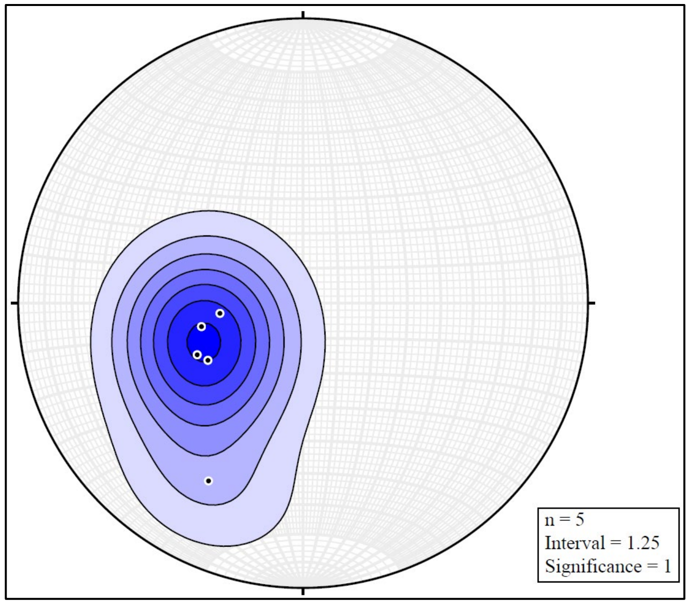

Figure 28: While more work should be done on Plate 4 faults, the limited data from this study show that the faults within Plate 4 near the contact with Plate 3 strike primarily to the NW and dip shallowly to the NE. This reflects the orientation of the upper Rand Thrust marking the contact between the Atolia Granodiorite and the Plate IV granite.

Darn Peak Prospects

97 strike and dip measurements of faults were taken from this group of prospects. These were collected from both the mouth of the prospect adits, as well as, from within the mines when possible (and safe!). Due to the highly faulted nature of this location, there is a relatively significant spread of fault orientations. However, overall, there are three general groupings of fault orientations as seen in the stereonets of Figures 29 and 30.

The tightest grouping of orientations represent NW to NNW strikes and moderate dips to the NE. The second grouping strikes NE and dips to the SE at a shallower angle. 7 rake measurements were gathered from the more coherent fault surfaces within the Darn Peak prospects. 6 of the rakes on NE trending faults indicated oblique motion to the NE ranging in angle from 14 to 71 degrees down from strike. 1 rake measurement on a fault striking N33W indicated movement to the NW at 45 degrees. 4 of the NE rakes are present on the NE striking SE dipping faults.

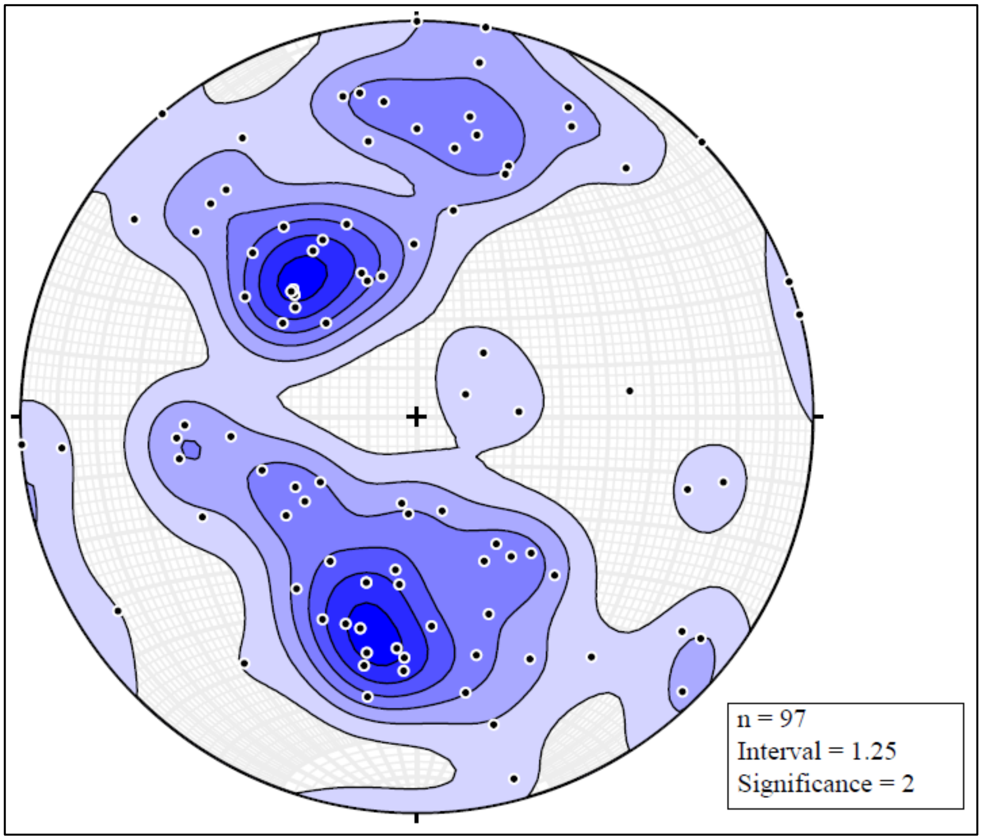

Figure 29: Contoured poles to the fault planes of the Darn Peak group of prospects. There are three primary clusters of orientations. The most prominent of these are the poles to NW and NNW striking faults with moderate to high angles of dip. Secondary to these are the moderate angle NE trending faults and higher angle ENE striking faults. These clusters may represent three different episodes of faulting.

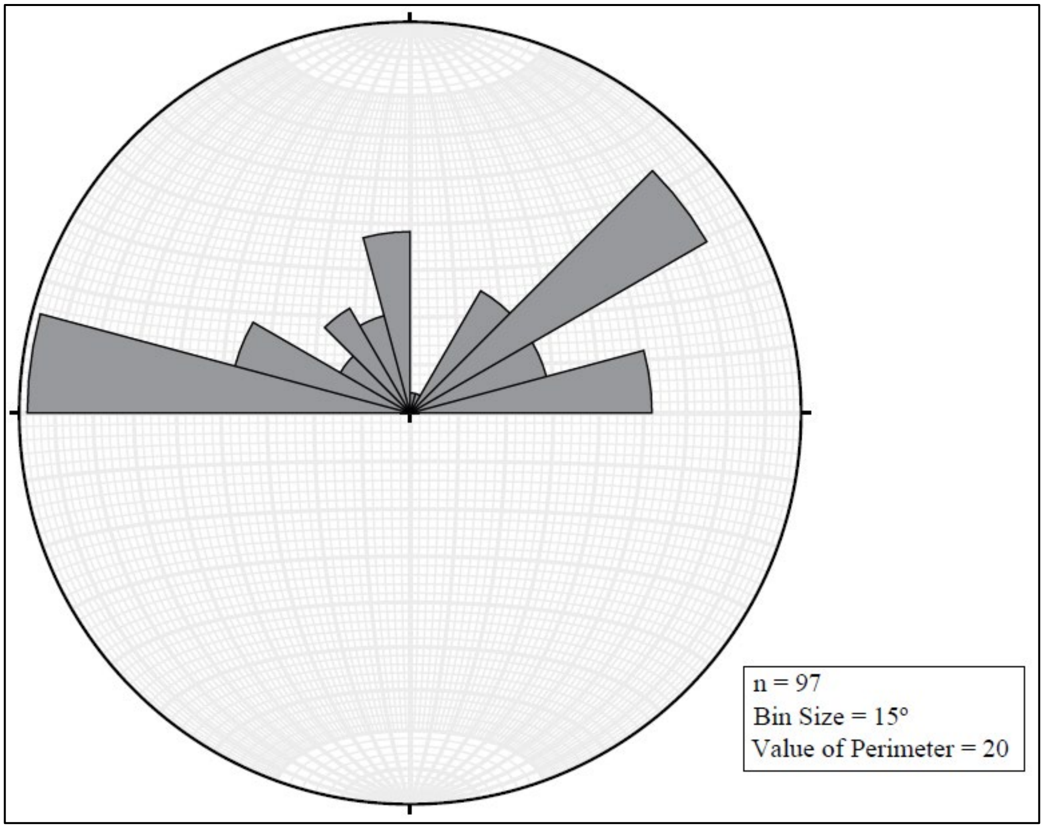

Figure 30: Rose diagram of Darn Peak faults illustrating that the dominant fault strikes are WNW, NE, and ENE with dips to the NE and SE. This uses the half circle method in which dips are eliminated such that all faults are plotted in the northern hemisphere. The length of the petals reflects the number of faults whose strikes fall within each petal's range of azimuths.

The prospect from which GSRM-5 and 67 were collected, contained possible oblique left-lateral normal faults with Riedel relationships in the mouth of the adit. The principal faults strike N45E-N53E and dip 44SE-49SE, with rakes from 44NE to 71NE. The riedel shears to these faults strike and dip at S75W/84NW.

Route 83 Fault Zone

49 strike and dips were gathered along many outcropping quartz-carbonate-limonite fault zones along the slope directly to the south of Route 83 near where it enters into a canyon. The resistant fault outcroppings standout against the landscape and have a characteristic yellow-orange iron-stained surface. Many of the outcrops displayed

polished and striated surfaces that were measured for rake and shear sense. Three groupings of orientations are illustrated in Figures 31 and 32.

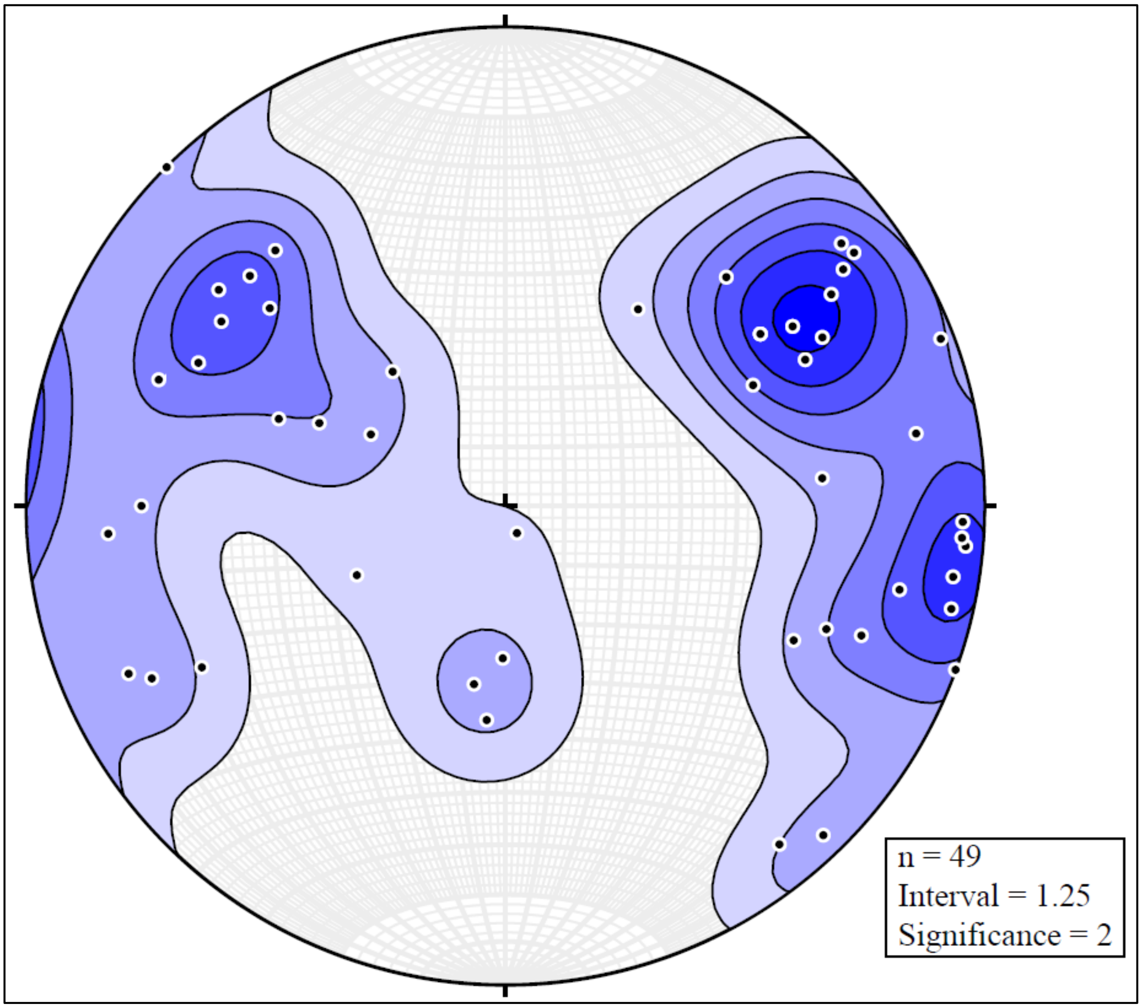

Figure 31: Contoured poles to fault planes in the R83 Fault Zone showing two broadly different orientations of large fault outcroppings. While most faults are moderately to steeply dipping, one set is striking to the NW as the other set is striking variably to the NE. Field observations indicated the NW striking faults are cut and displaced normally by the NE striking faults (see text in geology section).

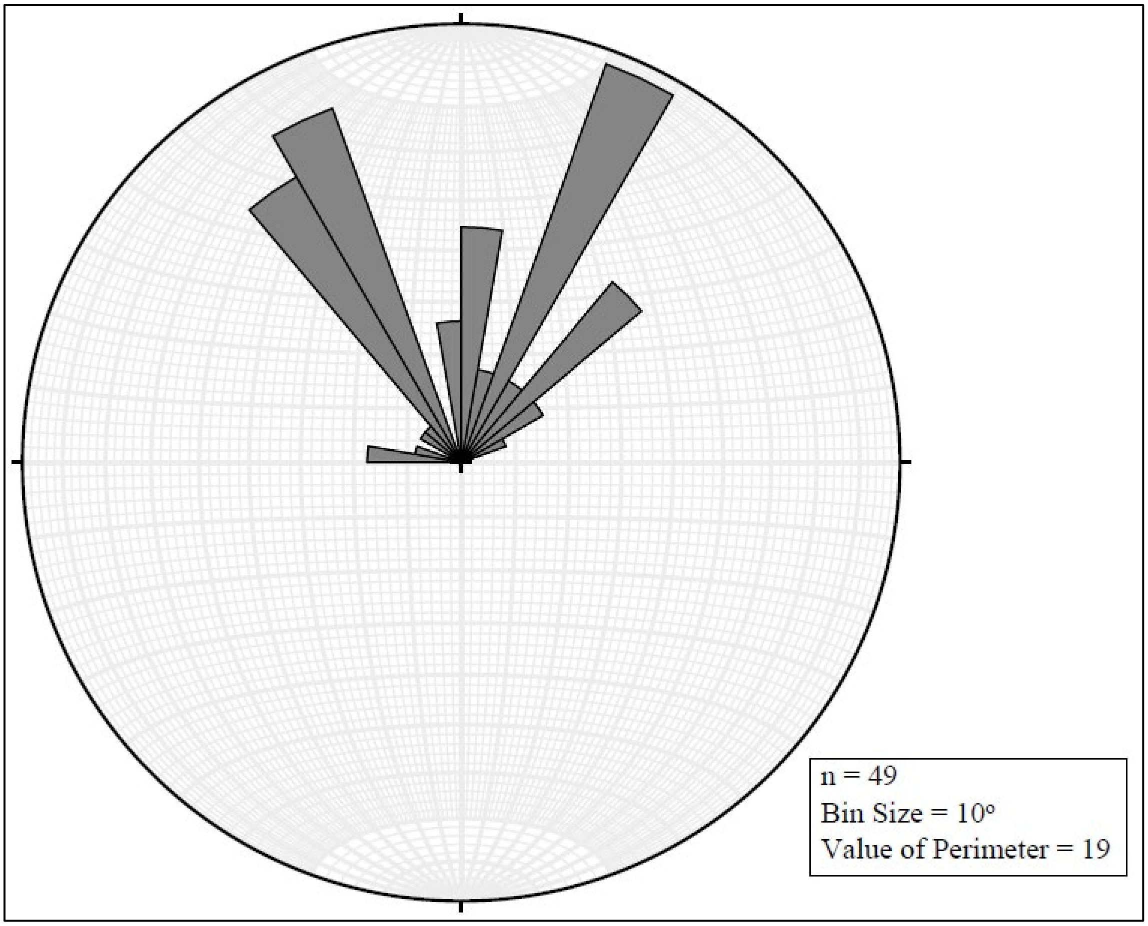

Figure 32: The rose diagram of the R83 Fault Zone shows two dominant trends; one to the NE with minor NNE and ENE components and another to the NW. This uses the half circle method in which dips are eliminated such that all faults are plotted in the northern hemisphere. The length of the petals reflects the number of faults whose strikes fall within each petal's range of azimuths.

The tightest and most numerous grouping had strikes to the NW at about 140 - 150 degrees and dips to the SW at steep angles of around 70 – 80 degrees. This group of faults had striated surfaces with rakes to the NW ranging from 33 – 62 degrees from horizontal. Sense of shear on these faults was normal movement with significant right lateral motion. The second grouping has strikes to the 30 – 50 degrees to the NE while dips are generally 25 – 70 degrees to the NW. This group forms a normal fault system that displaces the oblique-right lateral fault A third grouping of less densely grouped fault orientations taken from outcropping at the top of a vertical prospect ranges in strike from

180 – 193 and steep dips of 80 – 85 to the NW. The dip reversal of the two sets of NE trending faults suggests a possible conjugate relationship. These faults displayed striations with rakes at steeper angles of 67 – 84 degrees to the NE. This reflects a more significant amount of dip slip motion than the first group of faults.

Route 50 Knob

22 strike and dips of faults were measured within a major horizontal mine and associated stopes on the south slope of a lone-standing knob along Route 50 along the northwestern flank of the Rand Mountains. The moderately dipping faults were seen cutting through both the Rand Schist and Johannesburg Gneiss units that make up the knob. As seen in Figures 33 and 34, the majority of the faults are striking to the N26E to N83E and dipping to the NW at angles ranging from 30 to 65 degrees.

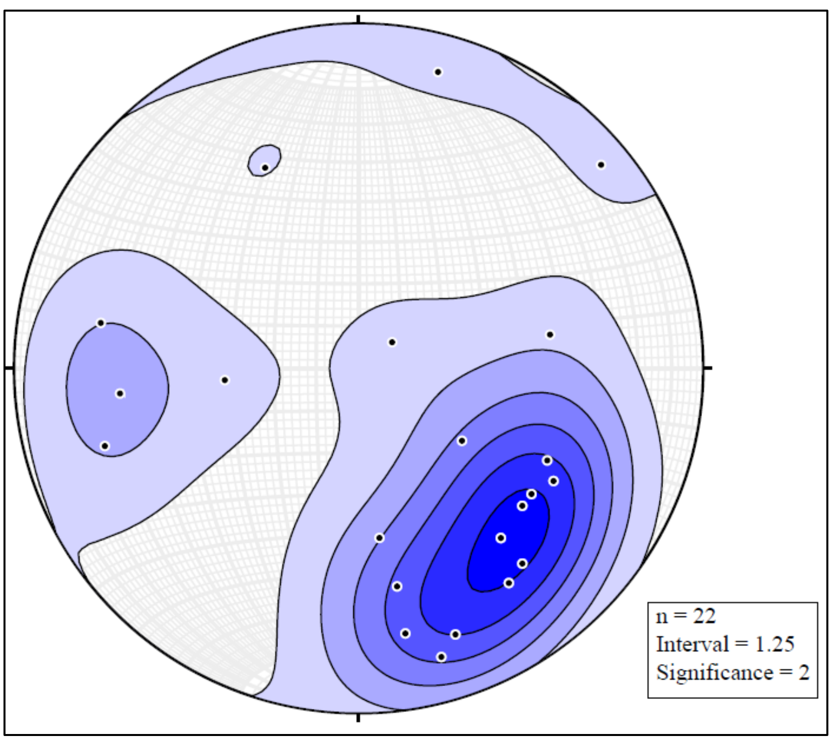

Figure 33: Poles to fault planes from within the mine shaft at the R50 knob location showing clear predominance of NE striking moderately to steeply dipping faults. Rakes from several of these faults indicate dominantly dip slip normal sense of shear with minor oblique motion.

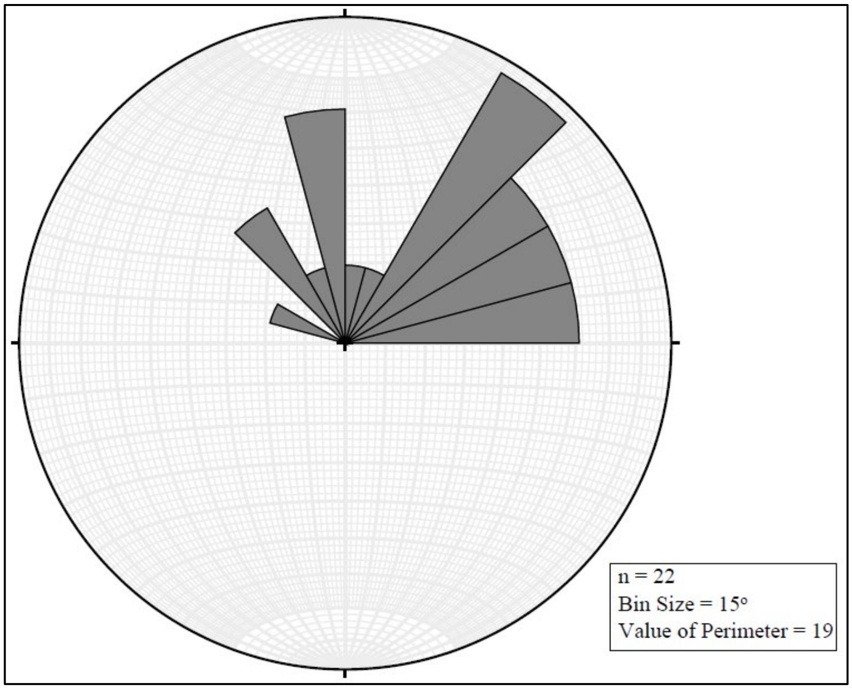

Figure 34: The rose diagram of the R50 Knob faults illustrates the dominance of the mineralized NE trending, NW dipping faults targeted by the miners. However, there is a wide spread from east to northeast strikes. Minor fault trends to the NNW and NW are also present at this location. This uses the half circle method in which dips are eliminated such that all faults are plotted in the northern hemisphere. The length of the petals reflects the number of faults whose strikes fall within each petal's range of azimuths.

7 rake measurements were gathered from the exposed faults within the horizontal mine shaft. While the rakes were consistently steep, between 66 and 84 degrees, they varied in direction between NW, NE, and SW. The steepness of the rakes suggests a primarily dip slip motion along the faults. One particularly well-exposed fault surface picture in Figure 14 preserves well-developed normal-sense brittle fault-slip indicators

Numerous foliation measurements of the schist and gneiss outcrops showed clear dip reversal from the west flank of the knob to the east flank (Figure 12). Mapped out, this represents a possible synclinal feature that is cut by the younger measured faults. The large scale folding along with the dip slip motion along the faults likely suggests a thrusting event, possibly followed by younger (Miocence?) extension reactivating the reverse faults as normal faults.

Route 43-Route 51 Cross-Fault

A continuously outcropping fault previously mapped by Nourse, 1989 and McLarty, 2012, along R43 was sampled and re-measured for this study. It was described by McLarty as an oblique left-lateral normal fault with significant throw. This fault may represent late Miocene extension along with left lateral motion influenced by early Garlock Fault movement. Like the R83 faults, exposures are characterized by large resistant outcrops of yellow-orange brecciated quartz-carbonate-limonite structures with smooth polished hematite surfaces where the fault surface is exposed. Additionally, I identified an extension of this cross-fault along strike a little over 1 km to the NE at the southern end of R51. Thirty-four strike and dip measurements were gathered along the cross-fault and its NE extension. Eleven of the measurements had NE strikes ranging from 10 to 64 degrees. Their dips were all to the NW at angles between 42 to 73 degrees. Six NE striking faults were measured between 20 and 79 degrees with dips ranging from 54 to 76 degrees to the SE. Two additional measurements featured vertical dips and strikes to the NE. A separate set of 9 NW striking faults varied greatly in strike and generally exhibited shallower dips of 30 to 50 degrees to the SW. The stereonets in Figures 35 and 36 show the two groupings of fault orientations.

Additional fault measurements were collected within a highly altered schist outcropping cut by the cross-fault. The schist was composed of two different packages. One package was muscovite schist with prevalent stockwork quartz veins and iron oxides. The other package consisted of black and orange highly carbonate altered mafic schist with bright green and blue micaceous nickel and chromium bearing minerals. The small faults measured here cut through both packages of schist. 5 rake measurements, 2 to the NE, 2 to the SE, and 1 vertical, were all steep angled, signifying prominent dip slip motion along the faults.

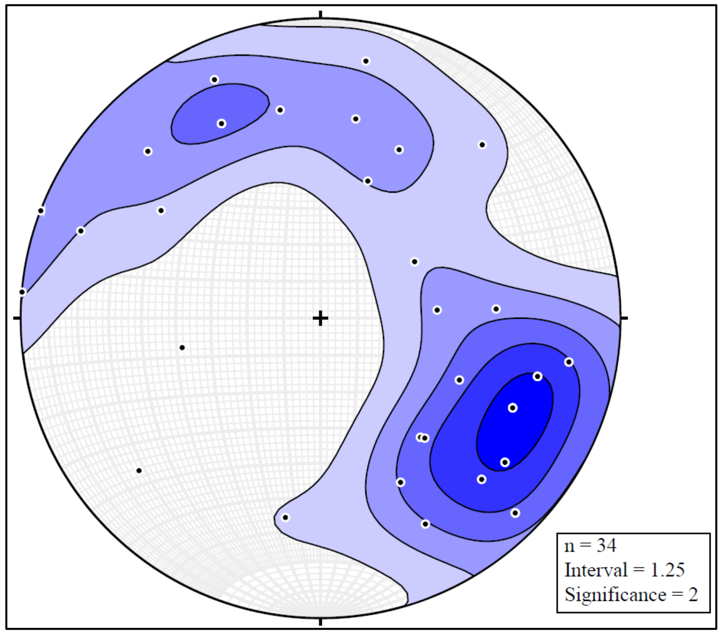

Figure 35: Contoured poles to fault planes from along and adjacent to a major NE striking cross fault stretching from R43 to the end of R51. NE striking moderate to high angle faults are predominant and often mineralized. NW striking faults were less common and show a wide spread in strikes and shallow to moderate dips.

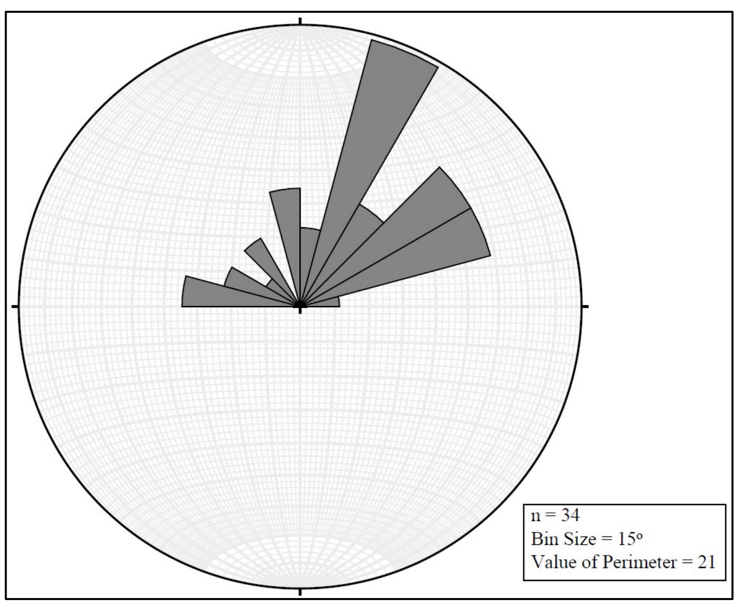

Figure 36: The rose diagram of the R43 cross fault, its northern extension, and surrounding minor faults shows an obvious preference for a NE- strike. There is a moderate preference for a northerly to NNW strike as well. Overall. NW trends are weak. This uses the half circle method in which dips are eliminated such that all faults are plotted in the northern hemisphere. The length of the petals reflects the number of faults whose strikes fall within each petal's range of azimuths.

Desert Tortoise Wilderness

Fault data was collected from an expansive portion of the Desert Tortoise Wilderness at the furthest southwest point of the study area. Faults from several mines and prospects along with unprospected outcropping faults and linear features were measured. Twenty-four strike and dips were collected from faults and entered into stereonets (Figures 37 and 38). Fifteen faults struck variably to the northeast between 1 and 83 degrees and had extremely variable dips between 9 and 72 degrees to the SE and 31 to 49 degrees to the NW. Nine faults trended to the NW between 289 and 350 degrees with moderate to steep dips and rarely shallow dips. Striations were uncommon, and as a result, only 5 rake measurements could be made. A SE striking fault gave the shallowest rake of 45 NW. The other 4 rakes were generally steep, but ranged from 52 to 90 degrees NE and were observed on NE-SW striking faults. This limited dataset suggests that the NE-SW trend of faults experienced a much more significant component of dip slip motion than that of the NW-SE trend.

Due to the expansiveness of this part of the study area, it was no surprise that there was a wide spread of orientations. However, it is clear that there are two strong trends in conjunction with some smaller ones. The most common trend is ENE on the half circle rose diagram in Figure 10). Following this is a strong NW orientation and a minor SW or NE orientation (Figure 10). Interestingly, the two trends were rarely observed occurring in the same location. NE-SW trends were the most widespread, while the NW-SE trend was found primarily in one location within a prospect.

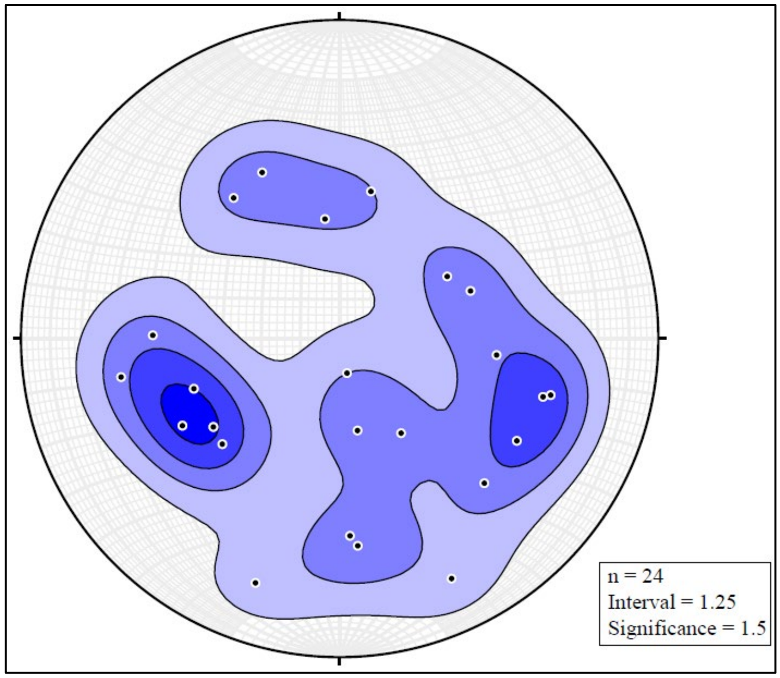

Figure 37: Contoured poles show the wide variation in fault orientations within the Desert Tortoise Wilderness. NW striking, NE dipping faults show the most consistency. NE striking, NW dipping faults form a common trend but show a wide spread within the quadrant.

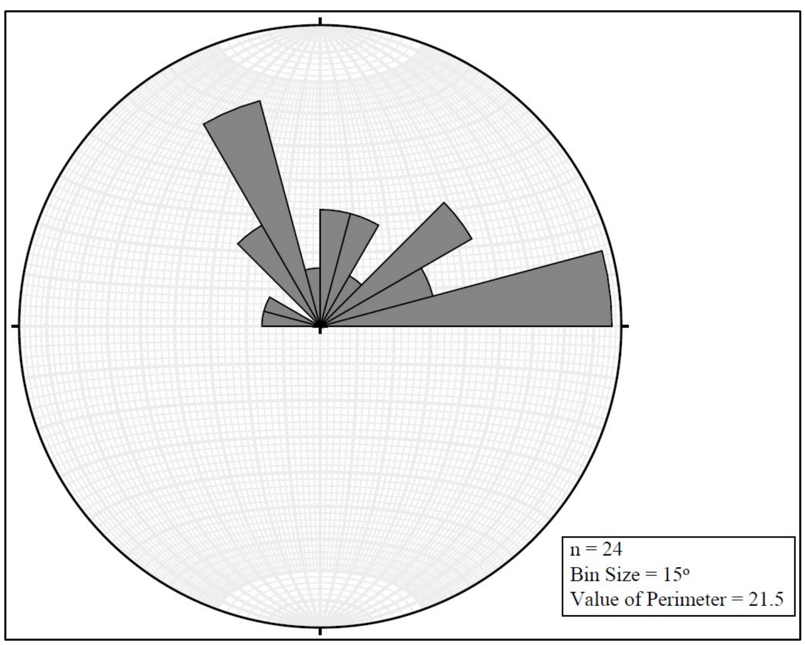

Figure 38: The half circle rose diagram of the Desert Tortoise Wilderness fault trends. The majority of faults followed a NE trend with a strong preference to the ENE. A second isolated trend exhibited strikes to the NW. This uses the half circle method in which dips are eliminated such that all faults are plotted in the northern hemisphere. The length of the petals reflects the number of faults whose strikes fall within each petal's range of azimuths.

R49-R46 Fault Zone

The ridgeline immediately south of the intersection between R49 and R46 (Figure 25) features prominent outcropping faults with visible striations (Figure 26). One 20-foot-deep prospect is dug vertically into a large outcropping fault at the top of the ridgeline. This fault has variable width between several inches to two feet in width and contains zoned veining of calcite, quartz, and iron carbonate breccia. A second 100 foot+ adit is excavated horizontally into the south side of the hill approximately 70 feet below the vertical prospect. It was not possible to explore this mine due to the poor air quality. Therefore, all fault measurements are from surface exposures.

Out of 11 total fault measurements, all are NW striking with steep dips between 54 and 84 degrees to the NE and SW (Figures 39 and 40). However, there are two sets of faults. The prominent set dips to the NE while a subordinate set dips to the SW. This could be representative of a conjugate pair. Two rake measurements were made. On a NE dipping fault, the rake was 61SE. Similarly, a SW dipping fault portrayed a rake of 62SE. This suggests that there was a substantial amount of oblique movement rather than just dip slip. Because most unrotated NW striking faults in the Rand Mountains were likely generated during Miocene extension, and the rakes detail oblique movement, I interpret these faults to be dextral transtensional faults. Because the NW striking, NE dipping faults are exposed sporadically for almost half a kilometer along a relatively linear transect, it is assumed that this is a single large fault rather than many small ones.

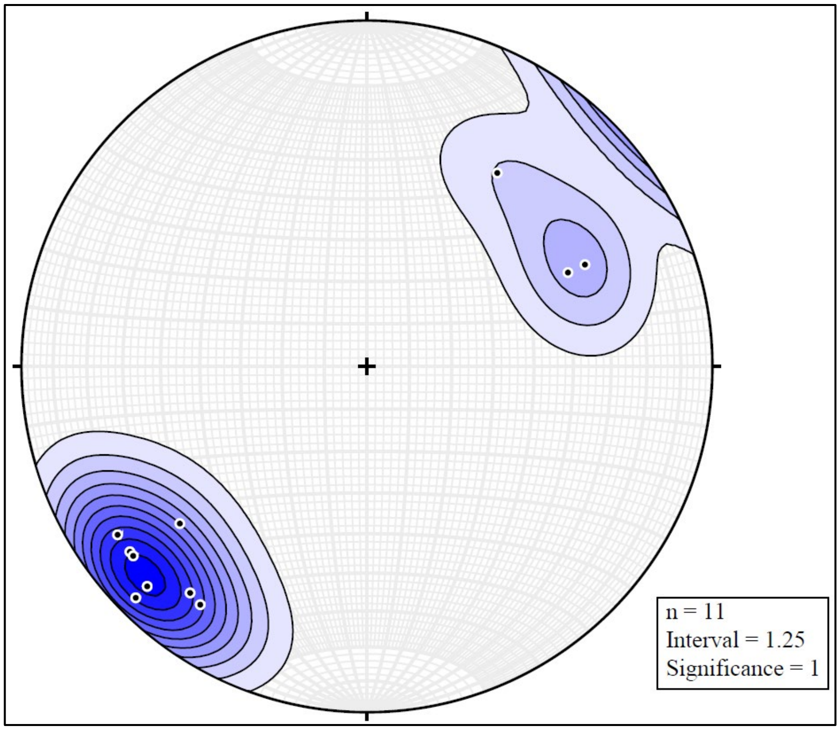

Figure 39: The contoured poles indicate two sets of faults; both striking to the NW but one set dips steeply to the NE while the other set dips moderately to the SW. In conjunction with the SE rakes, it may be inferred that these represent a conjugate pair of dextral transtensional faults.

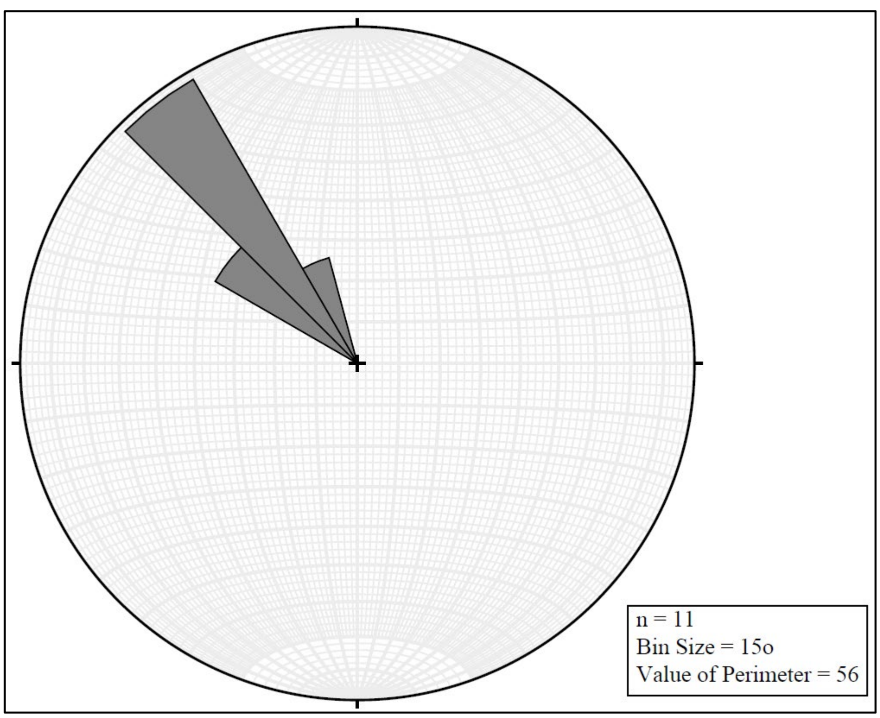

Figure 40: The half circle rose diagram illustrates the uniformity of strikes with various faults along the ridgeline of the hills to the south of the R49-R46 intersection. This uses the half circle method in which dips are eliminated such that all faults are plotted in the northern hemisphere. The length of the petals reflects the number of faults whose strikes fall within each petal's range of azimuths.

Assay Data

96 samples were collected for 35 element assays. Sample locations are shown on Figures 2, 6, 7, 10, 11, 15, 19, 23, and 25. Table 1 below compiles all of the samples with their gold concentrations, descriptions, and structure orientations. Included with each sample is its lithology, the type of geologic feature or structure from which the sample was collected, and its attitude or orientation. Samples are listed from highest gold value to lowest. Gold values below the detection limit of the ICP-MS are written as -.003. Anomalous gold concentrations are considered to be any analyses equal to or greater than .01 ppm (10 ppb) Au. Of the 96 samples assayed, 57 had concentrations of gold greater than .01 ppm. Samples JN-1826, JN-1905, Atolia GD #101, and ERT Plate IV were not assayed for gold. These samples are fresh, unaltered granites and granodiorite that presumably contain too little gold to be detected by the mass spectrometer. For complete tables of the assay results, including measured concentrations for all 35 elements, see Appendix B. Highlights of all 35 element assays are as follows:

- The highest-grade sample, GSRM-33, with 10ppm Au over a 2 meter transect, was hydrothermally altered fault gouge. It was collected from a subvertical NE striking extensional fault along north wall of minor abandoned prospect at the Darn Peak locality (Figure 10; Figure 41). Wall rock contained extensive iron carbonate alteration and veining as well as low grade gold mineralization. This sample was re-assayed (8. 21 ppm) to confirm that the gold anomaly was not due to nugget effect. Generally, most of the anomalous gold samples were from fault gouge and hydrothermally altered fault zones. However, some of the auriferous samples were altered or silicified wall rock directly adjacent to mineralized faults. Of the samples collected from intrusive felsitic dikes, only GSRM-81B contained significantly anomalous gold (.38 ppm).

Figure 41: This pair of very shallow prospects are host to 10 ppm Au. Sample GSRM-33 was taken as a 2-meter chip transect along a subvertical NE trending fault directly left of the large bush on the left side of the lower prospect. Two other minor shallow angle NW striking faults (I am pointing to one) contained small anomalies of gold. The image at right shows the fault gouge containing 10 ppm Au (view to NNW?). It is highly clay altered and contains abundant carbonate veinlets. The unassuming appearance of the gold zone suggests that more like it are likely present elsewhere in Plate III.

- Highly anomalous nickel and chromium occurrences were found in samples GSRM- 48, 57, 57B, 70, 71, 85, 87, 94, and 95. These samples contained prevalent magnesite, ankerite, dolomite or calcite, fuchsite (chromian mica), disseminated chromite, talc, and various green and blue cryptic nickel bearing minerals. Quartz was also present in minor to moderate amounts. Sample 57B (located on Figure 2) was a 3 inch long and 1.5-inch-thick pod of just fuchsite and chromite that was taken from the same tailings pile as GSRM-57 (magnesite-quartz-fuchsite rock) and GSRM-55 (blueschist with stockwork quartz veins grading at 3.68 ppm Au). These 9 samples contained chromium ranging from 1,015 ppm to 25,809 ppm.

- Silver was rarely anomalous and often below the detection limit of the mass spectrometer. Even the anomalous samples only contained small concentrations. However, it is interesting that all silver anomalies, with the exception of one, occurred in samples that also showed moderate to high gold anomalies. The highest silver concentration that occurred with a gold anomaly was 43.8 ppm from sample GSRM-BR (located on figure 11). The gold value for this sample was 3.17 ppm. It also was the only sample to contain significantly anomalous bismuth (249 ppm), cadmium (23.5 ppm), copper (3,147 ppm), and lead (202 ppm). After this sample, the next highest silver sample, GSRM-80C, only contained 6.9 ppm (located on figure 2). The highest gold sample, GSRM-33, contained 3.2 ppm silver.
- Sample GSRM-78 was a manganese oxide ore with over 50,000 ppm Mn. This was above the upper limit of what the mass spectrometer could measure, so it is unclear what the true manganese concentration actually is. This sample also contained by far the highest silver and molybdenum values of 18.1 ppm and 153 ppm respectively. Gold was only slightly anomalous at .013 ppm. The sample was collected from a swollen manganese seam of a manganiferous metachert unit within a dipping schist outcrop immediately to the south of the R43 canyon cross fault outcroppings (located on figure 19).
- Samples GSRM-90, 91, 92, 93, 94, and 95 were very highly anomalous in antimony (Figure 23 and 42). GSRM-92 contained an economic grade of 16% Sb (161,700 ppm). This sample also contained 1.24 ppm Au. The

other 4 samples ranged between 1,301 ppm Sb and 97,150 ppm Sb. All of these contained anomalous gold.

Figure 42: The picture at left shows the mine and brecciated structure that produced the high-grade antimony, low grade gold samples (GSRM-90 through 95). The red lines indicate the edges of the brecciated fault structure. The image at right is sample GSRM-92 which contained 161,700 ppm Sb and 1.24 ppm Au. The 1.25-inch-thick silvery vein is mostly solid stibnite (Sb_2S_3) and possibly native antimony.

- Sample GSRM-99B (located on Figure 23) contained far more iron (boxwork limonite) than any other sample at 236,824 ppm. This extremely high iron content along with anomalies of gold (.085 ppm), silver (1 ppm), arsenic (986 ppm), copper (301 ppm), and molybdenum (41 ppm) suggest that it could be a gossanous feature. It was found as a remnant component of a brecciated quartz rich structure with .11 ppm Au.

Table 1: This table displays sample IDs, coordinates, gold values, structural controls, and descriptions of all assayed samples. Sorting is from highest gold value.

Sample ID	Easting	Northing	Au ppm	Fault Strike/Dip	Sample Description
GSRM-33	433485	3906636	10.013	N50E/90	Same mine as GSRM 31 and 32. From fault gouge zone in N. Wall of mine adit with heavy lim/hem staining, qtz, siderite. Entirely in altered GD.
GSRM-55	434382	3910019	3.68	N71E/51SE.	Large 1m+ wide fault in altered schist Sample from tailings of this mine.
GSRM - BR	436261	3911441	3.17	S82W/90	Quartz vein with prevalent copper sulfides and oxides with pyrite infilling cracks. Entirely in blueschist.
GSRM-63	433483	3906624	2.86	N50E/90	Iron carbonate quartz vein material in altered granodiorite surrounding 10 ppm fault.
GSRM-72	429964	3909020	2.15	N29W/47NE	Altered schist material (oxidized pyrite) within fault with realgar/orpiment.
GSRM-80 C	442743	3911395	1.6	N40E/72NW	Chalcedonic or opaline blue-grey quartz vein with disseminated sulfides.
GSRM - 92	430727	3908584	1.24	N45E/54NW	Fault vein breccia with large rich stibnite veins and fracture fills.
GSRM-42	433903	3912200	1.03	S36W/52NW	Highly oxidized fault gouge within schist directly below gneiss unit. Contains large siderite.
GSRM - 98	429964	3909020	0.96	N29W/47NE	2-3 foot thick fault gouge stained red and yellow from presence of realgar and orpiment.
GSRM-80 B	442743	3911395	0.803		Silicified breccia vein with all parts of vein and some schist material.
GSRM-77	438687	3912607	0.656	N15W/45NE	Oxidized quartz vein with oxidized iron carbonates. All in schist of Big Gold Mine.
GSRM-45	436684	3912104	0.453	S43E/47SW	Sample from mine of GSRM 44. From hematitic fault gouge in roof of adit (1 ft wide).
GSRM - 91	430727	3908584	0.411	N45E/54NW	Fault vein breccia with large rich stibnite veins and fracture fills.
GSRM - 81B	434014	3905660	0.38	S64W/81SE	Brecciated fine limonite silicified felsite/rhyolite dike with inclusions of fine sulfides.
GSRM-76	438687	3912607	0.359	N61W/41NE	Oxidized quartz within fault vein. All in schist of Big Gold Mine.
GSRM-75	438687	3912607	0.35	N50W/20NE	Oxidized quartz within fault vein. All in schist of Big Gold Mine.
GSRM-65	433483	3906624	0.313	N50E/90	Brown iron carbonate veined altered granodiorite surrounding 10 ppm fault.
GSRM - 94	430727	3908584	0.282	N45E/54NW	Blue-green Cr-Ni minerals as crusts and veins in quartz-limonite schistose rock.
GSRM-68 B	434014	3905660	0.275	S38W/80NW	White felsite or rhyolite dike with sulfides.
GSRM-31	433485	3906636	0.248	N73W/36NE	Fault in altered GD 10-15cm wide.
GSRM-80 A	442743	3911395	0.248	N40E/67NW	Exposed sericitic alteration of vein.
GSRM-44	436684	3912104	0.206		From tailings pile. Some kind of aphanitic igneous rock (maybe felsite) with some porphyritic texture. Lots of sulfides. From mine in schist.
GSRM - 93	430727	3908584	0.193	N45E/54NW	Fine grained dark grey silicified breccia with disseminated stibnite and pieces of schist.
GSRM - 6	433275	3906800	0.161	N62E/42SE	1 meter chip transect across kaolinite - limonite - hematite - fault zone. In extremely damaged GD.
GSRM-62	436314	3912027	0.123	S12W/73NW	Limonitic qtz carb fault zone just exposed at surface.
GSRM-32	433485	3906636	0.121	N85W/49NE	Fault in altered GD 10-15cm wide.
GSRM - 95	430727	3908584	0.118	N45E/54NW	Schistose, limonitic, oxidized stibnite, fuchsitic rock.
GSRM-24	442195	3913142	0.117	N81E/82SE	Large vein qtz. From tailings of mine in GD with large fault. Heavily disseminated small stibnite.
GSRM - 86A	432898	3910052	0.117		Extremely hematitic schist likely from wall rock around fault within mine.
GSRM - 99A	430936	3908606	0.11	N53E/46SE	Either leucogranite dike of Plate III or brecciated quartz vein along outcropping limonitic fault zone.
GSRM-36	435576	3909576	0.106		Sample from tailings. Vuggy oxidized quartz presumably from qrtz lenses in the schist from the mine with GSRM 35.
GSRM-35	435576	3909576	0.092	S75E/55SW	Mine adit with 14-15 inch wide fault gouge (sample from gouge) with hematite staining in blue schist.
GSRM - 99B	430947	3908609	0.085	N53E/46SE	Along same trend as 99A, highly limonitic boxwork gossan like unit with black metallic veins and spots.
GSRM-37	436146	3908756	0.077		White Sydney Mine tailings. Large chunk of qtz covered in gray powder from host schist.
GSRM-69	433483	3906624	0.076	S76W/52NW	Brecciated altered GD within fault zone.
GSRM-74	436407	3912020	0.072	N26W/71NE	fault gouge within blueschist.
GSRM - 90	430727	3908584	0.071	N45E/54NW	Fault vein breccia with large rich stibnite veins and fracture fills.
GSRM-73	436291	3911853	0.055	S5W/86NW	qtz-carb-limonite fault vein breccia with some metachert.
GSRM-59	432819	3910011	0.04	N38W/76NE	From fault gouge within vertical shaft on top of hill directly above GSRM 58. Chalky gouge bordered by several inches of well crystalized calcite. All in schist.
GSRM-56	434395	3910019	0.038	N73E/52SE	Sample from tailings of different mine along same fault structure as GSRM 55 (altered schist).
GSRM-79	434462	3909572	0.037	N70E/53SE	Fault gouge within schist.
GSRM-25	433226	3906760	0.033	N7W/51NE	hem/lim clay altered plate 4 granite fault zone in roof of minor adit.

GSRM-27	433553	3906588	**0.03**	S50W/37NW	10cm wide fault with hem/lim staining in altered GD from same mine as GSRM 26. Major targeted structure.
GSRM - 97	430394	3908667	**0.027**	N1E/49E	Fault gouge within wedge between two faults.
GSRM-28	433553	3906588	**0.026**	N55W/44NE	Another 10 cm wide fault within the unaltered GD below the altered GD from GSRM 26 and 27.
GSRM - 84C	433154	3907947	**0.024**		Silicic and limonitic schistose rock with green and blue nickeliferous patches.
GSRM-70	433138	3907942	**0.023**		Fuchsite/Talc qtz-carbonate vein material. Listwanite? Disseminated sulfides.
GSRM-26	433553	3906588	**0.018**	N37W/29NE	Low angle fault in altered GD overlying unaltered GD.
GSRM-67	433483	3906624	**0.018**	N77E/72SE	Chloritized GD with orange brown iron oxide veinlets.
GSRM-57	434407	3910020	**0.017**	N82E/66SE	Fuchsitic quartzite from tailings of very deep vertical shaft targeting same fault structure as GSRM 55 and 54.
GSRM-58	432898	3910052	**0.016**		Large qtz vein material from tailings of mine in schist w/ metachert. Qtz has very intense maroon and orange veins within.
GSRM-38	432924	3907856	**0.015**	S38W/67NW	limonitic Qtz-carb outcrops along crossfault with some brecciation.
GSRM - 9	433252	3906806	**0.014**	S88E/58SW	Hanging wall above basal fault zone. Potential malachite and siderite. Iron carbonate and limonite alteration.
GSRM-78	433103	3907736	**0.013**		Black siliceos manganese oxide ore with patches of rhodonite from seam within schist N85E/44SE.
GSRM-30	433517	3906634	**0.012**	S54W/64NW	100 ft further in adit from GSRM 29. Sample from vein of barite/siderite and calcite 5 cm wide.
GSRM - 81A	434014	3905660	**0.012**	S60W/56NW	Brecciated fine limonite silicified felsite/rhyolite dike in fault.
GSRM-41	432361	3909981	**0.01**		Highly limonitic schist from manganese mine with nodule like orange bumps from tailings. Contains possible siderite/calcite veins.
GSRM - 7	433252	3906806	**0.009**	S82E/58SW	60 cm chip transect of fault zone (in hanging wall) above basal fault. Within Plate 3 GD
GSRM-50	433833	3909038	**0.009**	S63W/66NW	Hanging wall above fault in altered granite (hem/lim clay alteration). Sample might be felsite with sulfide masses.
GSRM-64	433483	3906624	**0.009**	N50E/90	Brown iron carbonate veined altered granodiorite surrounding 10 ppm fault.
GSRM - 85	433183	3907971	**0.009**		Green micaceous limonite seam in schist S49W/44NW.
GSRM - 84A	433154	3907947	**0.008**		Heavy quartz veining with iron oxides within Rand greyschist.
GSRM - 96	430394	3908667	**0.008**	N26E/58NW	Fault breccia within gray schist with minor alteration.
GSRM-43	433903	3912200	**0.007**		Altered wall rock (schist) near contact with fault from same mine as GSRM 42. Some calcite and siderite veinlets.
GSRM-48	436685	3912102	**0.007**		Altered schist near contact with altered GD. Has fuchsite lenses (maybe talc?).
GSRM - 84B	433154	3907947	**0.007**		Stock work quartz veining and stringers with iron oxides within Rand greyschist.
GSRM - 11	433255	3908120	**0.006**		Mix of Plate 4 Granite and qtz mylonite. Damaged limonite - hematite - silica altered granite. Local breccia gouge.
GSRM-39	432958	3907872	**0.006**	S45W/65NW	limonitic Qtz-carb outcrops along crossfault with some brecciation.
GSRM-68 A	434014	3905660	**0.006**	S42W/77NW	White felsite or rhyolite dike.
GSRM - 86B	432819	3910011	**0.006**	N40W/78NE	Zoned quartz, carbonate, breccia fault gouge from outcropping fault at top of hill.
GSRM - 4	434459	3907343	**0.005**		Granodiorite host rock 1.5 meters below Qtz Mylonite. Hornblende. Biotite altered to chlorite.
GSRM-61	436333	3911991	**0.005**	S36E/79SW	Long fault exposure with slicks and limonitic qtz carb outcrop.
GSRM-71	433218	3907988	**0.005**		Extremely orange and green fuchsite/talc carbonate schist.
GSRM - 87	433845	3909031	**0.005**		highly calcified orange schistose talc carbonate alteration material.
GSRM - 10	433262	3908142	**0.004**		Fault surface contact b/n upper Rand Schist and limonite - carbonate breccia at lowest part of hanging wall.
GSRM - 12	433255	3908120	**0.004**		Silica rich zone, brecciated vein qtz. with limonite - hematite stain. Foliated sheet similar to Plate 3&4 contact.
GSRM - 13	433255	3908120	**0.004**		Strongly altered granite protolith. Locally brecciated gouge. Limonite - hematite - kaolinite - malachite alteration.
GSRM-29	433517	3906634	**0.004**	S39W/75NW	Adit in moderate to strong altered GD hem/lim staining. Sample from limonitic fault gouge.
GSRM-66	433483	3906624	**0.004**	N50E/90	Mostly brown iron carbonate material with bits of altered granodiorite surrounding 10 ppm fault.
GSRM - 1	434459	3907343	**0.003**		Quartz Mylonite with hematite - limonite staining.
GSRM - 2	434459	3907343	**0.003**		Top of Plate 3 Granodiorite below Plate 4 Granite. Mylonitized beyond recognition.
GSRM - 3	434459	3907343	**0.003**	N26W/34NE	Whitish gouge zone, very crumbly with hemotite - limonite alteration.
GSRM - 5	433483	3906648	**0.003**	S58W/41SE	Highly altered Granodiorite. Hematite - limonite alteration, very crumbly.
GSRM - 8	433252	3906806	**0.003**	S82E/58SW	Chip transect beneath basal fault in limonite - hematite - carbonate footwall. Some malachite.
JN 1906			**0.003**		Mylonitic Plate IV Granite
GSRM-40	433053	3907916	**0.003**	S24W/42NW	limonitic Qtz-carb outcrops along crossfault with some brecciation. Entirely in GD and above schist.

GSRM-46	436685	3912102	**0.003**	S40E/68NE	Large qtz vein material within highly altered GD.
GSRM-47	436685	3912102	**0.003**		Chloritized GD, very crumbly from center of alteration zone within the vertical mine.
GSRM-51	433684	3909027	**0.003**	S64W/51NW	Limonitic qtz carb fault zone; slightly brecciated appearance. Within schist.
GSRM-52	433500	3909029	**0.003**	S65E/52SW	iron/clay altered granite along fault zone in the roof of two diggings.
GSRM-60	433092	3909804	**0.003**	N52W/72NE.	Hydrothermal breccia adjacent to fault traced down hill from GSRM 59. Brecciated vein qtz with very limonitic silicic groundmass.
GSRM - 57B	434407	3910020	**0.003**		Large pod of brilliantly green fuchsite and black chromite from same mines as GSRM 57 and 55.
JN 1826			**N/A**		Fresh Plate IV Granite
JN 1905			**N/A**		Fresh Plate IV Granite
Atolia GD #101	433549	3906594	**N/A**		Fresh Plate III Granodiorite
ERT Plate 4			**N/A**		Fresh Plate IV Granite

XRF Data

37 samples were analyzed by XRF for major oxides and trace elements. These included 3 samples of unaltered Plate 3 Atolia Granodiorite and 6 samples of unaltered Plate 4 Granite. The remaining 28 samples consist of hydrothermally altered versions of Plates 3 and 4, Plate 1 schist, felsite intrusives, quartz-carbonate fault vein material, and possible listwanitic material. Appendix C provides a table of all XRF results. The data is displayed on various plots below, using the GCD Kit (GeoChemical Data toolkit) on the R platform, to accomplish three objectives: (1) to confirm the lithological identity of the samples; (2) to show the shift in chemistry between unaltered and altered samples of the same units; and (3) to explore relationships between loss-on-ignition (LOI) and alteration products that may result from sample degassing during analysis. Legends to the plots are located in Appendix C.

Lithology Based on XRF Data

Six fresh, unaltered samples of the Plate 4 granite were plotted on a TAS (Total alkali vs silica) diagram (Middlemost, 1994) to confirm their identity. This diagram plots Na_2O + K_2O content against SiO_2 (Figure 43). 6 of the samples plotted in a tight group within the granite section. One sample, GSRM-53, plotted as a quartzolite.

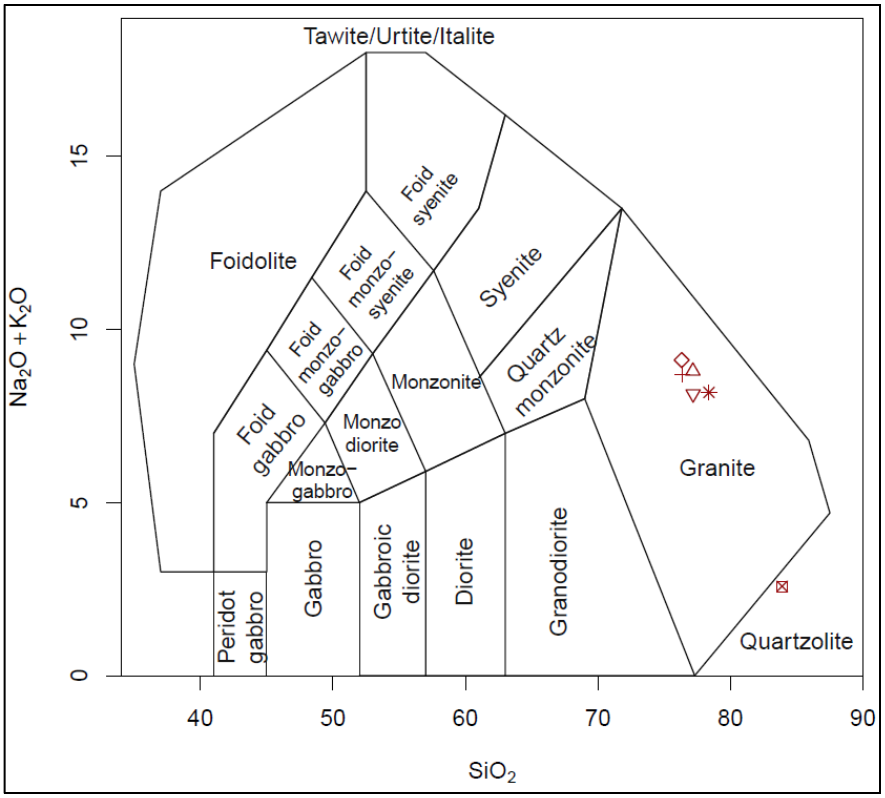

Figure 43: TAS Plot (Middlemost 1994) showing the compositional uniformity of the Plate 4 Granites. One outlier, GSRM-53, was so depleted in Na_2O and K_2O and enriched in SiO_2 that it is plotted as a quartzolite. This likely represents the effects of hydrothermal alteration rather than a special class of granite.

The four hydrothermally altered samples of Plate 4 were added to show their shift in chemistry (Figure 44). The altered samples plotted closer to the granodiorite and quartz monzonite sections of the TAS diagram. This indicates that hydrothermal fluids reduced the silica, sodium, and potassium contents of the original granite. The only exception was sample GSRM-13, which saw a slight increase in sodium and potassium. Sample JN1906, a quartz rich mylonitic derivative of JN1905 shows no change from that of the unaltered samples. This suggests that mylonitization had no effect on the geochemical composition of the granites.

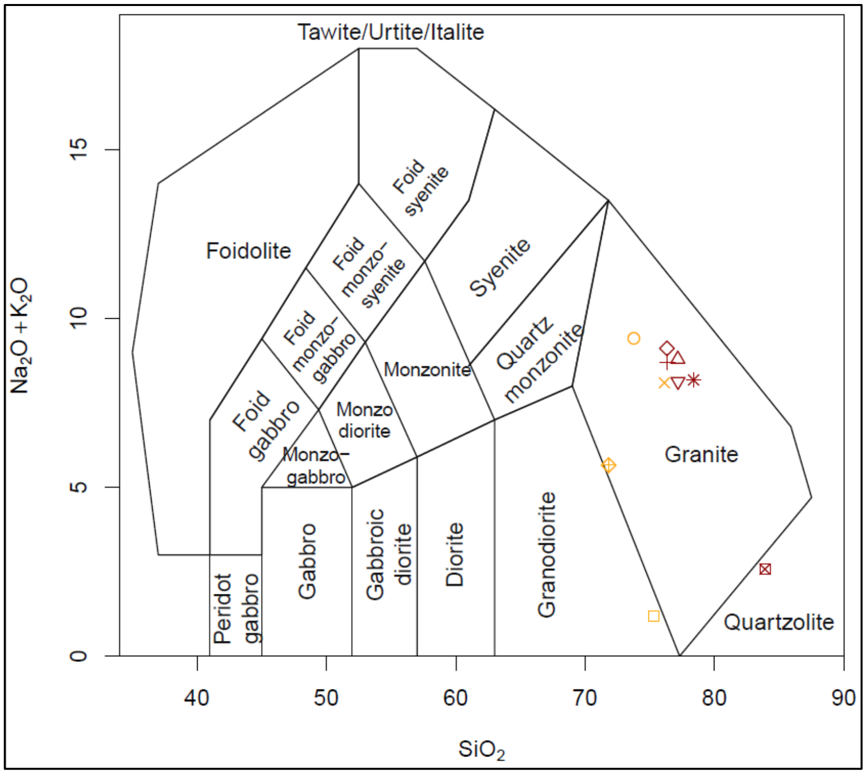

Figure 44: The TAS diagram illustrates how the altered granites experience a small loss in SiO_2 and generally, a moderate depletion in sodium and potassium. This is likely due to the destruction of biotite and orthoclase feldspar. Only sample GSRM-13 became more enriched in sodium and potassium. Red symbols = unaltered samples; Orange symbols = altered samples.

Three fresh, unaltered samples of the Plate 3 Atolia granodiorite and one mylonitized granodiorite were plotted on a TAS diagram to confirm their lithologic identity (Figure 45). All three of the samples plot closely within the granodiorite boundaries. The mylonitization and minor chlorite-epidote veining of sample ERT-721 had no effect on the chemical composition of the granodiorite.

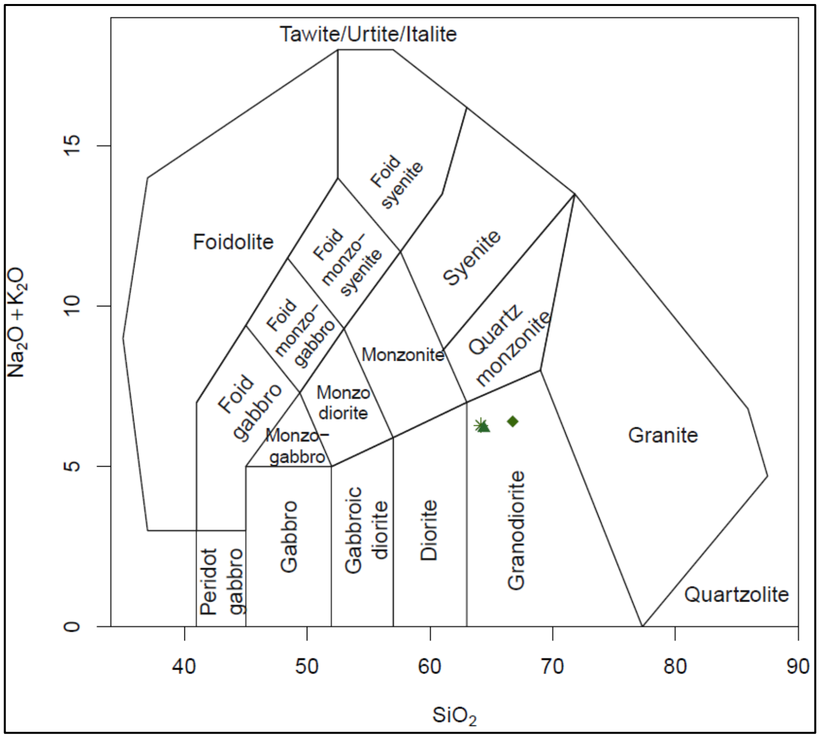

Figure 45: TAS Plot (Middlemost 1994) showing the compositional uniformity of the Plate 3 Granodiorites. Sample CAL SB Atolia gr #210 is compositionally slightly more enriched in SiO_2.

Seventeen hydrothermally altered granodiorite samples were added to the Middlemost TAS diagram to display the shift in chemistry from the unaltered samples (Figure 46). The change in chemistry is more complicated than in the Plate 4 granites. For the Atolia granodiorite samples, 10 of the samples decreased in Na_2O and K_2O, while 3 samples increased in those oxides. One sample saw no shift. 3 samples increased in SiO_2, 8 had little to no shift in SiO_2, and 5 samples saw a decrease in SiO_2 content. GSRM-33, with the highest gold concentration of 10 ppm, experienced no change in silica but did lose several % by weight in $Na_2O + K_2O$.

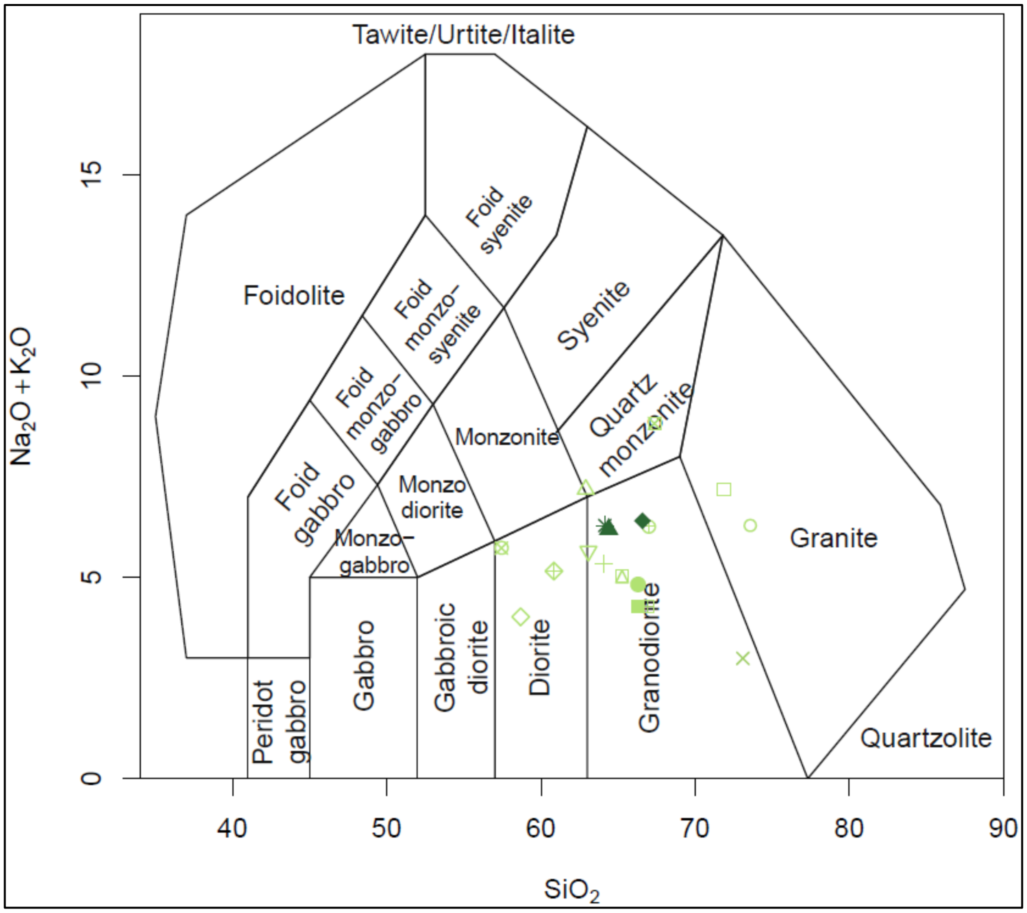

Figure 46: TAS plot showing the wide variability in geochemical change from unaltered to altered granodiorites. Field and hand sample observations did not reveal any obvious reason for this variability. This may indicate that hydrothermal fluids had unequal reactions with the Atolia Granodiorite over large areas. Dark green symbols = unaltered samples; Light green symbols = altered samples.

In the A/NK vs. A/CNK diagram (eg. Shand, 1943), the Atolia Granodiorite is metaluminous, while the Plate 4 granites are all peraluminous (Figure 47). A/NK represents the molar ratio of $Al_2O_3/(Na_2O+K_2O)$ and A/CNK represents the molar ratio of $Al_2O_3/(CaO+Na_2O+K_2O)$. Hydrothermally altered samples for both Plate 4 and Plate 3 shifted towards a more metaluminous direction (Figure 48). They decreased in A/CNK and gained in A/NK.

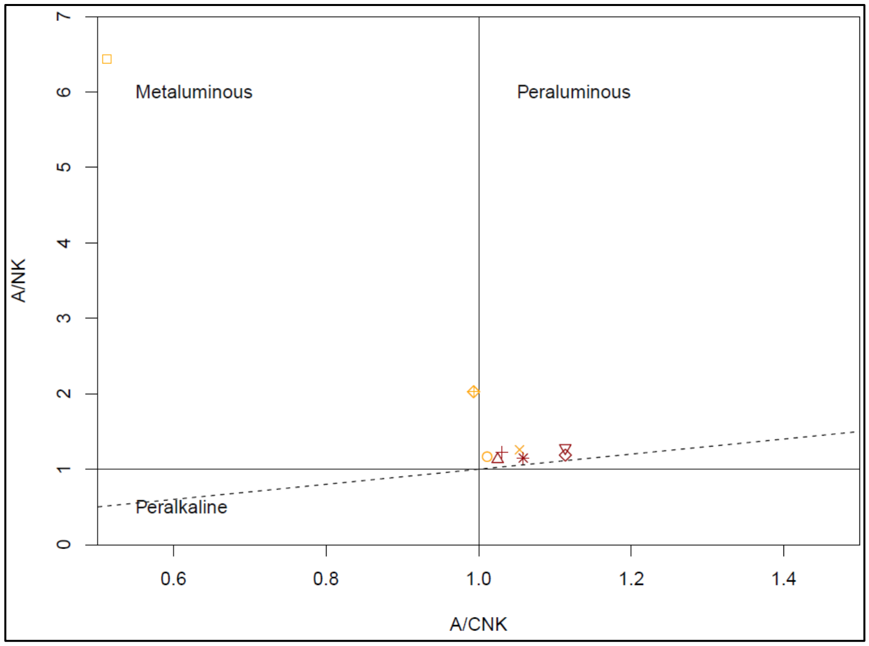

Figure 47: All unaltered Plate 4 samples show that the granites are peraluminous while altered granites become metaluminous. This is likely due to a gain in aluminum and calcium and loss of sodium and potassium during hydrothermal alteration. Red symbols = unaltered samples; Orange symbols = altered samples.

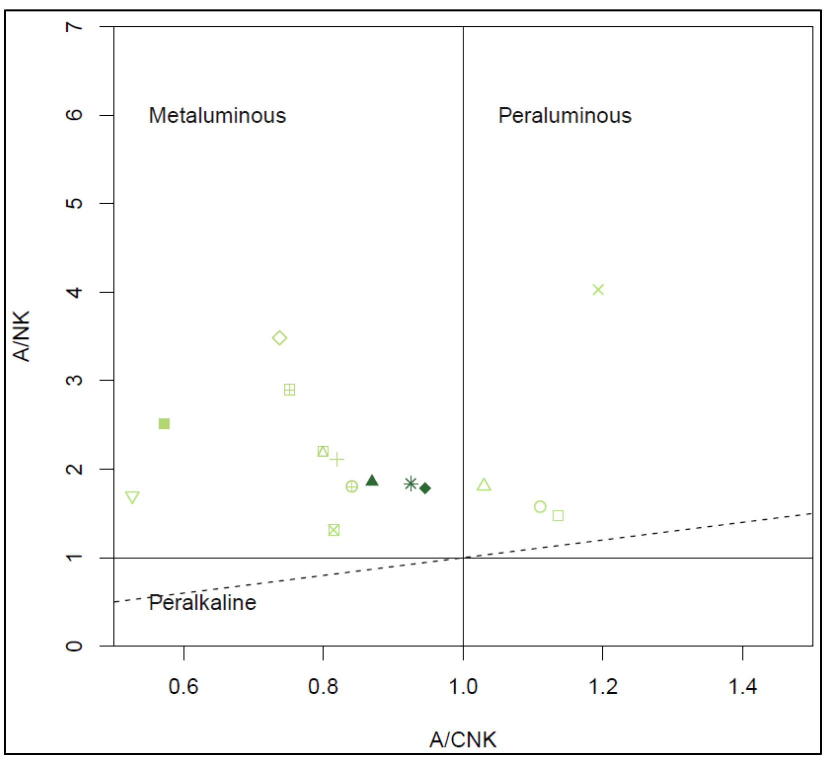

Figure 48: All unaltered Plate 3 samples show that the granodiorites are metaluminous and altered granodiorites generally became more metaluminous. This is likely due to a gain in aluminum and calcium and loss of sodium and potassium during hydrothermal alteration, similar to the granites. However, 4 samples actually became peraluminous and 4 did not plot. Dark green symbols = unaltered samples; Light green symbols = altered samples.

According to the Laurent et al. 2014 Source diagram, Plate 3 granodiorites are derived from intermediate potassium mafic rocks. Plate 4 granite samples, GSRM 53, ERT Plate IV, and JN 1906 were sourced from high potassium, moderate to low aluminum, and low calcium metasediments. The other four granites were derived from tonalitic melt (Figure 49).

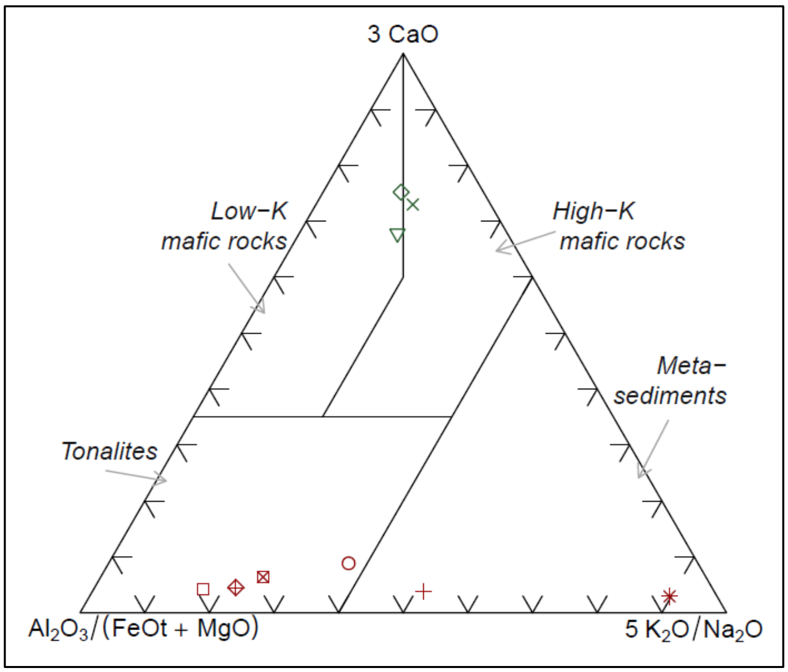

Figure 49: The Laurent et al. 2014 source diagram shows the different melt sources for the Plate 3 and Plate 4 samples. The Atolia Granodiorite probably had a singular source while the granites had variable sources either enriched in potassium or aluminum. Dark green symbols = Plate 3 Atolia Granodiorite; Red symbols = Plate 4 Granite.

The K_2O vs. SiO_2 plot by Pecerillo and Taylor, 1976, plots the Plate 3 granodiorite samples as Calc-alkaline series and the Plate 4 granites primarily as Shoshonite series (Figure 50). Granite samples GSRM – 82A and 53 did not plot within the bounds of the diagram.

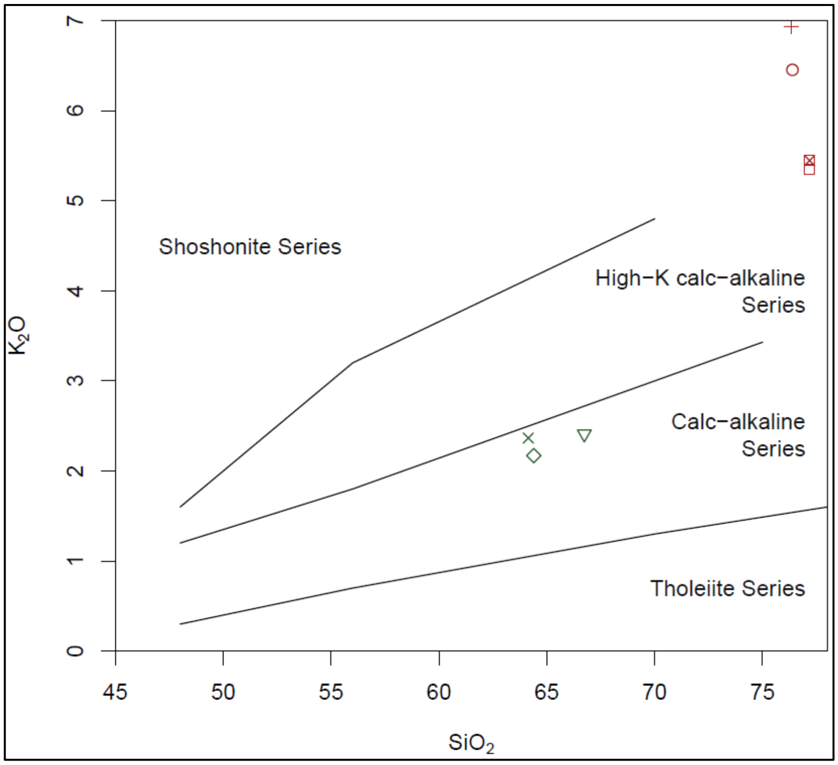

Figure 50: The K2O vs. SiO2 plot after Pecerillo and Taylor, 1976 illustrates the higher potassium and silica content of Plate 4 granites of the Shoshonite Series. Plate 3 granodiorites are calc-alkaline series. Dark green symbols = Plate 3 Atolia Granodiorite; Red symbols = Plate 4 Granite.

Several ternary diagrams were used to display the shifts in specific major element oxides. Na_2O vs. FeO vs. CaO ternary diagrams were used to plot both plate 3 and plate 4 samples separately (Figure 51). Plate 4 granite samples showed a clear change of chemistry between fresh and altered samples. The unaltered granites plotted between 50 and 80 % Na2O, while the altered samples plotted between 0 and 20 % Na_2O, indicating a loss on sodium during hydrothermal alteration. Calcium increased from 10-30% in fresh granite to 45-70% in altered samples. Lastly, iron increased slightly from 10-30% in unaltered granite to 30-50% in altered granite. The only exceptions to this were samples GSRM-13 and 53. GSRM-13, a hydrothermally altered granite, plotted with the unaltered samples. GSRM-53, a presumed fresh granite sample, plotted with the altered samples.

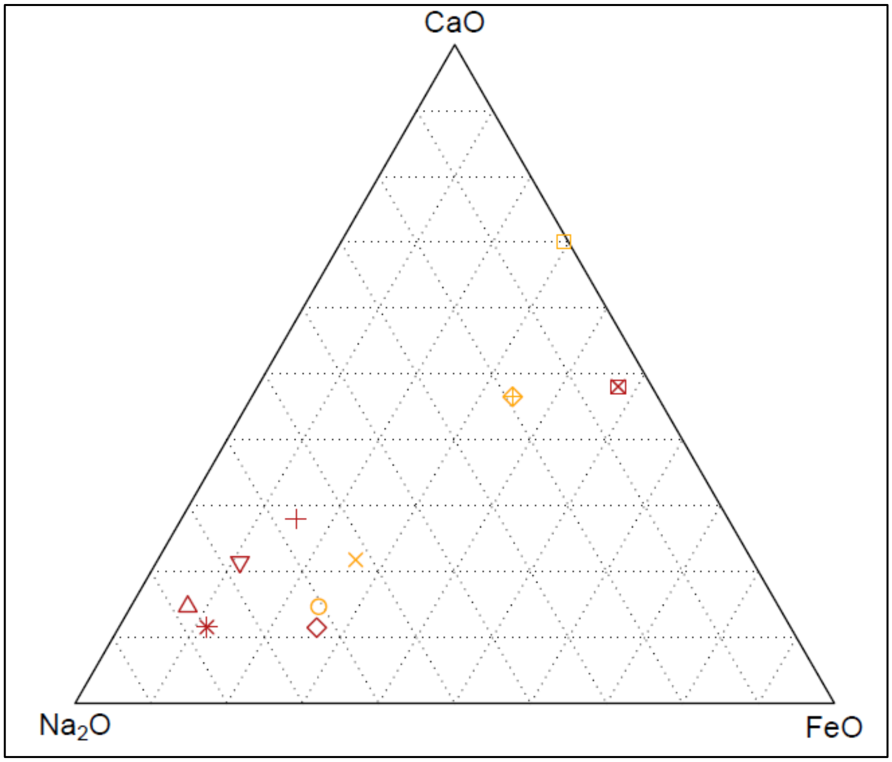

Figure 51: The ternary diagram shows that altered granites lose a substantial amount of sodium from destruction of feldspars and a significant gain in calcium from carbonation. A minor increase in iron may be due to deposition of hematite. Red symbols = unaltered samples; Orange symbols = altered samples.

Plate 3 generally saw a similar shift in chemistry on the Na_2O vs. FeO vs. CaO ternary diagram (Figure 52) in which sodium was leached while calcium was introduced into the granodiorite. Na_2O decreased from 30% in fresh granodiorite to about 3% in altered samples with a few exceptions that actually increased in sodium content. Calcium increased for all but three samples from 35-40% to upwards of 80%. The highest gold content sample, GSRM-33, experienced a decrease in Na_2O to about 15% and an increase in CaO to just under 70%. FeO content stayed mostly consistent with the unaltered granodiorite samples. However, there were samples that had small gains or losses in iron. GSRM-33 experienced the greatest loss of iron, from 30% to 15%.

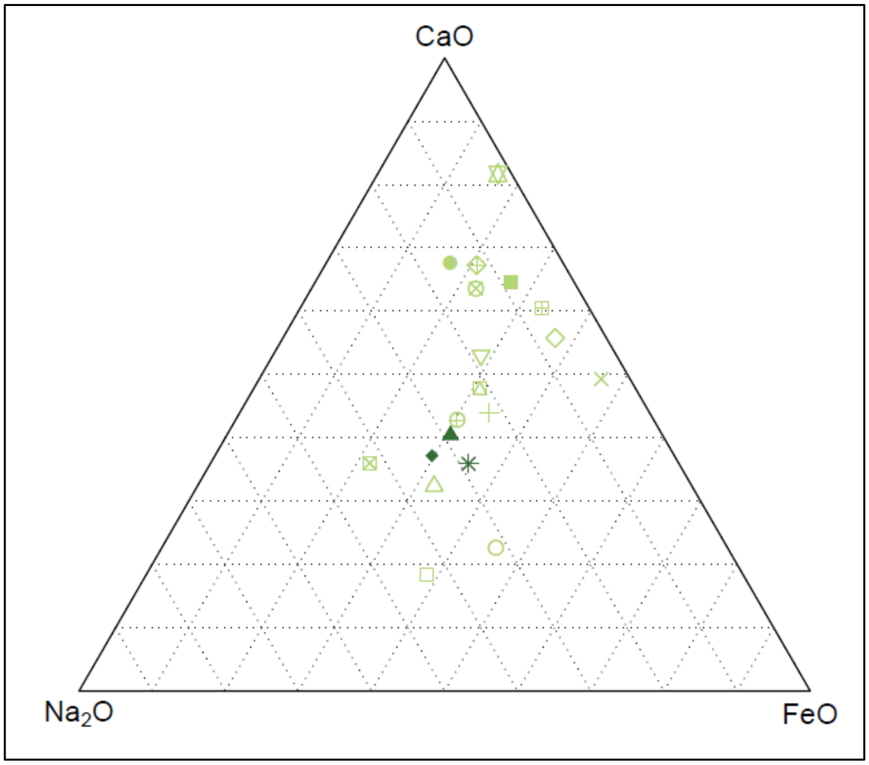

Figure 52: The ternary diagram shows that altered granodiorites exhibit variability in alterations. They generally lose a moderate amount of sodium from destruction of feldspars and a significant gain in calcium from carbonation. However, some samples have a loss in calcium and gain in sodium. The samples are generally either unchanged in iron or experience minor depletion, possibly due to biotite destruction and iron escaping the system. A minor increase in iron in 3 of the samples may be due to hematite. Dark green symbols = unaltered samples; Light green symbols = altered samples.

Loss-on ignition (LOI) is a measure of the volatile content (OH, CO_3, H_2O) in the samples that is driven off during XRF analysis. LOI clearly increased from unaltered plate 3 and plate 4 rocks to their altered counterparts (Figures 53 and 54). One possible explanation for this pattern is that the higher LOI values correspond to greater proportions of kaolinite and/or calcium carbonate (caliche?) that is common in the altered samples.

Altered Plate 3 samples, GSRM 2, 3, and 4, were taken from the mylonitized zone near the fault contact with Plate 4 northeast of the Darn Peak prospects (Figure 7). These three samples experienced the lowest LOI of the altered Plate 3 rocks (Figure 53). The majority of the rest of the altered granodiorite samples plotted between 5% and 15% LOI, with the exception of GSRM-30 that recorded 32%. This sample contained significant amounts of the iron carbonate minerals, siderite and ankerite, which likely resulted in the increased LOI of CO_2. Unaltered Plate 4 samples, except for GSRM-53, experienced LOI less than 2%. GSRM-53 had an LOI of just over 4%. Four altered counterparts all plotted between 6% and 12%, except for GSRM-13, which plotted at .8% LOI.

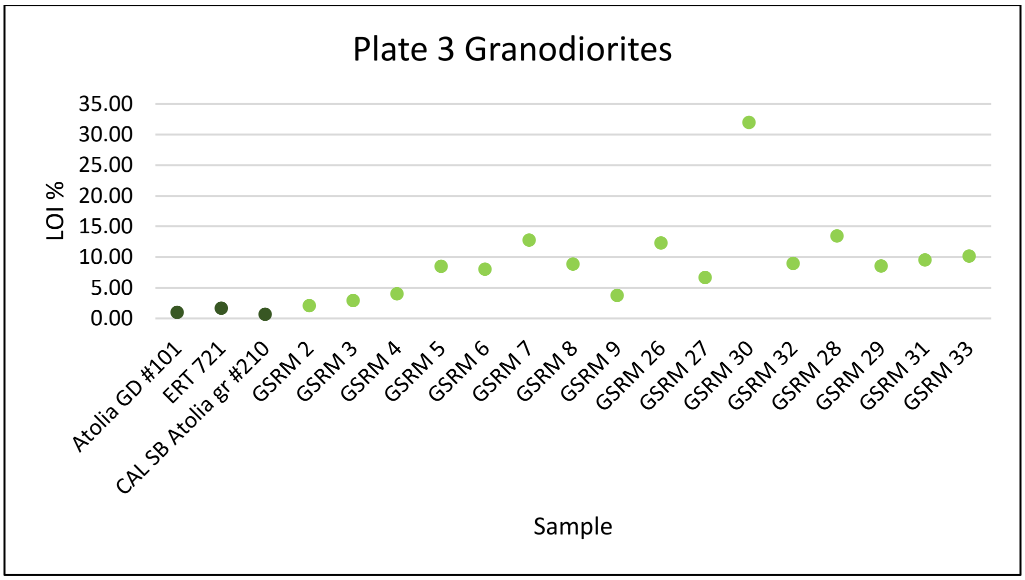

Figure 53: This plot clearly indicates that hydrothermally altered Atolia Granodiorite samples experienced significant LOI compared to unaltered granodiorite samples. From hand sample observations, this is the result of significant addition of carbonate minerals and the alteration of original minerals to hydrated clays. Dark green symbols = Fresh samples; Light green symbols = hydrothermally altered samples.

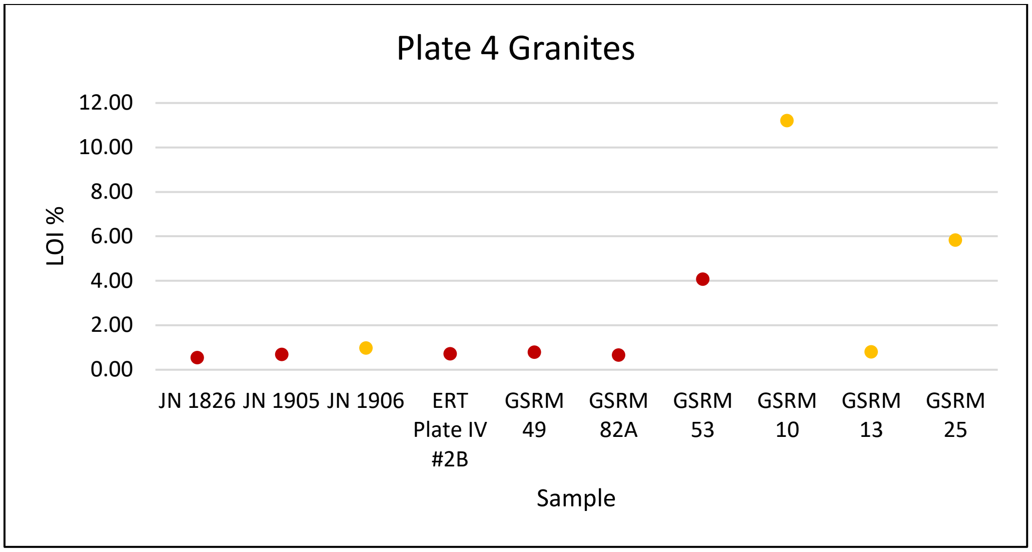

Figure 54: Plate 4 granites increase in LOI from the increase in carbonate mineralization and loss of quartz. GSRM-53 had unusual results that are difficult to explain. It's LOI is higher than the other unaltered granites despite it having significantly higher in SiO_2. Red symbols = Fresh samples; Orange symbols = hydrothermally altered samples.

I also plotted LOI against the major element oxides for both the Atolia Granodiorite and the Plate 4 Granites. For Atolia samples (Figure 55), an increase in LOI was accompanied by a significant leaching of MgO, and Na_2O. The minor to moderate loss of Al_2O_3 may indicate that some remained and was just mobilized into clay minerals like kaolinite or montmorillonite. Small negative shifts occurred with TiO_2 and P_2O_5. Increases in LOI were also associated most clearly with an increase in CaO (likely from introduction of $CaCO_3$). Increase in FeO and K_2O were weakly positively correlated with an increase in LOI. However, the highest gold sample, GSRM-33, decreased in both FeO and K_2O while increasing in LOI. There is little to no correlation between LOI and both MnO and SiO_2.

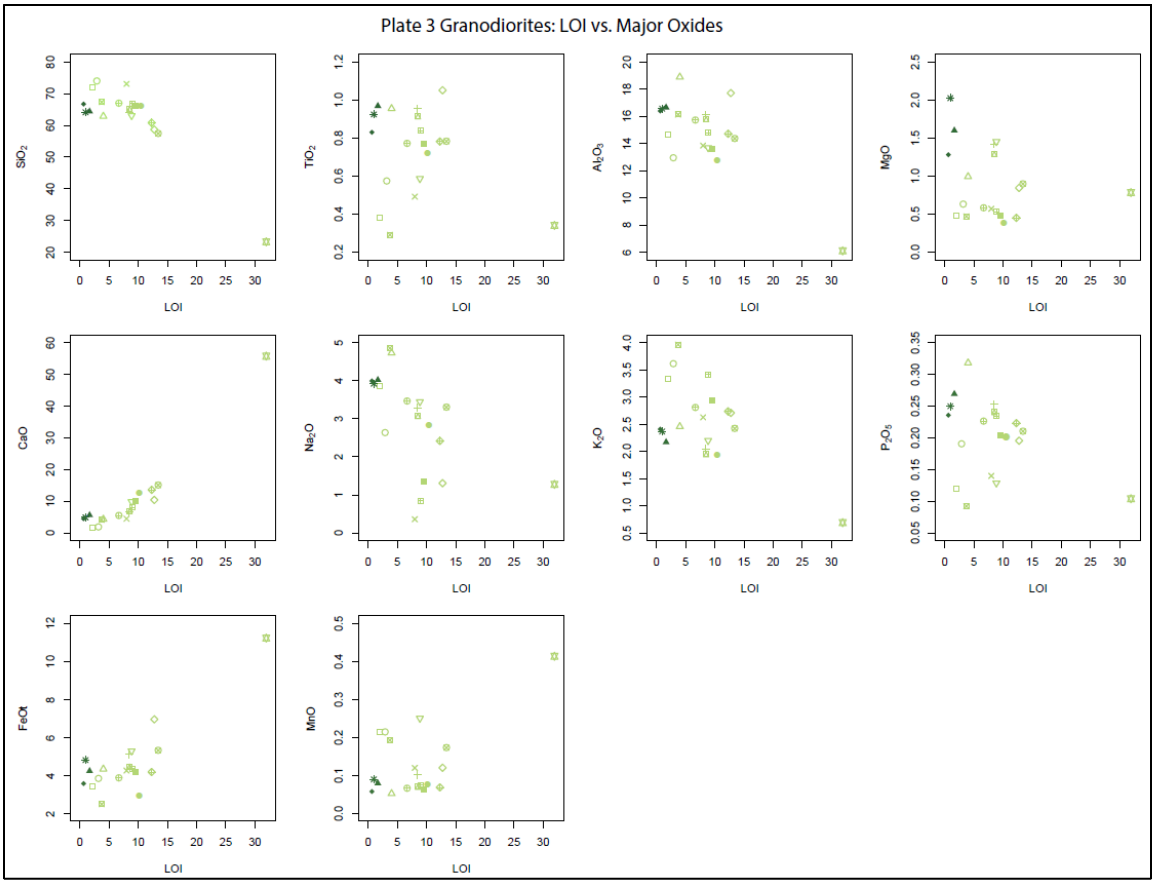

Figure 55: Plots of LOI% vs. major oxides for the Plate 3 Granodiorites. There is a positive relationship between LOI and calcium, potassium, iron, and manganese. These likely are due to increases in the Mn, Ca, and Fe carbonates or possibly caliche ($CaCO_3$). There is a negative correlation between LOI and all other oxides. Silica only decreases in the 4 highest LOI samples. Dark green symbols = unaltered samples; Light green symbols = altered samples.

For Plate 4 samples (Figure 56), an increase in LOI was accompanied by a decrease in SiO_2, Na_2O, and K_2O and an increase in TiO_2, Al_2O_3, FeO, MnO, MgO, CaO, and P_2O_5. The K_2O leached from the granite may have been mobilized and introduced into the Plate III granodiorites, thus resulting in the increase in K_2O of the altered granodiorite samples above. Leaching of the SiO2, Na2O, and K2O likely indicates acidic hydrothermal fluids.

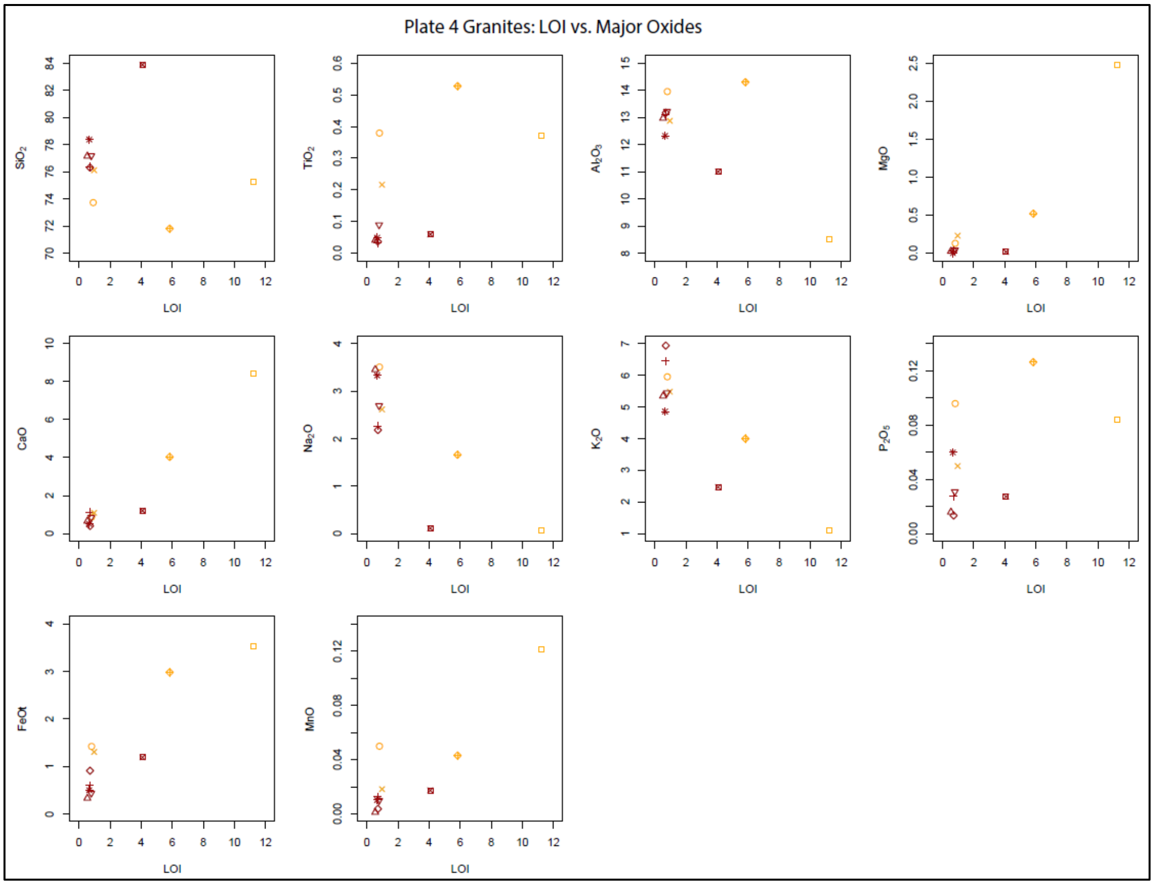

Figure 56: Plots of LOI% vs. major oxides for the Plate 4 Granites. There is a positive relationship between LOI and titanium, magnesium, calcium, phosphorous, iron, and manganese. These likely are due to increases in the Mn, Mg, Ca, and Fe carbonates. There is a negative correlation between LOI and silica, sodium, and potassium from the dissolution and destruction of quartz, biotite, and feldspar. Red symbols = unaltered samples; Orange symbols = altered samples.

All major element oxides were plotted against SiO_2 content of the samples. In general, SiO_2 did not change significantly between unaltered and altered samples of Plate 3 granodiorites. Hydrothermal alteration of the Atolia Granodiorite samples resulted in decreases of TiO_2, Al_2O_3, FeO, MgO, Na_2O, and P_2O_5 and enrichment of CaO and K_2O with respect to SiO_2 (Figure 57). However, the highest gold sample, GSRM-33, actually became more depleted in K_2O. MnO was immobile during the alteration of the granodiorites. Plate 4 samples experienced noticeable loss in SiO_2.

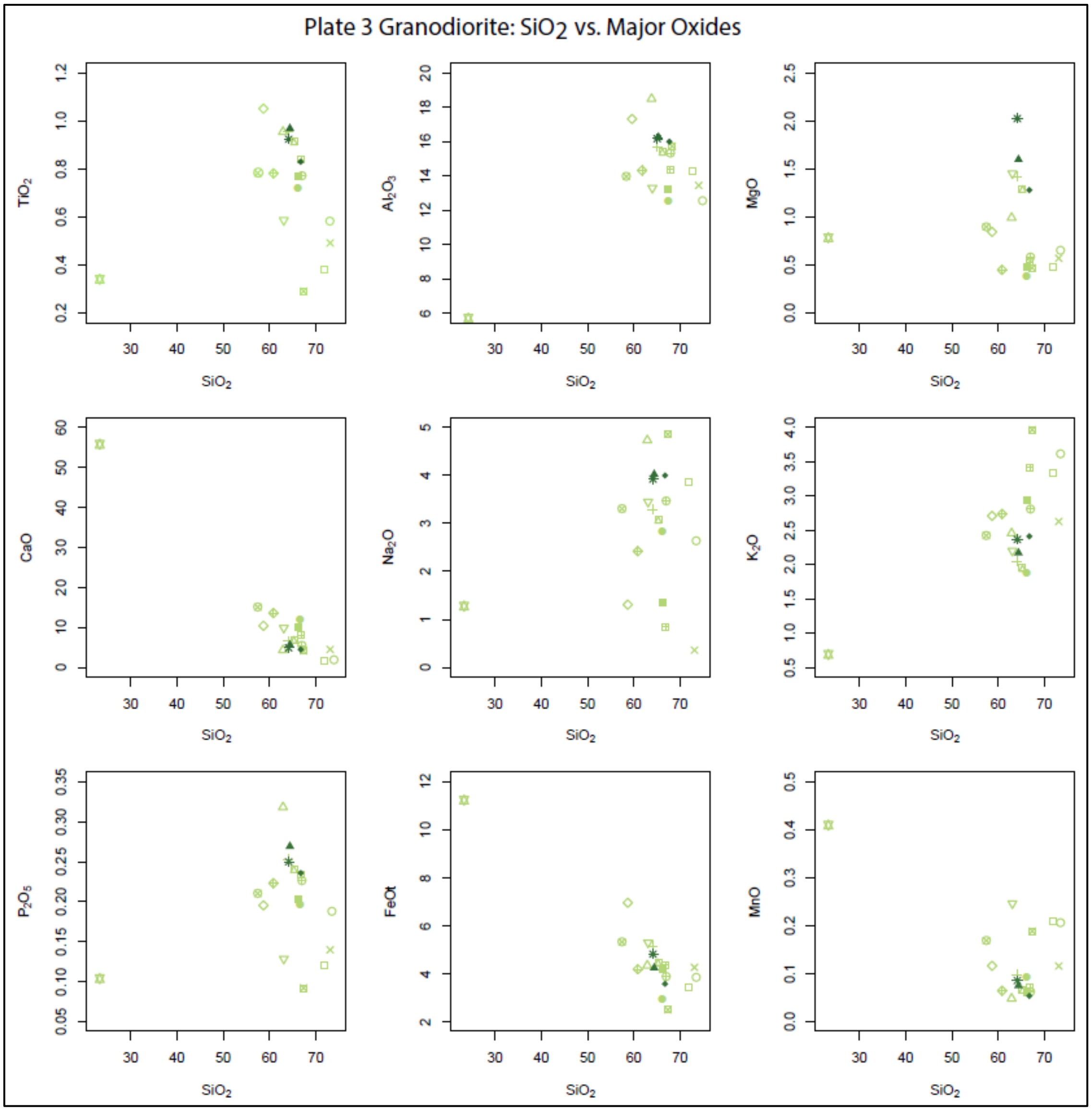

Figure 57: The variability of SiO_2 in altered granodiorites was accompanied by gains and losses of major oxides following the same trend as seen in the LOI plots. Dark green symbols = unaltered samples; Light green symbols = altered samples.

Hydrothermal alteration of the Plate 4 Granites caused depletion in Na_2O and K_2O. Enrichment of TiO_2, Al_2O_3, FeO, MnO, MgO, CaO, and P_2O_5 occurred (Figure 58). Altered sample GSRM-10 was the only sample to lose Al_2O_3, while GSRM-13 was the only sample to gain Na_2O and maintain the K_2O content of unaltered granites.

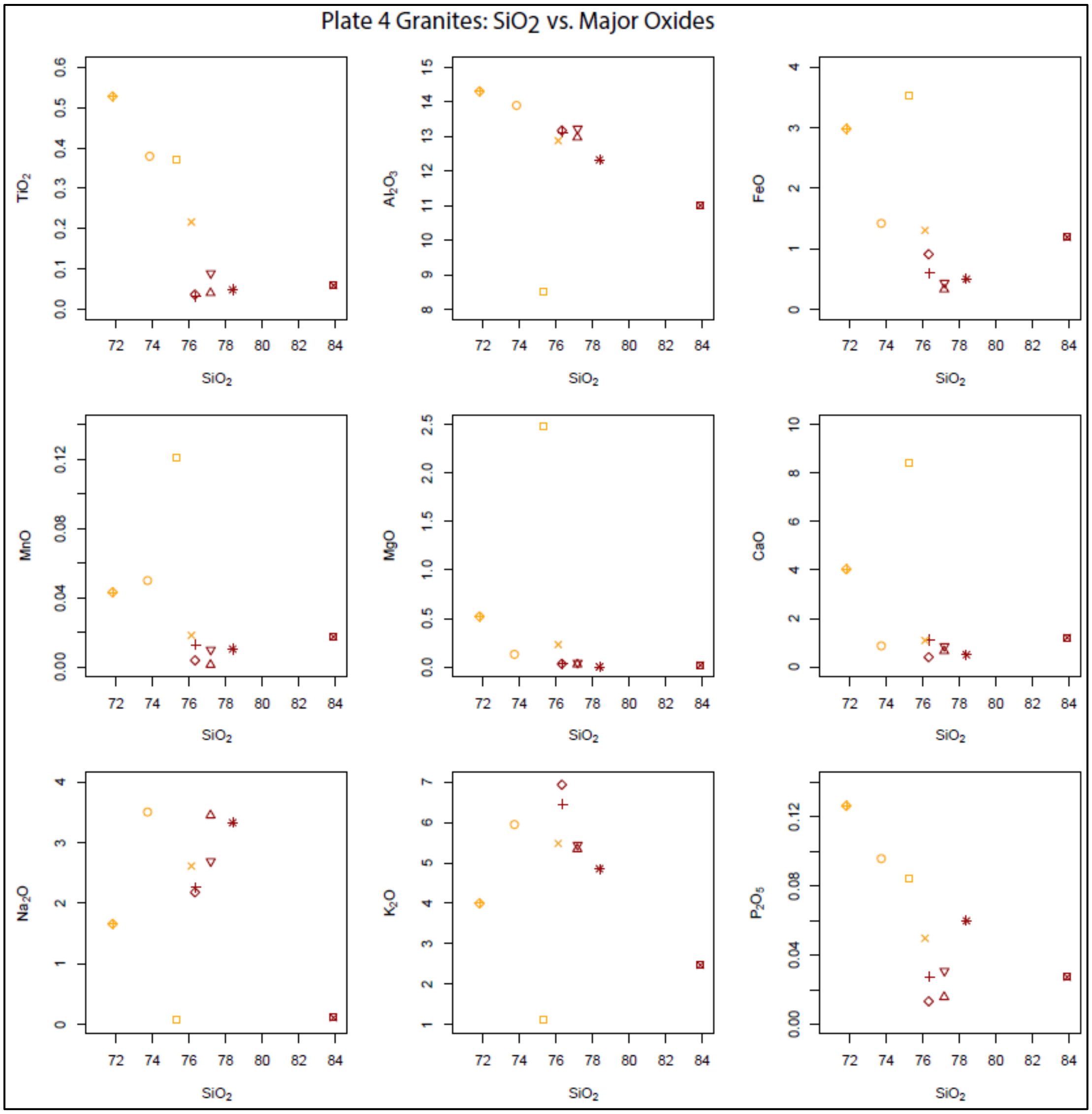

Figure 58: The slight loss of SiO_2 in granites was accompanied by gains and losses of major oxides following the same trend as seen in the LOI plots. Red symbols = unaltered samples; Orange symbols = altered samples.

$^{40}Ar/^{39}Ar$ Thermal History Results

All data, results, and analytical interpretations/explanations were kindly provided by Dr. Willis Hames of Auburn University. Samples GSRM-57B (pod of fuchsite/mariposite, muscovite, and chromite located in Figure 2) and GSRM-84C (brecciated chromium and nickel enriched and carbonate altered schist located on Figure 19) were both dated using the $^{40}Ar/^{39}Ar$ method. Dr. Hames performed the mineral separations for both samples. Unfortunately, due to an analytical artifact during the process and a lack of abundant micas, GSRM-84C did not produce usable or presentable results (Table 4).

GSRM-57B was collected from the tailings of a vertical mine targeting the footwall of a NE striking fault within the blueschist component of the Rand Schist. This fault was also the source of sample GSRM-55 with 3.68 ppm Au. Two coarse mica crystals, one muscovite and one fuchsite/mariposite, were separated from GSRM-57B and successfully dated. For both micas, the last 7 heating steps were averaged to produce an age of closure. The muscovite crystal produced an average age of 71.5±.39 Ma while the fuchsite/mariposite crystal produced an average age of 71.8± .40 Ma. When averaged together, the age is 71.64 ± 1.9 Ma (Figure 59). Each of the individual results were discordant indicating that a sufficient temperature was achieved at some point between 70 and 20-30 Ma to cause a diffusive loss of radiogenic ^{40}Ar. Because these crystals experienced ^{40}Ar loss, their discordance does not meet the statistical parameters for a plateau age. See Appendix D for the full data set.

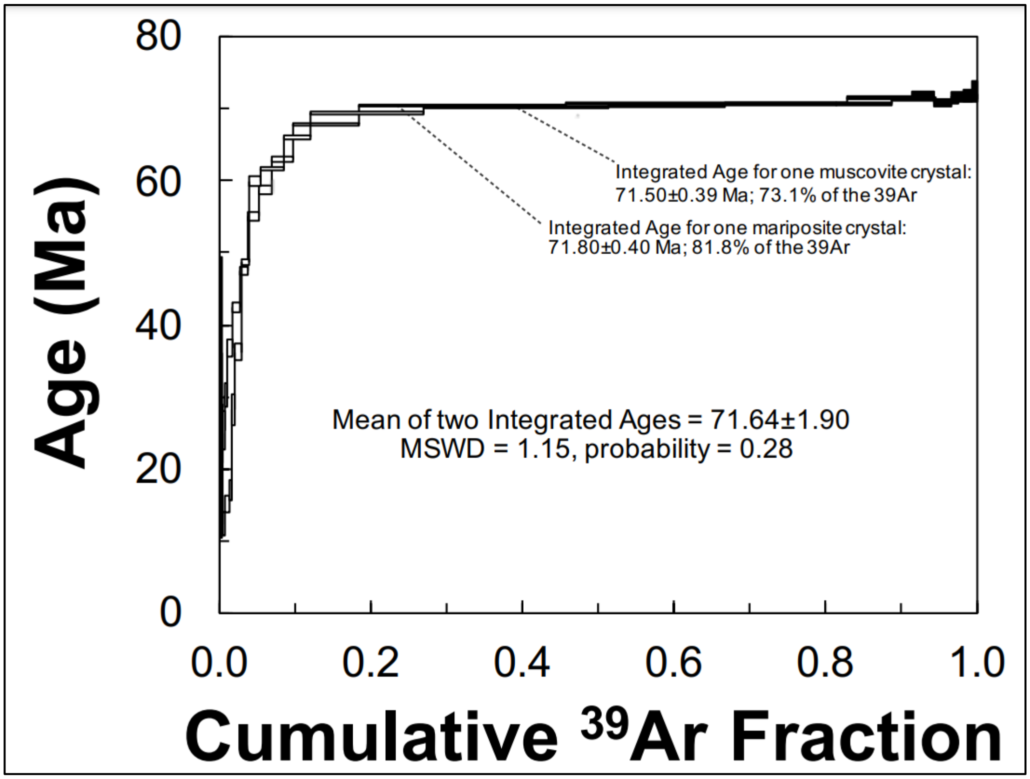

Figure 59: This plot shows the two superimposed $^{40}Ar/^{39}Ar$ age spectra for the muscovite crystal and fuchsite/mariposite crystal from GSRM-57B. The mean age of the two is 71.64 ± 1.9 Ma.

The 71.64 ± 1.9 Ma closure age from this study agrees well with regional metamorphic ages of the Rand Schist reported by Jacobson 1990 and Grove et al in preparation. In Jacobson 1990, two phengite samples (RA83 and RA100) obtained from Rand Schist (see Figure 2 for locations) were dated at 74 to 70 Ma and interpreted to represent metamorphism of the Rand Schist protolith. Newly dated phengite samples in Grove et al. also produced similar results. Sample RA82 from Jacobson 1990 (see Figure 2 for location) was a mafic schist containing hornblende that yielded a total gas age of 78 Ma. This is believed to represent peak metamorphism of the Rand Schist during accretion. The mean total gas age of the micas from GSRM-57B likely indicates time that metamorphic mica in the schist cooled below its closure temperature of ~ 450 degrees Celsius.

Interpretation of the argon loss experienced by both analyzed crystals in GSRM-57B is difficult, but interesting to ponder (Figure 59 and Appendix D). In one view, the lower ages may represent far-field effects of a discrete thermal pulse related to emplacement of the Yellow Aster intrusion at 19.6 Ma. Alternatively, the Rand schist at this locality may have remained sufficiently buried until early Miocene time such that ^{40}Ar was able to gradually diffuse from the crystal lattice over time. Unfortunately, these results do not directly date the age of gold mineralization in the mine where the fuchsite sample was taken. However, they do provide a very precise metamorphic age for the Rand Schist, in line with the work of Jacobson et al. (1990).

DISCUSSION AND INTERPRETATION OF RESULTS

Below I provide detailed discussion and interpretation of the results, along with some speculations on possible relationships between mineralized structures of the Randsburg Mining District and gold-bearing structures of the central and southwestern Rand Mountains. This discussion addresses the Research Questions posed earlier, roughly in the sequence presented in the Introduction.

Distribution of Mine Workings and Gold Mineralization

Gold mines (large workings with a significant amount of material removed) and prospects (minor workings and test pits) are most numerous and extensive immediately adjacent to the Yellow Aster Mine at the northeastern end of the Rand Mountains. Many more prospects are sporadically scattered along the entire length of the mountain range as far south as the Desert Tortoise Wilderness. However, these are less densely spaced and are far less significant in size. While some locations contained only single prospects or mines, in general, prospects were found in groupings of three or more. Each prospect within a particular group typically targeted the same features and/or rock units. Most prospects in the study area were small in size, ranging from 5 to 60 feet in total workings. However, a few mines with over 100 total feet of workings were encountered.

Curiously, the size of prospects did not necessarily always indicate whether anomalous gold was present. In fact, sample GSRM-33 with 10 ppm Au was taken from a prospect of only 15 feet in length. The majority of mines were horizontal adits tunneling into hill sides either along a fault or into the host rock until a large fault was encountered. Often side excavations were made along strike with the encountered fault.

Several mines and prospects were vertical and targeted either the footwall or hanging wall of high angled faults. These were often anywhere between 20 to over 60 feet deep. It was very obvious that prospectors were looking for large faults in the schist or highly fractured, faulted, and hydrothermally altered zones in the Atolia Granodiorite. However, many prospects appeared to have been dug in areas with no notable or recognizable structures or alterations that would suggest ore mineralization.

From this study, it is clear that significant amounts of gold mineralization extended far beyond the boundaries of the Randsburg Mining District. Gold grades of at least 10 ppm Au occur over 9 km to the southwest of the historical Yellow Aster Mine. At least 2 ppm Au mineralization persists into the Desert Tortoise Wilderness 12 km to the southwest of the Yellow Aster Mine. Within that same area, very high grades of antimony in stibnite veins occur, and most of the assayed samples contained anomalous gold concentrations between .01ppm and 1 ppm. This indicates that hydrothermal fluids laden with base and precious metals were present in great volumes throughout the entirety of the Rand Mountains and not just limited to the area of the Randsburg Mining District.

These observations have significant implications for future gold exploration in the region. The wide spread of mineralization may indicate that extension continued long after mineralization such that parts of the ore body were transported to the southwest from their origin. It may also indicate that hydrothermal fluids were dispersed along large-scale faults further than previously known and that heat from the Yellow Aster pluton endured over long distances and time. Another possibility is that either the Yellow Aster pluton is much larger than it appears, or that there is another unexposed intrusive below the central and southwestern Rand Mountains. Lastly, at least some of the anomalous gold in my study area may represent an older deposit with a genetically different and unrelated origin. Evidence for this last point, while not definitive, is presented and discussed towards the end of the thesis.

Lithologic Targets for Gold Exploration

The historic gold mines of the Randsburg Mining District primarily targeted mineralization withing the Plate 1 Schist and Plate 3 Atolia Granodiorite. This trend was also observed within my study area. One small group of trenches east of Darn Peak were dug into silicified and mylonitized portions of the shear zone of the upper Rand Thrust between Plate 3 and Plate 4 Granite (Figure 7). Along with some trenches near the granite-schist cross fault of Figure 19, these were the only prospects found to be targeting either Plate 4 or a structure related to Plate 4. Samples from these locations were completely barren of gold. Why this may be is discussed later in this thesis.

Plate 2 Johannesburg Gneiss was not a major ore bearing unit in the Randsburg Mining District. However, along the northern front of the southwestern Rands, two larger mines were found to target high angle faults where they cut the lower Rand Thrust between Rand Schist and Plate 2 Johannesburg Gneiss and Marble. Both locations contained anomalous gold. Discussion of the lower Rand Thrust as a structural control on gold mineralization is discussed later. No prospects or mines were found to target Plate 2 specifically. This is likely due more to there being sporadic occurrences of Plate 2 rather than it being an unaccommodating lithological unit to gold mineralization. From these observations, it can be concluded that while Plate 2 is not an ore bearing unit in the northeastern Rands, it does host structures with low grade gold in the central and southwestern reaches of the mountain range. All units exhibited varying magnitudes and styles of hydrothermal alteration where faults were present which implies that the gold mineralization is structurally controlled by faults.

Structural Control on Gold Mineralization

The gold in the Randsburg Mining District was primarily fault controlled with minor amounts of disseminated gold and auriferous arsenopyrite in surrounding wallrock. This was well recorded by both Hulin in 1925 and Morehouse in 1988. Generally, the gold was deposited within quartz veins into NW striking, NE dipping extensional faults around 19 million years ago during the emplacement of the Yellow Aster granodiorite stock. This was accompanied by a swarm of rhyolite dikes that were occasionally mineralized with gold where they cut quartz veins. However, in the central and southwestern Rand Mountains, I found conclusively that gold typically followed a different structural control. Figures 60 and 61 demonstrate that anomalous gold values (>.01 ppm) were predominantly found in NE-SW striking and NW-SW dipping oblique extensional faults. Except for one, the highest anomalies (1-10 ppm) were all from NE-SW striking faults. These mineralized faults range in scale from minor centimeter wide faults and fractures exposed within prospect adits to the larger, prominent regional scale quartz-carbonate-limonite cross faults previously mapped by A. McLarty and J. Nourse (2014).

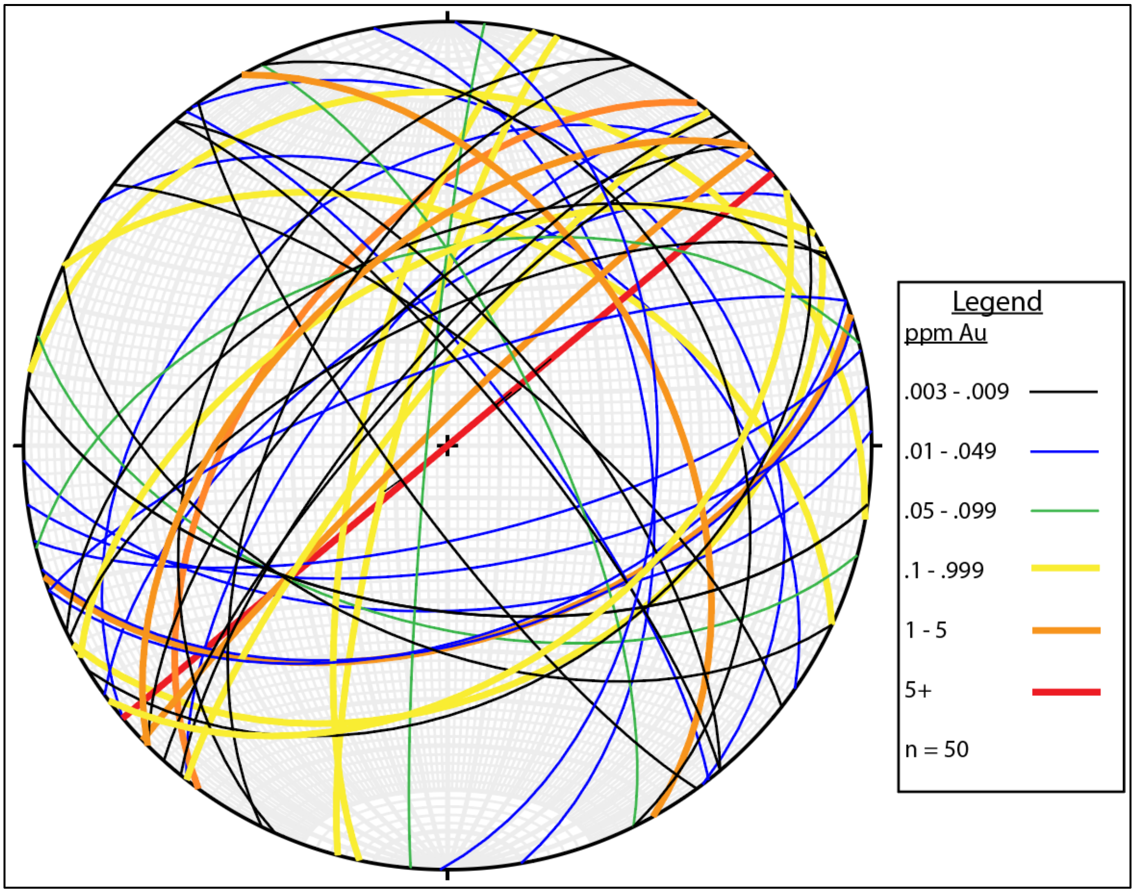

Figure 60: The color coded stereonet displays that most anomalous samples were obtained from NE striking faults. Due to the extremely variable dips and wide spread of strikes within each quadrant, this trend is difficult to visualize. Refer to figure 61 and 62 for better illustration of the structural control.

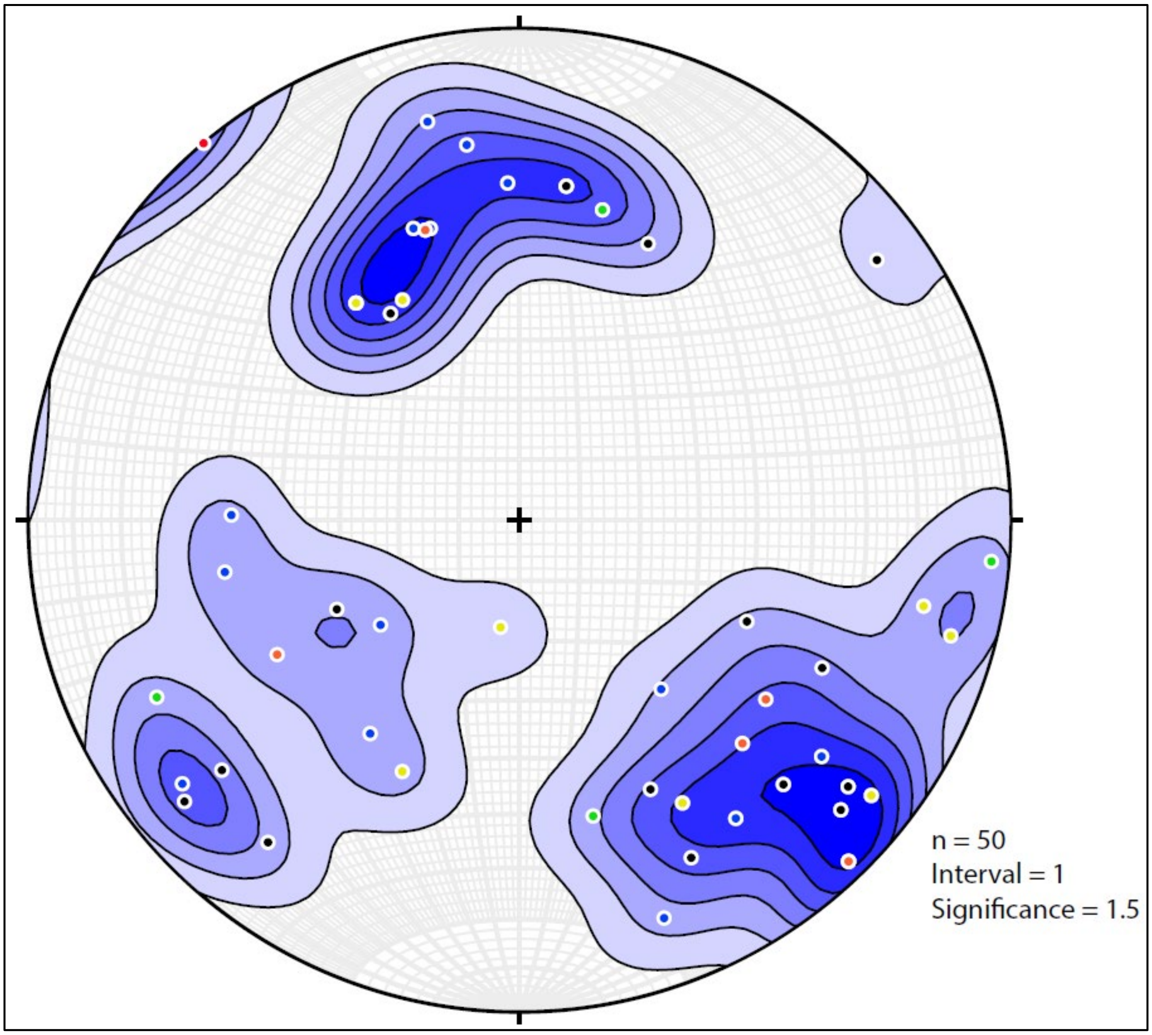

Figure 61: The contoured poles to the planes of Figure 55 better illustrate the structural control of the gold mineralization. Clearly, there is a preference for NE striking faults. Those that dip moderately to steeply to the NW are more common. Note that the pole to the highest-grade sample is located along the border in the NW quadrant. Almost all NW striking faults were NE dipping. Refer to the legend in Figure 60.

By ignoring the dip angle and direction, the structural control on anomalous gold is even more evident on a rose diagram of all mineralized structures (Figure 62). Mineralized faults are most often striking between N50-60E and N70-80E. Faults with the highest average gold grade are trending N50-60E and N40-50E. Several NW striking faults are mineralized but there is no dominant trend. Of the faults striking to the NW, the two between N20-30W contained the highest average gold grade of 1.11 ppm.

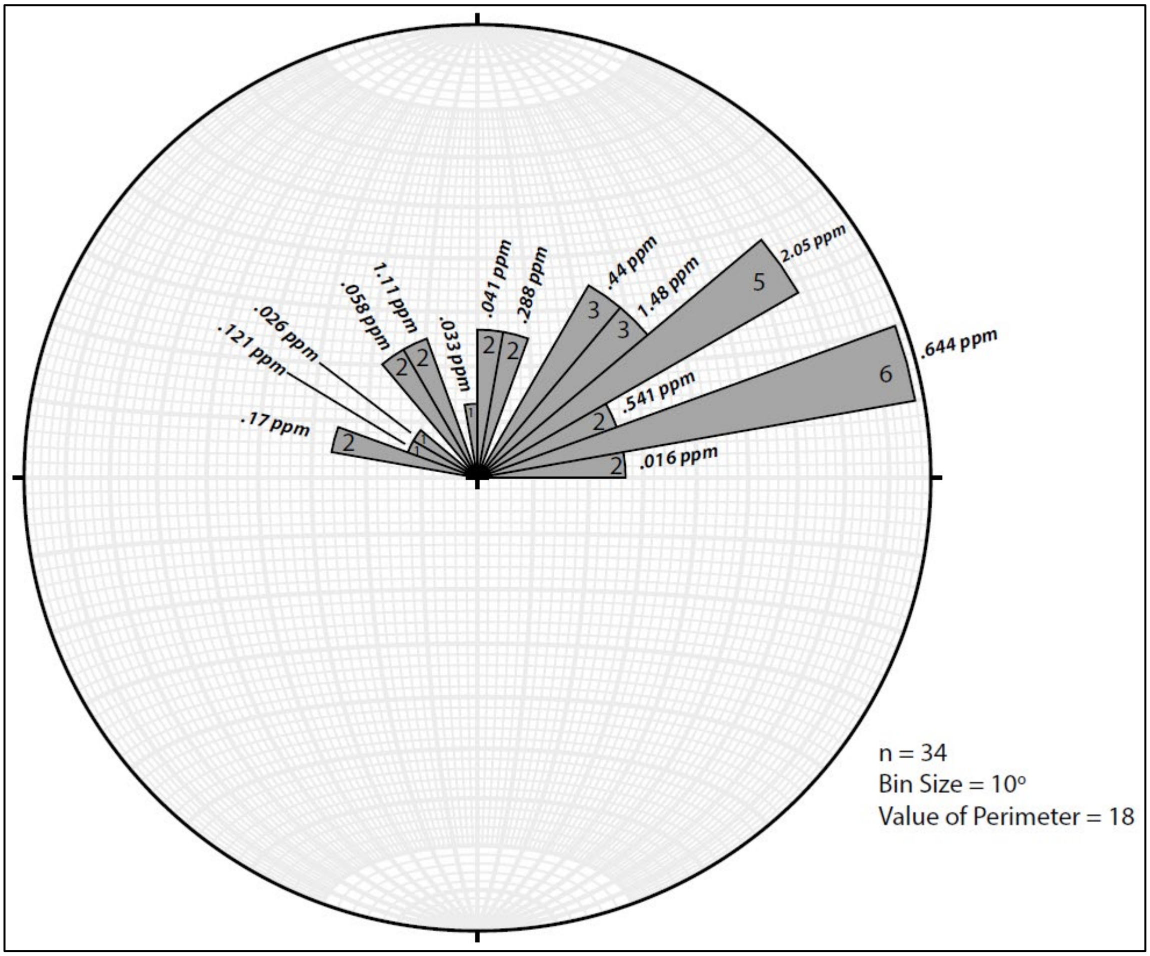

Figure 62: The half circle rose diagram clearly illustrates the strong structural control on gold mineralization in the central and southwestern Rand Mountains. While anomalous gold bearing faults are predominantly NE-SW striking in general, the strongest control are those striking N70-80E and N50-60E. The number within each petal represents the number of fault strike measurements. The number outside of the petals is the average gold grade of samples from those faults.

The structural control is more tightly constrained in the granodiorite than it is in the schist (Figure 63). While both display a preference towards structures of a N70-80E strike, the schist contains a higher percentage of mineralized NNE and NW trending faults, whereas the majority of gold-bearing faults in the granodiorite strike northeast. This may indicate a greater variability of clockwise rotation of faults within the schist, a theory discussed in the following section. Or, it may suggest that there are several genetically and temporally independent sets of mineralized faults. As is clearly observed in Figure 63, the strikes of the NE faults within the schist are not tightly grouped. A possible reason for this is discussed in the next section below.

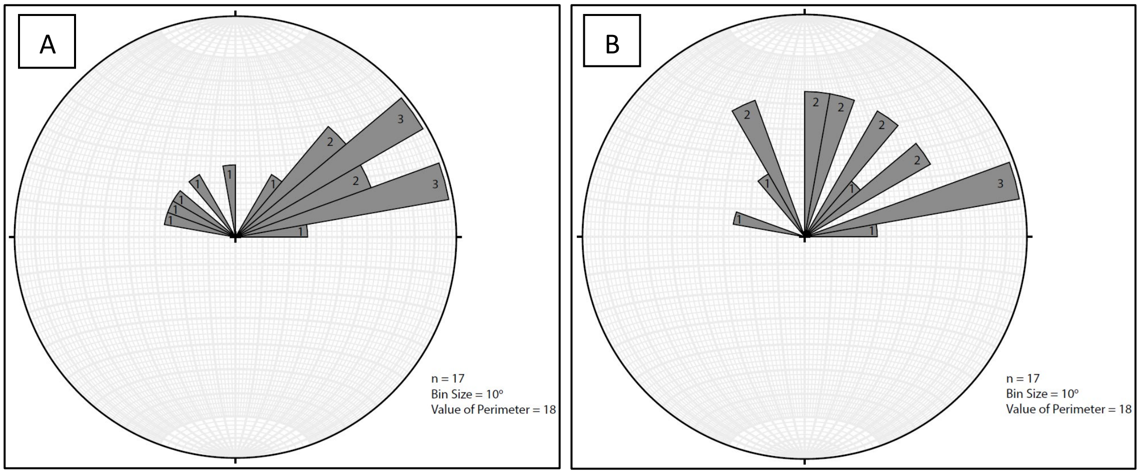

Figure 63: A) The structural control on gold in within Plate III Atolia Granodiorite faults shows dominance by faults at N70-80E and N50-60E. B) The structural control on gold in the Plate I Rand Schist is more variable. The strongest control is again N70-80E with minor controls to the NE, NNE, and NNW. Numbers in each petal reflect the number of fault strikes.

While the anomalous gold values were found primarily within NE-SW striking faults, this wasn't exclusive. In the both rose diagrams it is evident that anomalous values were also obtained from NW and SE striking faults. However, in general, these anomalies were smaller in value than those of the NE-SW striking faults.

Dips of mineralized faults were variable in direction, but consistently steeper than 50 degrees in angle. Given that most of the anomalous value faults were highly damaged by hydrothermal fluids and did not always display striations, the consistency of steep dips was a helpful indicator that the faults likely had extensional or strike- slip components rather than thrust. Those faults that did display good fault slip indicators record normal displacement, with variable amounts of strike slip. In the majority of cases the strike slip component was left-lateral on NE-striking faults, and right-lateral on NW-striking faults slip analyses on many other faults. These observations reinforce those of McLarty (2014) who documented several significant north-northeast striking faults with normal-left lateral oblique motion.

High angle extensional faults are common in the Rand Mountains. These are probably related to early Miocene extension (19-20 Ma) such as that documented in the Waterman Hills core complex (Walker et al., 1990), and possibly later left-lateral motion associated with the onset of the Garlock Fault to the north. The works of Hulin (1925) and Morehouse (1988) found that Miocene extension was accompanied by gold mineralization. Later sinistral transtensional faulting similar to that observed by McLarty (2014) was likely responsible for silver mineralization. As stated below, this transtensional motion may also be, at least, partially responsible for the wide distribution of anomalous gold within my study area.

Relationship to Randsburg Mining District Gold and Silver Mineralization

According to previous works by Hulin (1925), Morehouse (1988), and Hart (1986), the Miocene "Yellow Aster Episode" of gold mineralization is focused within NNW and NW trending extensional faults and quartz veins within the Yellow Aster Mine and other significant mines of the Randsburg Mining District. However, within my study area, 3-12 km southwest of the Randsburg Mining District, gold mineralized faults are primarily NE trending extensional and left lateral oblique faults as discussed previously. The precise reason for this difference in structural control is beyond the scope of this study. However, I have developed two hypotheses to be tested by future studies:

Hypothesis 1: The gold mineralized NE-SW striking faults of the central and southwestern Rand Mountains were originally NW trending extensional faults aligning with the NW trending dextral faults of the Eastern California Shear Zone. These would have developed synchronously with the Yellow Aster intrusion and channeled gold bearing hydrothermal fluids into the epithermal environment approximately 18-19 Ma. This is supported by K-Ar ages reported by Morehouse (1988) in which biotite from Randsburg Quartz Monzonite alteration yielded closure ages of 18.2 to 18.9 Ma and sericite from NW striking auriferous extensional veins produced closure ages of 18.3 Ma. As left lateral motion along the Garlock fault initiated, these mineralized NW trending faults rotated clockwise so that they are now striking to the NE. This is a process that was first proposed by McLarty (2014) to explain the large striated left lateral normal crossfaults separating rotational blocks of the southwestern and central Rand Mountains (Figure 57). These cross faults cut the Rand Mountains into numerous slender and oblong blocks as mapped previously by Andrew McLarty. McLarty found that each block rotated different amounts, typically between 45 and 90 degrees. Because the faults that I sampled are located within several different rotational blocks, the faults likely would have experienced varying magnitudes of rotation. This could explain why the NE trending mineralized faults have a wide spread of strikes within the NE and SW quadrants of the stereonet in Figure 60.

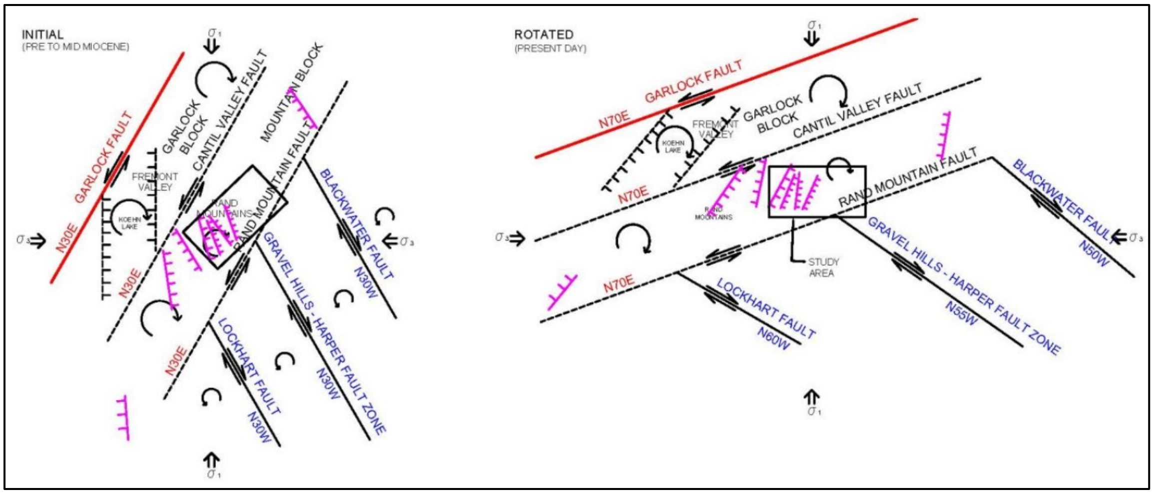

Figure 64: Andrew McLarty's 2014transrotation model of the Rand Mountains illustrating the clockwise rotation of various cross faults during left lateral motion along the range bounding Garlock and Rand Mountain faults. This could explain the differing structural control between my study area and the Randsburg Mining District.

Hypothesis 2: The mineralized NE-SW striking faults of the study area are related to the "Kelly Episode" of faulting and hydrothermal alteration as described by Morehouse (1988) (Figure 65). The Kelly Episode produced NE trending moderate to high-angle left lateral extensional faults within the Randsburg Mining District. Based on K-Ar ages from associated sericite, this event occurred approximately 11-15 Ma and was interpreted to be associated with the onset of motion along the Garlock Fault and continued Miocene extension. The Kelly Episode was responsible for rich localized silver mineralization, and was generally barren of gold or below economic concentration. However, in several mines, Morehouse found that Kelly Episode faults did contain economic concentrations of gold. Hence, the Kelly Episode's association with gold is unclear. Morehouse interpreted that anomalous gold found within these faults and quartz veins may have been remobilized from the slightly older Yellow Aster episode gold deposits. While proper geochronology on the auriferous NE trending faults of my study area have yet to be done, the structural nature and orientations suggest that they may be

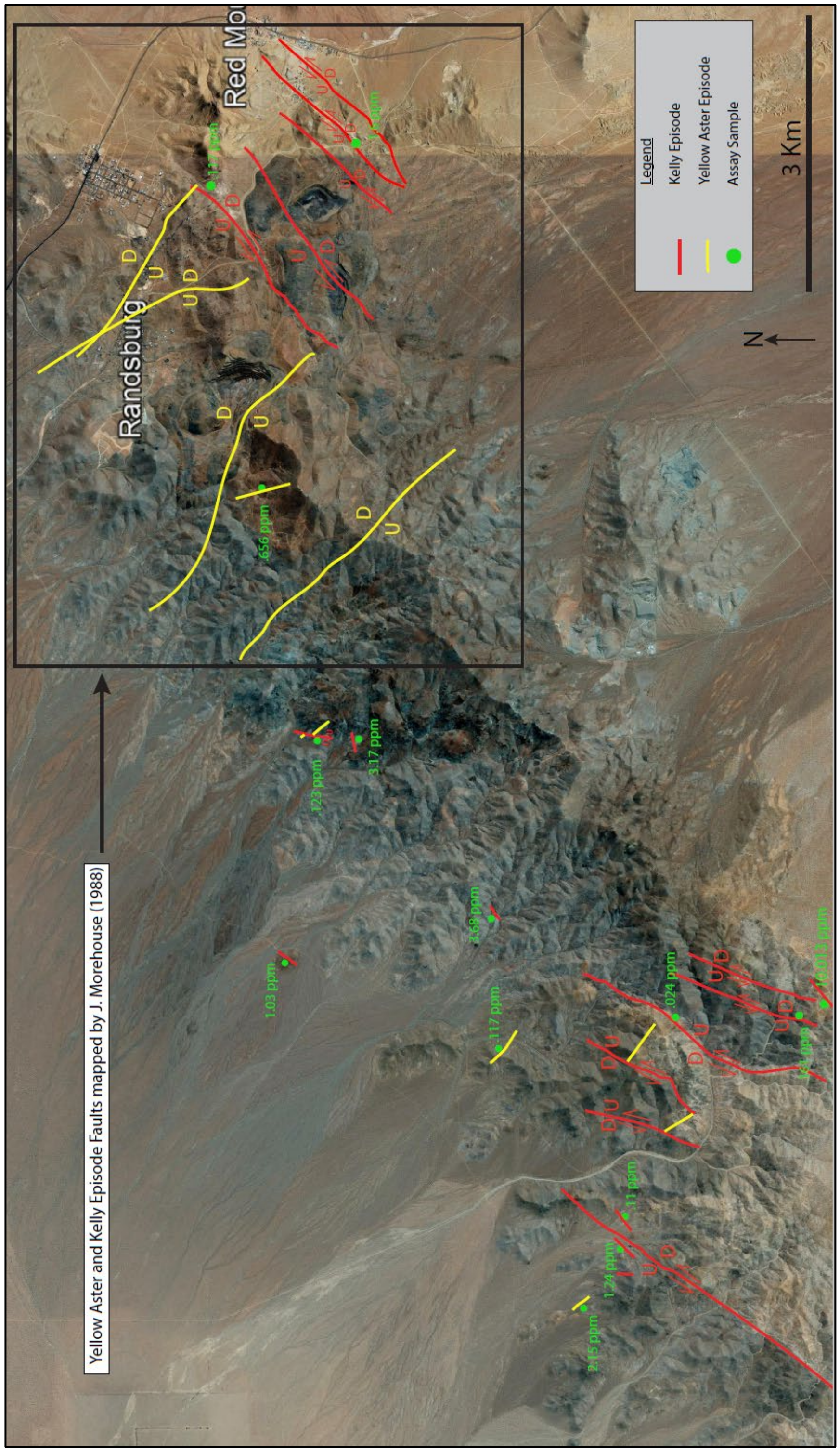

Figure 65: All faults within the black box were mapped by J. Morehouse 1988. These show the size and location of the main Kelly and Yellow Aster Episode faults. The faults outside of the box are those previously mapped by J. Nourse, A. McLarty (2014), and me. This indicates the possibility that NE striking faults of the central and southwestern Rand Mountains are associated with the Kelly Episode faulting that produced silver and moderate gold, while sparse NW striking faults are related to the gold rich Yellow Aster Episode faulting. Representative gold assay results of samples from these structures are in green. Note that north is to the left.

southwestern expressions of the Kelly Episode faulting. If so, it could be possible that the low-grade anomalous gold observed was likely remobilized by hydrothermal fluids from the original deposit in NW striking 19-20 Ma Yellow Aster Episode faults into younger 11-15 Ma Kelly Episode faults. Figure 65 illustrates several of the main faults of the Kelly and Yellow Aster Episodes as mapped by Morehouse. The larger scale NE striking oblique left lateral normal faults mapped by J. Nourse and A. McLarty along with several mineralized faults mapped by me in the central and southwestern Rand Mountains are also drawn in. This shows that faults with similar orientation and shear sense to the Kelly Episode structures are dominant southwest of the Randsburg Mining District. As a result, it may be interpreted that these structures and the hydrothermal fluids flowing through them are the controlling factors of the gold mineralization in my study area. Whether they are wholly responsible for supplying the gold or are simply remobilizing gold from 19-20 Ma NW striking faults is still unknown.

Gold Mineralization and its Possible Relationship to the Rand Thrust

This discussion would be incomplete without analyzing any possible relationship between gold mineralization and the significant Rand Thrust structures. The Rand Thrust is used as a name for two large scale shallow angle thrust faults that form the contacts between different units of the Rand Mountains. The basal thrust separates Plate I Rand Schist and Plate 2 Johannesburg gneiss and marble. Plate 2 sometimes is not obvious or well exposed, and/or Plate 3 Atolia granodiorite directly overlies the Rand Schist. Where it is exposed within the Randsburg Mining District, the Johannesburg gneiss is mylonitized and mixed with variable amounts of carbonate. The upper thrust separates the Plate 3 Atolia granodiorite from the Plate 4 granite. This contact between Plates 3 and 4 is often characterized by a zone of mylonitization and silicification. The thrusting event was initiated approximately 80-70 Ma as the oceanic plate and overlying sediment subducted and underplated the Sierran Batholith (Jacobson 1990). The resulting heat and pressure metamorphosed the sediments and basaltic rocks under green and blue schist facies conditions. This process has also generated the thrust faults that are now exposed along portions of the Rand Mountain anticline.

Morehouse proposed that the mylonitic gneiss and carbonate zone along the thrust between plates 1 and 3 may be an ideal location for gold mineralization and should be a target for future exploration. This low angle structure represents a structural, chemical, and lithological contrast within the epithermal environment. Morehouse suggested that this mylonitized horizon presents three possible mineralization environments:

1) a structural cap below which ore fluids would precipitate their contents.
2) a skarn environment in which the carbonate mylonite zone may act as a chemical contrast to assist with ore deposition.
3) In areas where the thrust is cut by younger high angle faulting, the carbonate and gneissic mylonite could form a brecciated zone to facilitate mineralization from ascending hydrothermal fluids in the younger faults.

This third environment of high angle faults cutting the lower thrust is an observation I made in several locations along the northern edge of the range front. These locations are the R50 Knob and the crestline of the hills immediately to the southwest of the R46/R49 junction. In addition, distinct yellow-orange weathered limonite-carbonate breccias are ubiquitous along the many cross faults that displace the low-angle mylonites of the Rand thrust. Many small prospects target these faults but the few samples we collected away from the Plate 1/Plate 2 contact were either barren or yielded low grades.

The R50 Knob Location

This small hill is pock marked with prospects, including one larger mine with several daylighted stopes (Figure 15). The bottom half of the hill is composed of a muscovite-chl-qtz-feldspar grayschist, while the upper half is composed of plate 2 dioritic gneisses and interbedded marble units. The contact between the plate 1 schists and plate 2 gneisses and marbles is the basal Rand Thrust. On the south end of the hill, schist and gneiss foliations dip moderately to the north. However, starting at a flat saddle on the top of the hill and continuing down the north end of the hill, the foliations dip to the south. This dip reversal suggests that the knob is a small synclinal structure. A large steeply dipping NE striking fault is targeted within the mine on the south end of the knob. The striations on the fault surface have a steep rake, suggesting a significant component of dip slip movement. Fault-slip indicators demonstrate normal displacement. Sample GSRM-42 taken from the fault gouge, contained an anomalous 1.03 ppm Au. Because this fault strikes to the NE and is steeply dipping, it likely is a younger fault associated with Miocene extension and movement on the Garlock Fault. Our mapping of the mine working and surface outcrops shows that it cuts through the much older Rand Thrust. This may suggest that the intersection of younger high angle faults and the low angle older thrust is an ideal environment for ore mineralization like Morehouse hypothesized. Not only would the intersection have created brecciation and space for ore fluids to collect and deposit, but the synclinal folding could also have played a role in creating fractures and brecciation. The relative timing of the synclinal folding was never determined, but similar folds of plate 2 are known in this part of the Rand Mountains. Another location with similar structure and lithologic components, but with the addition of substantial hydrothermal breccias is discussed below.

Hills Southwest of the R46/R49 Intersection

Two mines are driven into the hillside southwest of the R46/R49 intersection on the north front of the Rand Mountains. As described in the results and depicted in the geologic map in Figure 25 this hill is composed mostly of schist until just below the crestline where it comes into contact with marbles and gneisses. The dips reverse on either side of the crest so that the structure forms a tight synclinal feature. The NW striking fault running through the crestline is steeply dipping with dip-slip striations. It initially appears to represent the Rand Thrust itself, but is more likely a younger high angle extensional fault that happens to outcrop near the contact of plates 1 and 2. The fault runs through a vertical prospect on the crest of the hill. This was sampled, but turned up barren of any gold. However, altered hematitic schist from the tailings of a mine on the east facing slope of the hill contained .117 ppm Au. Brecciated hematitic quartz vein material was also collected from the tailings but was barren. While the air quality and stench of the mine was too poor to allow entrance, it is assumed that the large fault at the crest of the hill intersects the mine tunnel at some point. The hydrothermal alterations seen in the tailings likely would have resulted from fluids traveling along this fault. This is unfortunately only a hypothesis, and was not proven in the field.

The high angle fault continues down the southeast slope, disappears where it crosses R49, and reappears in two vertical prospects on the small ridgeline immediately east of R49. Within these prospects, the fault is bordered with a 1- to 2-foot-thick zone of intensely silicified and limonitic hydrothermal quartz breccia (Figure 27). The breccia was sampled but did not contain anomalous gold. However, this should warrant further sampling in the future.

So, these hills represent another occurrence of anomalous gold associated with likely Miocene extensional faults cutting through the basal Rand Thrust where there is synclinal folding. In this case however, it is accompanied by the presence of significant brecciation, evidence that additional space was created for the deposition from hydrothermal fluids.

While the lower Rand Thrust shows potential as a target for gold mineralization, the upper Rand Thrust between plate 3 Atolia granodiorite and plate 4 granite was not found to be mineralized. Within the study area, there was a notable lack of prospects at the contact between plate 3 and 4. In fact, the only area with any workings along the upper Rand Thrust contact was at the group of trenches northeast of the Darn Peak mine cluster location. The absence of prospects on this structure is a good clue that prospectors of old did not have much success with discovering gold. Additionally, four samples (GSRM-1,2,3, and 4) were assayed from this location. The rock types sampled were a quartz mylonite, mylonitized granodiorite, gouge material from shallow angle NW striking faults, and chloritized granodiorite below the quartz mylonite. These samples represent the shear zone of the upper Rand Thrust. All were completely barren of gold (at or below .003 ppm Au).

Why the upper thrust is a poor environment for gold mineralization is still a mystery. However, there are several possible reasons for this. 1) The upper thrust has simply been vastly underexplored by prospectors and this study. 2) The thrust is only found exposed as small localized features that do not cover much area. 3) Because of the lack of overall coverage, younger extensional faults rarely if ever intersect the upper thrust. Therefore, fluids traveling up the extensional faults never come into contact with the upper Rand Thrust. This requires further investigation that is beyond the scope of this study. 4) Hydrothermal fluids were spent entirely within the highly fractured and faulted Plate 3 Granodiorite before reaching the impermeable mylonitic zone below Plate 4. This last theory is discussed further in the Hydrothermal Alteration of Host Rocks section below.

Relative Timing of Gold Mineralization

The timing of gold mineralization has been well constrained within the Randsburg Mining District to early Miocene; specifically, 19-20 Ma (Hulin 1925, Morehouse 1988, Grove et al. in progress). However, with the structural controls observed within my study area, the timing of gold mineralization in the southwestern and central Rand Mountains is less clear. The gold hosting structures within Plate 3 did not contain minerals suitable to geochronological dating techniques. As a result, only relative age assumptions can be made based on crosscutting structural features. For example, if the moderate to steeply dipping NE striking faults are indeed rotated from their original Miocene NW trending orientations (Figure 64), it could be proposed that the gold within the southwestern Rand Mountains was deposited at the same time (19-20 Ma) as the gold in the main Randsburg

Mining district at the northeast end of the range. However, in one area (near Route 83) it is known that a NE-striking normal fault crosscuts a NW-striking oblique right-lateral normal fault, resulting in significant offset in map view. Also, it is difficult to rule out faulting generated by motion along the Garlock fault between 11-15 Ma (Morehouse 1988) as the mineralizing event. This would have introduced transtensional movement along newly formed or rotated older NE striking faults.

Transtensional faulting in general has been repeatedly shown to produce depressurized conduits conducive to hydrothermal fluid ascension. What we definitely know is that the gold mineralization is 1) younger than the Rand Thrust, and 2) associated with later high angle faults. This relationship is abundantly clear within a prospect dug into the cliffs east of the R83 Cross fault location (Figure11). The prospect targets a highly brecciated zone of intersecting faults within Rand Schist. The ceiling of the adit is the hanging wall of a nearly horizontal thrust fault, presumably related to the stresses that formed the Rand Thrust. Cutting through the low angle fault are both a NE striking high angle fault and a NW striking high angle fault. The relationship between the two high angle faults is not clear within this prospect. However, prominent fault outcrops below this prospect suggest that the NE trending faults are younger and offsetting the NW striking faults by extension. The rakes on the NE striking faults suggest a more significant component of extension than the NW trending faults which show a shallower rake indicating some oblique right-lateral movement. The other interesting finding here was that the NE trending fault at this location contained slightly anomalous gold (.123 ppm Au), while two samples from the NW trending fault contained only .003 and .005 ppm Au. This again supports the structural control on gold mineralization observed in the study area (where NE structures tend to run higher gold assays than NW structures). Unfortunately, it may not support the hypothesis that the anomalous gold found in the NE striking fault was originally emplaced with the Yellow Aster ore body in NW striking extensional faults 19 Ma. The barren NW trending fault at this location was likely one of the early Miocene extensional faults that was generated during the main gold mineralization event 19 Ma. It appears to be intersected to the north by the NE striking fault with anomalous gold, as shown in map Figure 11. This field observation suggests that this location of the Rand Mountains did not experience clockwise rotation like areas to the southwest. Instead of rotating to accommodate for the sinistral strain along the Garlock Fault, this block of the Rands to the south of R83 generated a younger set of NE trending left lateral extensional faults that cut and offset the older NW trending faults. The presence of anomalous gold within the NE trending fault at this location suggests that the gold was either remobilized out of the NW trending fault or that remnant circulating gold bearing hydrothermal fluids travelled up the younger NE striking faults. In this perspective, gold was deposited at approximately 15 Ma.

Hydrothermal Alteration of Host Rocks

Alteration of host rock by hydrothermal fluids is a significant aspect of the gold deposits and was a characteristic feature of the majority of the prospects visited for this study, particularly at the Darn Peak cluster. Because the prospects were also targeting fault zones, the hydrothermal fluids are using them as conduits to reach the epithermal zone. In this study, one objective was to observe the change in chemistry between fresh, unaltered rocks and their hydrothermally altered counterparts. While many different rock types were analyzed via XRF for major oxides and trace elements, the most meaningful results were generated from Plate 3 and Plate 4 samples. Altered Plate 1 samples did not have appropriate unaltered samples to be analyzed against.

In general, the Plate 3 Atolia Granodiorite experienced the most widespread alterations. The most common alteration associated with thrusting was chlorite – epidote propylitic alteration. This suggests mild hydrothermal fluid temperatures of 200 – 350 C. Much of the biotite in the granodiorite was altered to chlorite, while epidote veining and fracture fill was prevalent. This type of alteration represents the lowest grade of hydrothermal alterations and was always barren of gold in the assay results, for example, in the trenches cutting the footwall of the fault between Plates 3 and 4 northeast of Darn Peak. Chlorite-epidote alteration is typical of numerous epithermal and porphyry ore deposit models in which propylitic alteration represents the barren outer, most distal component of the alteration halos (Hedenquist et al. 2000). However, within my study site, the different zones, or shells, of alteration appear to be more localized along discrete fault zones rather than fit together as a progressively layered shell.

The other form of alteration encountered within the Atolia Granodiorite is an argillic alteration. This resulted in the complete destruction of the biotite and partial to complete destruction and leaching of the original feldspars. The feldspars were replaced by the clay minerals such as kaolinite ($Al_2Si_2O_5(OH)_4$) and possibly montmorillonite ($(Na,Ca)_{0.33}(Al,Mg)_2(Si_4O_{10})(OH)_2 \cdot nH_2O$) . The significant LOI in these samples can be explained by volatilization of water from clays minerals during XRF analysis. Detailed assessment of clay content would require a full XRD analysis to determine alteration minerals. Within the less competent altered rock, the quartz component was unchanged.

This is confirmed by the lack of change in SiO_2 content seen in the XRF results. The argillic alteration of Plate 3 is associated with the most anomalous gold samples. Additionally, the highest-grade sample, GSRM-33, experienced further alteration and saw somewhat different trends in major oxides than that of the argillic alteration zone. Within the fault zone that produced GSRM-33, there was a noticeable drop in Na_2O, FeO, K_2O, MgO, and TiO_2, indicating phyllic alteration. The biggest difference in major oxides between the GSRM-33 fault zone and the surrounding argillic alteration of Plate 3, are the trends in K_2O and FeO. All other Plate 3 samples actually gained potassium and saw little to no loss of iron. GSRM-33 on the other hand, showed significant loss of iron and potassium with respect to the unaltered granodiorite. This may represent the leaching of the potassium feldspars from the fault zone and mobilization of the potassium into the surrounding rocks. However, there is very little sericite within the GSRM-33 fault zone material. Typically, it would be expected that the leaching of potassium and destruction of feldspars be accompanied by sericitization. So, it may represent more of a transitional alteration zone between the argillic alteration and phyllic alteration zones rather than a pure phyllic alteration, likely due to insufficient temperature.

Carbonatization of the Atolia Granodiorite also may have played a role in the gold mineralization. The clear upward trend in CaO with LOI (loss on ignition) in altered granodiorite samples suggests calcite and other carbonate minerals were deposited. From field and hand sample observations, this indeed came in the form of caliche and siderite. Volatilization of CO_3 during XRF analysis could explain part of the LOI effect Additionally, these carbonate and iron carbonate minerals form stockwork veins of up to two inches thick through much of the fault gouge as well as the immediately surrounding wall rock. Therefore, it can be inferred that all other alterations preceded the carbonate alteration. It is difficult to definitively attribute the carbonatization to the gold mineralization instead of the earlier argillic and phyllic alterations. However, all gold samples of 1 ppm or higher, except GSRM-72, are associated, at least spatially, with intense carbonate mineralizations, whether it be siderite and calcite as observed in the Darn Peak and R50 Knob locations, or magnesite, ankerite, and dolomite as seen in the chromium and nickel enriched wall rock alteration surrounding the gold bearing quartz veinlets of sample GSRM-55 (3.68 ppm Au). All of these samples were taken from NE trending faults. This suggests that the carbonatization process was either the final stage of hydrothermal fluids in the gold depositional system or that younger transtensional movement due to motion on the Garlock Fault introduced large amounts of carbonate bearing fluids and possibly moderate amounts of gold.

A very likely source of $CaCO_3$ is the marble mylonite unit of Plate 2 Johannesburg gneiss that is localized along the lower Rand thrust between Plates 1 and 3. This marker horizon is intersected and displaced by most of the cross faults. The occurrence of limonite-carbonate breccias along most these faults is not a coincidence. It is hypothesized that hydrothermal fluids transported carbonate upward or laterally from the marble into the gold-bearing fault zones

From an exploration standpoint, gold-bearing structures within Plate 3 Granodiorite are found as kaolinite- and caliche-rich zones lacking noticeable sericite and silicification within a relatively broad zones of argillic alteration. LOI and CaO both increase dramatically within zones of anomalous gold and in surrounding alteration envelopes. In classifying epithermal gold deposits, it is important to determine whether they are a high, intermediate, or low sulfidation deposit. This helps to better understand the nature of the mineralizing fluids as well as provide an exploration framework for future work. Within Plate 3, the alteration characteristics and chemistry reflect that of a low sulfidation ore deposit in which hydrothermal fluids had a neutral pH. High and intermediate sulfidation deposits are driven by moderately to highly acidic hydrothermal fluids, and therefore, contain only minor amounts of carbonates. The evidence of this is listed below and is based on the characterization of epithermal gold deposits as written by Hedenquist et al., 2000:

1) The high amount of carbonate within both the ore bearing structure as well as the surrounding wall rock is a typical component of low sulfidation systems and a rare occurrence in acidic high sulfidation systems. These carbonates require a near neutral to mildly acidic pH to exist in the deposit. The hydrothermal fluids create argillic alteration halos of clays and siderite. The source of the carbonate is not well understood. However, it could be due to ascending acidic fluids dissolving the carbonate units within the Plate 2 Johannesburg Gneiss and Marbles. Additionally, the acidity could have caused the leaching and mobilization of the potassium and sodium in Plate 3, as seen in the XRF results. As the carbonates were dissolved and incorporated into the hydrothermal fluid, the pH increased and became increasingly neutral. The carbonate bearing fluid then mineralized Plate 3 Granodiorite as it ascended into the epithermal zone.
2) Bladed calcite and siderite are very common in the Darn Peak alterations. This carbonate morphology is very indicative of fluid boiling in low sulfidation deposits, the process responsible for precipitation of gold. Typically, this should

also be accompanied by colloform chalcedony veins. However, none were observed in the field.

3) The complete lack of vuggy quartz veins within any of Plate 3 in the study area suggests that it is not a high sulfidation deposit. Vuggy quartz veins are one of the most identifiable features of high sulfidation deposits due to the leaching of the rock by acidic fluids. Interestingly, vuggy quartz is a very common feature of the gold bearing veins of the main Randsburg Mining District area, therefore classifying it as a high sulfidation deposit. It is possible that the epithermal ore deposit style evolves towards the southwest into my study area such that it becomes low sulfidation. This could simply be due to the increased amount of Plate 2 carbonates in the southwestern Rand Mountains and not indicate a genetically or temporally different deposit.
4) Extensive amounts of propylitic alteration in the form of chlorite and epidote is intermingled with the argillic alterations. Propylitic alteration is not as extensive of a component of high sulfidation deposits but is very suggestive of low sulfidation deposits in which neutral pH allows for chlorite and epidote alteration of biotite. The presence of chlorite and epidote also indicates that the mineralization occurred at deeper parts of the epithermal system, around 300-500 meters. However, the lack of sericite means that the system could not have been much deeper than 300 meters. Additionally, there was no sinter or clay apron observed anywhere in the study area. These are typical components of the surfaces of low sulfidation systems. Their absence suggests that the mineralization occurred at greater depth and did not continue to the near surface

environment. However, because propylitic alteration in Plate III is spatially associated with the upper Rand Thrust, or possibly the later detachment along the thrust, it is not conclusive that the chlorite and epidote alteration is actually associated with gold deposition.

Plate 1 schist samples with anomalous gold also contain large amounts of carbonate material leading to large LOI and MgO values. Additionally, sericite in the form of coarse-grained fuchsite, either as part of listwanitic rocks or as fuchsite pods, is often associated with these gold bearing schist ores. This alteration style suggests a different genetic formation of the gold bearing structures in the schist and is discussed further in the sections below. Future studies will need to better delineate the changes in chemistry between unaltered schist and altered schist. This could be a complicated process since the schist bodies vary both in mineralogical composition due to different protolith material and metamorphic grade due to stratigraphic position during the subduction process.

Plate 4 granites experienced some similar geochemical trends compared to those of Plate 3 granodiorites. However, there were several differences in major oxide changes that may be responsible for the lack of gold mineralization in prospects targeting the granites. The most notable difference was the loss of SiO_2 and K_2Oin the altered granites. From field observations, quartz in the granites was likely dissolved and mobilized into the highly silicified mylonitic shear zone between Plates 3 and 4. The sweating of the silica from the granites may have occurred during the thrusting event or as a result of the reactivation as detachment fault during extension. Biotite did not experience chloritization resulting in a complete lack of propylitic alteration. Argillic alteration in the granite is not pervasive like in the granodiorites but is present in minor amounts. For the most part, the granites were largely unaltered in any significant way, such that Plate 4 is always immediately recognizable in the field. Appreciable alteration appeared to only occur within proximity to the mylonitic shear zone. Further out from this zone, the only sign of any kind of alteration was the rinds of iron oxidation around the margins of biotite crystals. This is in contrast to Plate 3, which is often almost unrecognizable due to the intensity of the argillization. Like the granodiorite samples, the granites also experienced similar increases in CaO and LOI from unaltered samples to altered samples. Unlike the granodiorites, this change in chemistry was not accompanied by anomalous gold in the granites.

My proposed hypothesis for why there is no gold in Plate 4 is that the remobilization of silica out of the granite and into the shear zone between Plate 4 and Plate 3 created an impenetrable seal through which hydrothermal fluids could not travel. The knobs of granite that often formed the tops of hills along the southern front of the Rand Mountains were also noticeably less faulted and fractured than the lower lying granodiorite. Due to the highly fractured and faulted nature of the Plate 3 Atolia Granodiorite, ascending hydrothermal fluids were able to dissipate outwards from the main conduit and mineralize the surrounding Plate 3 rocks.

It is also possible that at the time of gold mineralization, the Atolia Granodiorite on the southern front of the range was at the optimal depth for epithermal pressure and temperature conditions to allow for deposition of metals from the hydrothermal fluids. As a result, the majority of the hydrothermal fluid budget was spent before ascending to the silicified mylonitic shear zone marking the lower boundary of Plate 4. Any remaining fluid would have pooled and spread outwards below the shear zone. Normally, pooling of hydrothermal fluids below an impermeable barrier would be an ideal condition for gold deposition. Unfortunately, there was likely too little fluid coming into contact with this barrier and therefore, little to no gold being deposited. Even though all samples taken from immediately below the mylonitic shear zone were barren of gold, it may be worthwhile to more extensively explore this boundary in the future.

Elements as Possible Tracers for Gold and Silver Mineralization

Because the gold within the study sight is confined to narrow, unremarkable looking shear zones that are often times nearly indistinguishable from the surrounding host rock alterations, using trace elements as a tracker for potential gold concentrations can play an important role here. Silver is the most anomalous element to accompany gold in the ore material. When anomalous, silver values ranged from .8 ppm to 43.1 ppm but were most often between .8 ppm and 3 ppm. Typical Ag:Au ratios were extremely variable but generally between 2 and 13. GSRM-33 is the rare example in which the Ag:Au ratio is less than 1 (.32). However, the silver, like gold, is constrained within the gold bearing fault gouge and does not leach out into the surrounding alteration envelope.

Arsenic is likely the most telling of the elements included in the assay. Highly anomalous gold samples typically contained between several hundred ppm As to over 3000 ppm As. Average crustal arsenic concentration is 2 ppm. The slightly anomalous gold samples contained 50 to 300 ppm As. Samples from the alteration halos immediately surrounding gold zones usually were composed of lower arsenic levels of 20 to 40 ppm. This indicates that arsenic is most concentrated in the ore bearing materials yet remains at decreasingly elevated levels moving outwards from the ore bearing zone. Additionally, arsenic appears to more easily escape the main ore bearing structure and follow older, preexisting faults than gold does. This is evident at the two prospects that produced samples GSRM-33, 32, and 31. GSRM-33 with 10 ppm Au, was produced from a sub-vertical NE striking fault. Its arsenic content was 41 ppm. This fault cuts through two smaller low angle NW striking faults that produced samples GSRM-31 and 32, which contained .248 ppm Au and .121 ppm Au respectively. This suggests that gold is only minimally mobile outside of the main ore bearing structure. However, arsenic was found to be higher within the two shallower angle faults than in the 10ppm fault. It can be inferred from these observations that while anomalous arsenic often may not be found with highly anomalous gold, it can be used as an indicator of close proximity to main gold bearing zones.

Curiously, arsenic's largest anomalies (900 – 3,000 ppm) occur almost exclusively in NW striking faults within Plate I. No anomalies of this size occurred in Plates III and IV. Only two NE striking faults contained greater than 1000 ppm As, one of which was material from the Kelly silver vein near the town of Red Mountain. The timing of this vein's mineralization has been well constrained to 15 Ma. In contrast, 8 NW striking faults contained over 1,000 ppm As. In all cases, anomalous gold also occurred. This contrast in arsenic composition between NE and NW trending faults may indicate a difference in timing of ore deposition, and therefore, represent two different mineralizing events. Additionally, arsenic anomalies in the Plate III granodiorite samples maxed out at 281 ppm (most were less than 100 ppm), and mineralized samples from within the schist were regularly significantly higher in arsenic. This suggests that gold mineralization in schist bound faults occurred during a different event than the mineralization in the granodiorite. Alternatively, it may just represent an affinity of arsenic to some kind of mineralizing conditions present only in the schist. In any case, it is clear that very large arsenic anomalies often indicate proximity to gold bearing NW striking faults within Plate I.

Aside from silver and arsenic, antimony seems to have an interesting relationship with gold, as does the chromium-nickel enriched trends I have identified. Antimony, like arsenic, is a common component of gold deposits and various other epithermal and orogenic type ore deposits around the world (Hedenquist et al. 2000, Sillitoe and Hedenquist 2003). Within the majority of samples with anomalous gold, antimony enrichment was minor, but noticeable in comparison to most other unmineralized samples. Typical antimony concentrations in samples with anomalous gold ranged from 10 to 87 ppm Sb. Some samples contained less than 10 ppm, including most of those barren in gold. Antimony anomalies were also common in samples with anomalous silver, such as GSRM-80C and GSRM-24. In fact, Hulin found that stibnite, an antimony sulfide, was commonly present as veins, fracture and vug filling, and as a disseminated form in the silver producing veins of the Randsburg Mining District. He interpreted the stibnite to represent the last stage of the silver mineralization. Visible stibnite was identified in both GSRM-80C and abundantly in GSRM-24. However, what was blatantly obvious was the association of large antimony anomalies (100 – 161,000 ppm) with large chromium and nickel anomalies (and occasionally with small to moderate gold anomalies) and their spatial relationship with NE trending faults.

One of the objectives of the study was to sample un-mined or un-explored structures that may be prospective. The most notable of these structures are the large NE striking left lateral extensional cross-faults cropping out within the schist that split the Rand Mountains into rotational blocks. In several locations along these faults, outcroppings of a bright orange schistose rock with abundant bright green chromian mica (fuchsite or mariposite), magnesite, and patches and veins of nickel bearing minerals of various shades of green and blue. These outcrops were found adjacent to the R43 Cross Fault, as wall rock alteration at the R-57 mine that produced 3.6 ppm Au, and as outcropping alteration on top of the high-grade stibnite mineralized veining in one of the mines within the Desert Tortoise Wilderness. The latter mine is targeting a large NE striking fault that is running almost parallel and within close proximity to a very large-displacement cross fault through the Desert Tortoise Wilderness. Samples from this site contained between 1,301 and 161,700 ppm Sb, 362 and 1,326 ppm Cr, 73 and 602 ppm Ni, and .071 and 1.24 ppm Au. An additional occurrence was identified along a NE trending structure, possibly a fault, just to the north of the high-grade stibnite location. From hand sample analysis, it appears as though the more highly silicified components of these outcrops contain the trio of enrichments in antimony, chromium, and nickel, whereas the samples with little to no silicification are depleted in antimony. Only one mine within the study area has targeted these features, likely due to their cryptic appearance and difficulty of discovery. Because antimony is a critical trace element for many precious and base metal deposits, it's anomalous occurrence should be accounted for in future exploration in the Rand Mountains. However, due to antimony seeming to primarily be present in elevated amounts within the silicified parts of the chromium-nickel enriched outcrops, chromium and nickel should also be used as trace elements for possible hydrothermal ore deposits.

There are too many similarities between these antimony-chromium-nickel zones and the silver deposits within the Randsburg Mining District to immediately discount them as insignificant anomalies. The silver in the mining district is restricted to NE trending left lateral normal faults. The cross faults in the southwestern Rand Mountains with the zones of chromium-nickel-antimony anomalies are also left lateral normal faults striking primarily to the NE. Stibnite in the silver mines was present as veins, fracture fill, and disseminated form representing the final stage of silver mineralization. The same type of stibnite mineralization was found in the quartz vein producing sample GSRM-24 and in the silicified and brecciated fault zone of samples GSRM 90 – 95. Additionally, Hulin noted that sporadic aggregates of mariposite, a chromian mica variation of fuchsite, occurred along several outcroppings of the silver bearing structures. I have made the same observation along several of the NE trending cross faults within my study area, including at the high-grade antimony occurrence in the Desert Tortoise Wilderness. Unfortunately, assay results from these trends show that the abundance of antimony, chromium, and nickel is accompanied only by minor anomalous silver. Regardless, the presence of stibnite with intense hydrothermal alterations and silicification, and occasionally moderate gold anomalies, suggests that antimony could be one of the most useful elements for possible discoveries of precious metal deposits in the Rand Mountains.

Like the Randsburg Mining District, antimony anomalies within the southwestern portion of the Rand Mountains are common in low to higher grade gold bearing samples.

The larger antimony anomalies of 100 ppm and higher are also potentially linked to undiscovered silver or gold deposits within or adjacent to the extensive NE striking left lateral extensional crossfaults. These zones of antimony enrichment are commonly accompanied by large anomalies of nickel and chromium in the form of fuchsite, chromite, and various nickel carbonate minerals within a bright orange schistose iron carbonate rock. Interestingly, the nickel and chromium anomalies tend to be wider spread within these alteration zones than antimony. The antimony appears to mostly be restricted to narrower zones of silicification within the chromium-nickel-iron carbonate material. Therefore, chromium and nickel can at least be used as elements to vector in on hydrothermally mineralized structures in the Rand Mountains.

Alternative Orogenic Models for Mineralized Faults within the Rand Schist

Many of the large NE striking faults within the schist exhibit a unique alteration zone that at times resembles "listwanite", a product of metasomatism of ultra-mafic rocks. These rocks are typically composed of either quartz-carbonate (usually magnesite or ankerite), and chromian mica or just carbonate and chromian mica (Halls and Zhao, 1995). While not entirely well understood, listwanite formations typically occur in compressional or transpressional orogenic tectonic environments under greenschist facies temperature and pressure conditions. The metasomatism occurs as CO_2 rich fluids flow up faults generated by the compressional event (typically subduction related) and come into contact with ultramafics like serpentinite. As a result, this material exhibits high concentrations of chromium, nickel, and sometimes strontium. Cobalt experiences minor enrichment. This type of alteration has been widely found to be associated with mesothermal/orogenic Au, Au-Sb, Ag, and Au-Ag lode deposits in many Archean and Mesozoic greenstone belts (Buckman and Ashley, 2010, Groves et al., 1998, Halls and Zhao, 1995). For this reason, it is worthwhile to discuss its existence in the Rand Mountains.

Within my study area, listwanitic and fuchsite rich rocks with large chromium and nickel anomalies have been identified only along or within the moderate to steep NE trending faults where they outcrop in schist. Some of these faults represent the rotational left lateral normal faults mapped by A. McLarty and J. Nourse in previous studies. In each case, small to moderate anomalies of gold and moderate to large anomalies of antimony have been present. Listwanite (sample GSRM-70) with visible fuchsite adjacent to the R43 cross fault contained .023 ppm Au, 1015 ppm Cr, 441 ppm Ni, and 356 ppm Sb (Figure 66). GSRM-84C, also from the same location, is a

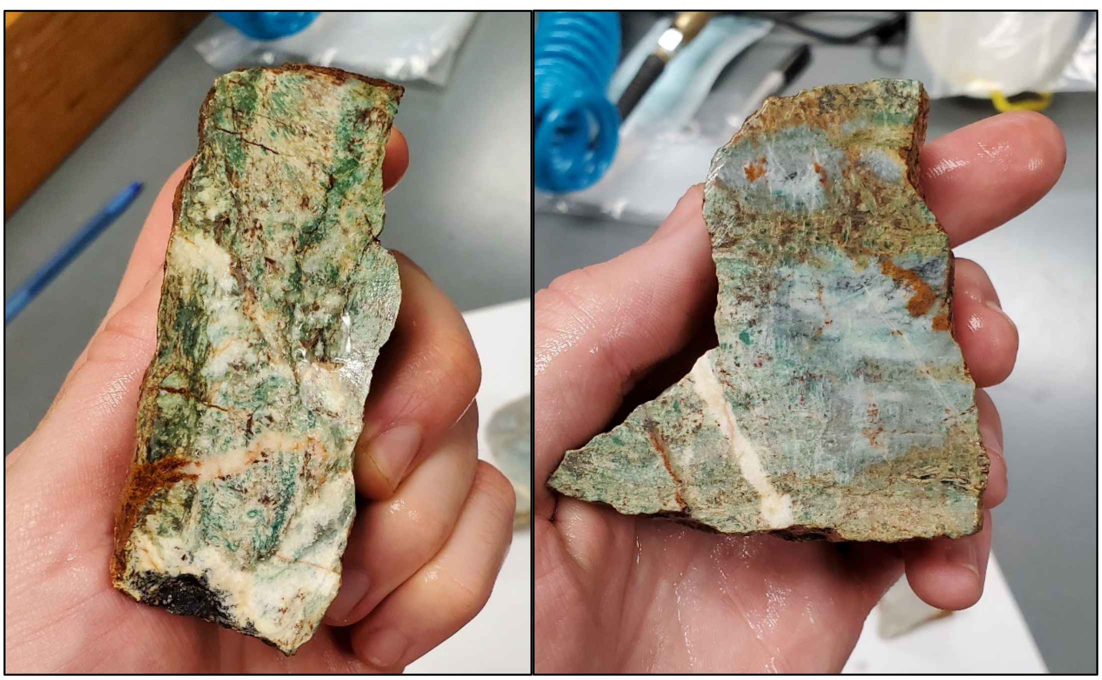

Figure 66: Sample GSRM-70 showing the listwanitic alteration of fuchsite/talc (green color), quartz (light grey to white), and iron carbonate (orange and dirty white veinlets). Several small sulfides can be seen in the quartz zones of the picture at right.

highly altered schist with .024 ppm Au, 744 ppm Cr, 169 ppm Ni, and 147 ppm Sb. Several other samples from this fault zone contained elevated levels of Cr and Ni but no anomalous Au (Figure 67).

Figure 67: GSRM-71 was taken from outcrop adjacent to the R43 cross-fault and near the outcrop of GSRM-84C. This unusual schistose rock contains highly anomalous Cr and Ni but no gold and very little Sb.

Another NE striking fault off R55, contained 3.68 ppm Au (Sample GSRM-55). Altered listwanitic wall rock from the footwall of the fault contained .017 ppm Au, 1427 ppm Cr, 1020 ppm Ni, and 26 ppm Sb (sample GSRM-57) (Figure 68). Additionally, a large pod of fuchsite and chromite from this location contained 25,809 ppm Cr and 277 ppm Ni (sample GSRM-57B). This sample was dated to 71.64 ± 1.9 Ma. Lastly, the NE striking fault containing high grade antimony in the Desert

Figure 68: Sample GSRM-57 is an extremely hard quartz-carbonate-fuchsite rock with disseminated sulfides and a weak foliation. While it appears to be a quartzite, it is only 57% SiO_2 and reacts very strongly with HCl when freshly powdered. The picture at right displays the coarse fuchsite pods distributed throughout the sample.

Tortoise Wilderness in the far southwest portion of the study area also exhibited a relatively narrow alteration halo of fuchsitic, silicic, and carbonate rocks, sometimes schistose, similar to those found along the R43 Cross Fault

While fuchsite is found ubiquitously in the Rands as very fine-grained minor patches creating a faint green sheen on the schist, the fuchsite from the alteration zones along these NE trending faults is coarse grained and a major component of the altered rock. Postlethwaite and Jacobson, 1987 also acknowledged the significance of the chromian mica as a component of the Rand Schist but suggest that it is a phengitic variation resulting from regional metasomatism. Additionally, several mines in the Rand Mountains, such as the Rainbow Prospect, produced gold from mariposite (chromian mica) carbonate veins and alteration zones concentrated around faults (Morehouse 1986, Troxel and Morton 1962). This suggests that hydrothermal fluids traveling up these faults were likely to have been responsible for the observed fuchsite/mariposite and listwanitic type alterations. Because this style of alteration is commonly associated with compressional tectonics and late stages of orogenies at greenschist facies conditions, it may be inferred that some of these NE striking faults were at least originally generated as thrust or high angle reverse faults at the time of hydrothermal alteration but after metamorphism of the schist.

Additionally, Jeff Morehouse reported two K/Ar ages of fuchsite in his incomplete thesis. Fuchsite is referred to as mariposite (another term for chromian phengite and often used interchangeably with fuchsite) in his study. The first age, 70.8 ± 1.6 my, represents the cooling age of mariposite schist, the material that is minor yet ubiquitous in the Rand Mountains. This age correlates well with the total gas ages of phengite from Rand Schist in Harrison et. al 2009, Jacobson 1990, and Grove et al in prep. This study found that phengite closure occurred 74-68 Ma. Grove et al. (in preparation) calculated closure took place at 70 Ma at a temperature of 425 C. This would represent midcrustal level under greenschist facies conditions. So, the mariposite schist closure timing from Morehouse likely represents peak metamorphism of the schist protolith during subduction. This is also consistent with the 71.64 ± 1.9 Ma total gas age of the fuchsite sample (GSRM-57B) that was dated for this study.

The second age for mariposite in the Morehouse study was 50 ± 1.6 Ma. This mariposite sample was a mariposite-ankerite material from a faulted vein. His description is similar to the listwanitic samples I have collected. Because the quartz-carbonate-fuchsite/mariposite alteration tends to form narrow envelopes around NE trending faults, it indicates that there were CO_2 rich hydrothermal solutions using faults as pathways through the already metamorphosed schist while still at mid-crustal levels. Because the two ages are separated by approximately 20 million years, it may be inferred that there was a relatively significant hydrothermal event occurring after the metamorphism of the schist. This makes sense since these mineralized faults are cutting through the schist. Grove et al. (in preparation) found that the schist did not begin exhumation until 19.6 Ma when the Yellow Aster Granodiorite intruded. Therefore, metasomatic alteration of the ultramafic lenses in the schist by hydrothermal fluids ascending fault pathways likely occurred when either: 1) compressional or transpressional forces from subduction and shallow angle subduction were still predominant, or 2) during the early stages of the Yellow Aster intrusion which would have caused partial argon loss in the fuchsite leading to an incorrect 50 Ma total gas age. This suggests that at least some of the NE trending faults with the listwanitic alteration zones may have originally been 50 Ma? high angle reverse faults generated at mid-crustal depth. Regardless, from the above observations, it can be proposed that NE trending faults contained within the greenschist facies portion of the Rand Schist, may be mineralized with orogenic gold of at least 50 Ma.

Following the 19.6 Ma Yellow Aster intrusion, Miocene epithermal gold was emplaced into the northeastern end of the Rand Mountains as well as the Plate 3 Granodiorite which shows very few geochemical similarities to the auriferous schist samples. This isn't to say that these faults weren't reactivated as normal faults during the Miocene exhumation of the metamorphic core. It is entirely possible that the gold was emplaced into these faults during the Yellow Aster intrusion rather than during the late stage of subduction process. It is also possible that the gold mineralized these faults during later (15 Ma) oblique left lateral normal faulting that produced the high-grade silver and low-grade gold mineralization dated by J. Morehouse, 1988. J. Nourse and A. McLarty found that many of the NE trending cross faults experienced this younger left lateral oblique extension during clockwise rotation.

In contrast to the orogenic theory, it could be argued that the initial onset of the Yellow Aster Intrusion and subsequent extension created the necessary pressure and temperature conditions and provided CO_2 rich hydrothermal fluids for listwanitic and other alterations within the NW trending faults. A proceeding period of transtension on these faults caused clockwise rotation culminating with the onset of the nearby left lateral Garlock Fault at 15 Ma. If enough residual heat from the intrusion remained between 19 Ma and 15 Ma, it could be possible to have the prevalent gold and carbonate remobilization and mineralization into the NE trending faults that was observed for this study. The 50 Ma mariposite age discussed above may actually represent partial argon loss from 70 Ma caused by fluids associated with the Yellow Aster intrusion. However, the timing of this alteration and mineralization requires a detailed geochronologic study that is beyond the means of this thesis.

CONCLUSIONS

My structural mapping and geochemical assessment of the gold prospects in the central and southwestern Rand Mountains has produced the following significant conclusions:

1) Gold mineralization is not limited to the boundaries of the Randsburg Mining District. Anomalous gold values as high as 2.15 ppm Au were found as far as 12 kilometers southwest of the Yellow Aster Mine within the Desert Tortoise Wilderness Area. The highest gold value was 10.013 ppm Au from a small prospect at the Darn Peak cluster location, 9.5 km southwest of the Yellow Aster Mine. This was a significant find in that it shows economic grades of gold persist at higher structural levels of the Rand Mountains outside of the mining district's borders. Additionally, gold targets were found to be prevalent on both the southern and northern fronts of the mountains.
2) The lithologies that were both targeted by previous prospectors and were the host of the gold bearing structures were found to be exclusively the Plate 1 Rand Schist and the Plate 3 Atolia Granodiorite. It was abundantly clear that prospectors only targeted faults within the schist and granodiorite. Very few prospects were found to directly target Plate 2 or Plate 4.
3) The gold is clearly fault controlled as most anomalous gold samples were obtained from fault gouge and altered wall rock directly adjacent to faults. The significant finding here is that while the anomalous samples were found in faults of varying azimuths, they were far more often from steeply dipping NE striking faults that record significant components of extension. This contradicts the

dominant structural control of NW striking extensional faults observed by other researchers within the gold mines at the Randsburg Mining district. Why the structural control in the central and southwestern Rand Mountains differs from that of the Randsburg Mining District is unclear. Two possibilities were hypothesized in this study. The first hypothesis states that the gold containing NE striking faults were originally trending to the NW when they were mineralized 19 Ma. Approximately 15 Ma, left lateral motion along the Garlock Fault to the north rotated the mineralized faults to their current NE strike. The second hypothesis states that the auriferous NE trending faults belong to a younger 11-15 Ma “Kelly Episode” event that was responsible for producing silver mineralized NE striking left lateral normal faults observed and mapped by Morehouse (1988) in the Randsburg Mining District.

4) Low grade gold is associated with high angle extensional faults that are cutting the lower Rand Thrust where plates 1 and 2 had been previously folded into a synform structure. The extensional faults have variable orientation, NE striking or NW striking. The intersection of the younger fault with the thrust in addition to the folding could be creating enough brecciation to accommodate mineralizing fluids and ore deposition; the thrust may also be acting as a permeability barrier resulting in pooling of ore bearing fluids. The upper Rand Thrust between plates 3 and 4 was barren where sampled and contained only one set of trenches and a single underground prospect within the study site. It likely is not a strong future exploration target.

5) Propylitic (possibly earlier alteration unrelated to gold mineralization) and argillic alteration is prevalent in Plate 3 Atolia Granodiorite. This is exacerbated by the highly faulted and fractured nature of the granodiorite allowing hydrothermal fluids to penetrate into much of the surrounding rocks. However, gold is primarily concentrated in narrow shear zones within the argillic alteration where there is also a loss of potassium and iron and a dramatic increase of LOI and CaO due to late carbonatization and hydrolysis. Interestingly, no silicification and little to no sericitization occurred (this would have required low temperatures of ~ 300^{o} C). Carbonatization in schist hosted gold ores also had high LOI, CaO, and MgO. Plate 4 Granites experienced only minor alteration except near the mylonitic boundary between Plates 3 and 4. Here there was a substantial loss of SiO2 from the granites that was then mobilized into the mylonitic shear zone. This created an impermeable silicic barrier that prevented hydrothermal fluids from further altering the overlying granite.
6) The timing of gold deposition in the central and southwestern Rand Mountains is somewhat cryptic and based largely on unpublished K-Ar dates by Morehouse (1986). If the NE striking faults that control the mineralization are indeed rotated from their original NW trend, the gold was likely deposited at ~18 Ma, the same age as the gold in Randsburg Mining District. However, if the NE striking faults were generated during later movement along the Garlock Fault, the gold deposits are likely to be around 11 – 15 Ma, the same age as the silver bearing quartz veins of the mining district. This will require a detailed geochronologic study to determine.

7) Sample GSRM-57B (mariposite pod) was dated using the $^{40}Ar/^{39}Ar$ thermal history method. Its mean integrated total gas age was 71.64 ± 1.9 Ma which agrees well with previous phengite ages by Jacobson et al. 1990 that date the metamorphism of the Rand Schist to between 74-70 Ma. Therefore, the mariposite likely represents metasomatism of ultramafic components of the schist during subduction rather than the timing of gold mineralization. Discordance in the step heating process indicates that there was loss by diffusion of radiogenic argon sometime between 70 and 20 Ma. This may be indicative of a thermal pulse from the Yellow Aster Intrusion at 19.6 Ma. Alternatively, it could be interpreted to mean that the schist was buried at a sufficient depth (with high enough temperatures) to allow for ^{40}Ar diffusion until its exhumation in the early Miocene.
8) Arsenic and silver were found to be anomalous within gold bearing rocks and the surrounding alteration envelope. Therefore, these elements can be used to track down zones of gold mineralization. Antimony, an element commonly present in the gold and silver ores of the Randsburg Mining District as the mineral stibnite, occurs as small anomalies within gold ores of the southwestern Rand Mountains. It also occurs as large anomalies in the form of disseminated and vein type stibnite where accompanied by chromium and nickel anomalies in sporadic outcroppings immediately adjacent to large NE trending left lateral normal faults. These localities may represent outcropping alteration zones above more significant hydrothermal gold, silver, or stibnite mineralization. Further exploration of these features is needed.

RECOMMENDATIONS

Much work is required yet to fully understand the structural controls, timing, and styles of metal deposits in the central and southwestern Rand Mountains. Recommendations for future work are presented below:

- Suitable minerals for precisely dating the gold hosted in NE striking faults were difficult to identify and will require a more focused effort to find. There was surprisingly little to no sericite within the gold bearing rocks of Plate 3. Fuchsite is present in altered wall rocks of some schist hosted gold anomalies, but may have formed during original Late Cretaceous metamorphism of the schist as is suggested by the 70 Ma closure age of GSRM-57B. This chromian mica can be dated, but it isn't clear from field observations whether it is temporally related to the gold mineralization.
- Morehouse's sample sites should be revisited to search for micas that could be dated with modern Ar-Ar techniques. Particularly intriguing is his reporting of a 15Ma sericite from one of the mines of the Randsburg mining district. It is important to determine whether gold mineralization was associated with a discrete thermal event during intrusion of the 19.6 Ma Yellow Aster granodiorite, or if significant hydrothermal fluid circulation persisted into Middle Miocene time
- Much more sampling of the large NE striking cross faults with resistant quartz-carbonate-limonite breccia outcrops should be undertaken. If these were generated at the same time as the gold bearing NE trending faults identified in this study, it is possible that they may host significant quantities of gold or silver. Listwanitic rocks were observed and collected along several NE trending faults. Listwanite is

a quartz-carbonate-fuchsite bearing rock that resulted from metasomatism of ultramafics like serpentinite. These are intimately associated with large orogenic and mesothermal gold deposits across the world, such as the Motherlode District in California and are often considered to be the source of the gold. In the Rands, it is difficult to say whether these are just minor lenses or represent larger scale alterations that are providing the gold in stockwork quartz veins like sample GSRM-55. Further exploration of the listwanites could provide further insight into the style of gold deposit present within the deeper schists of the Rand Mountains.

- Detailed X-Ray diffraction (XRD) analysis of samples from the various alteration zones around mineralized structures is necessary to obtain a complete understanding of the hydrothermal fluids and alteration processes. It would help to confirm the mineralogy of these alteration zones. I could only speculate on this when analyzing major oxide XRF data. XRD is especially well-suited for identifying and distinguishing different clay minerals and confirming the presence of carbonate minerals like caliche and siderite.
- Lastly, a series of intrusive felsic dikes cutting Plate 3 and exposed in a shallow prospect directly south of the Darn Peak cluster of mines contained anomalous gold of .38 ppm. These were also NE striking like the structural control described in this study. Intrusive dikes were rare within my study area, and the few that were encountered, did not contain anomalous gold. Understanding why these dikes south of Darn Peak were mineralized, what their timing was, and how widespread they are could lead to a broader undiscovered gold deposit below the

alluvium along the southern front of the Rand Mountains. Potentially these may be related to the Yellow Aster intrusion.

REFERENCES

Austrheim, H., Corfu, F., Renggli, C.J., 2021, From peridotite to fuchsite bearing quartzite via carbonation and weathering: with implications for the Pb budget of continental crust: Contributions to Mineralogy and Petrology, v. 176, #. 94, pp. 14, doi: 10.1007/s00410-021-01851-z.

Barth, A.P., and Schneiderman, J.S., 1996, A comparison of structures in the Andean orogen of northern Chile and exhumed midcrustal structures in southern California, USA: An analogy in tectonic style: International Geology Review, v. 38 p. 1075 – 1085, doi: 10.1080/00206819709465383.

Best, M.G., and Christiansen, E.H., 1991, Limited extension during peak tertiary volcanism, Great Basin of Nevada and Utah: Journal of Geophysical Research, v. 96, p. 13,509-13,528, doi: 0148-0227/91/91JB-00244$05.00.

Buckman, S. and Ashley, P., 2010, Silica-carbonate (Listwanites) Related Gold Mineralization Associated with Epithermal Alteration of Serpentinite Bodies: New England Orogen, v. 715, pp. 94-105.

Chapman, A. D., Kidder, S., Saleeby, J. B., and Ducea, M. N. (2010), Role of extrusion of the Rand and Sierra de Salinas schists in Late Cretaceous extension and rotation of the southern Sierra Nevada and vicinity, Tectonics, 29, TC5006, doi:10.1029/2009TC002597.

Cutts, J.A., Dipple, G.M., Hart, C.J.R., Milidragovich, D., 2020, Assessment of the Carbon Mineralization Potential of British Columbia by Quantifying the Response of Physical Properties to the Alteration of Ultramafic Rocks: Geoscience BC Summary of Activities, v. 1, p.137-144.

Dilles, J. H., and John, D. A., 2021, Porphyry and Epithermal Mineral Deposits: Encyclopedia of Geology, v. 2, p. 847-866, doi: https://doi.org/10.1016/B978-0-08-102908-4.00005-9.

Grove, M., Nourse, J.A., Jacobson, C.E, Shulaker, Z., Barth, A.P., Dawson, J.P., Silver, L.T., Coleman, D.S., Miller, B.V., [In preparation], Foundered Elements of the Rand Fault System within a Miocene Hypabyssal Pluton, Western Mojave Desert, California, 60 p.

Groves, D.I., Goldfarb, R.J., Gebre-Mariam, M., Hagemann, S.G., and Robert, F., 1998, Orogenic Gold Deposits: A Proposed Classification in the Context of their Crustal Distribution and Relationship to other Gold Deposit Types: Ore Geology Reviews, v. 13, pp. 7-27, https://doi.org/10.1016/S0169-1368(97)00012-7.

Groves, D.I., Goldfarb, R.J., Robert, F., Hart, C.J., 2003, Gold Deposits in Metamorphic Belts: Overview of Current Understanding, Outstanding Problems, Future Research, and Exploration Significance: Economic Geology, v. 98, pp. 1-29, 0361-0128/01/3313/1-29.

Groves, D.I., Santosh, M., Deng, J., Wang, Q., Yang, L., Zhang, L., 2019, A Holistic Model for the Origin of Orogenic Gold Deposits and its Implications for Exploration: Mineralium Deposita, v. 55, pp. 275-292, https://doi.org/10.1007/s00126-019-00877-5.

Hagemann, S.G., Gebre-Mariam, M., and Groves, D.I., 1994, Surface Water Influx in Shallow Level Archean Lode-Gold Deposits in Western Australia: Geology, v. 22, p. 1067-1070.

Halls, C. and Zhao, R., 1995, Listvenite and related rocks: perspectives on terminology and mineralogy with reference to an occurrence at Cregganbaun, Co. Mayo, Republic of Ireland: Mineralium Deposita, v. 30, p. 303-313.

Harrison, T.M., Celerier, J., Aikman, A.B., Hermann, J., Heizler, M.T., 2009, Diffusion of 40Ar in Muscovite: Geochemica et Cosmochimica Acta, vol. 73, no. 4, pp. 1039-1051, 10.1016/j.gca.2008.09.038.

Hart, D, 1986, An Evaluation of Fluid Inclusion Techniques as Tools in Mineral Exploration as Applied at the Yellow Aster Gold Mine, California [M.S. Thesis]: Fairbanks, University of Alaska, 304 p.

Hedenquist, J.W., Arribas, A.R., and Gonzalez-Urien, E., 2000, Exploration for Epithermal Gold Deposits: SEG Reviews, v. 13, p. 245-277

Hulin C.D., 1925, Geology and ore deposits of the Randsburg quadrangle of California: California State Mining Bureau, Bulletin, v. 95.

Izaguirre, A., Iriondo, A., Kunk, M.J., McAleer, R.J., Atkinson, W.W., Martínez-Torres, L.M., 2017, Tectonic Framework for Late Cretaceous to Eocene Quartz-Gold Vein Mineralization from the Caborca Orogenic Gold Belt in Northwestern Mexico: *Economic Geology*, v. 112, p. 1509–1529, doi: 10.5382/econgeo.2017.4519 0361-0128/17/1509-21.

Jacobson, C.E., 1990, The $^{40}Ar/^{39}Ar$ geochronology of the Pelona Schist and related rocks, southern California: Journal of Geophysical Research, v. 95, p. 509-528.

Jacobson, C.E., Dawson, M.R., and Postlethwaite, C.E., 1988, Structure, metamorphism, and tectonic significance of the Pelona, Orocopia, and Rand Schists, southern California, in Ernst, W.G., ed., Metamorphism and crustal evolution of the western United States (Rubey Volume VII): Englewood Cliffs, New Jersey, Prentice Hall, p. 976-997.

Laurent, O., Martin, H., Moyen, J.F., Doucelance, R., 2014, The diversity and evolution of late-Archean granitoids: Evidence for the onset of “modern-style” plate tectonics between 3.0 and 2.5 Ga: Lithos, v. 205, p. 208-235, doi: http://dx.doi.org/10.1016/j.lithos.2014.06.012

Maniar, P.D. and Piccoli, P.M., 1989, Tectonic discrimination of granitoids: Geological Society of America Bulletin, v. 101, p. 635-643.

McLarty, A.H., 2014, Structural Reactivation and Overprinting of the Eastern Rand Thrust Complex, Mojave Desert, Southern California [M.S. Thesis]: Pomona, California State Polytechnic University, 110 p.

McQuarrie, Nadine and Wernicke, Brian P., 2005, An animated tectonic reconstruction of southwestern North America since 36 Ma.: Geosphere, v. 1 (3). pp. 147-172, doi:10.1130/GES00016.1.

Middlemost, E.A.K., 1994, Naming materials in the magma/igneous rock system: Earth-Science Reviews, v. 37, p. 215-224, doi:0012-8252(94)00052-2.

Morehouse, J.A., 1988, A Synopsis of the Geologic and Structural History of the Randsburg Mining District [M.S. Thesis]: The University of Arizona, 77 p.

Ourhzif, Z., Algouti, A., Algouti, A., Hadach, F., 2019, Lithological mapping using LANDSAT 8 OLI and ASTER multispectral data in Imini-Ounilla District High Atlas of Marrakech: The International Archives of the Photogrammetry, Remote Sensing and Spatial Information Sciences, v. 42, p. 1255-1262, doi: https://doi.org/10.5194/isprs-archives-XLII-2-W13-1255-2019.

Postlethwaite, C.E. and Jacobson, C.E., 1987, Early History and Reactivation of the Rand Thrust, Southern California: Journal of Structural Geology, v. 9, pp. 195-205, 0191-8141/87.

Sillitoe, R.H., and Hedenquist, J.W., 2003, Linkages between Volcanotectonic Settings, Ore-Fluid Compositions, and Epithermal Precious Metal Deposits: Society of Economic Geologists, v. 10, p. 315-343.

Troxel, B.W., and Morton, P.K., 1962. Mines and mineral resources of Kern County, California: Calif. Div. of Mines and Geol. County report No.l, p. 49-51

Walker D. J., Bartley, J. M., Glazner, A. F., 1990, Large-Magnitude Miocene Extension in the central Mojave Desert: Implications for Paleozoic to Tertiary Paleogeography and Tectonics: Journal of Geophysical Research, v. 95, p. 557-569.

APPENDIX A

Composite Geologic Map of Parts of the Rand Mountains Investigated for Study


Explanation
Map Symbols
strike/dip of foliation, w/mylonitic lineation
mylonitic foliation, w/lineation on Fault III
lithologic contact
high-angle fault, showing dip in black font; Up/Down motion determined from map relations or Ridel shears; rake of striations plotted as red font in quadrant of acute angle. Average orientation plotted where multiple measurements taken
low-angle normal fault w/striations
mine shaft or adit
GSRM73 assay sample
JN1827 thin section sample
RA 83 dated sample location of Jacobson et al., 1990
JN1827 dated sample location of Nourse (unpublished)
fault trace, dashed where approximately located, dotted where buried; strike-slip component shown with arrows
low-angle detachment fault
Rock Units
Qa Quaternary alluvium
Qls Quaternary landslide or colluvium
qmy Quartz-rich mylonite
Klgr Cretaceous leucocratic Fe-rich biotite alkali granite (97 Ma; 98 Ma)
Rand Fault III (Miocene detachment)
Kmgr Cretaceous biotite monzogranite dike (87 Ma)
Kagd Cretaceous Atolia Granodiorite (87 Ma); dioritic component = Kdi)
Rand Fault II (locally reactivated thrust)
dign Johannesburg Gneiss- dioritic gneiss component (97 Ma; 103 Ma)
grgn Johannesburg Gneiss- granitic gneiss component (98 Ma; 104 Ma)
m Johannesburg Gneiss- marble-calcsilicate component (Paleozoic(?))
Rand Fault I (basal thrust)
Krs Cretaceous Rand Schist-metagraywacke component: chl+/-bio--musc-qtz-ab; depositional age ~ 80 Ma; Jacobson et al., 2011)
Krmch Cretaceous Rand Schist-metachert component: gt+/-musc-qtz
Krms Cretaceous Rand Schist-mafic (metabasalt) component of Jacobson (1995): chl-act-ep-ab; hbld presnet near Rand thrust
Krbs Cretaceous Rand Schist-blueschist component of Jacobson (1995): chl-ep-glaucophane/crossite/act-ab
Plate 1
Geologic and Structural Map of the East-Central Rand Mountains
compiled from thesis mapping by Nourse, 1989; McLarty, 2014; Stewart, 2019-22; also unpublished mapping by Nourse, 2016-22
Topographic base map is the 1967 USGS 7.5 minute Johannesburg, California quadrangle. Most data located using GPS receiver with datum of NAD27.
N
500m
Contour Interval = 40 ft

Appendix B

Assay Data for All Samples

SP0128908
FINAL REPORT

Multi Element Package

AMERICAN ASSAY LABORATORIES
1500 GLENDALE AVE.
SPARKS, NV USA 89431-5902
Ph.(775) 356-0606
Fax.(775) 356-1413
EMAIL: info@aallabs.com

Geology Department Cal Poly Pomona

COPIES TO :	Jonathan Nourse	CLIENT REFERENCE No:	GSRM-1 to BRT Plate 4	RECEIVED :	21-Nov-2019
:		No. SAMPLES :	18	REPORTED :	16-Dec-2019
:		MAIN SAMPLE TYPE :	PULP		
:					

COMPANY DISCLAIMER :-
When small samples are submitted, AAL may process the sample at smaller then specified weights to retain some pulp for quality control reassay.
When Values exceed upper limits, AAL will run an Over Range analysis, to establish an accurate value. Additional cost will apply.
Due to USDA Soil Quarantine programs - all foreign and some domestic soil material must be decontaminated by drying @ 125c for 48 hours, which will result in loss of Mercury (Hg).

NEVADA LEGISLATIVE DISCLAIMER :-
The results of this assay were based solely upon the content of the sample submitted. Any decision to invest should be made only after the potential investment value of the claim or deposit has been determined based on the results of assays of multiple samples of geological materials collected by the prospective investor or by a qualified person selected by him and based on an evaluation of all engineering data which is available concerning any proposed project. Nevada State Law NRS 519.130.

ANALYSIS	Au	Au	Ag	Al	As	Ba	Be	Bi	Ca	Cd	Ce	Co	Cr	Cu	Fe	Ga	K	La	Mg	Mn	Mo	Na	Ni	P	Pb	S
METHOD	FA-PB30-ICP	AVAu30'	5AO35	5AO35	5AO35	5AO35	5AO35	5AO35	5AO35	5AO35	5AO35	5AO35	5AO35	5AO35	5AO35	5AO35	5AO35	5AO35	5AO35	5AO35	5AO35	5AO35	5AO35	5AO35	5AO35	5AO35
UNIT	ppm	ppm	ppm	ppm	ppm	ppm	ppm	ppm	ppm	ppm	ppm	ppm	ppm	ppm	ppm	ppm	ppm	ppm	ppm	ppm	ppm	ppm	ppm	ppm	ppm	ppm
LOWER LIMIT	0.003	0.103	0.5	100	2	5	0.1	5	100	0.5	1	1	1	1	100	10	100	10	100	5	1	100	1	10	3	100

ANALYSIS	Sb	Sc	Sr	Th	Ti	Tl	U	V	W	Y	Zn
METHOD	ICP-5AO35	5AO35	5AO35	5AO35	5AO35	5AO35	5AO35	5AO35	5AO35	5AO35	5AO35
UNIT	ppm	ppm	ppm	ppm	ppm	ppm	ppm	ppm	ppm	ppm	ppm
LOWER LIMIT	2	1	1	20	10	10	10	1	2	1	2

SIGNATORY ANALYSIS
Au
ICP

Cover Page
AAL-006

SP0128908
FINAL REPORT

AMERICAN ASSAY LABORATORIES
1500 GLENDALE AVE.
SPARKS, NV USA 89431-5902
Ph.(775) 356-0606
Fax.(775) 356-1413
EMAIL: AALLABS@NVBELL.NET

	Abbreviation	Definition
Preparation	DIP	Sample Destroyed in Preparation
	DIS	Sample Destroyed in Shipment
	ISS	Insufficient Sample Submitted
	SDI	Sample Diesel Impregnated
	SHI	Sample Hydraulic Impregnated
	SNR	Sample Not Received
Analysis	STD - ??	International Reference Material Standar
	STD - AAL##	AAL generated standard material
	BLANK	AAL Laboratory Silica Blank
	DTF	Data to Follow
	DL	Detection Limit of Method
	< or -	Less Than Lower Detection Limit of Metho
	>	Greater than Upper Limit of Method
	N/A	Not Analyzed
	NR	Not Reported
	(R) column	Laboratory repeat weigh, digestion, analysis from original pulp or reject respl
	D or -D after Sample II	Client submitted duplicate rig split sampl
	-R after Sample II	Repeat analysis from original pulp reweigh, digestion and analysi
	-X after Sample II	Repeat analysis from reject resplit, preparation, weigh, digestion and analys
	ppb	Parts per Billion 0.001 ppm = 1 pp
	ppm	Parts per Million 1 ppm = 1 mg/K
	OPT	Troy Ounces per Short Ton(2,000 lbs)(1 ppm= 0.02917 OPT
	Oz	Troy Ounce = 31.103 grams
	%	Percent 1%=10,000 pp
	g	Grams 1g=0.001 Kilogra
	mg	Milligrams 1mg=0.001gram
	Kg	Kilograms 1Kg=1000grams
	lbs	Pounds 1lb=0.454Kilogra
Method	FA-PB##	Fire Assay Lead Collection - ## sample weight in gram
	GRAV	Gravimetric (Weighed) finish
	SF	Screen Fire Assay reporting a plus, 2 minus fractions and a head Cal
	+ ###	Plus Fraction (Retained on top of Mesh) ###Screen Siz
	- ###	Minus Fraction (Passed through Mesh) ###Screen Siz
	CN	Cyanide Extraction
	ORE GRADE	2g sample made to 1000ml volumetric for results > upper limit of meth
	OX-H2SO4 or -HCl	Dilute acid leach for oxide fraction in copper or molybdenum analysi
	QLA	Dilute 10%H2SO4/0.5%Fe2(SO4)3 30C leach for acid soluble copper
	QLT	Dilute 15%H2SO4 30C leach for acid soluble copper
	SAP	Dilute 5%H2SO4/0.5%Fe2(SO4)3 85C leach for acid soluble & chalcocite coppe
	D#A	Digestion #=2,3 or 4 Acids 2A=HCl/HNO3 3A=HCl/HNO3/HClO4 4A=HCl/HNO3/HF/HClO
	HCl	Hydrochloric Acid(37%w/v) Boiling Point 109
	HF	Hydrofluoric Acid(48%w/v) Boiling Point 108C Extreme Health Hazar
	HClO4	Perchloric Acid(69%w/v) Boiling Point 203C Extreme Fire/Explosion Haza
	HNO3	Nitric Acid(69%w/v) Boiling Point 121
	H2SO4	Sulfuric Acid(98% w/v) Boiling Point 338
	ICP-xB or -xZ	ICP-AES and/or ICP-MS analysis using x=2, 3 or 4 acid digestion
	LiBO2-C	Lithium Metaborate fusion in Carbon crucibl
	Na2O2-C	Sodium Peroxide fusion in Carbon crucibl
	Na2O2-Zr	Sodium Peroxide fusion in Zirconium crucibl
Technique	AAS	Atomic Absorption Spectroscopy
	ICP-AES	Inductively Coupled Plasma Atomic Emission Spectroscop
	ICP-MS	Inductively Coupled Plasma Mass Spectroscop
	RG	Research Grade (Low detection limit ICP-AES
	UT	Ultra Trace (ICP-AES+ICP-MS analyses
	XRF-ED or -WD	X-Ray Flourescence (-ED = Energy Dispersive) (-WD = Wavelength Dispersiv
	XRD	X-Ray Diffraction
	ELTRA-I	Carbon & Sulfur infrared detection analyzer inductive heatin
	ELTRA-R	Carbon, Hydrogen & Sulfur infrared detection analyzer resistance furnac
	LECO-I	Nitrogen & Oxygen infra red detection analyzer inductive heatin
	MW	Microwave Digestion (-PT is at 1500psig and 300C
	SG-WD or -HP	Specific Gravity-WD=Water Displacement -HP=Helium Pycnometer 1g/cm3=62.4lbs/f

Definitions Page
AAL-007

SP0128908

FINAL REPORT

CLIENT : Geology Department Cal Poly Pomona
PROJECT : Rand Mountains
REFERENCE : GSRM-1 to ERT Plate 4
REPORTED : 16-Dec-2019

	Au	Au	Ag	Al	As	Ba	Be	Bi	Ca	Cd	Ce	Co	Cr	Cu
	FA-PB30-ICP	GRAVAu30	ICP-5AO35	ICP-5AO35	ICP-5AO35	ICP-5AO35	ICP-5AO35	ICP-5AO35	ICP-5AO35	ICP-5AO35	ICP-5AO35	ICP-5AO35	ICP-5AO35	ICP-5AO35
	0.003	0.103	0.5	100	2	5	0.1	5	100	0.5	1	1	1	1
SAMPLES	ppm	ppm	ppm	ppm	ppm	ppm	ppm	ppm	ppm	ppm	ppm	ppm	ppm	ppm
GSRM - 1	-0.003		-0.5	5835	-2	152	-0.1	-5	255	-0.5	4	2	282	25
GSRM - 2	-0.003		-0.5	75043	10	1530	1.3	-5	11678	-0.5	58	8	225	35
GSRM - 2-X	-0.003		-0.5	76513	10	1565	1.3	-5	11789	-0.5	59	8	229	36
GSRM - 3	0.003		-0.5	68724	29	1249	1.1	-5	13807	-0.5	62	10	194	32
GSRM - 4	0.005		-0.5	89330	8	1438	1.7	-5	28130	-0.5	97	12	17	20
GSRM - 5	-0.003		-0.5	78544	-2	553	1.6	-5	48231	-0.5	71	15	30	5
GSRM - 6	0.161		1.4	69645	81	1226	1.1	-5	30607	-0.5	27	10	78	297
STD - OREAS 905			0.6	77586	32	2686	2.6	6	6231	-0.5	98	15	20	1588
STD - OxA131	0.069													
GSRM - 7	0.009		-0.5	80763	36	651	1.2	-5	72597	2.6	48	19	35	17
GSRM - 8	0.003		-0.5	66427	5	714	0.9	-5	70109	-0.5	21	12	144	18
GSRM - 9	0.014		-0.5	82633	6	1482	1.0	-5	29553	-0.5	48	5	126	11
GSRM - 10	0.004		-0.5	41547	34	548	1.1	-5	56143	-0.5	22	7	41	17
GSRM - 11	0.006		0.6	57892	33	708	0.7	-5	12177	-0.5	33	5	320	37
GSRM - 12	0.004		-0.5	60866	17	563	1.0	-5	13153	-0.5	49	7	204	29
GSRM - 12-X	0.003		-0.5	61398	17	560	1.0	-5	13180	-0.5	52	7	205	30
BLANK	-0.003		-0.5	1600	-2	-5	-0.1	-5	-100	-0.5	10	-1	2	1
GSRM - 13	0.004		-0.5	65984	41	744	1.0	-5	12369	-0.5	59	8	199	34
JN 1906	-0.003		-0.5	69182	19	1871	0.8	-5	6983	-0.5	83	3	28	9
JN 1826			-0.5	67196	31	65	0.7	-5	3129	-0.5	9	-1	34	15
JN 1905			-0.5	69105	-2	1925	0.8	-5	7944	-0.5	23	2	18	41
Atolia GD #101			-0.5	84431	-2	495	1.6	-5	34402	-0.5	76	15	59	6
ERT Plate 4			-0.5	67459	-2	1940	0.7	-5	5172	-0.5	7	2	93	31
ERT Plate 4-X			-0.5	66954	-2	1944	0.7	-5	5123	-0.5	7	2	92	32
STD - OREAS 602b			>100	55075	871	888	1.5	54	6671	4.7	56	7	37	4974

SP0128908

FINAL REPORT

CLIENT : Geology Depa
PROJECT : Rand Mountai
REFERENCE : GSRM-1 to EI
REPORTED : 16-Dec-2019

	Fe	Ga	K	La	Mg	Mn	Mo	Na	Ni	P	Pb	S	Sb	Sc
	ICP-5AO35	ICP-5AO35	ICP-5AO35	ICP-5AO35	ICP-5AO35	ICP-5AO35	ICP-5AO35	ICP-5AO35	ICP-5AO35	ICP-5AO35	ICP-5AO35	ICP-5AO35	ICP-5AO35	ICP-5AO35
	100	10	100	10	100	5	1	100	1	10	3	100	2	1
SAMPLES	ppm	ppm	ppm	ppm	ppm	ppm	ppm	ppm	ppm	ppm	ppm	ppm	ppm	ppm
GSRM - 1	14928	-10	3019	-10	262	2227	16	1121	57	35	-3	-100	-2	-1
GSRM - 2	26792	16	26638	34	2799	1827	13	25102	45	527	13	-100	-2	2
GSRM - 2-X	27425	16	27282	34	2820	1852	13	25600	45	532	12	-100	-2	2
GSRM - 3	29920	16	29177	37	3828	1731	15	18326	38	829	10	-100	3	3
GSRM - 4	28471	22	20272	55	5201	424	3	29298	4	1235	12	-100	3	7
GSRM - 5	34519	20	16146	34	7889	716	3	21090	9	1056	5	-100	2	7
GSRM - 6	29331	18	20249	15	3246	845	6	2953	15	569	3	735	4	3
STD - OREAS 905	42354	26	29635	46	2985	383	4	22686	10	284	31	708	2	5
STD - OxA131														
GSRM - 7	47235	25	20101	25	4582	756	4	8917	10	757	38	147	4	11
GSRM - 8	36149	12	17339	12	7907	1638	7	22626	30	509	7	-100	2	7
GSRM - 9	17379	14	31995	27	2732	1186	7	31049	26	391	8	-100	2	2
GSRM - 10	23323	-10	8493	12	13709	696	5	631	10	332	7	251	2	4
GSRM - 11	23308	13	31718	20	481	2536	76	17070	63	197	46	-100	3	1
GSRM - 12	23335	15	28402	23	1438	1700	43	23228	40	516	11	-100	2	2
GSRM - 12-X	23406	15	28092	25	1442	1717	43	22996	42	514	11	-100	3	2
BLANK	357	-10	667	-10	-100	-5	-1	114	-1	14	-3	-100	-2	-1
GSRM - 13	25714	16	34737	24	630	1831	47	19525	41	683	21	-100	5	3
JN 1906	11148	13	44955	50	1217	342	2	18174	6	345	13	-100	-2	2
JN 1826	5572	16	39459	-10	-100	306	14	23599	7	110	17	126	-2	-1
JN 1905	4955	13	47686	14	151	225	2	15970	4	125	20	211	-2	-1
Atolia GD #101	34210	21	19945	30	10852	982	4	25595	14	1011	9	-100	2	10
ERT Plate 4	11778	14	47719	-10	156	757	5	15618	19	52	18	-100	-2	-1
ERT Plate 4-X	11847	14	47904	-10	148	757	5	15153	19	50	17	-100	-2	-1
STD - OREAS 602b	25863	25	17967	27	780	188	8	13693	15	283	506	21849	107	3

SP0128908

FINAL REPORT

CLIENT : Geology Depa
PROJECT : Rand Mountai
REFERENCE : GSRM-1 to El
REPORTED : 16-Dec-2019

	Sr	Th	Ti	Tl	U	V	W	Y	Zn
	ICP-5A035	ICP-5A035	ICP-5A035	ICP-5A035	ICP-5A035	ICP-5A035	ICP-5A035	ICP-5A035	ICP-5A035
	1	20	10	10	10	1	2	1	2
SAMPLES	ppm	ppm	ppm	ppm	ppm	ppm	ppm	ppm	ppm
GSRM - 1	16	-20	126	-10	-10	6	27	-1	5
GSRM - 2	560	-20	2137	-10	-10	30	97	6	37
GSRM - 2-X	560	-20	2149	-10	-10	30	96	6	37
GSRM - 3	364	-20	3406	-10	-10	40	124	7	60
GSRM - 4	864	-20	5070	-10	-10	55	136	13	72
GSRM - 5	530	20	4862	-10	-10	70	4	19	102
GSRM - 6	126	-20	2789	-10	-10	38	9	6	60
STD - OREAS 905	168	-20	1255	-10	-10	10	2	15	142
STD - OxA131									
GSRM - 7	275	-20	4998	-10	-10	131	19	14	377
GSRM - 8	526	-20	3017	-10	-10	77	3	12	54
GSRM - 9	479	-20	1479	-10	-10	24	-2	5	31
GSRM - 10	217	-20	1874	-10	-10	45	12	6	62
GSRM - 11	275	-20	801	-10	-10	16	57	5	154
GSRM - 12	371	-20	2398	-10	-10	32	275	15	47
GSRM - 12-X	372	-20	2439	-10	-10	32	268	15	46
BLANK	3	-20	76	-10	-10	2	-2	-1	-2
GSRM - 13	357	-20	3075	-10	-10	39	276	15	104
JN 1906	223	-20	1242	-10	-10	8	4	5	22
JN 1826	87	-20	195	-10	-10	2	3	2	8
JN 1905	476	-20	179	-10	-10	7	2	1	6
Atolia GD #101	589	-20	5065	-10	-10	73	-2	18	98
ERT Plate 4	411	-20	206	-10	-10	14	2	2	8
ERT Plate 4-X	410	-20	204	-10	-10	14	-2	2	8
STD - OREAS 602b	241	-20	1486	-10	-10	15	11	8	771

AAL-008

SP0134506
FINAL REPORT

Multi Element Package

AMERICAN ASSAY LABORATORIES
1500 GLENDALE AVE.
SPARKS, NV USA 89431-5902
Ph.(775) 356-0606
Fax.(775) 356-1413
EMAIL: info@aallabs.com

Geology Department Cal Poly Pomona

COPIES TO	:	Jonathan Nourse janourse@cpp.edu	CLIENT REFERENCE No:	GSRM 24-62	RECEIVED	:	14-Dec-2020
	:		No. SAMPLES :	35	REPORTED	:	7-Jan-2021
	:		MAIN SAMPLE TYPE :	PULP	All Laboratory Analysis were preformed between the above Received and Reported dates		
	:						

COMPANY DISCLAIMER :-
When small samples are submitted, AAL may process the sample at smaller then specified weights to retain some pulp for quality control reassay.
When Values exceed upper limits, AAL will run an Over Range analysis, to establish an accurate value. Additional cost will apply.
Due to USDA Soil Quarantine programs - all foreign and some domestic soil material must be decontaminated by drying @ 125c for 48 hours, which will result in loss of Mercury (Hg).
NEVADA LEGISLATIVE DISCLAIMER :-
The results of this assay were based solely upon the content of the sample submitted. Any decision to invest should be made only after the potential investment value of the claim or deposit has been determined based on the results of assays of multiple samples of geological materials collected by the prospective investor or by a qualified person selected by him and based on an evaluation of all engineering data which is available concerning any proposed project. Nevada State Law NRS 519.130.

ANALYSIS	Au	Ag	Al	As	Ba	Be	Bi	Ca	Cd	Ce	Co	Cr	Cu	Fe	Ga	K	La	Mg	Mn	Mo	Na	Ni	P	Pb	S	Sb
METHOD	FA-PB30-ICP	-5A035	-5A035	-5A035	-5A035	-5A035	-5A035	-5A035	-5A035	-5A035	-5A035	-5A035	-5A035	-5A035	-5A035	-5A035	-5A035	-5A035	-5A035	-5A035	-5A035	-5A035	-5A035	-5A035	-5A035	-5A035
UNIT	ppm	ppm	ppm	ppm	ppm	ppm	ppm	ppm	ppm	ppm	ppm	ppm	ppm	ppm	ppm	ppm	ppm	ppm	ppm	ppm	ppm	ppm	ppm	ppm	ppm	ppm
LOWER LIMIT	0.003	0.5	100	2	5	0.1	5	100	0.5	1	1	1	1	100	10	100	10	100	5	1	100	1	10	3	100	2

ANALYSIS	Sc	Sr	Th	Ti	Tl	U	V	W	Y	Zn
METHOD	ICP-5A035	-5A035	-5A035	-5A035	-5A035	-5A035	-5A035	-5A035	-5A035	-5A035
UNIT	ppm	ppm	ppm	ppm	ppm	ppm	ppm	ppm	ppm	ppm
LOWER LIMIT	1	1	20	10	10	10	1	2	1	2

Digitally signed by Joshua R Zimmerman
DN: cn=Joshua R Zimmerman, o=American Assay Laboratories, ou, email=joshua.zimmerman@aallabs.com, c=US
Date: 2021.01.07 12:50:51 -08'00'

SIGNATORY ANALYSIS

Cover Page

SP0134506
FINAL REPORT

AMERICAN ASSAY LABORATORIES
1500 GLENDALE AVE.
SPARKS, NV USA 89431-5902
Ph.(775) 356-0606
Fax.(775) 356-1413
EMAIL: AALLABS@NVBELL.NET

	Abbreviation	Definition
Preparation	DIP	Sample Destroyed in Preparation
	DIS	Sample Destroyed in Shipment
	ISS	Insufficient Sample Submitted
	SDI	Sample Diesel Impregnated
	SHI	Sample Hydraulic Impregnated
	SNR	Sample Not Received
Analysis	STD - ??	International Reference Material Standard
	STD - AAL##	AAL generated standard material
	BLANK	AAL Laboratory Silica Blank
	DTF	Data to Follow
	DL	Detection Limit of Method
	< or -	Less Than Lower Detection Limit of Method
	>	Greater than Upper Limit of Method
	N/A	Not Analyzed
	NR	Not Reported
	(R) column	Laboratory repeat weigh, digestion, analysis from original pulp or reject resplit
	D or -D after Sample ID	Client submitted duplicate rig split sample
	-R after Sample ID	Repeat analysis from original pulp reweigh, digestion and analysis
	-X after Sample ID	Repeat analysis from reject resplit, preparation, weigh, digestion and analysis
	ppb	Parts per Billion 0.001 ppm = 1 ppb
	ppm	Parts per Million 1 ppm = 1 mg/Kg
	OPT	Troy Ounces per Short Ton(2,000 lbs)(1 ppm= 0.02917 OPT)
	Oz	Troy Ounce = 31.103 grams
	%	Percent 1%=10,000 ppm
	g	Grams 1g=0.001 kilogram
	mg	Milligrams 1mg=0.001grams
	Kg	Kilograms 1Kg=1000grams
	lbs	Pounds 1lb=0.454kilogram
Method	FA-PB##	Fire Assay Lead Collection - ## sample weight in grams
	GRAV	Gravimetric (Weighed) finish
	SF	Screen Fire Assay reporting a plus, 2 minus fractions and a head Calc
	+ ###	Plus Fraction (Retained on top of Mesh) ###Screen Size
	- ###	Minus Fraction (Passed through Mesh) ###Screen Size
	CN	Cyanide Extraction
	ORE GRADE	2g sample made to 1000ml volumetric for results > upper limit of method
	Ox-H2SO4 or -HCl	Dilute acid leach for oxide fraction in copper or molybdenum analysis
	QLA	Dilute 10%H2SO4/0.5%Fe2(SO4)3 30C leach for acid soluble copper
	QLT	Dilute 15%H2SO4 30C leach for acid soluble copper
	SAP	Dilute 5%H2SO4/0.5%Fe2(SO4)3 85C leach for acid soluble & chalcocite copper
	D#A	Digestion #-2,3 or 4 Acids 2A-HCl/HNO3 3A-HCl/HNO3/HClO4 4A-HCl/HNO3/HF/HClO4
	HCl	Hydrochloric Acid(37%w/v) Boiling Point 109C
	HF	Hydrofluoric Acid(48%w/v) Boiling Point 108C Extreme Health Hazard
	HClO4	Perchloric Acid(69%w/v) Boiling Point 203C Extreme Fire/Explosion Hazard
	HNO3	Nitric Acid(69%w/v) Boiling Point 121C
	H2SO4	Sulfuric Acid(98% w/v) Boiling Point 338C
	ICP-xB or -xZ	ICP-AES and/or ICP-MS analysis using x=2, 3 or 4 acid digestion
	LiBO2-C	Lithium Metaborate fusion in Carbon crucible
	Na2O2-C	Sodium Peroxide fusion in Carbon crucible
	Na2O2-Zr	Sodium Peroxide fusion in Zirconium crucible
Technique	AAS	Atomic Absorption Spectroscopy
	ICP-AES	Inductively Coupled Plasma Atomic Emission Spectroscopy
	ICP-MS	Inductively Coupled Plasma Mass Spectroscopy
	RG	Research Grade (Low detection limit ICP-AES)
	UT	Ultra Trace (ICP-AES+ICP-MS analyses)
	XRF-ED or -WD	X-Ray Flourescence (-ED = Energy Dispersive) (-WD = Wavelength Dispersive)
	XRD	X-Ray Diffraction
	ELTRA-I	Carbon & Sulfur infrared detection analyzer inductive heating
	ELTRA-R	Carbon, Hydrogen & Sulfur infrared detection analyzer resistance furnace
	LECO-I	Nitrogen & Oxygen infra red detection analyzer inductive heating
	MW	Microwave Digestion (-PT is at 1500psig and 300C)
	SG-WD or -HP	Specific Gravity-WD-Water Displacement -HP-Helium Pycnometer 1g/cm3=62.41lbs/ft3

Definitions Page
AAL-007

SP0134506

FINAL REPORT

CLIENT : Geology Department Cal Poly Pomona
PROJECT : Rand Mountains
REFERENCE : GSRM 24-62
REPORTED : 7-Jan-2021

	Au	Ag	Al	As	Ba	Be	Bi	Ca	Cd	Ce	Co	Cr	Cu	Fe	Ga	K
	FA-PB30-IC	ICP-5AO3	ICP-5AO3	ICP-5AO3	ICP-5AO3	ICP-5AO3	ICP-5AO3	ICP-5AO3	ICP-5AO3	ICP-5AO3	ICP-5AO3	ICP-5AO3	ICP-5AO3	ICP-5AO3	ICP-5AO3	ICP-5AO3
	0.003	0.5	100	2	5	0.1	5	100	0.5	1	1	1	1	100	10	100
SAMPLES	ppm	ppm	ppm	ppm	ppm	ppm	ppm	ppm	ppm	ppm	ppm	ppm	ppm	ppm	ppm	ppm
GSRM-24	0.117	1.1	13715	50	174	0.8	<5	491	<0.5	9	2	3	13	7089	<10	4425
GSRM-25	0.033	<0.5	71191	24	1628	1.2	<5	39692	<0.5	67	9	3	5	24024	15	26382
GSRM-26	0.018	<0.5	66870	18	344	0.9	<5	85370	<0.5	67	10	5	<1	25362	16	18799
GSRM-27	0.030	<0.5	74291	18	498	1.3	<5	42980	<0.5	54	10	5	1	26521	18	20370
GSRM-28	0.026	<0.5	59132	24	387	1.6	<5	115148	<0.5	63	11	5	<1	33867	14	15097
GSRM-29	0.004	<0.5	74530	3	634	1.6	<5	55108	<0.5	63	12	6	2	30627	19	12720
GSRM-30	0.012	<0.5	21104	9	1745	1.4	<5	282528	<0.5	48	13	2	5	57660	<10	3946
GSRM-31	0.248	0.5	62996	281	647	1.5	<5	76759	<0.5	53	12	4	3	29949	15	20339
GSRM-32	0.121	<0.5	65698	93	474	1.3	<5	51021	<0.5	52	12	6	7	27160	16	22032
GSRM-33	10.013	3.2	57206	41	322	1.2	<5	87548	<0.5	63	8	3	8	20477	14	13513
GSRM-35	0.092	<0.5	38343	1682	279	0.5	<5	146606	<0.5	25	9	42	4	18350	<10	7259
GSRM-36	0.106	<0.5	23378	2420	229	0.4	<5	110733	<0.5	15	6	26	4	18282	<10	6728
GSRM-37	0.077	<0.5	26152	69	123	0.2	<5	19991	<0.5	11	10	34	35	24489	<10	2359
GSRM-38	0.015	<0.5	28496	5	766	0.9	<5	166553	<0.5	21	9	2	<1	34543	<10	9172
GSRM-39	0.006	<0.5	22169	4	804	1.0	<5	147894	<0.5	24	7	17	5	30737	<10	3286
GSRM-40	0.003	<0.5	29558	5	305	1.2	<5	155524	<0.5	23	11	31	17	33866	<10	4528
GSRM-41	0.010	<0.5	25401	12	820	0.3	<5	225451	<0.5	15	7	6	7	56852	<10	2178
GSRM-42	1.030	<0.5	23958	1253	192	0.6	<5	61650	<0.5	14	13	39	6	23872	<10	8271
GSRM-43	0.007	<0.5	74278	16	736	2.5	<5	82533	<0.5	42	20	36	50	49947	10	5636
GSRM-44	0.206	<0.5	36333	54	39	<0.1	<5	5024	<0.5	14	35	87	67	50425	<10	472
GSRM-45	0.453	<0.5	38321	1408	81	0.3	<5	10404	<0.5	12	25	105	59	48312	<10	5846
GSRM-46	0.003	<0.5	2264	25	63	0.1	<5	75629	<0.5	5	<1	<1	1	5674	<10	530
GSRM-47	<0.003	<0.5	80851	12	1477	1.9	<5	23285	<0.5	68	11	3	5	27607	20	22630
GSRM-48	0.007	<0.5	19653	69	106	0.7	<5	159604	<0.5	6	39	1262	33	34692	<10	2292
GSRM-50	0.009	<0.5	46029	53	1617	1.2	<5	29967	<0.5	31	2	2	2	7917	<10	29856
GSRM-51	<0.003	<0.5	11858	7	197	0.7	<5	218980	<0.5	13	6	19	12	35553	<10	2541
GSRM-52	0.003	<0.5	75956	9	768	1.3	<5	34584	<0.5	67	9	3	<1	26551	17	15988
GSRM-55	3.680	0.5	49943	312	620	0.5	<5	35115	<0.5	23	6	67	11	22258	<10	5455
GSRM-56	0.038	<0.5	36130	282	257	0.4	<5	7960	<0.5	18	4	19	6	12520	<10	3686
GSRM-57	0.017	<0.5	10795	121	29	0.4	<5	81379	<0.5	1	45	1427	5	33018	<10	1331
GSRM-58	0.016	<0.5	7743	188	209	0.2	<5	56768	<0.5	6	4	6	<1	14289	<10	2832
GSRM-59	0.040	<0.5	28407	480	2051	0.3	<5	257406	<0.5	20	6	21	14	17570	<10	2260
GSRM-60	0.003	<0.5	13335	18	1669	0.3	<5	37060	<0.5	11	2	13	2	9518	<10	2617
GSRM-61	0.005	<0.5	16640	25	25	<0.1	<5	198084	<0.5	6	12	134	25	38497	<10	1492
GSRM-62	0.123	<0.5	17456	58	38	<0.1	<5	164835	<0.5	4	19	184	34	62034	<10	575

AAL-009

SP0134506

FINAL REPORT

CLIENT : Geology Department
PROJECT : Rand Mountains
REFERENCE : GSRM 24-62
REPORTED : 7-Jan-2021

	La	Mg	Mn	Mo	Na	Ni	P	Pb	S	Sb	Sc	Sr	Th	Ti	Tl	U
	ICP-5AO3	ICP-5AO3	ICP-5AO3	ICP-5AO3	ICP-5AO3	ICP-5AO3	ICP-5AO3	ICP-5AO3	ICP-5AO3	ICP-5AO3	ICP-5AO3	ICP-5AO3	ICP-5AO3	ICP-5AO3	ICP-5AO3	ICP-5AO3
	10	100	5	1	100	1	10	3	100	2	1	1	20	10	10	10
SAMPLES	ppm	ppm	ppm	ppm	ppm	ppm	ppm	ppm	ppm	ppm	ppm	ppm	ppm	ppm	ppm	ppm
GSRM-24	<10	193	12	<1	311	1	64	14	5982	3778	<1	34	<20	353	<10	<10
GSRM-25	38	3723	370	1	11605	2	564	9	112	6	3	338	<20	3071	<10	<10
GSRM-26	35	2318	385	<1	17719	2	798	5	<100	7	6	156	<20	3447	<10	<10
GSRM-27	23	3457	493	1	22627	2	834	6	417	7	6	278	<20	3792	<10	<10
GSRM-28	27	4431	1106	2	19450	3	689	7	172	6	7	328	<20	3449	<10	<10
GSRM-29	27	7133	494	2	17948	3	882	8	<100	6	7	496	<20	4408	<10	<10
GSRM-30	29	3101	1884	5	6713	4	262	19	718	3	8	554	<20	1009	<10	<10
GSRM-31	25	2837	506	2	9278	3	724	12	220	14	5	200	<20	3865	<10	<10
GSRM-32	24	2841	484	2	6777	2	833	14	496	10	5	103	<20	4128	<10	<10
GSRM-33	34	2110	566	1	19073	2	715	14	<100	12	3	431	<20	2966	<10	<10
GSRM-35	14	1947	815	<1	4124	37	264	8	193	6	6	114	<20	1039	<10	<10
GSRM-36	<10	1865	390	<1	6793	36	656	6	<100	14	4	107	<20	644	<10	<10
GSRM-37	<10	11085	427	<1	208	27	212	7	312	4	7	180	<20	2160	<10	<10
GSRM-38	13	46426	823	<1	5849	12	231	16	211	4	2	1065	<20	921	<10	<10
GSRM-39	13	33306	791	<1	522	17	495	12	301	8	4	614	<20	1307	<10	<10
GSRM-40	13	35799	744	<1	688	31	416	11	181	5	5	741	<20	1891	<10	<10
GSRM-41	11	1990	1737	5	134	25	125	20	356	12	3	152	<20	256	<10	<10
GSRM-42	<10	1361	653	1	751	28	625	8	459	32	7	90	<20	1741	<10	<10
GSRM-43	23	15390	806	<1	32501	24	633	7	<100	35	11	745	<20	5798	<10	<10
GSRM-44	<10	3113	512	<1	316	48	530	4	4870	61	13	20	<20	6002	<10	<10
GSRM-45	<10	2945	695	2	699	55	349	5	153	53	17	85	<20	3550	<10	<10
GSRM-46	<10	441	510	<1	<100	<1	22	7	<100	3	<1	205	<20	19	<10	<10
GSRM-47	28	8256	406	<1	27830	2	890	11	<100	9	6	757	<20	4250	<10	<10
GSRM-48	<10	22305	1129	2	1618	813	61	13	<100	4	8	91	<20	421	<10	<10
GSRM-50	21	2020	105	2	1391	2	54	11	578	11	<1	208	<20	464	<10	<10
GSRM-51	<10	62550	1222	<1	265	34	480	11	<100	4	5	938	<20	704	<10	<10
GSRM-52	32	2334	381	<1	12782	2	878	7	107	8	4	288	<20	3898	<10	<10
GSRM-55	13	17255	327	<1	23116	59	394	8	149	4	7	744	<20	1378	<10	<10
GSRM-56	10	3112	130	<1	16211	41	302	22	<100	4	3	325	<20	678	<10	<10
GSRM-57	<10	85183	1057	<1	178	1020	24	11	626	26	<1	698	<20	61	<10	<10
GSRM-58	<10	685	809	3	138	22	83	5	<100	11	1	29	<20	181	<10	<10
GSRM-59	12	6884	660	3	13074	23	356	4	656	7	5	550	<20	986	<10	<10
GSRM-60	<10	762	154	2	211	7	97	8	508	4	2	81	<20	529	<10	<10
GSRM-61	<10	90154	1049	<1	170	69	161	4	158	37	7	764	<20	2428	<10	<10
GSRM-62	<10	66985	1440	<1	187	122	364	5	395	87	11	456	<20	2157	<10	<10

AAL-009

SP0134506

FINAL REPORT

CLIENT : Geology Department
PROJECT : Rand Mountains
REFERENCE : GSRM 24-62
REPORTED : 7-Jan-2021

	V	W	Y	Zn
	ICP-5AO35	ICP-5AO35	ICP-5AO35	ICP-5AO35
	1	2	1	2
SAMPLES	ppm	ppm	ppm	ppm
GSRM-24	4	4	1	8
GSRM-25	48	6	11	63
GSRM-26	73	16	11	70
GSRM-27	93	6	13	78
GSRM-28	74	5	24	76
GSRM-29	70	3	15	81
GSRM-30	56	8	47	165
GSRM-31	65	12	11	81
GSRM-32	68	10	10	84
GSRM-33	53	5	14	52
GSRM-35	38	14	15	35
GSRM-36	31	29	7	37
GSRM-37	76	452	5	60
GSRM-38	34	9	5	111
GSRM-39	57	11	10	84
GSRM-40	54	14	10	91
GSRM-41	20	24	20	72
GSRM-42	60	204	8	30
GSRM-43	88	8	17	110
GSRM-44	138	52	8	75
GSRM-45	150	24	8	85
GSRM-46	5	117	8	19
GSRM-47	73	20	15	72
GSRM-48	64	7	6	61
GSRM-50	7	12	1	35
GSRM-51	74	4	17	65
GSRM-52	51	16	21	85
GSRM-55	58	21	6	23
GSRM-56	34	19	3	19
GSRM-57	29	<2	1	54
GSRM-58	8	36	10	29
GSRM-59	27	7	12	19
GSRM-60	17	3	7	18
GSRM-61	70	12	5	13
GSRM-62	97	8	8	16

AAL.006

SP0135587
FINAL REPORT

Multi Element Package

AMERICAN ASSAY LABORATORIES
1500 GLENDALE AVE.
SPARKS, NV USA 89431-5902
Ph.(775) 356-0606
Fax.(775) 356-1413
EMAIL: info@aallabs.com

Geology Department Cal Poly Pomona

COPIES TO :	Jonathan Nourse janourse@cpp.edu	CLIENT REFERENCE No:	GSRM-63 to BR-RCM-2	RECEIVED :	25-Mar-2021
:		No. SAMPLES :	23	REPORTED :	16-Apr-2021
:		MAIN SAMPLE TYPE :	PULP	All Laboratory Analysis were preformed between the above Received and Reported dates	
:					

COMPANY DISCLAIMER :-
When small samples are submitted, AAL may process the sample at smaller then specified weights to retain some pulp for quality control reassay.
When Values exceed upper limits, AAL will run an Over Range analysis, to establish an accurate value. Additional cost will apply.
Due to USDA Soil Quarantine programs - all foreign and some domestic soil material must be decontaminated by drying @ 125c for 48 hours, which will result in loss of Mercury (Hg).
NEVADA LEGISLATIVE DISCLAIMER :-
The results of this assay were based solely upon the content of the sample submitted. Any decision to invest should be made only after the potential investment value of the claim or deposit has been determined based on the results of assays of multiple samples of geological materials collected by the prospective investor or by a qualified person selected by him and based on an evaluation of all engineering data which is available concerning any proposed project. Nevada State Law NRS 519.130.

ANALYSIS	Au	Ag	Al	As	Ba	Be	Bi	Ca	Cd	Ce	Co	Cr	Cu	Fe	Ga	K	La	Mg	Mn	Mo	Na	Ni	P	Pb	S	Sb
METHOD	FA-PB30-ICP	-5AO35	-5AO35	-5AO35	-5AO35	-5AO35	-5AO35	-5AO35	-5AO35	-5AO35	-5AO35	-5AO35	-5AO35	-5AO35	-5AO35	-5AO35	-5AO35	-5AO35	-5AO35	-5AO35	-5AO35	-5AO35	-5AO35	-5AO35	-5AO35	-5AO35
UNIT	ppm	ppm	ppm	ppm	ppm	ppm	ppm	ppm	ppm	ppm	ppm	ppm	ppm	ppm	ppm	ppm	ppm	ppm	ppm	ppm	ppm	ppm	ppm	ppm	ppm	ppm
LOWER LIMIT	0.003	0.5	100	2	5	0.1	5	100	0.5	1	1	1	1	100	10	100	10	100	5	1	100	1	10	3	100	2

ANALYSIS	Sc	Sr	Th	Ti	Tl	U	V	W	Y	Zn	Ag
METHOD	ICP-5AO35	-5AO35	-5AO35	-5AO35	-5AO35	-5AO35	-5AO35	-5AO35	-5AO35	-5AO35	0-GRAV
UNIT	ppm	ppm	ppm	ppm	ppm	ppm	ppm	ppm	ppm	ppm	ppm
LOWER LIMIT	1	1	20	10	10	10	1	2	1	2	10

Digitally signed by Joshua R Zimmerman
DN: cn=Joshua R Zimmerman, o=American Assay Laboratories, ou, email=joshua.zimmerman@aallabs.com, c=US
Date: 2021.04.16 10:22:50 -07'00'

SIGNATORY ANALYSIS

SP0135587
FINAL REPORT

AMERICAN ASSAY LABORATORIES
1500 GLENDALE AVE.
Fax.(775) 356-1413
EMAIL: AALLABS@NVBELL.NET

	Abbreviation	Definition
Preparation	DIP	Sample Destroyed in Preparation
	DIS	Sample Destroyed in Shipment
	ISS	Insufficient Sample Submitted
	SDI	Sample Diesel Impregnated
	SHI	Sample Hydraulic Impregnated
	SNR	Sample Not Received
Analysis	STD - ??	International Reference Material Standard
	STD - AAL##	AAL generated standard material
	BLANK	AAL Laboratory Silica Blank
	DTF	Data to Follow
	DL	Detection Limit of Method
	< or -	Less Than Lower Detection Limit of Method
	>	Greater than Upper Limit of Method
	N/A	Not Analyzed
	NR	Not Reported
	(R) column	Laboratory repeat weigh, digestion, analysis from original pulp or reject resplit
	D or -D after Sample ID	Client submitted duplicate rig split sample
	-R after Sample ID	Repeat analysis from original pulp reweigh, digestion and analysis
	-X after Sample ID	Repeat analysis from reject resplit, preparation, weigh, digestion and analysis
	ppb	Parts per Billion 0.001 ppm = 1 ppb
	ppm	Parts per Million 1 ppm = 1 mg/Kg
	OPT	Troy Ounces per Short Ton(2,000 lbs)(1 ppm= 0.02917 OPT)
	Oz	Troy Ounce = 31.103 grams
	%	Percent 1%=10,000 ppm
	g	Grams 1g=0.001 kilogram
	mg	Milligrams 1mg=0.001grams
	Kg	Kilograms 1Kg=1000grams
	lbs	Pounds 1lb=0.454kilogram
Method	FA-PB##	Fire Assay Lead Collection - ## sample weight in grams
	GRAV	Gravimetric (Weighed) finish
	SF	Screen Fire Assay reporting a plus, 2 minus fractions and a head Calc
	+ ###	Plus Fraction (Retained on top of Mesh) ###Screen Size
	- ###	Minus Fraction (Passed through Mesh) ###Screen Size
	CN	Cyanide Extraction
	ORE GRADE	2g sample made to 1000ml volumetric for results > upper limit of method
	Ox-H2SO4 or -HCl	Dilute acid leach for oxide fraction in copper or molybdenum analysis
	QLA	Dilute 10%H2SO4/0.5%Fe2(SO4)3 30C leach for acid soluble copper
	QLT	Dilute 15%H2SO4 30C leach for acid soluble copper
	SAP	Dilute 5%H2SO4/0.5%Fe2(SO4)3 85C leach for acid soluble & chalcocite copper
	D#A	Digestion #=2,3 or 4 Acids 2A-HCl/HNO3 3A-HCl/HNO3/HClO4 4A-HCl/HNO3/HF/HClO4
	HCl	Hydrochloric Acid(37%w/v) Boiling Point 109C
	HF	Hydrofluoric Acid(48%w/v) Boiling Point 108C Extreme Health Hazard
	HClO4	Perchloric Acid(69%w/v) Boiling Point 203C Extreme Fire/Explosion Hazard
	HNO3	Nitric Acid(69%w/v) Boiling Point 121C
	H2SO4	Sulfuric Acid(98% w/v) Boiling Point 338C
	ICP-xB or -xZ	ICP-AES and/or ICP-MS analysis using x=2, 3 or 4 acid digestion
	LiBO2-C	Lithium Metaborate fusion in Carbon crucible
	Na2O2-C	Sodium Peroxide fusion in Carbon crucible
	Na2O2-Zr	Sodium Peroxide fusion in Zirconium crucible
Technique	AAS	Atomic Absorption Spectroscopy
	ICP-AES	Inductively Coupled Plasma Atomic Emission Spectroscopy
	ICP-MS	Inductively Coupled Plasma Mass Spectroscopy
	RG	Research Grade (Low detection limit ICP-AES)
	UT	Ultra Trace (ICP-AES+ICP-MS analyses)
	XRF-ED or -WD	X-Ray Flourescence (-ED = Energy Dispersive) (-WD = Wavelength Dispersive)
	XRD	X-Ray Diffraction
	ELTRA-I	Carbon & Sulfur infrared detection analyzer inductive heating
	ELTRA-R	Carbon, Hydrogen & Sulfur infrared detection analyzer resistance furnace
	LECO-I	Nitrogen & Oxygen infra red detection analyzer inductive heating
	MW	Microwave Digestion (-PT is at 1500psig and 300C)
	SG-WD or -HP	Specific Gravity-WD=Water Displacement -HP=Helium Pycnometer 1g/cm3=62.4lbs/ft3

Definitions Page
AAL-007

SP0135587

FINAL REPORT

CLIENT : Geology Department Cal Poly Pomona
PROJECT : Rand Mountains
REFERENCE : GSRM-63 to BR-RCM-2
REPORTED : 16-Apr-2021

	Au	Ag	Al	As	Ba	Be	Bi	Ca	Cd	Ce	Co	Cr	Cu	Fe	Ga	K
	FA-PB30-IC	ICP-5AO3	ICP-5AO3	ICP-5AO3	ICP-5AO3	ICP-5AO3	ICP-5AO3	ICP-5AO3	ICP-5AO3	ICP-5AO3	ICP-5AO3	ICP-5AO3	ICP-5AO3	ICP-5AO3	ICP-5AO3	ICP-5AO3
	0.003	0.5	100	2	5	0.1	5	100	0.5	1	1	1	1	100	10	100
SAMPLES	ppm	ppm	ppm	ppm	ppm	ppm	ppm	ppm	ppm	ppm	ppm	ppm	ppm	ppm	ppm	ppm
GSRM-63	2.860	0.8	36572	87	474	0.9	<5	40711	<0.5	28	6	3	15	15248	12	12542
GSRM-64	0.009	<0.5	54367	5	>5000	1.1	<5	150005	<0.5	46	14	5	5	42260	14	16891
GSRM-65	0.313	0.8	38762	36	2096	0.5	<5	128015	<0.5	30	6	3	4	35023	<10	12332
GSRM-66	0.004	<0.5	18137	4	248	0.9	<5	285954	<0.5	22	7	2	3	28686	<10	6779
GSRM-67	0.018	<0.5	73424	63	577	1.4	<5	43703	<0.5	54	14	8	37	56810	20	16942
GSRM-68 A	0.006	<0.5	12043	13	160	0.4	<5	14115	<0.5	9	2	1	2	7553	<10	4080
GSRM-68 B	0.275	0.7	25119	194	1292	0.7	<5	66210	<0.5	23	5	2	3	32714	<10	9556
GSRM-69	0.076	<0.5	32001	33	563	0.7	<5	18669	<0.5	26	5	2	2	13241	10	10937
GSRM-70	0.023	<0.5	15347	316	182	0.4	<5	117901	<0.5	3	27	1015	3	36692	<10	3511
GSRM-71	0.005	<0.5	14977	69	80	0.4	<5	98172	<0.5	3	46	1447	2	36875	<10	1126
GSRM-72	2.150	<0.5	58051	2169	355	<0.1	<5	7117	0.8	14	33	156	63	60579	13	7246
GSRM-73	0.055	<0.5	23788	57	37	<0.1	<5	156461	<0.5	7	20	189	47	56712	<10	1369
GSRM-74	0.072	<0.5	44418	1158	138	0.3	<5	94267	1.4	12	21	155	217	61118	11	9120
GSRM-75	0.350	<0.5	19771	1127	245	0.7	<5	1058	0.5	9	2	14	6	14068	<10	7167
GSRM-76	0.359	<0.5	25008	1305	220	0.9	<5	66712	0.6	8	4	25	16	17538	<10	10803
GSRM-77	0.656	0.9	15781	943	136	0.5	<5	1846	<0.5	10	2	14	8	8815	<10	6553
GSRM-78	0.013	18.1	18815	39	486	<0.1	8	10773	2.8	22	17	31	92	8132	<10	3650
GSRM-79	0.037	<0.5	57478	207	425	1.1	<5	34107	<0.5	26	20	289	22	45744	13	12838
GSRM-80 A	0.248	2.0	39767	651	271	1.0	<5	1037	<0.5	25	2	31	11	16785	14	16799
GSRM-80 B	0.803	0.8	11325	877	135	0.6	<5	321	0.5	6	<1	7	2	3797	<10	3686
GSRM-80 C	1.600	6.9	19016	3229	108	0.8	<5	679	3.2	8	2	38	4	13150	<10	7037
BR-RCM-1	0.020	>100	1112	255	>5000	4.2	<5	1511	<0.5	65	17	6	88	173611	<10	408
BR-RCM-2	0.003	92.4	885	80	4808	4.8	<5	939	<0.5	16	7	3	115	64956	<10	233

AAL-008

SP0135587

FINAL REPORT

CLIENT : Geology Department
PROJECT : Rand Mountains
REFERENCE : GSRM-63 to BR-RCI
REPORTED : 16-Apr-2021

	La	Mg	Mn	Mo	Na	Ni	P	Pb	S	Sb	Sc	Sr	Th	Ti	Tl	U
	ICP-5AO3	ICP-5AO3	ICP-5AO3	ICP-5AO3	ICP-5AO3	ICP-5AO3	ICP-5AO3	ICP-5AO3	ICP-5AO3	ICP-5AO3	ICP-5AO3	ICP-5AO3	ICP-5AO3	ICP-5AO3	ICP-5AO3	ICP-5AO3
	10	100	5	1	100	1	10	3	100	2	1	1	20	10	10	10
SAMPLES	ppm	ppm	ppm	ppm	ppm	ppm	ppm	ppm	ppm	ppm	ppm	ppm	ppm	ppm	ppm	ppm
GSRM-63	13	1427	318	3	4540	2	341	30	162	20	2	166	<20	1781	<10	<10
GSRM-64	19	2855	923	<1	11571	3	746	9	1546	3	5	272	<20	2977	<10	<10
GSRM-65	13	1947	992	2	10891	2	483	9	534	9	3	412	<20	1450	<10	<10
GSRM-66	12	2023	1084	<1	4293	2	261	15	<100	4	2	436	<20	859	<10	<10
GSRM-67	23	10429	562	3	17574	4	1077	10	371	4	9	490	<20	4139	<10	<10
GSRM-68 A	<10	530	152	<1	167	<1	264	<3	<100	36	<1	19	<20	331	<10	<10
GSRM-68 B	13	1403	515	2	275	1	302	7	2126	31	2	232	<20	1068	<10	<10
GSRM-69	12	2168	186	3	1562	<1	360	5	156	28	2	54	<20	1618	<10	<10
GSRM-70	<10	55630	1462	<1	212	441	82	35	206	356	8	2047	<20	169	<10	<10
GSRM-71	<10	53131	713	<1	359	818	114	13	<100	5	4	992	<20	533	<10	<10
GSRM-72	<10	3558	1039	2	305	61	596	8	142	51	21	117	<20	4752	<10	<10
GSRM-73	<10	78171	1050	<1	228	88	324	<3	<100	41	10	708	<20	3021	<10	<10
GSRM-74	<10	22739	1313	<1	10531	58	652	13	593	6	18	151	<20	3303	<10	<10
GSRM-75	<10	1013	728	1	310	11	60	72	<100	28	2	12	<20	330	<10	<10
GSRM-76	<10	1555	423	1	487	17	66	12	103	20	5	39	<20	579	<10	<10
GSRM-77	<10	759	116	1	221	6	49	175	265	19	1	10	<20	352	<10	<10
GSRM-78	15	3417	>50000	153	988	192	1820	37	808	<2	5	1882	<20	524	189	<10
GSRM-79	14	29173	966	2	12180	217	477	8	458	9	13	541	<20	1972	<10	<10
GSRM-80 A	13	2874	73	<1	759	2	466	9	3278	144	5	111	<20	969	<10	<10
GSRM-80 B	<10	667	37	<1	203	2	49	<3	1770	62	<1	36	<20	213	<10	<10
GSRM-80 C	<10	1500	34	<1	257	6	60	6	8221	247	3	28	<20	842	<10	<10
BR-RCM-1	48	1343	46381	7	221	13	268	26	1970	75	2	586	<20	20	31	<10
BR-RCM-2	11	401	24183	3	122	6	124	25	2390	52	<1	1839	<20	12	14	<10

AAL-008

SP0135587

FINAL REPORT

CLIENT : Geology Department
PROJECT : Rand Mountains
REFERENCE : GSRM-63 to BR-RCI
REPORTED : 16-Apr-2021

	V	W	Y	Zn	Ag
	ICP-5AO3!	ICP-5AO3!	ICP-5AO3!	ICP-5AO3!	FA-PB30-GRAV
	1	2	1	2	10
SAMPLES	ppm	ppm	ppm	ppm	ppm
GSRM-63	33	566	7	38	
GSRM-64	47	4	17	102	
GSRM-65	33	4	12	28	
GSRM-66	31	4	13	61	
GSRM-67	66	3	15	97	
GSRM-68 A	16	5	3	16	
GSRM-68 B	60	19	10	45	
GSRM-69	27	3	5	44	
GSRM-70	39	2	4	38	
GSRM-71	34	<2	2	77	
GSRM-72	197	52	14	68	
GSRM-73	90	10	8	24	
GSRM-74	175	14	11	185	
GSRM-75	24	26	3	25	
GSRM-76	45	38	7	24	
GSRM-77	16	9	2	114	
GSRM-78	247	<2	15	225	
GSRM-79	91	9	9	68	
GSRM-80 A	35	9	4	6	
GSRM-80 B	7	4	<1	10	
GSRM-80 C	25	10	1	9	
BR-RCM-1	10	2	46	176	136
BR-RCM-2	4	4	21	71	

AAL-000

SP0136901
FINAL REPORT

Multi Element Package

AMERICAN ASSAY LABORATORIES
1500 GLENDALE AVE.
SPARKS, NV USA 89431-5902
Ph.(775) 356-0606
Fax.(775) 356-1413
EMAIL: info@aallabs.com

Geology Department Cal Poly Pomona

COPIES TO :	Jonathan Nourse janourse@cpp.edu	CLIENT REFERENCE No:	GSRM-57B TO GSRM-63	RECEIVED :	6-Jul-2021
:		No. SAMPLES :	13	REPORTED :	3-Aug-2021
:		MAIN SAMPLE TYPE :	ROCK		All Laboratory Analysis were preformed between the above Received and Reported dates
:					

COMPANY DISCLAIMER :-
When small samples are submitted, AAL may process the sample at smaller then specified weights to retain some pulp for quality control reassay.
When Values exceed upper limits, AAL will run an Over Range analysis, to establish an accurate value. Additional cost will apply.
Due to USDA Soil Quarantine programs - all foreign and some domestic soil material must be decontaminated by drying @ 125c for 48 hours,
which will result in loss of Mercury (Hg).
NEVADA LEGISLATIVE DISCLAIMER :-
The results of this assay were based solely upon the content of the sample submitted. Any decision to invest should be made only after the potential investment value of the claim or deposit has been determined based on the results of assays of multiple samples of geological materials collected by the prospective investor or by a qualified person selected by him and based on an evaluation of all engineering data which is available concerning any proposed project. Nevada State Law NRS 519.130.

ANALYSIS	Wt	Au	Ag	Al	As	Ba	Be	Bi	Ca	Cd	Ce	Co	Cr	Cu	Fe	Ga	K	La	Mg	Mn	Mo	Na	Ni	P	Pb	S
METHOD	WEIGH	15-ICP	-5A035	-5A035	-5A035	-5A035	-5A035	-5A035	-5A035	-5A035	-5A035	-5A035	-5A035	-5A035	-5A035	-5A035	-5A035	-5A035	-5A035	-5A035	-5A035	-5A035	-5A035	-5A035	-5A035	-5A035
UNIT	kg	ppm	ppm	ppm	ppm	ppm	ppm	ppm	ppm	ppm	ppm	ppm	ppm	ppm	ppm	ppm	ppm	ppm	ppm	ppm	ppm	ppm	ppm	ppm	ppm	ppm
LOWER LIMIT	0.01	0.003	0.5	100	2	5	0.1	5	100	0.5	1	1	1	1	100	10	100	10	100	5	1	100	1	10	3	100

ANALYSIS	Sb	Sc	Sr	Th	Ti	Tl	U	V	W	Y	Zn
METHOD	ICP-5A035	-5A035	-5A035	-5A035	-5A035	-5A035	-5A035	-5A035	-5A035	-5A035	-5A035
UNIT	ppm	ppm	ppm	ppm	ppm	ppm	ppm	ppm	ppm	ppm	ppm
LOWER LIMIT	2	1	1	20	10	10	10	1	2	1	2

SIGNATORY ANALYSIS

Cover Page
AAL-005

Digitally signed by Joshua R Zimmerman
DN: cn=Joshua R Zimmerman, o=American Assay Laboratories, ou, email=joshua.zimmerman@aallabs.com, c=US
Date: 2021.08.03 15:03:27 -07'00'

SP0136901
FINAL REPORT

AMERICAN ASSAY LABORATORIES
1500 GLENDALE AVE.
SPARKS, NV USA 89431-5902
Ph.(775) 356-0606
Fax.(775) 356-1413
EMAIL: AALLABS@NVBELL.NET

	Abbreviation	Definition
Preparation	DIP	Sample Destroyed in Preparation
	DIS	Sample Destroyed in Shipment
	ISS	Insufficient Sample Submitted
	SDI	Sample Diesel Impregnated
	SHI	Sample Hydraulic Impregnated
	SNR	Sample Not Received
Analysis	STD - ??	International Reference Material Standard
	STD - AAL##	AAL generated standard material
	BLANK	AAL Laboratory Silica Blank
	DTF	Data to Follow
	DL	Detection Limit of Method
	< or -	Less Than Lower Detection Limit of Method
	>	Greater than Upper Limit of Method
	N/A	Not Analyzed
	NR	Not Reported
	(R) column	Laboratory repeat weigh, digestion, analysis from original pulp or reject resplit
	D or -D after Sample ID	Client submitted duplicate rig split sample
	-R after Sample ID	Repeat analysis from original pulp reweigh, digestion and analysis
	-X after Sample ID	Repeat analysis from reject resplit, preparation, weigh, digestion and analysis
	ppb	Parts per Billion 0.001 ppm = 1 ppb
	ppm	Parts per Million 1 ppm = 1 mg/Kg
	OPT	Troy Ounces per Short Ton(2,000 lbs)(1 ppm= 0.02917 OPT)
	Oz	Troy Ounce = 31.103 grams
	%	Percent 1%=10,000 ppm
	g	Grams 1g=0.001 kilogram
	mg	Milligrams 1mg=0.001grams
	Kg	Kilograms 1Kg=1000grams
	lbs	Pounds 1lb=0.454kilogram
Method	FA-PB##	Fire Assay Lead Collection - ## sample weight in grams
	GRAV	Gravimetric (Weighed) finish
	SF	Screen Fire Assay reporting a plus, 2 minus fractions and a head Calc
	+ ###	Plus Fraction (Retained on top of Mesh) ###Screen Size
	- ###	Minus Fraction (Passed through Mesh) ###Screen Size
	CN	Cyanide Extraction
	ORE GRADE	2g sample made to 1000ml volumetric for results > upper limit of method
	Ox-H2SO4 or -HCl	Dilute acid leach for oxide fraction in copper or molybdenum analysis
	QLA	Dilute 10%H2SO4/0.5%Fe2(SO4)3 30C leach for acid soluble copper
	QLT	Dilute 15%H2SO4 30C leach for acid soluble copper
	SAP	Dilute 5%H2SO4/0.5%Fe2(SO4)3 85C leach for acid soluble & chalcocite copper
	D#A	Digestion #=2,3 or 4 Acids 2A=HCl/HNO3 3A=HCl/HNO3/HClO4 4A=HCl/HNO3/HF/HClO4
	HCl	Hydrochloric Acid(37%w/v) Boiling Point 109C
	HF	Hydrofluoric Acid(48%w/v) Boiling Point 108C Extreme Health Hazard
	HClO4	Perchloric Acid(69%w/v) Boiling Point 203C Extreme Fire/Explosion Hazard
	HNO3	Nitric Acid(69%w/v) Boiling Point 121C
	H2SO4	Sulfuric Acid(98% w/v) Boiling Point 338C
	ICP-xB or -xZ	ICP-AES and/or ICP-MS analysis using x=2, 3 or 4 acid digestion
	LiBO2-C	Lithium Metaborate fusion in Carbon crucible
	Na2O2-C	Sodium Peroxide fusion in Carbon crucible
	Na2O2-Zr	Sodium Peroxide fusion in Zirconium crucible
Technique	AAS	Atomic Absorption Spectroscopy
	ICP-AES	Inductively Coupled Plasma Atomic Emission Spectroscopy
	ICP-MS	Inductively Coupled Plasma Mass Spectroscopy
	RG	Research Grade (Low detection limit ICP-AES)
	UT	Ultra Trace (ICP-AES+ICP-MS analyses)
	XRF-ED or -WD	X-Ray Flourescence (-ED - Energy Dispersive) (-WD - Wavelength Dispersive)
	XRD	X-Ray Diffraction
	ELTRA-I	Carbon & Sulfur infrared detection analyzer inductive heating
	ELTRA-R	Carbon, Hydrogen & Sulfur infrared detection analyzer resistance furnace
	LECO-I	Nitrogen & Oxygen infra red detection analyzer inductive heating
	MW	Microwave Digestion (-PT is at 1500psig and 300C)
	SG-WD or -HP	Specific Gravity-WD-Water Displacement -HP-Helium Pycnometer 1g/cm3=62.4lbs/ft3

Definitions Page
AAL-007

SP0136901
FINAL REPORT
CLIENT : Geology Department Cal Poly Pomona
PROJECT : Rand Mountains
REFERENCE : GSRM-57B TO GSRM-63
REPORTED : 3-Aug-2021

SAMPLES	Wt WEIGH 0.01 kg	Au FA-PB15-ICP 0.003 ppm	Ag ICP-5AO35 0.5 ppm	Al ICP-5AO35 100 ppm	As ICP-5AO35 2 ppm	Ba ICP-5AO35 5 ppm	Be ICP-5AO35 0.1 ppm	Bi ICP-5AO35 5 ppm	Ca ICP-5AO35 100 ppm	Cd ICP-5AO35 0.5 ppm	Ce ICP-5AO35 1 ppm	Co ICP-5AO35 1 ppm	Cr ICP-5AO35 1 ppm
GRSM - 57B		<0.003	<0.5	88599	29	2685	3.0	<5	7524	<0.5	96	14	25809
GRSM - 81A		0.012	<0.5	15522	13	193	0.4	<5	29421	<0.5	14	1	11
GRSM - 81B		0.380	0.8	20980	353	1592	0.5	<5	1310	<0.5	15	2	3
GRSM - 84A		0.008	<0.5	22898	29	107	0.2	<5	22269	<0.5	7	2	26
GRSM - 84B		0.007	<0.5	46770	26	223	0.4	<5	39462	<0.5	17	3	31
GRSM - 84C		0.024	<0.5	14809	227	221	0.3	<5	122154	<0.5	4	18	744
GRSM - 85		0.009	<0.5	31335	102	273	0.4	<5	55491	<0.5	19	41	1097
GRSM - 86A		0.117	<0.5	75445	226	519	1.3	<5	14444	<0.5	55	6	50
GRSM - 86B		0.006	<0.5	36958	39	194	0.5	<5	173577	<0.5	14	13	78
GRSM - 87		0.005	<0.5	10196	90	214	0.5	<5	188975	<0.5	2	49	1260
GRSM - 33		8.210											
GRSM - 55		1.020											
GRSM - 63		1.530											

SP0136901
FINAL REPORT
CLIENT : Geology Department
PROJECT : Rand Mountains
REFERENCE : GSRM-57B TO GSR
REPORTED : 3-Aug-2021

SAMPLES	Cu ICP-5AO35 1 ppm	Fe ICP-5AO35 100 ppm	Ga ICP-5AO35 10 ppm	K ICP-5AO35 100 ppm	La ICP-5AO35 10 ppm	Mg ICP-5AO35 100 ppm	Mn ICP-5AO35 5 ppm	Mo ICP-5AO35 1 ppm	Na ICP-5AO35 100 ppm	Ni ICP-5AO35 1 ppm	P ICP-5AO35 10 ppm	Pb ICP-5AO35 3 ppm	S ICP-5AO35 100 ppm
GRSM - 57B	<1	23679	65	53643	38	25635	535	<1	1008	277	52	7	<100
GRSM - 81A	1	9937	<10	4396	<10	694	222	<1	125	<1	334	4	<100
GRSM - 81B	3	23637	<10	6423	<10	647	29	2	130	<1	255	10	1157
GRSM - 84A	3	12344	<10	2794	<10	7618	589	<1	175	15	172	6	<100
GRSM - 84B	4	22219	<10	5447	11	13811	1030	<1	255	13	269	7	<100
GRSM - 84C	4	48776	<10	5008	<10	36416	2038	3	236	169	72	33	<100
GRSM - 85	8	40294	<10	7034	12	38257	1498	1	1202	478	278	25	<100
GRSM - 86A	10	26673	17	20819	29	3191	331	1	581	23	488	15	<100
GRSM - 86B	30	31613	<10	1943	<10	1454	736	20	132	54	628	9	<100
GRSM - 87	7	35671	<10	409	<10	3581	918	1	175	884	86	67	190
GRSM - 33													
GRSM - 55													
GRSM - 63													

SP0136901

FINAL REPORT

CLIENT : Geology Department
PROJECT : Rand Mountains
REFERENCE : GSRM-57B TO GSR
REPORTED : 3-Aug-2021

	Sb	Sc	Sr	Th	Ti	Tl	U	V	W	Y	Zn
	ICP-5AO35	ICP-5AO35	ICP-5AO35	ICP-5AO35	ICP-5AO35	ICP-5AO35	ICP-5AO35	ICP-5AO35	ICP-5AO35	ICP-5AO35	ICP-5AO35
	2	1	1	20	10	10	10	1	2	1	2
SAMPLES	ppm	ppm	ppm	ppm	ppm	ppm	ppm	ppm	ppm	ppm	ppm
GRSM - 57B	15	9	85	<20	515	<10	<10	172	<2	4	166
GRSM - 81A	37	<1	68	<20	589	<10	<10	14	5	6	25
GRSM - 81B	42	<1	129	<20	979	<10	<10	28	6	2	29
GRSM - 84A	24	3	136	<20	546	<10	<10	15	5	4	15
GRSM - 84B	10	5	268	<20	840	<10	<10	33	10	8	19
GRSM - 84C	147	8	1027	<20	209	<10	<10	43	3	8	23
GRSM - 85	51	11	561	<20	595	<10	<10	72	2	13	69
GRSM - 86A	9	8	38	<20	2325	<10	<10	63	9	11	66
GRSM - 86B	15	10	173	<20	1750	<10	<10	66	15	13	63
GRSM - 87	3	3	115	<20	248	<10	<10	35	3	3	44
GRSM - 33											
GRSM - 55											
GRSM - 63											

AAL-008

SP0140769
FINAL REPORT

Multi Element Package

AMERICAN ASSAY LABORATORIES
1500 GLENDALE AVE.
SPARKS, NV USA 89431-5902
Ph.(775) 356-0606
Fax.(775) 356-1413
EMAIL: info@aallabs.com

Geology Department Cal Poly Pomona

COPIES TO :	Jonathan Nourse janourse@cpp.edu	CLIENT REFERENCE No:	GSRM - 90 to BR-RCM-3	RECEIVED :	2-Mar-2022
:		No. SAMPLES :	13	REPORTED :	13-Apr-2022
:		MAIN SAMPLE TYPE :	ROCK	All Laboratory Analysis were preformed between the above Received and Reported dates	
:					

COMPANY DISCLAIMER :-
When small samples are submitted, AAL may process the sample at smaller then specified weights to retain some pulp for quality control reassay.
When Values exceed upper limits, AAL will run an Over Range analysis, to establish an accurate value. Additional cost will apply.
Due to USDA Soil Quarantine programs - all foreign and some domestic soil material must be decontaminated by drying @ 125c for 48 hours, which will result in loss of Mercury (Hg).

NEVADA LEGISLATIVE DISCLAIMER :-
The results of this assay were based solely upon the content of the sample submitted. Any decision to invest should be made only after the potential investment value of the claim or deposit has been determined based on the results of assays of multiple samples of geological materials collected by the prospective investor or by a qualified person selected by him and based on an evaluation of all engineering data which is available concerning any proposed project. Nevada State Law NRS 519.130.

ANALYSIS	Au	Ag	Al	As	Ba	Be	Bi	Ca	Cd	Ce	Co	Cr	Cu	Fe	Ga	K	La	Mg	Mn	Mo	Na	Ni	P	Pb	S	Sb
METHOD	FA-PB10-ICP	-5AO35	-5AO35	-5AO35	-5AO35	-5AO35	-5AO35	-5AO35	-5AO35	-5AO35	-5AO35	-5AO35	-5AO35	-5AO35	-5AO35	-5AO35	-5AO35	-5AO35	-5AO35	-5AO35	-5AO35	-5AO35	-5AO35	-5AO35	-5AO35	-5AO35
UNIT	ppm	ppm	ppm	ppm	ppm	ppm	ppm	ppm	ppm	ppm	ppm	ppm	ppm	ppm	ppm	ppm	ppm	ppm	ppm	ppm	ppm	ppm	ppm	ppm	ppm	ppm
LOWER LIMIT	0.003	0.5	100	2	5	0.1	5	100	0.5	1	1	1	1	100	10	100	10	100	5	1	100	1	10	3	100	2

ANALYSIS	Sc	Sr	Th	Ti	Tl	U	V	W	Y	Zn	Sb
METHOD	ICP-5AO35	-5AO35	-5AO35	-5AO35	-5AO35	-5AO35	-5AO35	-5AO35	-5AO35	-5AO35	-5AORE
UNIT	ppm	ppm	ppm	ppm	ppm	ppm	ppm	ppm	ppm	ppm	ppm
LOWER LIMIT	1	1	20	10	10	10	1	2	1	2	2

Joshua R Zimmerman

Digitally signed by Joshua R Zimmerman
Date: 2022.04.13 12:35:42 -07'00'

SIGNATORY ANALYSIS

Cover Page
AAL-036

SP0140769
FINAL REPORT

AMERICAN ASSAY LABORATORIES
1500 GLENDALE AVE.
SPARKS, NV USA 89431-5902
Ph.(775) 356-0606
Fax.(775) 356-1413
EMAIL: AALLABS@NVBELL.NET

	Abbreviation	Definition
Preparation	DIP	Sample Destroyed in Preparation
	DIS	Sample Destroyed in Shipment
	ISS	Insufficient Sample Submitted
	SDI	Sample Diesel Impregnated
	SHI	Sample Hydraulic Impregnated
	SNR	Sample Not Received
Analysis	STD - ??	International Reference Material Standard
	STD - AAL##	AAL generated standard material
	BLANK	AAL Laboratory Silica Blank
	DTF	Data to Follow
	DL	Detection Limit of Method
	< or -	Less Than Lower Detection Limit of Method
	>	Greater than Upper Limit of Method
	N/A	Not Analyzed
	NR	Not Reported
	(R) column	Laboratory repeat weigh, digestion, analysis from original pulp or reject resplit
	D or -D after Sample ID	Client submitted duplicate rig split sample
	-R after Sample ID	Repeat analysis from original pulp reweigh, digestion and analysis
	-X after Sample ID	Repeat analysis from reject resplit, preparation, weigh, digestion and analysis
	ppb	Parts per Billion 0.001 ppm = 1 ppb
	ppm	Parts per Million 1 ppm = 1 mg/Kg
	OPT	Troy Ounces per Short Ton(2,000 lbs)(1 ppm= 0.02917 OPT)
	Oz	Troy Ounce = 31.103 grams
	%	Percent 1%=10,000 ppm
	g	Grams 1g=0.001 kilogram
	mg	Milligrams 1mg=0.001grams
	Kg	Kilograms 1Kg=1000grams
	lbs	Pounds 1lb=0.454kilogram
Method	FA-PB##	Fire Assay Lead Collection - ## sample weight in grams
	GRAV	Gravimetric (Weighed) finish
	SF	Screen Fire Assay reporting a plus, 2 minus fractions and a head Calc
	+ ###	Plus Fraction (Retained on top of Mesh) ###Screen Size
	- ###	Minus Fraction (Passed through Mesh) ###Screen Size
	CN	Cyanide Extraction
	ORE GRADE	2g sample made to 1000ml volumetric for results > upper limit of method
	Ox-H2SO4 or -HCl	Dilute acid leach for oxide fraction in copper or molybdenum analysis
	QLA	Dilute 10%H2SO4/0.5%Fe2(SO4)3 30C leach for acid soluble copper
	QLT	Dilute 15%H2SO4 30C leach for acid soluble copper
	SAP	Dilute 5%H2SO4/0.5%Fe2(SO4)3 85C leach for acid soluble & chalcocite copper
	D#A	Digestion #=2,3 or 4 Acids 2A-HCl/HNO3 3A-HCl/HNO3/HClO4 4A-HCl/HNO3/HF/HClO4
	HCl	Hydrochloric Acid(37%w/v) Boiling Point 109C
	HF	Hydrofluoric Acid(48%w/v) Boiling Point 108C Extreme Health Hazard
	HClO4	Perchloric Acid(69%w/v) Boiling Point 203C Extreme Fire/Explosion Hazard
	HNO3	Nitric Acid(69%w/v) Boiling Point 121C
	H2SO4	Sulfuric Acid(98% w/v) Boiling Point 338C
	ICP-xB or -xZ	ICP-AES and/or ICP-MS analysis using x=2, 3 or 4 acid digestion
	LiBO2-C	Lithium Metaborate fusion in Carbon crucible
	Na2O2-C	Sodium Peroxide fusion in Carbon crucible
	Na2O2-Zr	Sodium Peroxide fusion in Zirconium crucible
Technique	AAS	Atomic Absorption Spectroscopy
	ICP-AES	Inductively Coupled Plasma Atomic Emission Spectroscopy
	ICP-MS	Inductively Coupled Plasma Mass Spectroscopy
	RG	Research Grade (Low detection limit ICP-AES)
	UT	Ultra Trace (ICP-AES+ICP-MS analyses)
	XRF-ED or -WD	X-Ray Flourescence (-ED = Energy Dispersive) (-WD = Wavelength Dispersive)
	XRD	X-Ray Diffraction
	ELTRA-I	Carbon & Sulfur infrared detection analyzer inductive heating
	ELTRA-R	Carbon, Hydrogen & Sulfur infrared detection analyzer resistance furnace
	LECO-I	Nitrogen & Oxygen infra red detection analyzer inductive heating
	MW	Microwave Digestion (-PT is at 1500psig and 300C)
	SG-WD or -HP	Specific Gravity-WD=Water Displacement -HP=Helium Pycnometer 1g/cm3=62.41bs/ft3

Definitions Page
AAL-007

SP0140769

FINAL REPORT

CLIENT : Geology Department Cal Poly Pomona
PROJECT : Rand Mountains
REFERENCE : GSRM - 90 to BR-RCM-3
REPORTED : 13-Apr-2022

SAMPLES	Au FA-PB10-ICP 0.003 ppm	Ag ICP-5AO35 0.5 ppm	Al ICP-5AO35 100 ppm	As ICP-5AO35 2 ppm	Ba ICP-5AO35 5 ppm	Be ICP-5AO35 0.1 ppm	Bi ICP-5AO35 5 ppm	Ca ICP-5AO35 100 ppm	Cd ICP-5AO35 0.5 ppm	Ce ICP-5AO35 1 ppm	Co ICP-5AO35 1 ppm	Cr ICP-5AO35 1 ppm	Cu ICP-5AO35 1 ppm
GSRM - 90	0.071	0.6	42205	39	508	0.5	<5	1833	<0.5	14	9	362	19
GSRM - 91	0.411	0.9	39967	43	981	0.6	<5	5596	<0.5	8	17	366	18
GSRM - 92	1.240	3.0	28901	29	666	0.4	<5	5721	<0.5	8	11	457	37
GSRM - 93	0.107	<0.5	23404	68	554	0.3	<5	1984	<0.5	7	14	475	20
GSRM - 94	0.282	1.3	10229	285	437	0.3	<5	4100	<0.5	<1	52	1326	45
GSRM - 95	0.118	<0.5	37224	537	223	0.5	<5	4677	<0.5	5	29	1134	21
GSRM - 96	0.008	<0.5	59330	14	1345	0.9	<5	63219	<0.5	39	8	129	8
GSRM - 97	0.027	<0.5	76965	16	781	1.4	<5	25084	<0.5	50	8	171	14
GSRM - 98	0.960	<0.5	56237	2028	368	0.6	<5	58019	<0.5	5	30	125	35
GSRM - 99A	0.110	<0.5	63812	61	266	0.7	<5	11018	<0.5	23	10	112	18
GSRM - 99B	0.085	1.0	20100	986	683	0.2	<5	5197	<0.5	48	41	84	301
GSRM - BR	3.170	43.8	588	1171	96	<0.1	249	1035	23.5	<1	5	264	3147
BR-RCM-3	0.299	151.0	1856	424	>5000	2.7	<5	2004	<0.5	68	17	96	321

AAL 038

SP0140769

FINAL REPORT

CLIENT : Geology Department
PROJECT : Rand Mountains
REFERENCE : GSRM - 90 to BR-RC
REPORTED : 13-Apr-2022

SAMPLES	Fe ICP-5AO35 100 ppm	Ga ICP-5AO35 10 ppm	K ICP-5AO35 100 ppm	La ICP-5AO35 10 ppm	Mg ICP-5AO35 100 ppm	Mn ICP-5AO35 5 ppm	Mo ICP-5AO35 1 ppm	Na ICP-5AO35 100 ppm	Ni ICP-5AO35 1 ppm	P ICP-5AO35 10 ppm	Pb ICP-5AO35 3 ppm	S ICP-5AO35 100 ppm	Sb ICP-5AO35 2 ppm
GSRM - 90	15359	<10	9073	<10	2114	164	7	444	73	76	29	945	>10000
GSRM - 91	14374	<10	7932	<10	2411	144	5	748	260	80	13	12139	>10000
GSRM - 92	14266	<10	4988	<10	1534	124	10	743	117	55	21	33381	>10000
GSRM - 93	14254	<10	5316	<10	1596	146	10	388	146	103	18	369	>10000
GSRM - 94	18460	<10	518	<10	788	184	14	268	602	17	24	209	>10000
GSRM - 95	38413	<10	6224	<10	4927	800	5	270	502	62	14	<100	1301
GSRM - 96	27257	13	13554	24	22967	709	3	3713	29	401	13	363	21
GSRM - 97	26258	18	19152	29	13693	363	5	13769	27	645	8	<100	33
GSRM - 98	73466	13	10370	<10	25081	2133	3	1345	30	686	<3	342	47
GSRM - 99A	30277	13	5711	15	1472	128	13	199	10	526	3	162	26
GSRM - 99B	236824	<10	1124	33	2177	38	41	150	5	286	9	541	43
GSRM - BR	26841	<10	127	<10	196	142	12	134	11	<10	202	5107	63
BR-RCM-3	135534	<10	795	46	1940	44525	10	365	13	86	24	4226	66

AAL 038

SP0140769

FINAL REPORT

CLIENT : Geology Department
PROJECT : Rand Mountains
REFERENCE : GSRM - 90 to BR-R(
REPORTED : 13-Apr-2022

	Sc	Sr	Th	Ti	Tl	U	V	W	Y	Zn	Sb
	ICP-5AO35	ICP-5AO35	ICP-5AO35	ICP-5AO35	ICP-5AO35	ICP-5AO35	ICP-5AO35	ICP-5AO35	ICP-5AO35	ICP-5AO35	ICP-5AORE
	1	1	20	10	10	10	1	2	1	2	2
SAMPLES	ppm	ppm	ppm	ppm	ppm	ppm	ppm	ppm	ppm	ppm	ppm
GSRM - 90	7	88	<20	1465	<10	<10	58	7	6	41	16130
GSRM - 91	6	253	<20	977	<10	<10	55	5	3	39	97150
GSRM - 92	6	242	<20	1020	<10	<10	46	4	4	32	161700
GSRM - 93	5	122	<20	1002	<10	<10	40	4	3	41	18840
GSRM - 94	1	72	<20	95	<10	<10	34	<2	<1	23	13080
GSRM - 95	7	61	<20	1503	<10	<10	79	5	3	103	
GSRM - 96	5	245	<20	1728	<10	<10	43	5	18	62	
GSRM - 97	8	272	<20	2884	<10	<10	63	8	16	58	
GSRM - 98	34	217	<20	7772	<10	<10	328	58	22	87	
GSRM - 99A	6	142	<20	1883	<10	<10	53	20	6	61	
GSRM - 99B	1	136	<20	225	<10	<10	48	8	3	76	
GSRM - BR	<1	11	<20	25	<10	<10	15	9	<1	217	
BR-RCM-3	2	1157	<20	44	<10	<10	15	3	38	157	

Appendix C

XRF Data for All Samples and Plot Legends

Run 0220, Jonathan Nourse, Cal Poly Pomona

	JNO GSRM 2	JNO GSRM 3	JNO GSRM 4	JNO GSRM 5	JNO GSRM 6	JNO GSRM 7	JNO GSRM 8	JNO GSRM 9	JNO GSRM 10	JNO GSRM 13	JNO JN 1826	JNO JN 1905	JNO JN 1906	JNO ERT Plate IV #2B	JNO Atolia GD #101	JNO GSRM 24	JNO GSRM 26	JNO GSRM 27	JNO GSRM 30	JNO GSRM 32	JNO 1548	JNO 1549	JNO GSRM 25	JNO GSRM 28	JNO GSRM 29	JNO GSRM 31	JNO GSRM 33	JNO GSRM 3	JNO GSRM 3®
SO3 >/=	0.00	0.00	0.00	0.00	0.01	0.00	0.00	0.00	0.00	0.00	0.00	0.00	0.00	0.00	0.00	0.00	0.00	0.01	0.10	0.01	0.23	0.00	0.00	0.00	0.00	0.00	0.00	0.00	0.00
Cl >/=	0.00	0.00	0.00	0.00	0.37	0.00	0.00	0.00	0.00	0.00	0.00	0.00	0.00	0.00	0.00	0.00	0.00	0.15	0.01	0.00	0.00	0.00	0.00	0.33	0.00	0.00	0.00	0.00	0.00
Unnormalized Major Elements (Weight %):																													
SiO2	69.83	70.86	59.93	58.36	66.60	50.79	57.22	64.62	66.37	72.72	76.38	75.50	74.89	75.34	63.34	94.92	53.04	62.24	15.62	60.62	54.85	57.02	67.33	49.21	59.34	59.67	59.19	70.86	71.00
TiO2	0.370	0.554	0.910	0.869	0.449	0.910	0.532	0.280	0.328	0.374	0.040	0.032	0.213	0.036	0.913	0.058	0.682	0.717	0.229	0.759	1.001	1.204	0.495	0.671	0.832	0.694	0.644	0.554	0.555
Al2O3	14.28	12.48	18.00	14.66	12.61	15.33	12.42	15.48	7.52	13.70	12.84	12.96	12.67	13.00	16.36	2.16	12.83	14.61	4.09	13.39	29.05	27.82	13.41	12.31	14.37	12.24	11.46	12.48	12.51
FeO*	3.33	3.71	4.14	4.68	3.89	6.02	4.81	2.40	3.12	1.40	0.33	0.59	1.28	0.90	4.76	0.81	3.65	3.60	7.53	3.95	1.46	1.01	2.80	4.56	4.07	3.77	2.65	3.71	3.73
MnO	0.209	0.203	0.050	0.093	0.110	0.105	0.227	0.185	0.107	0.049	0.001	0.012	0.018	0.004	0.089	0.001	0.060	0.062	0.278	0.068	0.005	0.004	0.040	0.149	0.064	0.058	0.069	0.203	0.202
MgO	0.47	0.61	0.95	1.30	0.52	0.73	1.32	0.45	2.19	0.13	0.03	0.03	0.23	0.03	2.00	0.04	0.39	0.54	0.53	0.48	0.80	1.06	0.49	0.77	1.18	0.44	0.34	0.61	0.61
CaO	1.59	1.82	4.14	6.02	4.09	9.02	8.95	3.97	7.42	0.85	0.65	1.10	1.07	0.40	4.83	0.07	11.84	5.10	37.41	7.25	0.52	0.31	3.79	12.92	6.30	9.09	10.76	1.82	1.81
Na2O	3.75	2.54	4.51	3.00	0.33	1.13	3.13	4.66	0.06	3.46	3.42	2.24	2.57	2.15	3.88	0.02	2.11	3.22	0.86	0.77	5.96	3.78	1.55	2.83	2.80	1.22	2.54	2.54	2.54
K2O	3.24	3.48	2.34	1.86	2.39	2.35	1.99	3.80	0.98	5.87	5.29	6.37	5.39	6.85	2.34	0.48	2.39	2.61	0.46	3.10	3.59	5.94	3.75	2.08	1.77	2.64	1.71	3.48	3.49
P2O5	0.117	0.181	0.303	0.230	0.128	0.169	0.117	0.088	0.074	0.094	0.016	0.027	0.049	0.013	0.247	0.018	0.195	0.210	0.070	0.212	0.288	0.117	0.118	0.180	0.219	0.183	0.179	0.181	0.182
Sum	97.19	96.44	95.28	91.07	91.12	86.56	90.71	95.93	88.18	98.65	98.99	98.87	98.39	98.73	98.76	98.58	87.18	92.91	67.08	90.60	97.52	98.26	93.77	85.68	90.93	89.99	89.54	96.44	96.64
LOI %	2.06	2.90	4.01	8.45	7.99	12.75	8.86	3.72	11.21	0.81	0.53	0.69	0.97	0.71	0.96	1.25	12.28	6.67	31.93	8.93	1.67	1.35	5.83	13.41	8.51	9.52	10.16	2.90	2.90
Normalized Major Elements (Weight %):																													
SiO2	71.86	73.47	62.90	64.08	73.09	58.68	63.08	67.36	75.27	73.72	77.16	76.36	76.12	76.31	64.14	96.29	60.83	66.99	23.29	66.91	56.25	58.03	71.81	57.44	65.26	66.30	66.11	73.47	73.47
TiO2	0.38	0.57	0.96	0.95	0.49	1.05	0.59	0.29	0.37	0.38	0.04	0.03	0.22	0.04	0.92	0.06	0.78	0.77	0.34	0.84	1.03	1.23	0.53	0.78	0.91	0.77	0.72	0.57	0.57
Al2O3	14.69	12.94	18.89	16.10	13.84	17.71	13.69	16.14	8.53	13.89	12.97	13.11	12.88	13.17	16.57	2.20	14.71	15.72	6.10	14.78	29.79	28.32	14.30	14.37	15.80	13.60	12.80	12.94	12.94
FeO*	3.43	3.85	4.35	5.14	4.27	6.96	5.30	2.50	3.54	1.42	0.33	0.60	1.31	0.91	4.82	0.82	4.19	3.88	11.23	4.36	1.49	1.03	2.98	5.33	4.48	4.19	2.95	3.85	3.86
MnO	0.21	0.21	0.05	0.10	0.12	0.12	0.25	0.19	0.12	0.05	0.00	0.01	0.02	0.00	0.09	0.00	0.07	0.07	0.41	0.08	0.00	0.00	0.04	0.17	0.07	0.06	0.08	0.21	0.21
MgO	0.48	0.63	0.99	1.42	0.57	0.85	1.45	0.47	2.48	0.13	0.03	0.03	0.23	0.03	2.03	0.04	0.45	0.58	0.79	0.53	0.82	1.08	0.52	0.90	1.29	0.49	0.38	0.63	0.63
CaO	1.64	1.88	4.35	6.61	4.49	10.42	9.87	4.14	8.42	0.86	0.65	1.11	1.09	0.40	4.89	0.07	13.58	5.49	55.77	8.00	0.53	0.31	4.04	15.08	6.93	10.10	12.01	1.88	1.88
Na2O	3.86	2.63	4.73	3.29	0.36	1.31	3.45	4.86	0.07	3.50	3.45	2.27	2.61	2.18	3.92	0.02	2.42	3.47	1.28	0.85	6.11	3.85	1.66	3.30	3.08	1.35	2.83	2.63	2.63
K2O	3.33	3.61	2.46	2.05	2.63	2.71	2.20	3.97	1.12	5.95	5.35	6.45	5.48	6.94	2.37	0.49	2.74	2.81	0.69	3.42	3.68	6.04	4.00	2.42	1.95	2.94	1.91	3.61	3.62
P2O5	0.12	0.19	0.32	0.25	0.14	0.20	0.13	0.09	0.08	0.10	0.02	0.03	0.05	0.01	0.25	0.02	0.22	0.23	0.10	0.23	0.30	0.12	0.13	0.21	0.24	0.20	0.20	0.19	0.19
Total	100.00	100.00	100.00	100.00	100.00	100.00	100.00	100.00	100.00	100.00	100.00	100.00	100.00	100.00	100.00	100.00	100.00	100.00	100.00	100.00	100.00	100.00	100.00	100.00	100.00	100.00	100.00	100.00	100.00
Unnormalized Trace Elements (ppm):																													
Ni	25	20	5	9	17	10	31	30	12	2	5	2	3	2	6	2	4	4	6	3	1	4	2	3	3	4	1	20	15
Cr	224	201	10	31	79	37	169	174	55	5	4	3	4	5	10	5	5	6	2	8	130	167	4	6	7	5	3	201	198
Sc	1	3	8	8	4	13	8	2	5	2	1	1	2	0	13	14	7	6	10	6	21	29	4	9	8	6	4	3	3
V	33	43	63	73	41	134	83	28	47	32	4	11	11	15	83	5	76	91	62	70	198	208	42	78	72	65	56	43	43
Ba	1543	1233	1634	553	1176	669	725	1519	530	1185	68	1984	1779	2071	455	137	365	506	4296	512	439	624	1912	447	672	597	318	1233	1232
Rb	70	71	43	71	75	71	55	76	27	74	87	116	108	144	84	15	83	98	19	98	74	127	77	87	63	95	75	71	73
Sr	520	343	838	469	118	228	434	417	203	470	84	470	225	391	534	39	144	270	517	100	117	94	340	296	512	200	439	343	345
Zr	162	193	321	208	174	154	87	142	96	147	80	146	163	107	224	34	191	214	60	201	183	378	132	163	207	182	194	193	192
Y	8	9	17	21	8	16	15	6	9	16	3	1	5	3	21	3	16	16	55	15	65	71	12	26	17	15	17	9	9
Nb	5.7	8.8	13.9	17.5	5.0	9.6	6.2	4.5	4.2	12.3	3.9	0.5	5.0	2.5	19.8	1.6	14.4	15.9	3.9	14.4	22.3	28.8	8.8	13.9	16.2	13.6	12.3	8.8	9.0
Ga	15	16	24	20	18	26	13	14	10	17	16	12	13	14	24	3	19	21	8	19	36	37	16	18	20	17	15	16	16
Cu	30	27	22	5	272	15	19	13	16	14	11	46	4	25	4	11	3	3	9	9	3	4	6	3	3	6	8	27	28
Zn	33	54	70	95	54	355	52	29	58	36	2	4	19	6	104	3	69	68	166	74	2	5	49	77	73	74	46	54	54
Pb	14	12	15	8	5	38	9	11	9	20	16	22	15	21	10	4	7	8	17	15	12	19	11	8	8	13	12	12	12
La	29	41	53	31	14	26	8	29	12	19	6	10	53	5	36	5	37	22	31	29	85	98	36	28	26	29	36	41	41
Ce	57	71	97	69	26	51	23	52	19	44	7	12	90	7	82	8	77	59	57	66	171	199	64	66	62	68	75	71	69
Th	5	6	7	7	2	5	2	6	3	5	10	4	21	4	9	0	7	5	3	6	23	27	8	5	5	6	6	6	7
Nd	23	26	43	36	13	24	12	20	10	24	5	4	30	3	40	3	33	31	29	31	77	89	26	33	31	29	31	26	26
U	2	2	2	3	2	2	1	2	4	1	2	2	1	1	3	0	3	3	10	3	7	5	2	3	3	6	3	2	2
As >/=	20	36	20	10	94	44	18	12	44	19	15	9	34	8	10	132	22	24	4	111	10	3	23	30	8	271	32	36	36
sum tr.	2819	2415	3306	1744	2197	1928	1771	2586	1170	2144	428	2860	2587	2834	1770	423	1182	1473	5365	1391	1676	2217	2776	1398	1818	1702	1385	2415	2410
in %	0.28	0.24	0.33	0.17	0.22	0.19	0.18	0.26	0.12	0.21	0.04	0.29	0.26	0.28	0.18	0.04	0.12	0.15	0.54	0.14	0.17	0.22	0.28	0.14	0.18	0.17	0.14	0.24	0.24
sum m+tr	97.47	96.69	95.61	91.25	91.34	86.75	90.89	96.19	88.29	98.86	99.04	99.16	98.65	99.01	98.93	98.62	87.30	93.06	67.61	90.74	97.68	98.48	94.05	85.82	91.11	90.17	89.68	96.69	96.88
M+Toxides	97.52	96.73	95.67	91.28	91.39	86.79	90.92	96.24	88.32	98.90	99.04	99.20	98.69	99.05	98.97	98.63	87.33	93.09	67.69	90.77	97.73	98.54	94.09	85.85	91.15	90.21	89.71	96.73	96.93
w/LOI	99.58	99.63	99.67	99.74	99.75	99.54	99.78	99.95	99.53	99.70	99.58	99.89	99.66	99.76	99.93	99.89	99.61	99.92	99.72	99.71	99.62	99.89	99.92	99.59	99.66	99.73	99.88	99.63	99.82
if Fe3+	99.95	100.04	100.13	100.26	100.18	100.21	100.32	100.22	99.87	99.86	99.61	99.95	99.80	99.86	100.46	99.98	100.01	100.32	100.56	100.15	99.78	100.00	100.23	100.10	100.11	100.14	100.17	100.04	100.24

Major elements are normalized on a volatile-free basis, with total Fe expressed as FeO.
® denotes a duplicate bead made from the same rock powder.

Perform X Run 0221, Jonathan Nourse, Cal Poly Pomona

Date	ERT 721 JNO 2356-1 ########	CAL SB Atolia gr #210 JNO 2356-2 26-Sep-21	GSRM-38 JNO 2356-3 26-Sep-21	GSRM-49 JNO 2356-4 26-Sep-21	GSRM-53 JNO 2356-5 26-Sep-21	GSRM-57 JNO 2356-6 26-Sep-21	GSRM-70 JNO 2356-7 26-Sep-21	GSRM-71B JNO 2356-8 26-Sep-21	GSRM-81B JNO 2356-9 26-Sep-21	GSRM-82A JNO 2356-10 26-Sep-21	GSRM-84C JNO 2356-11 ########	USGS AGV-2 PV	AGV-2 USGS CRM-1 26-Sep-21	AGV-2 USGS CRM-1 27-Sep-21	USGS BCR-2 PV	BCR-2 USGS CRM-2 26-Sep-21	BCR-2 USGS CRM-2 27-Sep-21	USGS GSP-2 GeoRem	GSP-2 USGS CRM-3 26-Sep-21	GSP-2 USGS CRM-3 ########
Unnormalized Major Elements (Weight %):																				
SiO2	63.14	66.10	81.37	76.52	80.49	41.82	42.06	50.61	90.62	77.69	43.92	59.14	59.61	59.49	54.00	53.92	53.89	66.60	66.72	66.67
TiO2	0.950	0.822	0.190	0.089	0.087	0.017	0.042	0.141	0.163	0.048	0.049	1.051	1.044	1.044	2.265	2.253	2.255	0.660	0.676	0.676
Al2O3	16.33	16.24	5.49	13.11	10.86	1.96	2.71	24.23	3.66	12.21	2.67	17.03	17.02	16.97	13.48	13.43	13.44	14.90	14.96	14.91
FeO*	4.16	3.55	4.46	0.43	1.24	4.21	4.62	1.46	2.77	0.50	6.24	6.10	6.04	6.04	12.39	12.42	12.43	4.41	4.40	4.41
MnO	0.078	0.056	0.120	0.010	0.017	0.155	0.220	0.019	0.003	0.010	0.310	0.100	0.100	0.100	0.197	0.198	0.198	0.041	0.042	0.042
MgO	1.57	1.27	7.45	0.04	0.02	14.29	9.20	4.41	0.10	0.00	6.44	1.80	1.76	1.76	3.60	3.58	3.59	0.96	0.93	0.93
CaO	5.49	4.44	21.84	0.85	1.16	10.92	15.40	0.07	0.19	0.50	17.09	5.15	5.23	5.22	7.11	7.11	7.10	2.10	2.12	2.12
Na2O	3.94	3.96	0.65	2.67	0.21	0.02	0.03	0.24	0.05	3.30	0.04	4.20	4.16	4.16	3.12	3.11	3.11	2.78	2.78	2.77
K2O	2.13	2.39	1.16	5.40	2.37	0.14	0.33	10.13	0.79	4.31	0.56	2.90	2.91	2.90	1.77	1.77	1.78	5.38	5.46	5.46
P2O5	0.264	0.234	0.062	0.031	0.026	0.009	0.023	0.011	0.043	0.059	0.019	0.483	0.476	0.474	0.359	0.349	0.350	0.290	0.285	0.284
Sum	98.06	99.05	72.82	99.24	95.94	73.54	75.45	91.32	98.38	99.13	77.35	97.96	98.36	98.18	98.30	98.18	98.14	98.12	98.37	98.28
LOI %	1.65	0.63	27.17	0.76	4.06	25.75	23.82	8.15	1.43	0.66	22.34									
Normalized Major Elements (Weight %):																				
SiO2	64.39	66.74	43.26	77.18	83.90	57.00	56.81	55.42	92.21	78.38	56.78	60.37	60.59	60.59	54.93	54.93	54.91	67.88	67.83	67.84
TiO2	0.97	0.83	0.26	0.09	0.09	0.02	0.06	0.15	0.17	0.05	0.06	1.07	1.06	1.06	2.30	2.30	2.30	0.67	0.69	0.69
Al2O3	16.65	16.39	7.57	13.22	11.01	2.67	3.60	26.53	3.72	12.32	3.45	17.39	17.30	17.28	13.71	13.69	13.70	15.19	15.20	15.17
FeO*	4.24	3.58	6.15	0.44	1.29	5.72	6.12	1.60	2.82	0.50	8.07	6.23	6.14	6.15	12.60	12.66	12.66	4.49	4.47	4.49
MnO	0.08	0.06	0.27	0.01	0.02	0.21	0.29	0.02	0.00	0.01	0.40	0.10	0.10	0.10	0.20	0.20	0.20	0.04	0.04	0.04
MgO	1.60	1.28	10.27	0.04	0.02	19.29	12.20	4.83	0.10	0.00	8.33	1.84	1.79	1.80	3.66	3.65	3.66	0.98	0.95	0.95
CaO	5.60	4.48	29.71	0.85	1.21	14.85	20.41	0.07	0.19	0.50	22.09	5.26	5.32	5.31	7.24	7.25	7.24	2.14	2.15	2.15
Na2O	4.02	4.00	0.94	2.69	0.22	0.03	0.04	0.27	0.05	3.33	0.06	4.29	4.23	4.26	3.17	3.17	3.17	2.83	2.83	2.82
K2O	2.17	2.41	1.60	5.45	2.47	0.19	0.44	11.09	0.80	4.35	0.73	2.96	2.96	2.96	1.80	1.81	1.81	5.48	5.55	5.56
P2O5	0.27	0.24	0.09	0.03	0.03	0.01	0.03	0.01	0.04	0.06	0.02	0.49	0.48	0.48	0.37	0.36	0.36	0.30	0.29	0.29
Total	100.00	100.00	100.00	100.00	100.00	100.00	100.00	100.00	100.00	100.00	100.00	100.00	100.00	100.00	100.00	100.00	100.00	100.00	100.00	100.00
Unnormalized Trace Elements (ppm):																				
Ni	5	4	16	5	0	1171	820	118	1	4	192	19	19	18	13	12	11	17	15	14
Cr	10	3	5	3	3	1779	1231	19712	24	5	865	16	16	16	16	13	14	20	20	21
Sc	6	6	3	0	3	3	15	7	0	0	12	13	14	14	34	34	34	6	6	7
V	89	65	31	1	2	29	44	307	25	0	40	119	120	118	418	402	399	52	52	51
Ba	696	1109	845	1569	237	19	177	3226	1190	69	213	1134	1131	1133	684	680	682	1340	1330	1337
Rb	50	56	25	96	41	6	14	335	23	139	19	68	67	67	46	46	46	245	247	247
Sr	1036	752	1001	395	27	695	2031	34	90	19	1019	660	666	664	337	330	331	240	240	240
Zr	273	237	69	115	107	5	19	0	50	81	11	232	237	237	187	183	189	550	576	575
Y	12	13	7	2	2	2	6	2	2	7	10	19	20	20	36	35	35	28	27	28
Nb	16.4	16.3	3.9	0.5	0.0	0.0	2.5	0.0	2.0	9.5	1.5	14.1	14.1	14.2	12.4	12.5	12.6	27.0	26.6	26.0
Ga	24	21	6	11	10	3	4	32	4	13	4	20	19	19	22	21	22	22	23	22
Cu	4	12	6	0	5	3	3	1	2	7	5	52	51	50	20	20	17	43	43	43
Zn	86	80	111	7	11	50	45	15	19	7	25	87	89	89	130	131	131	120	119	111
Pb	15	12	16	18	7	9	59	1	6	11	31	13	15	13	11	9	10	42	42	42
La	44	59	13	28	20	2	0	5	9	16	2	38	36	34	25	21	25	180	197	195
Ce	82	96	21	39	38	21	15	0	18	30	6	69	64	69	53	47	49	410	436	436
Th	7	11	2	7	16	0	1	1	3	12	2	6	6	6	6	5	5	105	106	107
Nd	33	35	8	9	16	0	1	0	6	17	2	30	29	30	28	28	29	200	200	201
U	2	2	1	2	1	0	0	0	1	2	3	2	1	1	2	2	2	2	3	2
As >/=	0	0	2	2	4	1358	436	4	365	0	257	1	4	0	1	3	0	0	3	2
sum tr.	2490	2613	2196	2312	547	5160	4625	23803	1842	447	2727	2612	2619	2614	2079	2034	2032	3650	3707	3708
in %	0.25	0.26	0.22	0.23	0.05	0.52	0.46	2.38	0.18	0.04	0.27	0.26	0.26	0.26	0.21	0.20	0.20	0.36	0.37	0.37
sum m+tr	98.31	99.31	72.73	99.37	95.99	74.06	75.91	93.70	98.57	99.17	77.63	98.22	98.64	98.44	98.51	98.38	98.34	98.49	98.74	98.65
M+Toxides	98.36	99.36	72.77	99.41	96.00	74.26	76.08	94.67	98.61	99.18	77.71	98.27	98.69	98.49	98.56	98.43	98.40	98.56	98.81	98.72
w/LOI	100.01	100.00	99.94	100.19	100.06	100.01	99.87	99.82	100.04	99.84	100.06	98.27	98.69	98.49	98.56	98.40	98.40	98.56	98.81	98.72
if Fe3+	100.47	100.39	100.44	100.24	100.21	100.46	100.35	99.99	100.35	99.89	100.74	98.95	99.37	99.17	99.93	99.78	99.77	99.04	99.30	99.21

Major elements are normalized on a volatile-free basis, with total Fe expressed as FeO.
® denotes a duplicate bead made from the same rock powder.

Legend for Figures 45, 46, 48, 52, 55, 57

- GSRM 2
- GSRM 3
- GSRM 4
- GSRM 5
- GSRM 6
- GSRM 7
- GSRM 8
- GSRM 9
- Atolia GD #101
- GSRM 26
- GSRM 27
- GSRM 30
- GSRM 32
- GSRM 28
- GSRM 29
- GSRM 31
- GSRM 33
- ERT 721
- CAL SB Atolia gr #210

Legend for Figures 43, 44, 47, 51, 56, 58

- GSRM 10
- GSRM 13
- JN 1826
- JN 1905
- JN 1906
- ERT Plate IV #2B
- GSRM 49
- GSRM 53
- GSRM 82A
- GSRM 25

Legend for Figures 49 & 50

- JN 1826
- JN 1905
- ERT Plate IV #2B
- Atolia GD #101
- ERT 721
- CAL SB Atolia gr #210
- GSRM 49
- GSRM 53
- GSRM 82A

Appendix D

40Ar/39Ar Geochronology Data Tables

These analyses were determined in the Auburn Noble Isotope Mass Analysis Lab (ANIMAL).

Irradiation Package: AU-37
Median Date of Irradiation: 7/2/21
Monitors, Ages
(as summarized in Schaen et al., 2021):
GA1550 Biotite Age (Ma): 9.944E+07
FC Sanidine Age (Ma): 2.820E+07
Date of Analysis: 8/31/2021
Measured 40/36 of Air during analyses: 291.6±1.5
Assumed 40Ar/36Ar of Air (Nier, 1950): 295.5
Irradiation Production Factors:
(36/37)Ca: 0.0003046±0.0000084
(39/37)Ca: 0.0007380±0.0000370
(40/39)K: 0±0.0044
(38/39)Cl: 0.01±0.01

The GLM-110 mass spectrometer was used for analysis, that is a 10-cm radius 90° sector instrument with double focusing geometry, a Nier-type source, and a single detector (an ATP discrete dynode-style electron multiplier, see Hames, 2020 for additional description). Samples were fused for gas extraction with a CO_2 laser. Operation of the laser, extraction line and mass spectrometer were fully automated. The time required for one complete analysis cycle is 20 minutes (4 minutes gettering, followed by generally 10 measurements per peak and baseline, 30 measurements of m/e=36). Sample inlet and equilibration time is 5 s for a half-split of a sample and 20 s for an entire sample. Blanks were measured following every 5th analysis. Blank corrections to 36 Ar measurements are based on an average or regression of several blanks measured for a given day of analysis. Air aliquots are typically analyzed 3 times per day (generally at the beginning of the day). Data were reduced using an Excel spreadsheet and Isoplot (Ludwig, 2012, Sp. Pub. BGC, 75 p.). Samples were irradiated for 16 hours with Cd shielding in the US Geological Survey TRIGA research reactor in Denver, CO.

Unless indicated otherwise, the data for individual measurements are in volts and errors are the standard deviation of measurement and do not include the error in estimating the J-Value (0.15% at the 95% confidence level). P = Laser Power Level (10 = 100%), t = laser heating time (s). Data are corrected for blank, mass discrimination, and interfering nuclear reactions.

The rubric for irradiation filenames is: 'AU + package"+ "layer, radial position" + "phase" + "planchet hole # and sequence", saved as a text file. All samples for this study were within layers 1 and 4 of AU37, with positions labeled as in sketch to the right, and the monitor data for these layers are included in the dataset below.

	P	t	m/e=40	39	38	37	36	moles 40	40Ar/36Ar	40Ar/38Ar
A representative anlaysis of a procedural 'blank' during the course of this analytical work.										
blank.8.3.21.b.txt			0.00676 ±0.000061	0.00018 ±0.000015	0.00004 ±0.000004	0.00010 ±0.000006	0.000043 ±0.000003	4.60E-17		
A representative analysis of air from a pipette during the course of this analysis.										
air.8.2.21.a.txt			11.29876 ±0.002652	-0.00034 ±0.000062	0.00742 ±0.000056	0.00006 ±0.000012	######## ±0.000094	7.69E-14	291.91 ±0.71444	1523.7 ±11.51

Sample	P	t	40Ar(*+atm)	39ArK	38Ar(atm+Cl)	37ArCa	36Ar(atm)	moles 40Ar	%Rad	R	Age (Ma)	%-sd
Measurements of argon isotopes and the J-value for single crystals of GA-1550 biotite (Layers 1 and 4 of AU37).												
au37.1a.bio.3a.txt	2	10	1.55101 ±0.001348	0.09699 ±0.000345	0.00077 ±0.000008	0.00023 ±0.000016	0.000754 ±0.000010	1.06E-14	86%	13.69341	97.258 ±0.473	0.49%
au37.1a.bio.5a.txt	2	10	1.77431 ±0.002117	0.12665 ±0.000379	0.00092 ±0.000012	0.00469 ±0.000053	0.000092 ±0.000005	1.21E-14	98%	13.79511	97.961 ±0.333	0.34%
au37.1a.bio.6a.txt	2	10	0.67903 ±0.000547	0.04383 ±0.000148	0.00035 ±0.000006	0.00240 ±0.000033	0.000245 ±0.000005	4.62E-15	89%	13.84065	98.276 ±0.462	0.47%
au37.1e.bio.8a.txt	3	10	2.82518 ±0.001807	0.19781 ±0.000571	0.00148 ±0.000011	0.02571 ±0.000123	0.000378 ±0.000006	1.92E-14	96%	13.71823	97.430 ±0.308	0.32%
au37.1e.bio.13a.txt	3	10	1.46834 ±0.001223	0.10473 ±0.000329	0.00074 ±0.000011	0.00038 ±0.000013	0.000083 ±0.000010	9.99E-15	98%	13.78563	97.896 ±0.384	0.39%
au37.1i.bio.15a.txt	3	10	0.41327 ±0.000659	0.02799 ±0.000143	0.00021 ±0.000005	0.00007 ±0.000010	0.000096 ±0.000004	2.81E-15	93%	13.74903	97.643 ±0.646	0.66%
au37.1i.bio.16a.txt	3	10	4.69618 ±0.002844	0.31959 ±0.000309	0.00249 ±0.000021	0.00079 ±0.000020	0.001057 ±0.000010	3.19E-14	93%	13.71768	97.426 ±0.138	0.14%
au37.1i.bio.17a.txt	3	10	0.29708 ±0.000279	0.02088 ±0.000092	0.00016 ±0.000006	0.00008 ±0.000014	0.000021 ±0.000011	2.02E-15	98%	13.92512	98.860 ±1.163	1.18%
au37.1i.bio.18a.txt	3	10	0.57463 ±0.000978	0.03813 ±0.000229	0.00031 ±0.000007	0.00008 ±0.000010	0.000174 ±0.000009	3.91E-15	91%	13.72006	97.442 ±0.829	0.85%
au37.1i.bio.19a.txt	3	10	1.30336 ±0.001343	0.09229 ±0.000314	0.00064 ±0.000008	0.00304 ±0.000039	0.000115 ±0.000008	8.87E-15	97%	13.75559	97.688 ±0.404	0.41%
au37.1s.bio.21a.txt	3	10	1.10632 ±0.000785	0.07310 ±0.000247	0.00057 ±0.000008	0.00026 ±0.000015	0.000354 ±0.000009	7.53E-15	91%	13.70421	95.927 ±0.455	0.47%
au37.1s.bio.22a.txt	3	10	0.93538 ±0.000910	0.06385 ±0.000248	0.00046 ±0.000009	0.00008 ±0.000017	0.000229 ±0.000008	6.36E-15	93%	13.59167	95.160 ±0.493	0.52%
au37.1s.bio.23a.txt	3	10	0.41249 ±0.000424	0.02879 ±0.000164	0.00025 ±0.000005	0.00010 ±0.000017	0.000077 ±0.000008	2.81E-15	94%	13.53529	94.775 ±0.810	0.85%
au37.1s.bio.24a.txt	3	10	2.21299 ±0.001675	0.15750 ±0.000282	0.00117 ±0.000011	0.00462 ±0.000034	0.000230 ±0.000009	1.51E-14	97%	13.61935	95.348 ±0.226	0.24%
au37.4c.bio.65a.txt	3	10	3.02901 ±0.002570	0.20399 ±0.000615	0.00139 ±0.000012	0.00143 ±0.000025	0.000615 ±0.000008	2.06E-14	94%	13.95783	99.086 ±0.341	0.34%
au37.4c.bio.66a.txt	3	10	10.06090 ±0.006963	0.70688 ±0.000631	0.00471 ±0.000030	0.02205 ±0.000182	0.000749 ±0.000010	6.84E-14	98%	13.91964	98.822 ±0.118	0.12%
au37.4c.bio.67a.txt	3	10	6.52556 ±0.005413	0.44544 ±0.000642	0.00308 ±0.000014	0.00990 ±0.000063	0.001103 ±0.000013	4.44E-14	95%	13.91822	98.812 ±0.184	0.19%
au37.4c.bio.68a.txt	3	10	3.89317 ±0.005026	0.26993 ±0.000374	0.00186 ±0.000030	0.00025 ±0.000025	0.000463 ±0.000008	2.65E-14	96%	13.91649	98.800 ±0.203	0.21%
au37.4g.bio.70a.txt	3	10	5.33266 ±0.002900	0.35918 ±0.000703	0.00243 ±0.000031	0.00080 ±0.000016	0.001057 ±0.000009	3.63E-14	94%	13.97736	99.220 ±0.220	0.22%
au37.4g.bio.71a.txt	3	10	12.46453 ±0.005966	0.89363 ±0.001179	0.00566 ±0.000027	0.00147 ±0.000021	0.000215 ±0.000018	8.48E-14	99%	13.87700	97.104 ±0.143	0.15%
au37.4g.bio.72a.txt	3	10	3.56518 ±0.002939	0.22136 ±0.000371	0.00169 ±0.000018	0.00044 ±0.000016	0.001622 ±0.000027	2.43E-14	87%	13.94093	98.969 ±0.336	0.34%
au37.4g.bio.73a.txt	3	10	2.74447 ±0.002220	0.19092 ±0.000364	0.00128 ±0.000015	0.00078 ±0.000023	0.000256 ±0.000007	1.87E-14	97%	13.97850	99.228 ±0.224	0.23%
au37.4g.bio.74a.txt	3	10	2.40387 ±0.002478	0.16496 ±0.000522	0.00109 ±0.000008	0.00086 ±0.000034	0.000316 ±0.000008	1.64E-14	96%	14.00692	99.425 ±0.359	0.36%
au37.4k.bio.75a.txt	3	10	4.14068 ±0.002257	0.26537 ±0.000336	0.00198 ±0.000010	0.00054 ±0.000022	0.001493 ±0.000012	2.82E-14	89%	13.94085	98.968 ±0.181	0.18%
au37.4k.bio.76a.txt	3	10	5.39160 ±0.002926	0.37598 ±0.000650	0.00268 ±0.000027	0.00109 ±0.000030	0.000502 ±0.000019	3.67E-14	97%	13.94536	98.999 ±0.212	0.21%
au37.4k.bio.77a.txt	3	10	4.42706 ±0.004040	0.31458 ±0.000755	0.00223 ±0.000038	0.01049 ±0.000094	0.000221 ±0.000006	3.01E-14	99%	13.86499	98.444 ±0.260	0.26%
au37.4k.bio.78a.txt	3	10	0.79401 ±0.000724	0.05404 ±0.000279	0.00036 ±0.000006	0.00012 ±0.000007	0.000127 ±0.000005	5.40E-15	95%	13.99973	99.375 ±0.586	0.59%
au37.4k.bio.79a.txt	3	10	0.84103 ±0.000972	0.05862 ±0.000245	0.00040 ±0.000007	0.00016 ±0.000014	0.000043 ±0.000009	5.72E-15	98%	14.13023	100.276 ±0.545	0.54%
au37.4s.bio.80a.txt	3	10	13.58551 ±0.009494	0.95115 ±0.001483	0.00652 ±0.000028	0.00972 ±0.000050	0.001023 ±0.000014	9.24E-14	98%	13.96544	99.138 ±0.176	0.18%
au37.4s.bio.81a.txt	3	10	4.34159 ±0.002126	0.30725 ±0.000542	0.00207 ±0.000016	0.00194 ±0.000026	0.000202 ±0.000012	2.95E-14	99%	13.93642	98.938 ±0.202	0.20%
au37.4s.bio.82a.txt	3	10	6.39031 ±0.003840	0.44245 ±0.000528	0.00300 ±0.000027	0.00466 ±0.000059	0.000720 ±0.000009	4.35E-14	97%	13.96198	99.114 ±0.143	0.14%
au37.4s.bio.83a.txt	3	10	4.10710 ±0.003036	0.28855 ±0.000607	0.00195 ±0.000014	0.01577 ±0.000122	0.000281 ±0.000008	2.79E-14	98%	13.94615	99.005 ±0.233	0.24%
au37.4s.bio.84a.txt	3	10	1.47549 ±0.000890	0.10504 ±0.000372	0.00070 ±0.000008	0.00057 ±0.000012	0.000031 ±0.000009	1.00E-14	99%	13.96089	99.107 ±0.403	0.41%

Measuremnt of argon isotopes and J-values for the monitor FCS (layers 1 and 4 of AU37).

au37.1a.san.23a.txt	2	10	6.83918 ±0.005883	1.78671 ±0.000962	0.00547 ±0.000030	0.01238 ±0.000116	0.000069 ±0.000009	4.65E-14	100%	3.81644	27.638 ±0.030	0.11%
au37.1a.san.24a.txt	2	10	8.52888 ±0.010604	2.21576 ±0.002732	0.00648 ±0.000033	0.01530 ±0.000087	0.000195 ±0.000005	5.80E-14	99%	3.82314	27.686 ±0.049	0.18%
au37.1a.san.25a.txt	2	10	5.09930 ±0.005809	1.33504 ±0.002128	0.00360 ±0.000016	0.00899 ±0.000065	0.000029 ±0.000004	3.47E-14	100%	3.81315	27.614 ±0.055	0.20%
au37.1a.san.26a.txt	2	10	4.00553 ±0.003380	1.04241 ±0.000816	0.00311 ±0.000028	0.00835 ±0.000078	0.000110 ±0.000005	2.73E-14	99%	3.81142	27.602 ±0.033	0.12%
au37.1a.san.27a.txt	2	10	4.47884 ±0.003057	1.17123 ±0.001833	0.00367 ±0.000035	0.00865 ±0.000087	0.000009 ±0.000006	3.05E-14	100%	3.82184	27.676 ±0.050	0.18%
au37.1s.san.28a.txt	2	10	8.07649 ±0.006593	2.10848 ±0.002253	0.00548 ±0.000029	0.01360 ±0.000084	0.000198 ±0.000006	5.49E-14	99%	3.80274	27.134 ±0.037	0.14%
au37.1s.san.29a.txt	2	10	4.17555 ±0.003604	1.00264 ±0.001222	0.00395 ±0.000033	0.00789 ±0.000075	0.001165 ±0.000011	2.84E-14	92%	3.82125	27.672 ±0.051	0.18%
au37.1s.san.30a.txt	2	10	6.33309 ±0.003929	1.63307 ±0.002165	0.00433 ±0.000025	0.01089 ±0.000057	0.000055 ±0.000005	4.31E-14	100%	3.86802	27.596 ±0.041	0.15%
au37.1s.san.31a.txt	2	10	3.66229 ±0.001447	0.95841 ±0.001006	0.00278 ±0.000020	0.00684 ±0.000063	0.000020 ±0.000004	2.49E-14	100%	3.81502	27.627 ±0.033	0.12%
au37.1s.san.32a.txt	2	10	4.47230 ±0.003369	1.15340 ±0.001039	0.00345 ±0.000018	0.01076 ±0.000098	0.000211 ±0.000005	3.04E-14	99%	3.82354	27.689 ±0.035	0.12%
au37.4c.san.43a.txt	3	10	7.59588 ±0.006947	1.95599 ±0.002087	0.00593 ±0.000036	0.01396 ±0.000177	0.000098 ±0.000008	5.17E-14	100%	3.86853	28.012 ±0.041	0.14%
au37.4c.san.44a.txt	3	10	5.67845 ±0.003890	1.45798 ±0.000830	0.00441 ±0.000037	0.01038 ±0.000057	0.000140 ±0.000006	3.86E-14	99%	3.86631	27.996 ±0.027	0.10%
au37.4c.san.45a.txt	3	10	12.15613 ±0.008308	3.13823 ±0.002681	0.00912 ±0.000038	0.02183 ±0.000120	0.000120 ±0.000017	8.27E-14	100%	3.86226	27.967 ±0.033	0.12%
au37.4c.san.46a.txt	3	10	4.90994 ±0.003072	1.26473 ±0.001233	0.00380 ±0.000035	0.00866 ±0.000061	0.000002 ±0.000003	3.34E-14	100%	3.88184	28.108 ±0.035	0.12%
au37.4c.san.47a.txt	3	10	4.46241 ±0.003876	1.14239 ±0.001192	0.00394 ±0.000040	0.02049 ±0.000059	0.000204 ±0.000006	3.04E-14	99%	3.85353	27.904 ±0.040	0.14%
au37.4s.san.48a.txt	3	10	5.74058 ±0.005492	1.47883 ±0.002547	0.00431 ±0.000035	0.01006 ±0.000090	0.000027 ±0.000009	3.91E-14	100%	3.87643	28.069 ±0.057	0.20%
au37.4s.san.49a.txt	3	10	9.29625 ±0.009058	2.29727 ±0.003360	0.00705 ±0.000048	0.06134 ±0.000201	0.001305 ±0.000008	6.32E-14	96%	3.87882	28.086 ±0.052	0.19%
au37.4s.san.50a.txt	3	10	4.54780 ±0.005844	1.16354 ±0.001659	0.00348 ±0.000033	0.00795 ±0.000090	-0.000002 -±0.000106	3.09E-14	100%	3.90915	28.304 ±0.057	0.20%
au37.4s.san.51a.txt	3	10	6.90161 ±0.005573	1.77141 ±0.001319	0.00510 ±0.000024	0.01599 ±0.000159	0.000179 ±0.000006	4.70E-14	99%	3.86623	27.995 ±0.032	0.11%
au37.4s.san.52a.txt	3	10	4.85291 ±0.003692	1.25056 ±0.000820	0.00349 ±0.000029	0.00827 ±0.000126	0.000038 ±0.000004	3.30E-14	100%	3.87171	28.035 ±0.029	0.10%

J-Values used for layers 1 and 4 on the basis of GA-1550 and FCS analyses above, all errors 2 sigma:

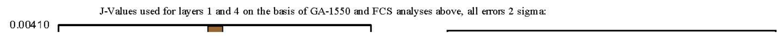

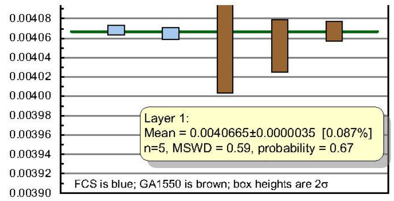

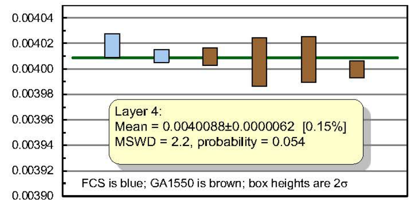

GSRM-57B, Clear to silver-grey muscovite, a single crystal ca. 0.7 mm in diameter (from 18/20 mesh size range).

Sample	P	t	40Ar(*+atm)	39ArK	38Ar(atm+Cl)	37ArCa	36Ar(atm)	Moles 40Ar	%Rad	R	Age (Ma)	%-sd
au37.1b.mus.1a.txt	1	30	0.04684 ± 0.000223	0.00182 ± 0.000033	0.00004 ± 0.000006	0.00338 ± 0.000043	0.000141 ± 0.000006	3.19E-16	10.9%	2.80848	20.8 ± 8.4	40.5%
au37.1b.mus.1b.txt	1	30	0.02099 ± 0.000214	0.00105 ± 0.000024	0.00003 ± 0.000007	0.00108 ± 0.000025	0.000060 ± 0.000006	1.43E-16	16.0%	3.19036	23.6 ± 13.0	55.0%
au37.1b.mus.1c.txt	1	30	0.06190 ± 0.000303	0.00433 ± 0.000032	0.00007 ± 0.000006	0.00280 ± 0.000038	0.000159 ± 0.000008	4.21E-16	23.9%	3.42101	25.3 ± 4.1	16.3%
au37.1b.mus.1d.txt	1	30	0.05206 ± 0.000243	0.00790 ± 0.000042	0.00008 ± 0.000006	0.00179 ± 0.000050	0.000131 ± 0.000006	3.54E-16	25.8%	1.69866	12.6 ± 1.7	13.2%
au37.1b.mus.1e.txt	1	30	0.05252 ± 0.000292	0.01078 ± 0.000058	0.00010 ± 0.000006	0.00240 ± 0.000070	0.000102 ± 0.000006	3.57E-16	42.5%	2.07249	15.36 ± 1.17	7.6%
au37.1b.mus.1f.txt	1	30	0.03606 ± 0.000184	0.00832 ± 0.000042	0.00008 ± 0.000004	0.00170 ± 0.000054	0.000056 ± 0.000005	2.45E-16	54.0%	2.34023	17.34 ± 1.41	8.1%
au37.1b.mus.1g.txt	1	30	0.04233 ± 0.000302	0.00885 ± 0.000058	0.00008 ± 0.000004	0.00160 ± 0.000044	0.000027 ± 0.000009	2.88E-16	81.1%	3.87704	28.63 ± 2.23	7.8%
au37.1b.mus.1h.txt	1	30	0.12533 ± 0.000397	0.02029 ± 0.000145	0.00016 ± 0.000004	0.00318 ± 0.000052	0.000082 ± 0.000010	8.53E-16	80.7%	4.98330	36.72 ± 1.19	3.2%
au37.1b.mus.1i.txt	1	30	0.20536 ± 0.000366	0.02619 ± 0.000079	0.00013 ± 0.000004	0.00256 ± 0.000037	0.000099 ± 0.000005	1.40E-15	85.8%	6.72653	49.40 ± 0.46	0.9%
au37.1b.mus.1j.txt	1	30	0.31588 ± 0.000497	0.03630 ± 0.000125	0.00012 ± 0.000003	0.00128 ± 0.000044	0.000049 ± 0.000011	2.15E-15	95.4%	8.30230	60.78 ± 0.69	1.1%
au37.1b.mus.1k.txt	2	30	0.62563 ± 0.000711	0.06945 ± 0.000177	0.00019 ± 0.000003	0.00080 ± 0.000022	0.000109 ± 0.000006	4.26E-15	94.8%	8.54256	62.51 ± 0.26	0.4%
au37.1b.mus.1l.txt	2	30	0.81186 ± 0.000422	0.08533 ± 0.000333	0.00023 ± 0.000004	0.00057 ± 0.000018	0.000102 ± 0.000006	5.52E-15	96.3%	9.16279	66.97 ± 0.32	0.5%
au37.1b.mus.1m.txt	2	30	3.43125 ± 0.002036	0.34904 ± 0.001002	0.00090 ± 0.000006	0.00074 ± 0.000050	0.000231 ± 0.000006	2.33E-14	98.0%	9.63468	70.35 ± 0.21	0.3%
au37.1b.mus.1n.txt	2	30	5.64926 ± 0.002925	0.57278 ± 0.001001	0.00154 ± 0.000009	0.00061 ± 0.000028	0.000222 ± 0.000013	3.84E-14	98.8%	9.74814	**71.16 ± 0.14**	0.2%
au37.1b.mus.1o.txt	2	30	3.55000 ± 0.002422	0.36007 ± 0.000385	0.00110 ± 0.000015	0.00036 ± 0.000025	0.000107 ± 0.000006	2.42E-14	99.1%	9.77119	**71.33 ± 0.10**	0.1%
au37.1b.mus.1p.txt	2	30	3.42260 ± 0.002073	0.34546 ± 0.000730	0.00089 ± 0.000008	0.00027 ± 0.000023	0.000109 ± 0.000009	2.33E-14	99.1%	9.81451	**71.64 ± 0.17**	0.2%
au37.1b.mus.1q.txt	2	30	1.69619 ± 0.001588	0.17148 ± 0.000286	0.00052 ± 0.000008	0.00019 ± 0.000023	0.000043 ± 0.000008	1.15E-14	99.3%	9.81711	**71.65 ± 0.17**	0.2%
au37.1b.mus.1r.txt	2	30	1.35885 ± 0.001068	0.13578 ± 0.000304	0.00033 ± 0.000006	0.00013 ± 0.000021	0.000046 ± 0.000008	9.24E-15	99.0%	9.90834	**72.31 ± 0.22**	0.3%
au37.1b.mus.1s.txt	3	20	0.69080 ± 0.000521	0.06997 ± 0.000212	0.00016 ± 0.000003	0.00009 ± 0.000021	-0.000014 ± 0.000010	4.70E-15	######	9.87329	**72.06 ± 0.38**	0.5%
au37.1b.mus.1t.txt	3	20	0.57850 ± 0.000622	0.05776 ± 0.000267	0.00014 ± 0.000003	0.00009 ± 0.000027	0.000018 ± 0.000010	3.94E-15	99.1%	9.92442	**72.42 ± 0.50**	0.7%

Ages in bold were used to calculate an 'integrated' (mean) age.

Age = 71.50±0.39 Ma
(95% conf.), including J-error of .125%)
MSWD = 5.0, probability = 0.000
73.1% of the 39Ar, steps 14 through 20

GSRM-57B, Blue-Green Mariposite (fuchsite), a single crystal ~0.7 mm in diamter (from 18/20 mesh size range).

Sample	P	t	40Ar(*+atm)	39ArK	38Ar(atm+Cl)	37ArCa	36Ar(atm)	Moles 40Ar	%Rad	R	Age (Ma)	%-sd
au37.1b.fus.2a.txt	1	30	0.01934 ± 0.000189	0.00213 ± 0.000040	0.00001 ± 0.000003	0.00020 ± 0.000020	0.000028 ± 0.000011	1.32E-16	57.5%	5.21292	38.40 ± 11.75	30.6%
au37.1b.fus.2b.txt	1	30	0.02571 ± 0.000193	0.00323 ± 0.000029	0.00002 ± 0.000003	0.00025 ± 0.000033	0.000054 ± 0.000009	1.75E-16	37.4%	2.97354	22.00 ± 6.03	27.4%
au37.1b.fus.2c.txt	1	30	0.05242 ± 0.000234	0.00748 ± 0.000055	0.00005 ± 0.000005	0.00137 ± 0.000051	0.000089 ± 0.000009	3.57E-16	49.8%	3.48546	25.76 ± 2.72	10.6%
au37.1b.fus.2d.txt	1	30	0.07827 ± 0.000275	0.01264 ± 0.000064	0.00008 ± 0.000004	0.00230 ± 0.000037	0.000087 ± 0.000009	5.32E-16	67.1%	4.15687	30.68 ± 1.65	5.4%
au37.1b.fus.2e.txt	1	30	0.09508 ± 0.000293	0.01600 ± 0.000115	0.00007 ± 0.000004	0.00155 ± 0.000044	0.000047 ± 0.000009	6.47E-16	85.3%	5.06946	37.35 ± 1.22	3.3%
au37.1b.fus.2f.txt	1	30	0.15320 ± 0.000368	0.02470 ± 0.000138	0.00008 ± 0.000002	0.00058 ± 0.000027	0.000029 ± 0.000007	1.04E-15	94.4%	5.85370	43.06 ± 0.67	1.6%
au37.1b.fus.2g.txt	1	30	0.19463 ± 0.000344	0.02845 ± 0.000113	0.00007 ± 0.000003	0.00023 ± 0.000019	0.000028 ± 0.000007	1.32E-15	95.7%	6.54783	48.10 ± 0.57	1.2%
au37.1b.fus.2h.txt	1	30	0.27201 ± 0.000397	0.03571 ± 0.000155	0.00008 ± 0.000002	0.00027 ± 0.000026	-0.000003 ± 0.000008	1.85E-15	######	7.61689	55.84 ± 0.56	1.0%
au37.1b.fus.2i.txt	1	30	0.37538 ± 0.000841	0.04598 ± 0.000343	0.00010 ± 0.000002	0.00029 ± 0.000022	0.000006 ± 0.000008	2.55E-15	99.5%	8.12497	59.50 ± 0.61	1.0%
au37.1b.fus.2j.txt	1	30	0.63022 ± 0.000792	0.07205 ± 0.000253	0.00017 ± 0.000003	0.00035 ± 0.000027	0.000006 ± 0.000009	4.29E-15	99.7%	8.72350	63.81 ± 0.37	0.6%
au37.1b.fus.2k.txt	2	30	2.09265 ± 0.001960	0.22100 ± 0.000377	0.00061 ± 0.000006	0.00069 ± 0.000033	0.000043 ± 0.000013	1.42E-14	99.4%	9.41094	68.75 ± 0.19	0.3%
au37.1b.fus.2l.txt	2	30	6.93528 ± 0.005281	0.70480 ± 0.001026	0.00191 ± 0.000016	0.00118 ± 0.000033	0.000133 ± 0.000015	4.72E-14	99.4%	9.78434	**71.42 ± 0.13**	0.2%
au37.1b.fus.2m.txt	2	30	9.43578 ± 0.009114	0.95489 ± 0.001149	0.00276 ± 0.000025	0.00214 ± 0.000053	0.000165 ± 0.000010	6.42E-14	99.5%	9.83042	**71.75 ± 0.11**	0.2%
au37.1b.fus.2n.txt	2	30	2.22036 ± 0.001590	0.22204 ± 0.000538	0.00066 ± 0.000010	0.00042 ± 0.000029	0.000046 ± 0.000010	1.51E-14	99.4%	9.93794	**72.52 ± 0.21**	0.3%
au37.1b.fus.2o.txt	2	30	0.75746 ± 0.001085	0.07564 ± 0.000298	0.00022 ± 0.000004	0.00013 ± 0.000015	0.000005 ± 0.000011	5.15E-15	99.8%	9.99325	**72.92 ± 0.44**	0.6%
au37.1b.fus.2p.txt	2	30	0.58840 ± 0.000714	0.05932 ± 0.000291	0.00016 ± 0.000003	0.00000 ± 0.000022	0.000019 ± 0.000008	4.00E-15	99.1%	9.82717	**71.73 ± 0.46**	0.6%
au37.1b.fus.2q.txt	2	30	0.40037 ± 0.000598	0.04016 ± 0.000128	0.00011 ± 0.000002	0.00004 ± 0.000027	-0.000015 ± 0.000009	2.72E-15	######	9.97021	**72.75 ± 0.54**	0.7%
au37.1b.fus.2r.txt	2	30	0.30438 ± 0.000621	0.03044 ± 0.000179	0.00008 ± 0.000002	0.00005 ± 0.000029	0.000003 ± 0.000010	2.07E-15	99.7%	9.97215	**72.76 ± 0.82**	1.1%
au37.1b.fus.2s.txt	3	20	0.15742 ± 0.000296	0.01560 ± 0.000061	0.00004 ± 0.000002	0.00001 ± 0.000030	-0.000010 ± 0.000009	1.07E-15	######	10.09060	**73.61 ± 1.27**	1.7%

Ages in bold were used to calculate an 'integrated' (mean) age.

Age = 71.80_0.40 Ma
(95% conf.), including J-error of .125%)
MSWD = 5, probability = 0.000
81.8% of the 39Ar, steps 12 through 19

Meanof two mica ages:
71.6_1.9 [2.7%] 95% conf.
Wtd by data-pt errs only, 0 of 2 rej.
MSWD = 1.15, probability = 0.28

GSRM84C, Muscovite, 60/80 mesh size range; analyses of about 10 small and very thin crystals, each ca. 0.15 mm in diameter

Sample	P	t	40Ar(*+atm)	39ArK	38Ar(atm+Cl)	37ArCa	36Ar(atm)	Moles 40Ar	%Rad	R	Age (Ma)	%-sd
au37.4o.mus.4a.txt	1	30	0.04110 ± 0.000232	0.00640 ± 0.000060	0.00003 ± 0.000004	0.00151 ± 0.000044	0.000011 ± 0.000010	2.80E-16	92%	5.93279	43.03 ± 3.37	8%
au37.4o.mus.4b.txt	1	30	0.03933 ± 0.000238	0.00541 ± 0.000056	0.00004 ± 0.000004	0.00118 ± 0.000033	0.000009 ± 0.000008	2.68E-16	93%	6.78032	49.09 ± 3.32	7%
au37.4o.mus.4c.txt	1	30	0.09873 ± 0.000389	0.00861 ± 0.000077	0.00006 ± 0.000005	0.00193 ± 0.000041	0.000014 ± 0.000010	6.72E-16	96%	10.99567	78.96 ± 2.72	3%
au37.4o.mus.4d.txt	1	30	0.37622 ± 0.000371	0.02176 ± 0.000076	0.00009 ± 0.000004	0.00699 ± 0.000143	0.000028 ± 0.000010	2.56E-15	98%	16.91096	120.07 ± 1.15	1%
au37.4o.mus.4e.txt	1	30	0.65831 ± 0.001013	0.02888 ± 0.000081	0.00012 ± 0.000005	0.00792 ± 0.000085	0.000032 ± 0.000011	4.48E-15	99%	22.46738	157.86 ± 0.98	1%
au37.4o.mus.4f.txt	1	30	0.60075 ± 0.000528	0.02603 ± 0.000100	0.00008 ± 0.000003	0.00369 ± 0.000071	0.000022 ± 0.000009	4.09E-15	99%	22.82930	160.30 ± 0.99	1%
Crystals moved during analysis such that they were heated and degassed unevenly - subsequent analyses repeat the overall pattern of the first 6 steps.												
au37.4o.mus.4g.txt	1	30	0.54420 ± 0.000916	0.04066 ± 0.000161	0.00013 ± 0.000005	0.00141 ± 0.000055	0.000030 ± 0.000009	3.70E-15	98%	13.16548	94.15 ± 0.62	1%
au37.4o.mus.4h.txt	1	30	0.88510 ± 0.000910	0.05014 ± 0.000127	0.00014 ± 0.000004	0.00035 ± 0.000026	0.000040 ± 0.000005	6.02E-15	99%	17.41748	123.55 ± 0.41	0%
au37.4o.mus.4i.txt	1	30	0.62318 ± 0.000705	0.04995 ± 0.000254	0.00012 ± 0.000004	0.00019 ± 0.000025	0.000053 ± 0.000005	4.24E-15	97%	12.16151	87.14 ± 0.52	1%
au37.4o.mus.4j.txt	1	30	0.81006 ± 0.000722	0.05046 ± 0.000146	0.00015 ± 0.000004	0.00016 ± 0.000023	0.000054 ± 0.000006	5.51E-15	98%	15.73838	111.99 ± 0.42	0%
au37.4o.mus.4k.txt	1	30	0.50917 ± 0.000568	0.03772 ± 0.000221	0.00011 ± 0.000003	0.00002 ± 0.000020	0.000027 ± 0.000005	3.46E-15	98%	13.28964	95.01 ± 0.64	1%
au37.4o.mus.4l.txt	2	30	0.33071 ± 0.000273	0.03170 ± 0.000085	0.00009 ± 0.000003	0.00002 ± 0.000024	0.000021 ± 0.000005	2.25E-15	98%	10.23658	73.62 ± 0.39	1%
au37.4o.mus.4m.txt	2	30	0.22125 ± 0.000301	0.02022 ± 0.000102	0.00006 ± 0.000002	0.00003 ± 0.000022	0.000027 ± 0.000008	1.51E-15	96%	10.55102	75.83 ± 0.92	1%
au37.4o.mus.4n.txt	2	30	0.20602 ± 0.000487	0.01832 ± 0.000102	0.00005 ± 0.000002	0.00005 ± 0.000019	0.000012 ± 0.000008	1.40E-15	98%	11.04743	79.32 ± 1.04	1%
au37.4o.mus.4o.txt	2	30	0.20743 ± 0.000537	0.01767 ± 0.000089	0.00006 ± 0.000002	-0.00001 ± 0.000021	0.000010 ± 0.000008	1.41E-15	99%	11.57326	83.01 ± 1.09	1%
au37.4o.mus.4p.txt	2	20	0.12397 ± 0.000262	0.01063 ± 0.000053	0.00003 ± 0.000002	0.00004 ± 0.000022	0.000004 ± 0.000005	8.43E-16	99%	11.55292	82.87 ± 1.06	1%
au37.4o.mus.4q.txt	2	20	0.08428 ± 0.000215	0.00547 ± 0.000081	0.00002 ± 0.000003	0.00002 ± 0.000018	0.000004 ± 0.000005	5.73E-16	98%	15.17580	108.11 ± 2.45	2%
au37.4o.mus.4r.txt	2	20	0.06887 ± 0.000258	0.00497 ± 0.000039	0.00002 ± 0.000003	0.00003 ± 0.000020	0.000001 ± 0.000008	4.69E-16	99%	13.78178	98.44 ± 3.50	4%
au37.4o.mus.4s.txt	3	20	0.05198 ± 0.000220	0.00419 ± 0.000043	0.00001 ± 0.000001	-0.00012 ± 0.000036	0.000003 ± 0.000004	3.54E-16	98%	12.18328	87.29 ± 2.31	3%
au37.4o.mus.4t.txt	3	20	0.03452 ± 0.000194	0.00279 ± 0.000038	0.00001 ± 0.000002	0.00000 ± 0.000025	0.000006 ± 0.000004	2.35E-16	95%	11.74107	84.19 ± 3.51	4%

Results for this incremental heating analysis were compromised by an analytical artifact. The apparent ages range from ca. 43 to 160 Ma, however any interpretations of geological significance for these ages (for this sample of muscovite collected from a fault breccia) would be ambiguous.